Doctorate Dissertation

博士論文

Floquet engineering of topological phenomena and nonlinear systems

(トポロジカル現象と非線形系のフロケエンジニアリング)

A Dissertation Submitted for Degree of Doctor of Philosophy

December 2018

平成30年12月 博士（理学）申請

Department of Physics, Graduate School of Science,

The University of Tokyo

東京大学大学院理学系研究科物理学専攻

Sho Higashikawa

東川　翔

Abstract

Periodically driven systems have a long history of study in many subfields of physics and periodic drives have long served as flexible experimental tools for controlling and even engineering non-equilibrium systems. Owing to the rapid development in laser and ultrafast spectroscopy techniques, this form of engineering of quantum systems, which is usually termed as Floquet engineering, has become an emergent field of research over the last decade. Exotic states of matter, that are not accessible in equilibrium systems, have been realized by means of Floquet engineering. In this thesis, we consider two applications of Floquet engineering to topological quantum phenomena and nonlinear classical systems.

In the first part of the study, we consider topological band structures in periodically driven systems. A Weyl fermion, which is a prototypical example of topological semimetals, has recently attracted considerable interest owing to its exotic magnetic response, namely the chiral magnetic effect. However, this response vanishes in a static lattice system such as a solid because Weyl fermions should appear in pairs within a single band because of the Nielsen-Ninomiya theorem. Here, we present a concrete model on a periodically driven three-dimensional lattice that features a single Weyl fermion within a single band, thereby surpassing the above limitation. The key idea is to utilize the nontrivial topology in the Floquet unitary operator, namely the periodicity of quasienergies. Its nontrivial topology ensures the presence and the stability of a single Weyl fermion in its quasienergy spectrum. Because of the emergent single Weyl fermion in the Floquet unitary operator, a spin-polarized gas moves parallel to its spin polarization under the external drive, which is a consequence of the spin-momentum locking of a Weyl fermion. Moreover, when we apply a magnetic field, a current flows antiparallel to the magnetic field and this current takes a quantized value for suitable band filling and temperature, which is a Floquet realization of the chiral magnetic effect. By generalizing the above idea to include symmetries, we give a topological classification of Floquet unitary operators in the Altland-Zirnbauer symmetry classes for all dimensionalities and construct concrete models with nontrivial topological numbers for each class and dimensionality. From these results, we show that all gapless surface states of topological insulators and superconductors can emerge in bulk quasienergy spectra in Floquet systems.

In the second part of the study, we consider periodically driven nonlinear systems governed by nonlinear stochastic equations. In periodically driven quantum systems, it is known that their dynamics is, on average, described by a static effective Hamiltonian according to the Floquet theorem and that the effective Hamiltonian is systematically determined from the high-frequency expansion. However, we cannot directly apply this theorem and the high-frequency expansion to nonlinear classical systems because they can be applied only to linear equations like the Schrödinger equation. Here, we overcome this difficulty by employing a master-equation approach and thereby develop the high-frequency expansion of their equations of motion. Our formalism is applicable not only to classical systems but also to quantum ones in symmetry-

broken phases and covers both isolated and open systems. By analytically evaluating the higher-order terms of the high-frequency expansion, we find that an effective equation of motion derived from the high-frequency expansion well describes the exact time evolution for a high-frequency drive. In particular, for driven dissipative systems, it well reproduces the exact dynamics until they reach their non-equilibrium steady states. This result is in stark contrast to driven isolated systems, where the high-frequency expansion works only in the intermediate regime before they heat up to infinite-temperature states. These analytical findings are numerically confirmed for a single-body system and a many-body system by examples of the Kapitza pendulum with friction and a laser-driven magnet coupled with a thermal bath, respectively. Finally, we present an application to spintronics, where we demonstrate an optical control of a spin chirality by a laser.

Publication List

This thesis is based on the following publications:

[1] S. Higashikawa, M. Nakagawa, and M. Ueda, *Floquet chiral magnetic effect*, arXiv: 1806.06868 (2018).

[2] S. Higashikawa, H. Fujita, and M. Sato, *Floquet engineering of classical systems*, arXiv: 1810.01103 (2018).

The following publications are not directly related to this thesis:

[3] T. Yoshino, S. Furukawa, S. Higashikawa, M. Ueda, *Collective modes of vortex lattices in two-component Bose-Einstein condensates under synthetic gauge fields*, New Journal of Physics 21, 015001 (2019). [invited paper in Spotlight on Multicomponent Matter]

[4] K. Kawabata, S. Higashikawa, Z. Gong, Y. Ashida, and M. Ueda, *Topological Unification of Time-Reversal and Particle-Hole Symmetries in Non-Hermitian Physics*, Nature Communications 10, 297 (2019). [selected in Editors' Highlights]

[5] Z. Gong, Y. Ashida, K. Kawabata, K. Takasan, S. Higashikawa, and M. Ueda, *Topological phases of non-Hermitian systems*, Physical Review X 8, 031079 (2018). [highlighted in Viewpoint]

[6] Z. Gong, S. Higashikawa, and M. Ueda. *Zeno Hall effect*, Physical Review Letters 118, 200401 (2017). [selected as Editors' Suggestion]

[7] S. Higashikawa and M. Ueda, *Influence of topological constraints and topological excitations: Decomposition formulas for calculating homotopy groups of symmetry-broken phases*, Physical Review B 95, 134520 (2017).

[8] S. Higashikawa and M. Ueda, *μ-symmetry breaking: An algebraic approach to finding mean fields of quantum many-body systems*, Physical Review A 94, 013613 (2016).

List of Abbreviations

- ASEP: asymmetric simple exclusion process
- AZ symmetry classes: Altland-Zirnbauer symmetry classes
- BZ: Brillouin zone
- CME: chiral magnetic effect
- CS: chiral symmetry
- DM interaction: Dzyaloshinskii-Moriya interaction
- EOM: equation of motion
- ETH: eigenstate thermalization hypothesis
- FM HFE: Floquet-Magnus high-frequency expansion
- FP equation, FP operator: Fokker-Planck equation, Fokker-Planck operator
- GP equation: Gross-Pitaevskii equation
- HFE: high-frequency expansion
- LLG equation: Landau-Lifshitz-Gilbert equation
- NESS: non-equilibrium steady state
- PHS: particle-hole symmetry
- QSH insulator: quantum spin Hall insulator
- sLLG equation: stochastic Landau-Lifshitz-Gilbert equation
- SPT phase: symmetry-protected topological phase
- SSH model: Su-Schrieffer–Heeger model
- TI: topological insulator
- TKNN formula: Thouless-Kohmoto-Nightingale-den-Nijs formula
- TRS: time-reversal symmetry

- TSC: topological superconductor
- vV HFE: van Vleck high-frequency expansion
- WSM: Weyl semimetal

Contents

Chapter 1

Introduction

1.1 Rise of Floquet engineering

Periodically driven systems, which are usually termed as Floquet systems in physics, have attracted incessant interest for quite a long time in many subfields of physics, where a number of interesting phenomena have been found including dynamical localization [9, 10], stochastic resonance [11, 12], and dynamical stabilization [13–16]. Owing to the rapid developments in laser and ultrafast spectroscopy techniques, it has recently been shown that periodic drives can be used as flexible experimental tools to control quantum systems for realizing exotic states of matter including Floquet topological insulators [17–22] and Floquet time crystals [23–26]. This form of engineering of quantum systems, which is known as *Floquet engineering*, has become an emergent field of research over the last decade [27–29]. Its key ingredient is the *Floquet theorem* [30,31], which is a temporal analog of the Bloch theorem and dictates that the time evolution of a periodically driven quantum system be described by a time-independent *effective Hamiltonian* on average. Thus, it reduces the problem in a non-equilibrium system to an analysis of a static effective Hamiltonian and therefore greatly simplifies the problem. The effective Hamiltonian is systematically determined from the driving protocol by means of the *high-frequency expansion*, which is a perturbative expansion in the inverse of the driving frequency. Thus, by choosing a suitable driving protocol, one can tailor a static effective Hamiltonian with desired properties, namely engineering of a Hamiltonian.

Floquet engineering is commonly used in ultracold atomic gases owing to their excellent controllability by a laser field [20, 32–38]. A prime example is the realization of the Haldane model [20, 39]. In this experiment, the complex next-nearest-neighbor hoppings, which are hard to implement in a static system, can be induced by shaking an optical lattice. Another remarkable achievement is the realization of the Thouless pump [40, 41], where the quantized transport protected by topology is demonstrated using the state-of-the-art laser technology. Floquet engineering by a laser is also intensively studied in solid-state systems because it has potential applications to ultrafast electronics and spintronics [22, 29, 42–49]. For example, photo-induced superconductors [50–52] and laser-induced demagnetization [53–55] have been realized experimentally. Additionally, there are a number of theoretical proposals using Floquet engineering to induce new states of matter in semiconductors [17, 56–60], strongly correlated electron systems [61–70], and magnets [71–82].

1.2 Present study

In this thesis, we apply Floquet engineering to two fields of research, namely topological quantum phenomena and nonlinear systems.

Recent years have witnessed rapid progress in topological phases of matter both experimentally and theoretically [83,84]. In a periodically driven lattice system, an effective Hamiltonian, which is an analog of a Hamiltonian in a static system, can possess a topologically nontrivial band structure and exotic edge states like a static Hamiltonian, namely Floquet topological insulator [17, 56]. Moreover, periodically driven lattice systems can exhibit topological band structures *that are prohibited in static systems* by utilizing nontrivial topology of its time-evolution operator [85–87]. Interestingly, the Thouless pump [88], which is a canonical example of topological pumps, features such a lattice-prohibited band structure, namely a single chiral fermion. Although several examples with such lattice-prohibited band structures are known in one dimension [85, 89], concrete models in higher dimensionalities are still lacking. Moreover, a topological classification of general lattice-prohibited band structures has remained elusive.

In the first part of our work, we present yet another model that exhibits a band structure that is prohibited in a static lattice system, i.e, a single Weyl fermion. It is well-known that a single Weyl fermion is impossible to realize within a single band of a static three-dimensional lattice because of the Nielsen-Ninomiya theorem [90,91]. This leads to the absence of the chiral current originating from the chiral magnetic effect [92,93], which is a current flowing *antiparallel* to an applied magnetic field. However, we here show that one can surpass the above limitation in static systems by presenting a concrete example of a periodically driven lattice system that has a single Weyl fermion within a single band. The presence and stability of a single Weyl fermion is ensured by the nontrivial topology of the Floquet unitary operator, which is the time-evolution operator per one period. In our driving protocol, a spin-polarized thermal gas moves parallel to its spin polarization, which is a manifestation of the spin-momentum locking of a Weyl fermion. When a magnetic field is applied, a quantized current flows antiparallel to the magnetic field, which is a Floquet realization of the chiral magnetic effect. Finally, generalizing the above discussion to include symmetries, we give a topological classification of Floquet unitary operators in the Altland-Zirnbauer symmetry classes for all dimensionalities and construct concrete models in each symmetry class and dimensionality. From these results, we show that all gapless surface states of topological insulators and superconductors can be realized in bulk quasienergy spectra in Floquet systems.

In the second part of our work, we consider classical stochastic systems governed by nonlinear stochastic equations. Unfortunately, we can apply neither Floquet theorem nor the high-frequency expansion directly to these systems because of the nonlinearity and the stochasticity of their equations of motion because the Floquet theorem is applicable only to linear equations like the Schrödinger equation. Yet, it is clearly important to extend these Floquet methodologies established in quantum systems to nonlinear stochastic equations of motion. Such a generalization has a wide range of applications from purely classical systems (e.g., the Langevin systems) to quantum ones in symmetry-broken phases (e.g., Bose-Einstein condensates) and to both isolated systems and open ones coupled with thermal reservoirs.

To resolve the above problems, we develop the high-frequency expansion for a classical Floquet system described by a nonlinear stochastic equation. The key idea is using the master equation corresponding to its equation of motion. Since the master equations is linear with respect to the probability distribution function and periodic in time, one can safely apply the

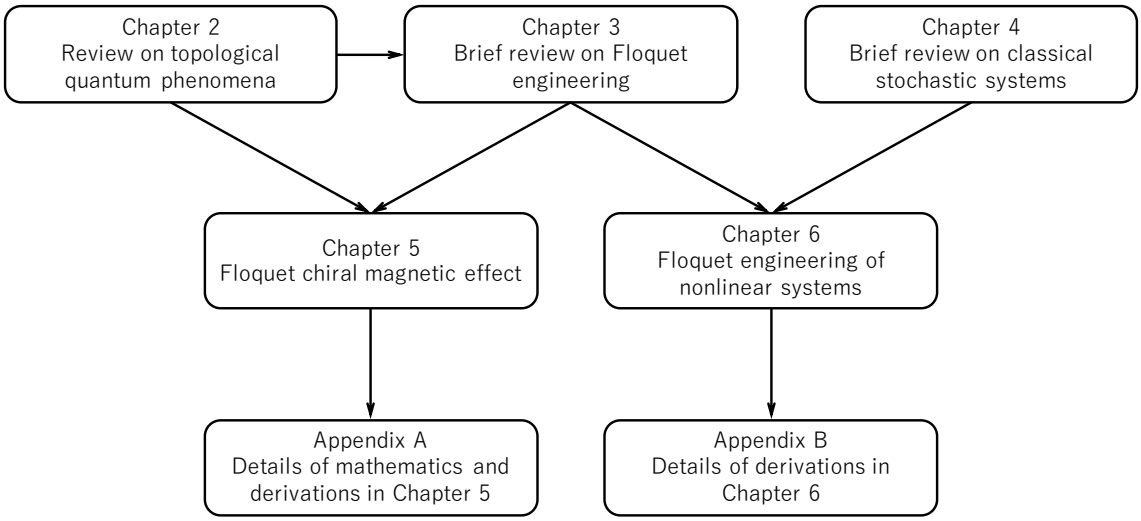

Figure 1.1: Relations between chapters.

Floquet theorem and perform the high-frequency expansion. The effective equation of motion is obtained from the high-frequency expansion of the master equation through the correspondence between the equation of motion and the master equation. By analytically studying the convergent properties of the high-frequency expansion, we show that the description based on the effective equations of motion obtained from the high-frequency expansion is valid for a non-chaotic few-body system and a generic many-body system under a high-frequency drive. To illustrate the procedure to obtain an effective equation of motion and numerically support the above analytical findings, we consider the following two examples of open classical systems: (i) the Kapitza pendulum [13] with friction and (ii) laser-irradiated magnets. In both cases, we numerically confirm that the exact time evolution is well reproduced from the effective equations of motion *until the non-equilibrium steady states*. This agreement is in stark contrast to the results in closed quantum systems where the truncated high-frequency expansion fails to capture the eventual heating to infinite-temperature states [27, 94–98]. Finally, we present an application to spintronics, where we analyze a multiferroic spin chain irradiated by a circularly polarized laser. We show that a synthetic Dzyaloshinskii-Moriya interaction [99, 100] emerges, leading to a spiral magnetic order in the non-equilibrium steady states.

1.3 Construction of the thesis

This thesis is constituted of reviews and two original works on Floquet engineering. The rest of this thesis is outlined as follows:

Chapter 2 reviews several selected topics in topological quantum phenomena. In Sec. 2.1, we first overview basic notions on topological insulators and topological superconductors including a bulk topological invariant, edge states, and their relation, namely the bulk-edge correspondence [83, 84]. Then, we discuss symmetry-protected topological phases, which are topological phases of matter protected by symmetries, and their classification by means of the K theory [101, 102]. The K theory provides a powerful method of classifying various types of topological phases in static and Floquet systems [102–105]. In Sec. 2.2, we review a Weyl

fermion [106], which is a prime example of topological semimetals. After presenting its definition, we discuss an exotic magnetic response of a Weyl fermion known as the chiral magnetic effect [92, 93]. Then, we introduce a Weyl semimetal [107], which is a solid-state analog of a Weyl fermion, and discuss the Nielsen-Ninomiya theorem [90, 91]. In Sec. 2.3, we discuss adiabatic pumps, which are topological quantum phenomena in *dynamical* systems and show some quantized transport. We start from their well-known example, the Thouless pump [88, 108], and then discuss their classification in terms of the K theory [103], showing its close relationship with the classification of topological insulators and superconductors in Sec. 2.1.

Chapter 3 briefly reviews Floquet engineering and its applications. In Sec. 3.1, we overview the Floquet theorem [30, 31], which is a fundamental theorem on Floquet engineering, and the high-frequency expansion of the effective Hamiltonian [109, 110]. Two variants of the high-frequency expansion, the van Vleck high-frequency expansion [109, 111–113] and the Floquet-Magnus high-frequency expansion [114], are introduced. The convergence property of the high-frequency expansion in an isolated system and its relation to the Floquet prethermalization are discussed. In Secs. 3.2 and 3.3, we discuss applications of Floquet engineering to topological quantum phenomena and symmetry-broken quantum systems, respectively. The Thouless pump reviewed in Sec. 2.3 is again analyzed from a Floquet viewpoint. Its quasienergy band structure possesses a single chiral fermion [85] though it is prohibited in a static lattice system. Floquet engineering is applied to control superfluids and magnets, which have potential applications to quantum simulations and future spintronics. In Sec. 3.4, we discuss some applications of Floquet engineering to *classical* systems. We first consider the Kapitza pendulum [13], which is a well-known example of dynamical stabilization, and next discuss the recent numerical and analytical studies on the Floquet prethermalization in driven classical spins [115–117].

Chapter 4 reviews stochastic classical systems described by stochastic differential equations. We first discuss a prototypical example, the Langevin equation [118, 119] in Sec. 4.1 and then consider a general classical stochastic system in Sec. 4.2. The correspondence between a stochastic differential equation and a general master equation is discussed. In Sec. 4.3, we consider the Landau-Lifshitz-Gilbert equation [120, 121] and its stochastic generalization [122] for the use in Chapter 6. They describe a magnetic dynamics subject to a damping and thermal fluctuations, and are widely used in spintronics.

In Chapters 5 and 6, we present our original works.

Chapter 5 applies the idea of Floquet engineering to realize an exotic topological band structure that is not accessible in a static lattice system. In Sec. 5.1, we define our model on a periodically driven three-dimensional lattice and show that its Floquet unitary operator is characterized by nontrivial topology. In Secs. 5.2 and 5.3, we analyze the quasienergy spectra and the dynamics under a periodic drive without and with a magnetic field, respectively. Without the magnetic field, a single Weyl fermion appears within a single band of the quasienergy spectrum and a current flows parallel to its spin polarization owing to the spin-momentum locking of the Weyl fermion. In the presence of an external magnetic field, a spin-polarized chiral fermion emerges between the Landau gaps in the quasienergy spectrum. This chiral fermion gives rise to chiral transport antiparallel to the magnetic field under the drive, which is a Floquet realization of the chiral magnetic effect. In Sec. 5.4, we discuss experimental implementations in terms of ultracold atomic gases in optical lattices. In Sec. 5.5, we give a classification of topologically nontrivial gapless spectra of Floquet unitary operators. We clarify its close connection to the classification of topological insulators and superconductors in Sec. 2.1 and its difference from that of adiabatic pumps in Sec. 2.3. Some mathematical background, derivations of equations,

and concrete models for a given symmetry and dimensionality are given in Appendix A. The main content of this chapter is based on the following publication:

[**1**] "Floquet chiral magnetic effect", Sho Higashikawa, Masaya Nakagawa, and Masahito Ueda, arXiv:1806.06868

Although the classification of topologically nontrivial gapless spectra is mainly done by the collaborator, Masaya Nakagawa, we include it for the sake of the self-containedness of the presentation.

Chapter 6 develops the high-frequency expansion for nonlinear stochastic systems. In Sec. 6.1, we derive the high-frequency expansion for a general nonlinear stochastic equation based on the master equation reviewed in Sec. 4.2. We show that our method includes as specific examples the previous results reviewed in Sec. 3.4. In Sec. 6.2, we analytically examine the higher-order terms of the Floquet-Magnus high-frequency expansion and its convergent property, where we show that the effective equation based on the high-frequency expansion is valid for a non-chaotic few-body system and a generic many-body system under a high-frequency drive. In Secs. 6.3 and 6.4, we apply the high-frequency expansion to two examples, the Kapitza pendulum with friction and interacting classical spins driven by a laser, respectively. In both examples, the analytical findings in Sec. 6.2 are numerically confirmed. In Sec. 6.5, we present an application of our formalism to spintronics, where we demonstrate a controlled generation of a spin vector chirality in a spin chain in its non-equilibrium steady state. A distinction from the previous study reviewed in Sec. 3.3 is clarified. A rigorous analysis on a Markov process and detailed calculations of the high-frequency expansion in Chapter 6 are given in Appendix B. The main content of this chapter is based on the following publication:

[**2**] "Floquet engineering of classical systems", Sho Higashikawa, Hiroyuki Fujita, and Masahiro Sato, arXiv:1810.01103

Chapter 7 concludes the thesis with a summary and some future prospects. In Sec. 7.1, we give a summary for each chapter. In Sec. 7.2, we discuss some future prospects.

The relations between chapters are illustrated in Fig. 1.1.

Throughout this thesis, we adopt a system of units in which the Planck constant and the Boltzmann constant taken as unity: $\hbar = k_B = 1$.

Chapter 2

Review on topological quantum phenomena

Topological phases of matter [83, 84, 105, 107] have attracted growing interest over the last decade in many subfields of physics including condensed-matter physics, ultracold atomic gases, photonics, and mechanics. Topological phase transitions lie outside the Ginzburg-Landau-Wilson paradigm of spontaneous symmetry breaking and can occur even in noninteracting systems. In this chapter, we first introduce their basic notions by way of a prototypical example, a Chern insulator, and then review symmetry-protected topological (SPT) phases, which are topological phases under certain symmetry. Finally, we overview the classification of topological insulators (TIs) and topological superconductors (TSCs) by means of the K theory.

2.1 Topological insulators and superconductors

2.1.1 Basic concepts on topological insulators and superconductors

We start from one of the simplest models of topological insulators (TIs), i.e., a Chern insulator. Consider the translationally invariant system on a square lattice with the following Bloch Hamiltonian

$$h(\boldsymbol{k}) = \lambda \sin k_x \sigma_x + \lambda \sin k_y \sigma_y + (t_0 \cos k_x + t_0 \cos k_y + m)\sigma_z =: \boldsymbol{d}(\boldsymbol{k}) \cdot \boldsymbol{\sigma}, \tag{2.1}$$

where $\boldsymbol{k} := (k_x, k_y)$ and $\boldsymbol{\sigma} := (\sigma_x, \sigma_y, \sigma_z)$ are the two-dimensional momentum and the Pauli matrices, respectively [123] (the lattice constant is set to be unity). Here, λ, t_0, and m denote the strength of a spin-orbit coupling, the hopping amplitude, and an effective mass, respectively. Physically, this model describes the quantum anomalous Hall effect realized with both the strong spin-orbit coupling (σ_x and σ_y terms) and ferromagnetic polarization (σ_z term), which can be physically realized in quantum wells with an appropriate amount of magnetic doping [124].

Let $|\alpha, \boldsymbol{k}\rangle$ and $E(\alpha, \boldsymbol{k})$ be the Bloch state and the energy of the Bloch band α, respectively: $h(\boldsymbol{k})\,|\alpha, \boldsymbol{k}\rangle = E(\alpha, \boldsymbol{k})\,|\alpha, \boldsymbol{k}\rangle$. We denote the U(1) Berry connection associated with the occupied band and the corresponding Berry curvature as $\mathcal{A}_{k_i}$ and $\mathcal{F}_{k_x k_y}(\boldsymbol{k})$, respectively:

$$\mathcal{A}_{k_i} := -i \sum_{\alpha:\mathrm{occ}} \langle \alpha, \boldsymbol{k}|\, \partial_{k_i}\, |\alpha, \boldsymbol{k}\rangle\,, \tag{2.2}$$

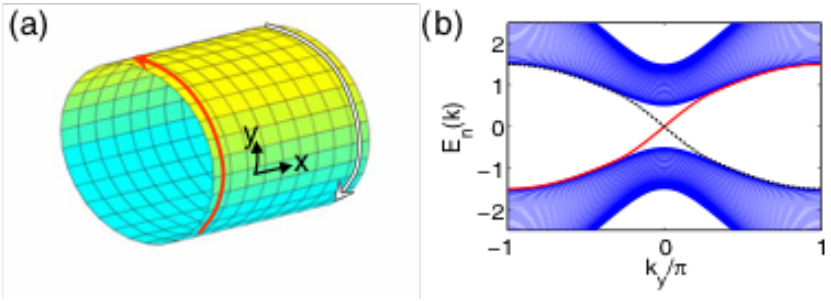

Figure 2.1: (a) Illustration of a square lattice with cylindrical geometry and the chiral edge states on the boundary (red and white arrows). (b) One-dimensional energy spectrum of the model (2.1) with $m = -1.5$ and $t = 1$. The red solid and black dashed lines stand for the left- and right-moving chiral edge states, respectively, while all other blue lines are bulk energy levels. Reproduced from Fig. 2 of Ref. [128]. © 2008 by the American Physical Society.

$$\mathcal{F}_{k_x k_y}(\boldsymbol{k}) := \partial_{k_x}\mathcal{A}_{k_y}(\boldsymbol{k}) - \partial_{k_y}\mathcal{A}_{k_x}(\boldsymbol{k}). \tag{2.3}$$

The topology of the Bloch Hamiltonian (2.1) is characterized by the first Chern number, which is expressed by the so-called Thouless-Kohmoto-Nightingale-den Nijs (TKNN) formula [88,125]:

$$Ch_1 := \int \frac{d\boldsymbol{k}}{2\pi}\mathcal{F}_{k_x k_y}(\boldsymbol{k}). \tag{2.4}$$

To be concrete, the first Chern number of the model (2.1) is given by the winding number of the map $\boldsymbol{k} \mapsto \hat{\boldsymbol{d}}(\boldsymbol{k}) := \boldsymbol{d}(\boldsymbol{k})/|\boldsymbol{d}(\boldsymbol{k})|$:

$$Ch_1 = \int \frac{d\boldsymbol{k}}{4\pi}\hat{\boldsymbol{d}}\cdot\left(\partial_{k_x}\hat{\boldsymbol{d}}\times\partial_{k_x}\hat{\boldsymbol{d}}\right) = \begin{cases} 1 & 0 < m < 2; \\ -1 & -2 < m < 0; \\ 0 & \text{otherwise.} \end{cases} \tag{2.5}$$

Remarkably, this purely mathematical object has a profound physical implication: the quantization of the Hall conductance σ_H, which is called the quantum anomalous Hall effect [39]:

$$\sigma_{xy} = \frac{e^2}{2\pi}Ch_1, \tag{2.6}$$

where e is the elementary charge. This quantization is explained from the viewpoint of an edge state. When we solve the tight binding model with an open (periodic) boundary condition along the x (y) direction (see Fig. 2.1 (a)), the energy spectrum exhibits gapless chiral edge states as shown in Fig. 2.1 (b). These are unidirectional edge states localized on the boundaries. When the bulk Chern number is Ch_1, $|Ch_1|$ pieces of edge bands with chirality $\mathrm{sgn}\,(Ch_1)$ appear. This is an example of the *bulk-edge correspondence* [126]: if a bulk insulating phase shows some nontrivial topology, there should be gapless states localized on the real-space boundaries. Remarkably, the existence of the edge state and the quantization of the Hall conductance (2.6) are robust against disorder and perturbations on the Hamiltonian as experimentally verified with high precision [127].

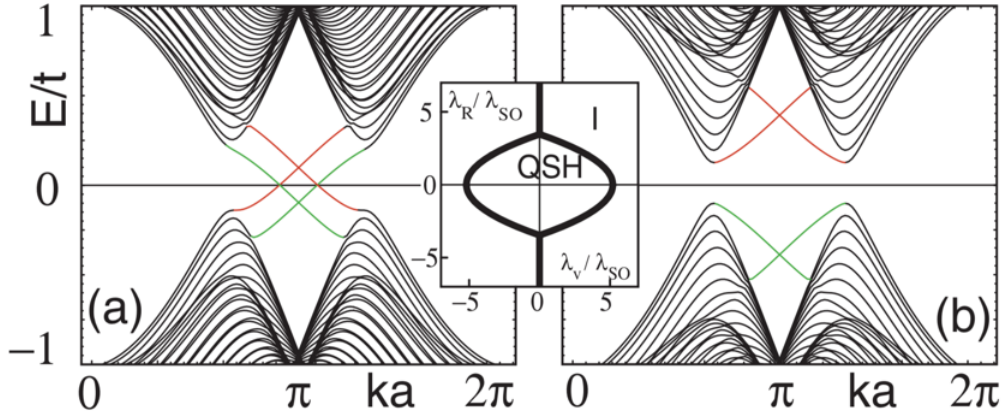

Figure 2.2: Energy bands for a one-dimensional "zigzag" strip in the (a) QSH phase $\lambda_v = 0.1t$ and (b) the trivial phase $\lambda_v = 0.4t$. The red and green lines stand for the helical edge states localized at different boundaries. In both cases, $\lambda_{SO} = 0.06t$ and $\lambda_R = 0.05t$. The inset shows the phase diagram as a function of λ_v and λ_R when $0 < \lambda_{SO} \ll t$. Reproduced from Fig. 2 of Ref. [130]. © 2005 by the American Physical Society.

2.1.2 Symmetry-protected topological phases

One of the breakthroughs in the field of TIs and TSCs is the discovery of a quantum spin Hall (QSH) insulator [129, 130], which is a prime example of the SPT phases. In SPT phases, a bulk topological invariant and edge states are stable against the disturbance *that respects a certain symmetry*. Unlike a quantum Hall state, they are fragile against a perturbation that breaks the symmetry.

Quantum spin Hall insulator

The QSH insulator is first introduced as a model of graphene with a spin-orbit coupling [129, 130]. Its Bloch Hamiltonian reads

$$h(\boldsymbol{k}) = \sum_{a=1}^{5} d_a(\boldsymbol{k})\gamma_a + \sum_{a,b=1}^{5} d_{ab}(\boldsymbol{k})\gamma_{ab}, \tag{2.7}$$

where $\gamma_{(1,2,3,4,5)} := (\sigma_x \otimes \sigma_0, \sigma_z \otimes \sigma_0, \sigma_y \otimes \sigma_x, \sigma_y \otimes \sigma_y, \sigma_y \otimes \sigma_z)$ are the gamma matrices and $\gamma_{ab} := (\gamma_a\gamma_b + \gamma_b\gamma_a)/2$. Here, the coefficients $d_a(\boldsymbol{k})$ and $d_{ab}(\boldsymbol{k})$ are defined by

$$d_a(\boldsymbol{k}) = \begin{cases} t_0(1 + 2\cos x \cos y) & a = 1; \\ \lambda_v & a = 2; \\ \lambda_R(1 - \cos x \cos y) & a = 3; \\ \sqrt{3}\lambda_R \sin x \sin y & a = 4; \\ 0 & a = 5, \end{cases}$$

$$d_{ab}(\boldsymbol{k}) = \begin{cases} -2t_0 \cos x \cos y & (a,b) = (1,2); \\ \lambda_{SO}(2\sin 2x - 4 \sin x \cos y) & (a,b) = (1,5); \\ -\lambda_R \cos x \sin y & (a,b) = (2,3); \\ -\sqrt{3}\lambda_R \sin x \cos y & (a,b) = (2,4); \\ 0 & \text{otherwise}, \end{cases} \tag{2.8}$$

where $x := k_x a/2$ and $y = \sqrt{3}k_y a/2$ are the normalized momenta (a is the lattice constant of the graphene). The parameters t_0 and λ_v represents the nearest-neighbor hopping amplitude and the staggered potential between the sublattices, respectively. The other two, λ_R and λ_{SO}, represent the strengths of the spin-orbit coupling.

This Bloch Hamiltonian is invariant under the time-reversal symmetry (TRS) $\Theta = i(\sigma_0 \otimes s_y)\mathcal{K}$:

$$\Theta h(\boldsymbol{k})\Theta^{-1} = h(-\boldsymbol{k}), \tag{2.9}$$

where $\mathcal{K}$ denotes the complex conjugation. Here, Θ satisfies $\Theta^2 = -1$, which immediately leads to the presence of the Kramers pairs. Its bulk topological number, the so-called $\mathbb{Z}_2$ index $(-1)^\nu$, is defined as follows: For a Bloch state $|\alpha, \boldsymbol{k}\rangle$, we define the *sewing matrix* $w(\boldsymbol{k})$ with its matrix element given by $w_{\alpha\beta}(\boldsymbol{k}) := \langle \alpha, -\boldsymbol{k}| \, \Theta \, |\beta, \boldsymbol{k}\rangle$. Then, it satisfies

$$w(\boldsymbol{k}) = -w(-\boldsymbol{k})^{\mathrm{tr}}, \tag{2.10}$$

where $^{\mathrm{tr}}$ denotes the transpose of a matrix. This indicates that $w(\boldsymbol{k})$ is an asymmetric matrix for time-reversal invariant momenta, where we denote its Pfaffian as $\mathrm{Pf}\,[w(\boldsymbol{k})]$.* The $\mathbb{Z}_2$ index $(-1)^\nu$ is defined as follows [129, 130]:

$$(-1)^\nu := \prod_{\boldsymbol{k}:\mathrm{TRIM}} \frac{\mathrm{Pf}\,[w(\boldsymbol{k})]}{\sqrt{\mathrm{Det}\,[w(\boldsymbol{k})]}}, \tag{2.12}$$

where $\boldsymbol{k}$ runs over all the time-reversal invariant momenta.† This bulk topological invariant cannot change as far as the band gap does not close and the TRS is preserved. Reflecting the nontrivial bulk invariant, this model hosts gapless helical edge states on the boundaries as shown in the left panel of Fig. 2.2 (red and green lines). The gapless point of the helical edge states is protected by the TRS because the hybridization between the edge states is prohibited by the Kramers theorem, namely the *symmetry protection of edge states*. Because of the nontrivial

*The Pfaffian $\mathrm{Pf}\,(w)$ of an asymmetric matrix $w = \{w_{\alpha\beta}|\alpha, \beta = 1, 2, \cdots 2N\}$ with size $2N$ is defined by

$$\mathrm{Pf}\,(w) := \frac{1}{2^n n!} \sum_{\sigma \in S_N} \mathrm{sgn}\,(\sigma) \prod_{i=1}^{N} w_{\sigma(2i-1)\sigma(2i)}, \tag{2.11}$$

where S_N is the permutation group with order N. In general, we can show that $\mathrm{Pf}\,(w)^2 = \mathrm{Det}\,(w)$ and hence $\mathrm{Pf}\,[w(\boldsymbol{k})]\,/\sqrt{\mathrm{Det}\,[w(\boldsymbol{k})]} = \pm 1$.

†This formula reduces to the famous Fu-Kane parity formula [131] when the system has an inversion symmetry.

helical edge states, the spin Hall conductance is quantized as follows:

$$\sigma_{SH} = \frac{e^2}{2\pi}. \tag{2.13}$$

The existence of the edge state and the quantization of conductance are robust against disorder *that preserves the TRS*, though they are fragile against disorder that breaks the TRS, such as magnetic impurities. The QSH insulator and the quantized spin Hall conductance have experimentally been realized in a HgTe quantum well [132] following the theoretical proposal [133].

Other symmetry-protected topological phases

Another example of SPT phases appears in the Su-Schrieffer–Heeger (SSH) model [134], which is a one-dimensional model with alternating hopping amplitude. Its Hamiltonian is given by

$$H(t) = \sum_{j=1}^{L} \left(\frac{t_0}{2} + (-1)^j \frac{\delta}{2} \right) \left(c_{j+1}^\dagger c_j + c_j^\dagger c_{j+1} \right) = \sum_k \left(c_{k,A}^\dagger, c_{k,B}^\dagger \right) h(k) \begin{pmatrix} c_{k,A} \\ c_{k,B} \end{pmatrix}, \tag{2.14}$$

$$h(k) = \left(v + w\mathrm{e}^{-ik} \right) \sigma_+ + \left(v + w\mathrm{e}^{+ik} \right) \sigma_-, \tag{2.15}$$

where $c_{k,A}$ ($c_{k,B}$) is the annihilation operator of a particle with momentum k at the sublattice A (B) constituted from the even (odd) sites; L is the number of the lattice sites. Here, $v := t_0 + \delta$ ($w := t_0 - \delta$) is the hopping amplitude within (between) the unit cell. The Bloch Hamiltonian $h(\boldsymbol{k})$ has chiral symmetry (CS) $\Gamma = \sigma_3$, which is expressed as $\Gamma h(\boldsymbol{k}) \Gamma^\dagger = -h(\boldsymbol{k})$. When $|\boldsymbol{k}\rangle$ is a Bloch state of $h(\boldsymbol{k})$ with energy $E(\boldsymbol{k})$, so is $\Gamma |\boldsymbol{k}\rangle$ with energy $-E(\boldsymbol{k})$ because of the CS. The energy eigenvalue of Eq. (2.15) is given by $E(\boldsymbol{k}) = \pm |v + w\mathrm{e}^{-ik}|$. Its bulk topological number is given by the winding number around the gap-closing point defined by $v + w\mathrm{e}^{-ik} = 0$:

$$\nu = \int_0^{2\pi} \frac{dk}{2\pi} \partial_k \arg \left[v + w\mathrm{e}^{-ik} \right] \in \mathbb{Z}. \tag{2.16}$$

When the bulk topological number is nontrivial $\nu \neq 0$, $|\nu|$ pieces of zero-energy modes appear at each edge, which are immune to disorder as far as the CS is preserved.

Another example of SPT phases is the Kitaev chain [135], which is a prototypical example of TSCs. It is a one-dimensional fermionic system interacting with p-wave symmetry and its Bogoliubov-de-Gennes Hamiltonian is given by

$$h(k) := \Delta \sin k \tau_x + (t \cos k - \mu) \tau_z, \tag{2.17}$$

where t, Δ, and μ are the kinetic energy, the paring amplitude, and the chemical potential, respectively. Here, the two bands for momentum k are spanned by the Nambu spinor (c_k, c_{-k}), with c_k being the annihilation operator of the fermion with momentum k, and the Pauli matrices $\boldsymbol{\tau} := (\tau_x, \tau_y, \tau_z)$ are taken in this basis. The first term represents the p-wave paring gap while the second one represents the Hamiltonian of the normal state. This model has the particle-hole symmetry (PHS) $C = \tau_x \mathcal{K}$: $Ch(k)C^{-1} = -h(-k)$. From the PHS, $h(k)$ satisfies $h(0), h(\pi) \in \mathbb{R}$ at the pariticle-hole-invariant momenta $k = 0, \pi$, from which we can define the $\mathbb{Z}_2$ index $(-1)^\nu$

as follows:

$$(-1)^{\nu} := \mathrm{sgn}\left[h(0)h(\pi)\right]. \tag{2.18}$$

Remarkably, because of the nontrivial $\mathbb{Z}_2$ number, the Kitaev chain host the Majorana zero modes at their edges, which can be used as a building block of topological quantum computation [136]. While the Majorana zero modes in a p-wave superconductor are hard to realize in a natural solid-state setup, it was predicted that they also appear at the interface between a semiconductor with a strong spin-orbit coupling and an s-wave superconductor [137–139]. Following these proposals, the zero-bias conductance peak and the fractional Josephson effect originating the Majorana zero modes are observed in a superconductor on the top of a semiconductor [140, 141].

2.1.3 Classification of topological insulators and superconductors

Altland-Zirnbauer symmetry classes

As we have explained in the previous subsection, symmetries play an essential role in the existence of SPT phases and the protection of their edge states. Symmetries are, in general, divided into two classes: global and crystalline symmetries. Examples of the former include the TRS, the PHS, and the global spin SU(2) symmetry. Global symmetry divides an entire Hilbert space into the direct sum of irreducible representations of the symmetry group. Assuming that the global unitary symmetries like the spin SU(2) symmetry are already diagonalized, we consider the remaining symmetries in irreducible blocks. The remaining symmetries are an antiunitary symmetry such as the TRS and PHS and a unitary symmetry that anti-commutes with the Hamiltonian such as the CS. Those symmetries constitute the Altland-Zirnbauer (AZ) symmetry classes [142].

As fundamental symmetries of a fermion, we consider three symmetries, the TRS Θ, the PHS C, and the CS Γ, which act on a Bloch Hamiltonian $h(\boldsymbol{k})$ as follows:

$$\Theta h(\boldsymbol{k})\Theta^{-1} = h(-\boldsymbol{k}), \quad Ch(\boldsymbol{k})C^{-1} = -h(-\boldsymbol{k}), \quad \Gamma h(\boldsymbol{k})\Gamma^{-1} = -h(\boldsymbol{k}). \tag{2.19}$$

While Γ is unitary: $\Gamma i\Gamma^{-1} = i$, Θ and C are antiunitary: $\Theta i\Theta^{-1} = -i$ and $CiC^{-1} = -i$, because they include the complex conjugation $\mathcal{K}$. These are all two-fold symmetry: their squares are always either $+1$ or -1 depending on the representation of the symmetries. For example, the TRS $\Theta = i\sigma_y\mathcal{K}$ with $\Theta^2 = -1$ appears in a spin-half system, while $\Theta = \mathcal{K}$ with $\Theta^2 = 1$ appears in a spin-integer system. For the case of the PHS, $C = \tau_x\mathcal{K}$ with $C^2 = 1$ is used for a usual SC ($\boldsymbol{\tau}$ is the spin operator in the Nambu basis), while $\Theta = \tau_y\mathcal{K}$ with $C^2 = -1$ is chosen if the system has a global SU(2) symmetry. The CS emerges as the combined symmetry $\Gamma = \Theta C$ when the system has both the TRS and PHS. The sign of its square is the product of those of Θ and C, i.e., $\Gamma^2 = \Theta^2 C^2$, when they commute.

Depending on the presence and absence of the symmetries, together with the value of their square ± 1, Bloch Hamiltonians are divided into the ten classes known as the *AZ symmetry classes* (see Table 2.1). Usually, these ten classes are broken down into the two wider classes: the complex class and real class, and assigned an integer s called a symmetry class. In the complex class, two classes, which are called class A and class AIII, are labeled by the value $s = 0$ and $s = 1$, respectively. In the real class, the integers $s = 0, 1, 2, \cdots, 7$ are assigned to

Table 2.1: Tenfold-way topological classification of TIs and TSCs for spatial dimensionality $d = 0, 1, \cdots, 7$ [101, 102, 143] The values $\pm 1, 0$ in the third, fourth, and fifth columns represent the square of Θ, C, and Γ, respectively, where 0 shows the absence of the symmetry. The topological invariant of the symmetry class $(\mathbb{F}, s)$ and the dimensionality d is given by the K group $K_{\mathbb{F}}(s, d)$. The topological number $2\mathbb{Z}$ means that the same types of edge states always appear in pairs. The K groups in a higher dimensionality $d \geq 8$ are determined from the Bott periodicity (2.23).

s	class	Θ	C	Γ	$d=0$	$d=1$	$d=2$	$d=3$	$d=4$	$d=5$	$d=6$	$d=7$
0	A	0	0	0	$\mathbb{Z}$	0	$\mathbb{Z}$	0	$\mathbb{Z}$	0	$\mathbb{Z}$	0
1	AIII	0	0	1	0	$\mathbb{Z}$	0	$\mathbb{Z}$	0	$\mathbb{Z}$	0	$\mathbb{Z}$
0	AI	1	0	0	$\mathbb{Z}$	0	0	0	$2\mathbb{Z}$	0	$\mathbb{Z}_2$	$\mathbb{Z}_2$
1	BDI	1	1	1	$\mathbb{Z}_2$	$\mathbb{Z}$	0	0	0	$2\mathbb{Z}$	0	$\mathbb{Z}_2$
2	D	0	1	0	$\mathbb{Z}_2$	$\mathbb{Z}_2$	$\mathbb{Z}$	0	0	0	$2\mathbb{Z}$	0
3	DIII	-1	1	1	0	$\mathbb{Z}_2$	$\mathbb{Z}_2$	$\mathbb{Z}$	0	0	0	$2\mathbb{Z}$
4	AII	-1	0	0	$2\mathbb{Z}$	0	$\mathbb{Z}_2$	$\mathbb{Z}_2$	$\mathbb{Z}$	0	0	0
5	CII	-1	-1	1	0	$2\mathbb{Z}$	0	$\mathbb{Z}_2$	$\mathbb{Z}_2$	$\mathbb{Z}$	0	0
6	C	0	-1	0	0	0	$2\mathbb{Z}$	0	$\mathbb{Z}_2$	$\mathbb{Z}_2$	$\mathbb{Z}$	0
7	CI	1	-1	1	0	0	0	$2\mathbb{Z}$	0	$\mathbb{Z}_2$	$\mathbb{Z}_2$	$\mathbb{Z}$

the eight classes AI, BDI, D, DIII, AII, CII, C, and CI, respectively.

Topological periodic table

A Bloch Hamiltonian $h(\boldsymbol{k})$ on a d-dimensional space is formally a map from the BZ $\mathbb{T}^d$ to the space of Hamiltonians. The complete classification of TIs and TSCs is obtained by classifying these maps under the constraint of certain symmetries. As in Ref. [102], we will simplify the topological classification by replacing the BZ $\mathbb{T}^d$ with the d-dimensional sphere S^d. This replacement allows us to focus on d-dimensional strong topological invariants which do not appear in lower dimensionalities, and to ignore weak topological invariants [131].

Let us set the Fermi level E_{fermi} to be zero: $E_{\text{fermi}} = 0$. Consider continuous deformation of the original Hamiltonian $h(\boldsymbol{k})$ into a simpler Hamiltonian whose eigenvalue spectrum is "flattened" so that the energy eigenvalue may be either $+1$ or -1. Then, the space of flattened Hamiltonians forms the Grassmannian

$$G_{n,k} = \frac{U(N)}{U(k) \times U(N-k)}, \tag{2.20}$$

where k $(N-k)$ denotes the number of occupied (unoccupied) bands. It is also worthwhile to introduce the notion of *stable equivalence*. Two families of Hamiltonians are stably equivalent if they can be deformed to each other after adding or removing an arbitrary number of trivial bands. Stable equivalence can be implemented into the set of the Grassmannians by considering an expanded space called the *classifying space* $\mathcal{C}_0$. The classifying space $\mathcal{C}_0$ includes an infinite number of extra occupied and unoccupied bands:

$$\mathcal{C}_0 := \bigcup_{k=0}^{\infty} G_{\infty,k}. \tag{2.21}$$

The classification of TIs in class A in d dimensions is given by the homotopy group $K_{\mathbb{C}}(s = 0, d) := \pi_d(\mathcal{C}_0)$. Symmetries impose constraints on the classifying space. For class AIII, $N = 2k$ follows from the CS and the classifying space becomes the subset $\mathcal{C}_1 := \bigcup_{k=0}^{\infty} G_{2k,k}$ of $\mathcal{C}_0$. The antiunitary symmetries, i.e., TRS and PHS, impose further constraints. At the special points where $\boldsymbol{k}$ and $-\boldsymbol{k}$ coincide, the allowed Hamiltonians are described by the eight classifying spaces $\mathcal{R}_s$ $(s = 0, 1, \cdots, 7)$ of the real K theory.

For a given symmetry class s, the topological classification of TIs and TSCs is obtained as a set of stably equivalent classes of maps from S^d to the classifying space subject to the symmetry constraints. These classes form the so-called *K group*, which we denote by $K_{\mathbb{C}}(s, d)$ for the complex symmetry classes and $K_{\mathbb{R}}(s, d)$ for the real symmetry classes. The K group for the AZ symmetry classes is shown in Table 2.1, which exhibits a remarkable stair-like pattern originating from the fundamental relation in the K group:

$$K_{\mathbb{F}}(s, d + 1) = K_{\mathbb{F}}(s + 1, d), \tag{2.22}$$

where $\mathbb{F} = \mathbb{R}$ or $\mathbb{C}$. Thanks to this relation, the calculation of $K_{\mathbb{F}}(s, d)$ reduces to that of $K_{\mathbb{F}}(s + d, 0)$, which is a zero-dimensional problem and hence can efficiently be solved [102]. We note that the topological numbers in a higher dimensionality, $d \geq 2$ for the complex classes and $d \geq 8$ for the real classes, the K groups are determined from the Bott periodicity [144]:

$$K_{\mathbb{C}}(s, d + 2) = K_{\mathbb{C}}(s, d), \quad K_{\mathbb{R}}(s, d + 8) = K_{\mathbb{R}}(s, d). \tag{2.23}$$

This is the reason why the classification table (Tab. 2.1) is called the *topological periodic table*.

It is worth mentioning that the K theory is a powerful tool for calculating topological invariants of maps, and hence it has been used for the classification of various topological phases and phenomena including topological phases with crystalline symmetries [104, 105, 145], topological edge states unique to Floquet systems [146], and even dynamical topological phases in non-Hermitian systems [5].

2.2 Weyl fermion and chiral magnetic effect

Weyl fermions have recently played a key role in cross-fertilizing ideas of high-energy and condensed-matter physics. Weyl semimetals, which are semimetals that possess Weyl fermions as their low-energy excitations, are canonical examples of topological semimetals. They attract growing interest in condensed-matter physics owing to their exotic magnetic response, namely the *chiral magnetic effect* (CME), which was first proposed and discussed in high-energy physics [92, 93].

2.2.1 Weyl fermion and Weyl semimetal

In 1929, Hermann Weyl showed the existence of a massless fermion in the Dirac equation [106], which was later called the *Weyl fermion*. Its Hamiltonian is given by

$$h(\boldsymbol{k}) = \boldsymbol{\sigma} \cdot \boldsymbol{k}, \tag{2.24}$$

where $\boldsymbol{k} := (k_x, k_y, k_z)$ is the three-dimensional momentum. Its Bloch state $|\boldsymbol{k}\rangle$ satisfies $\boldsymbol{\sigma}\,|\boldsymbol{k}\rangle = \pm\hat{\boldsymbol{k}}\,|\boldsymbol{k}\rangle$, implying that the spin direction of $|\boldsymbol{k}\rangle$ is parallel to its momentum, a phenomenon

known as the *spin-momentum locking*. Its topological number χ is given by the winding number around the gapless point $\boldsymbol{k} = 0$ called the Weyl point:

$$\chi = \int_{S^2} d\boldsymbol{k}\ \mathcal{F}(\boldsymbol{k}), \tag{2.25}$$

where S^2 and $\mathcal{F}(\boldsymbol{k})$ are a two-dimensional sphere enclosing the gapless point $\boldsymbol{k} = 0$ and the Berry curvature on S^2 at $\boldsymbol{k}$, respectively. This topological number counts the winding number of a hedgehog structure of the spin texture of the Bloch state $|\boldsymbol{k}\rangle$ around the Weyl point. In this sense, a Weyl fermion is called a *monopole* in the momentum space. A remarkable consequence of topology is that this monopole charge protects the Weyl point. In other words, we cannot remove the gapless point by a weak perturbation without the pair annihilation with a Weyl point with opposite monopole charge because of the conservation of the monopole charge. In this sense, Weyl fermions are topological objects though they are gapless unlike TIs and TSCs.

In solid-state band structures, Weyl fermions exist as low-energy excitations of a Weyl semimetal (WSM) [107, 147–149], where the dispersion relations are linear around the gapless points. WSMs have been discovered in condensed-matter systems quite recently. In the early 2015, four WSM materials, TaAs, TaP, NbAs, and NbP, were discovered through numerical calculations [150, 151], the observation of its surface states known as the surface Fermi arcs [152–154], and the measurement of anomalous transport [155–157], realizing Weyl fermions for the first time. It is known that either the inversion symmetry or the TRS must be broken to realize a WSM [148,158] and that the Weyl points with opposite chirality must appear in pairs within a single band [90, 91]. A model Hamiltonian of a WSM near the gapless points $\boldsymbol{k} = \pm\boldsymbol{\lambda}$ is given by

$$h(\boldsymbol{k}) = \begin{pmatrix} (\boldsymbol{k}+\boldsymbol{\lambda})\cdot\boldsymbol{\sigma} - \lambda_0 & 0 \\ 0 & -(\boldsymbol{k}-\boldsymbol{\lambda})\cdot\boldsymbol{\sigma} + \lambda_0 \end{pmatrix}, \tag{2.26}$$

where the Weyl points are located at $\pm\boldsymbol{\lambda}$ in the BZ and the energy shifts at the Weyl points are given by $\pm\lambda_0$. A nonzero $\boldsymbol{\lambda}$ (λ_0) corresponds to the breaking of the inversion (time-reversal) symmetry.

2.2.2 Chiral magnetic effect

A Weyl fermion attracts great interest owing to its peculiar magnetic response known as the *chiral magnetic effect* [92, 93] originating from the chiral anomaly [159, 160]. To clarify this, we introduce a U(1) gauge field $(A_0, \boldsymbol{A})$ in Eq. (2.26):

$$h(\boldsymbol{k}, A_0, \boldsymbol{A}) = \begin{pmatrix} (\boldsymbol{k}+\boldsymbol{\lambda}+\boldsymbol{A})\cdot\boldsymbol{\sigma} - \lambda_0 - A_0 & 0 \\ 0 & -(\boldsymbol{k}-\boldsymbol{\lambda}+\boldsymbol{A})\cdot\boldsymbol{\sigma} + \lambda_0 - A_0 \end{pmatrix}. \tag{2.27}$$

After integrating out the fermion field using Fujikawa's method [161], we obtain the low-energy action S_{eff} of the WSM: $S_{\text{eff}} = S_0 + S_\theta$ [162–165]. The first term S_0 is the effective action of the Dirac semimetal, i.e., Eq. (2.27) with $\boldsymbol{\lambda} = \lambda_0 = 0$. The second term S_θ known as the *θ-term* is written as

$$S_\theta = \frac{e^2}{16\pi^2} \int d\boldsymbol{x} dt \theta(\boldsymbol{x}) \epsilon_{\mu\nu\rho\lambda} F_{\mu\nu} F_{\rho\lambda}, \tag{2.28}$$

where $\epsilon^{\mu\nu\rho\lambda}$, $F_{\mu\nu}$, and $\theta(\boldsymbol{x})$ are the totally antisymmetric tensor with rank 4, the electromagnetic field tensor, and the Heaviside step function with $\theta(\boldsymbol{x}) = 1$ inside the WSM, respectively. The θ-term is responsible for the anomalous electromagnetic response of the WSM. The charge density ρ and current $\boldsymbol{j}$ originating from the θ-term are given by

$$\rho := \frac{\delta S_\theta}{\delta A_0} = \frac{e^2}{2\pi^2}\boldsymbol{\lambda} \times \boldsymbol{B}, \tag{2.29}$$

$$\boldsymbol{j} := \frac{\delta S_\theta}{\delta \boldsymbol{A}} = \frac{e^2}{2\pi^2}\boldsymbol{\lambda} \times \boldsymbol{E} + \frac{e^2}{2\pi^2}\lambda_0 \boldsymbol{B}. \tag{2.30}$$

While Eq. (2.29) and the first term on the right-hand side of Eq. (2.30) give rise to the anomalous Hall effect, the second term on the right-hand side of Eq. (2.30) gives rise to the CME, that represents the current *parallel* to the applied magnetic field $\boldsymbol{B}$. This is in stark contrast to a usual magneto-transport where the current flows *perpendicular* to $\boldsymbol{B}$ because of the Lorentz force.

The theoretical prediction of the CME in a WSM has aroused considerable interest not only from condensed-matter physics but also from non-equilibrium statistical physics because it leads to the existence of a nonzero current in the ground state [166, 167]. However, the total current from the CME is found to vanish in any static lattice system [167] as a consequence of the Nielsen-Ninomiya theorem [90, 91], which dictates the impossibility of realizing a single Weyl fermion in a static lattice system. Because of the periodicity of the BZ, two Weyl points are connected at the deep inside the Fermi sea, which gives the correction term to Eq. (2.30) to cancel out the chiral current. We can prove that the net equilibrium current always vanishes irrespective of lattices, band dispersions, and temperature [167]. Note that the anomalous Hall response in Eqs. (2.29) and (2.30), on the other hand, is not prohibited and indeed numerically shown to exist even in a lattice system [167].

Nevertheless, chiral-anomaly induced transport is experimentally detected through the negative magnetoresistance [151, 156, 158, 168–170]. In WSMs, the chiral anomaly induces a negative magnetoresistance originating from the chiral zero modes of the Landau levels and the suppressed backscattering of fermions with opposite chirality. It is worthwhile to mention that numerous attempts to obtain a finite chiral current have been made [169, 171–177], e.g., by introducing a non-uniform magnetic field and using non-equilibrium fermion distribution.

2.3 Adiabatic topological pump

Consider a time-dependent Hamiltonian $H(t)$ which has a finite energy gap Δ between the ground state and the first excited state. In an adiabatic pump, we consider $H(t)$ with period T which is much slower than Δ^{-1}: $H(t) = H(t+T)$ and $T\Delta \gg 1$. After one cycle, while the parameters of the Hamiltonian return to its initial value, the state may not, which leads to quantized transport protected by topology.

2.3.1 Thouless pump

An adiabatic charge pump, namely the Thouless pump [178], is the integrated charge transport during an adiabatic cycle. The pumped charge is quantized into an integer value and shows topological robustness against perturbations. A prototypical example of the Thouless pump is

given by *Rice-Mele model* [108], which is a one-dimensional model with its hopping amplitudes and sublattice difference varied with period T. Its Hamiltonian is given by

$$H(t) := \sum_{j=1}^{L} \left(\frac{t_0}{2} + (-1)^j \frac{\delta(t)}{2} \right) \left(c_{j+1}^\dagger c_j + \text{h.c.} \right) + \Delta(t) \sum_i (-1)^i c_i^\dagger c_i \tag{2.31}$$

$$= \sum_k \left(c_{k,A}^\dagger, c_{k,B}^\dagger \right) h(k,t) \begin{pmatrix} c_{k,A} \\ c_{k,B} \end{pmatrix}, \tag{2.32}$$

$$h(k,t) := t_0 \cos k\sigma_x - \delta(t) \sin k\sigma_y + \Delta(t)\sigma_z, \tag{2.33}$$

where $c_{k,A}$ ($c_{k,B}$) is the annihilation operator of a particle with momentum k on the sublattice A (B) constituted from the even (odd) sites; L is the number of the lattice sites. Here, $t_0 \pm \delta(t)$ represent the alternating hopping amplitudes and $\Delta(t)$ is the potential difference between the sublattices. Here, $\delta(t)$ and $\Delta(t)$ are periodic in time with period T. The first term on the right-hand side of Eq. (2.31) is the SSH model with time-dependent hopping amplitude while the second term is the potential difference between the even and odd sites.

Starting from the ground state of $h(k,0)$, we consider the adiabatic change of $\delta(t)$ and $\Delta(t)$ from $t = 0$ to $t = T$. Under this cycle, the Hamiltonian returns to its initial value $h(k,0)$ while the state may not. In an adiabatic pump, the fermions are pumped from left to right, and its pumped fermion number N per cycle is quantized, which is obtained by integrating the adiabatic current J_{ad} [178–180]:

$$N = \int_0^T dt\ J_{ad}(t) = -\frac{1}{2\pi} \int dk dt\ \mathcal{F}_{kt}(k,t) = -Ch_1, \tag{2.34}$$

where $\mathcal{F}_{kt}(k,t)$ is the Berry curvature of the occupied band of $H(k,t)$. Thus, the pumped charge per cycle is quantized irrespective of the detailed parameters of $h(k,t)$, and solely expressed by the first Chern number similarly to the Chern insulator. This quantization is stable against perturbations, weak interactions, and disorder, similarly to the quantized transport in a Chern insulator [181]. The Rice-Mele model is realized in ultracold atomic gases and quantized transport is observed [40, 41, 182, 183].

2.3.2 General adiabatic pumps

An adiabatic pump is generalized to including symmetries [103, 184, 185], where the pumped object is no longer a charge but a fermion parity, charges of a Kramers doublet, and so on. Consider the time-dependent Hamiltonian $h(\boldsymbol{k},t)$. The TRS Θ, the PHS C, and the CS Γ act on it as follows:

$$\Theta h(\boldsymbol{k},t)\Theta^{-1} = h(-\boldsymbol{k},t), \quad Ch(\boldsymbol{k},t)C^{-1} = -h(-\boldsymbol{k},t), \quad \Gamma h(\boldsymbol{k},t)\Gamma^{-1} = -h(\boldsymbol{k},t). \tag{2.35}$$

Note that the time t does not change its sign under the action.

The K theory employed for classifying TIs and TSCs also provides the classification of such topological adiabatic pumps. According to Eq. (2.35), the set of adiabatic pumps are classified into the ten categories from class A to class CI as shown in Table 2.1. After flattening the bands and ignoring weak invariants, we can regard an adiabatic pump in the complex (real) class with symmetry class s as a map from S^{d+1} to the classifying space $\mathcal{C}_s$ ($\mathcal{R}_s$). Similarly to

Table 2.2: Tenfold-way topological classification of adiabatic pumps for spatial dimensionality $d = 0, 1, \cdots, 7$ [103]. The notations are the same as in Table 2.1.

s	class	Θ	C	Γ	$d=0$	$d=1$	$d=2$	$d=3$	$d=4$	$d=5$	$d=6$	$d=7$
0	A	0	0	0	0	$\mathbb{Z}$	0	$\mathbb{Z}$	0	$\mathbb{Z}$	0	$\mathbb{Z}$
1	AIII	0	0	1	$\mathbb{Z}$	0	$\mathbb{Z}$	0	$\mathbb{Z}$	0	$\mathbb{Z}$	0
0	AI	1	0	0	$\mathbb{Z}_2$	$\mathbb{Z}$	0	0	0	$2\mathbb{Z}$	0	$\mathbb{Z}_2$
1	BDI	1	1	1	$\mathbb{Z}_2$	$\mathbb{Z}_2$	$\mathbb{Z}$	0	0	0	$2\mathbb{Z}$	0
2	D	0	1	0	0	$\mathbb{Z}_2$	$\mathbb{Z}_2$	$\mathbb{Z}$	0	0	0	$2\mathbb{Z}$
3	DIII	-1	1	1	$2\mathbb{Z}$	0	$\mathbb{Z}_2$	$\mathbb{Z}_2$	$\mathbb{Z}$	0	0	0
4	AII	-1	0	0	0	$2\mathbb{Z}$	0	$\mathbb{Z}_2$	$\mathbb{Z}_2$	$\mathbb{Z}$	0	0
5	CII	-1	-1	1	0	0	$2\mathbb{Z}$	0	$\mathbb{Z}_2$	$\mathbb{Z}_2$	$\mathbb{Z}$	0
6	C	0	-1	0	0	0	0	$2\mathbb{Z}$	0	$\mathbb{Z}_2$	$\mathbb{Z}_2$	$\mathbb{Z}$
7	CI	1	-1	1	$\mathbb{Z}$	0	0	0	$2\mathbb{Z}$	0	$\mathbb{Z}_2$	$\mathbb{Z}_2$

the case of static TIs and TCSs, we denote the K group of adiabatic pumps with AZ symmetry class $(\mathbb{F}, s)$ by $K_{\mathbb{F}}^{\mathrm{AP}}(s, d)$. The space of maps after taking the quotient by the stable equivalence formally defines the K group $K_{\mathbb{F}}(s, d, \delta)$, where δ is the number of coordinates that does not change the sign under Θ, C, and Γ. In the case of adiabatic pumps (2.35), we have $\delta = 1$, i.e. $K_{\mathbb{F}}^{\mathrm{AP}}(s, d) = K_{\mathbb{F}}(s, d, 1)$. In the case of $\delta = 0$, $K_{\mathbb{F}}(s, d, 0)$ coincides with the K group $K_{\mathbb{F}}(s, d)$ for TIs and TSCs with the same symmetry class $(\mathbb{F}, s)$. Their classification is performed by applying the periodicity in the K theory [103]:

$$K_{\mathbb{F}}(s, d, \delta + 1) = K_{\mathbb{F}}(s + 1, d, \delta). \tag{2.36}$$

By substituting $\delta = 0$ in Eq. (2.36), we arrive at the classification of adiabatic pumps as shown in Table 2.2. Comparing Tables 2.1 and 2.2, we can find that the classification of adiabatic pumps in a certain symmetry class is the same as that of TIs and TSCs but in the shifted symmetry class:

$$K_{\mathbb{F}}^{\mathrm{AP}}(s, d) = K_{\mathbb{F}}(s + 1, d). \tag{2.37}$$

This is a natural generalization of the correspondence between the Thouless pump and the Chern insulator. In fact, for $\mathbb{F} = \mathbb{C}, s = 0$, and $d = 1$, we have

$$K_{\mathbb{C}}^{\mathrm{AP}}(0, 1) = K_{\mathbb{C}}(0, 1, 1) = K_{\mathbb{C}}(1, 1, 0) = K_{\mathbb{C}}(0, 2, 0) = \mathbb{Z}, \tag{2.38}$$

where we used Eq. (2.22) in the second equality. The K groups $K_{\mathbb{C}}(0, 1, 1)$ and $K_{\mathbb{C}}(0, 2, 0)$ give the topological number of the Thouless pump and that of the Chern insulator, respectively.

Chapter 3

Brief review on Floquet engineering

Floquet engineering, the control of quantum systems using periodic drives, has a long history of studies in condensed-matter physics, such as the works on the inverse Faraday effect [186, 187]. Recently, this concept has attracted renewed interest owing to the rapid developments in laser and ultrafast spectroscopy techniques [27–29, 46, 47]. In this chapter, we first review two key ingredients of Floquet engineering, namely the Floquet theorem and the high-frequency expansion (HFE), and then present its applications to topological phenomena, symmetry-broken quantum systems, and classical systems.

3.1 Floquet theorem and high-frequency expansion

3.1.1 Floquet theorem and effective Hamiltonian

Let us consider the time-dependent Schrödinger equation driven by a time-dependent Hamiltonian $H(t)$:

$$i\frac{d}{dt}\left|\psi\right\rangle = H(t)\left|\psi\right\rangle, \tag{3.1}$$

where $H(t)$ is periodic in time with period T: $H(t) = H(t+T)$, and we denote the driving frequency as ω: $\omega := 2\pi/T$. The time evolution operator $U(t_f, t_i)$ from t_i to t_f is formally given by

$$U(t_f, t_i) = \mathcal{T}_t \exp\left[-i\int_{t_i}^{t_f} dt H(t)\right], \tag{3.2}$$

where $\mathcal{T}_t$ is the time-ordering operator.

The Floquet-Lyapunov representation theorem, usually called the Floquet theorem for short, dictates that $U(t_f, t_i)$ be written in terms of a Hermitian operator $K(t)$ and the *time-independent* Hamiltonian H_F as follows [30, 31, 188]:

$$U(t_f, t_i) = \mathrm{e}^{-iK(t_f)}\mathrm{e}^{-iH_F(t_f-t_i)}\mathrm{e}^{iK(t_i)}. \tag{3.3}$$

Here, $H_F, K(t)$, and $\mathrm{e}^{\pm iK(t)}$ are called the *effective Hamiltonian*, the *kick operator*, and the *micromotion operator*, respectively. The physical implication of the Floquet theorem is that

the time evolution of the time-periodic Schrödinger equation (3.1) is generated by the *static* effective Hamiltonian H_F apart from the kick operators at initial ($t = t_i$) and final ($t = t_f$) times. The kick operator $K(t)$ is time-periodic with period T and its average over one period vanishes:

$$K(t) = K(t+T), \quad \int_0^T dt\ K(t) = 0. \tag{3.4}$$

The unitary operator $U(T,0)$, which describes the time evolution over one period, is called the *Floquet operator*. For the eigenvalue $\mathrm{e}^{-i\epsilon_a T}$ of the unitary operator $U(T,0)$, the exponent ϵ_a is called the *quasienergy* in analogy with the energy in a static system with a being the label of the eigenstates. The quasienergy is the eigenvalue of the effective Hamiltonian H_F:

$$H_F := \sum_a \epsilon_a \left|\widetilde{u}_a\right\rangle \left\langle\widetilde{u}_a\right|, \tag{3.5}$$

where $|\widetilde{u}_a\rangle$ is the eigenstate. Despite its apparent similarity with energy in a static system, the quasienergy has one important difference: *the quasienergy is periodic with period* $2\pi/T$ since it is formally defined in the exponential form $\mathrm{e}^{-i\epsilon_a T}$. This additional topology gives rise to the difference about realizable topological band structures, as we will see in Sec. 3.2. From the eigenstate $|\widetilde{u}_a\rangle$, we can construct the *Floquet mode* $|u_a(t)\rangle := \mathrm{e}^{-iK(t)}|\widetilde{u}_a\rangle$ that satisfy the periodicity: $|u_a(t+T)\rangle = |u_a(t)\rangle$ and the *Floquet state* $|\psi_a(t)\rangle := \mathrm{e}^{-i\epsilon_a t}|u_a(t)\rangle$ which is a stationary state of the time-dependent Schrödinger equation (3.1):

$$i\frac{d}{dt}\left|\psi_a(t)\right\rangle = H(t)\left|\psi_a(t)\right\rangle, \quad \left|\psi_a(t+T)\right\rangle = \mathrm{e}^{-i\epsilon_a T}\left|\psi_a(t)\right\rangle. \tag{3.6}$$

Equation (3.3) is not a unique decomposition in terms of a time-independent Hamiltonian and a time-periodic kick operator. In another decomposition that is related with the Magnus expansion [189], $U(t_f,t_i)$ is written as

$$U(t_f,t_i) = \mathrm{e}^{-iK^{\mathrm{FM}}(t_f)}\mathrm{e}^{-iH^{\mathrm{FM}}_{F,t_i}(t_f-t_i)}. \tag{3.7}$$

Here, the kick operator $K(t)$ is a time-periodic Hermitian operator that satisfies $K(t_i) = 0$ and the effective Hamiltonian H^{FM}_{F,t_i} depends on the initial time t_i. The effective Hamiltonian $H^{\mathrm{FM}}_{F,t}$ is unitary equivalent to H_F defined above:

$$H^{\mathrm{FM}}_{F,t} = \mathrm{e}^{-iK(t)}H_F\mathrm{e}^{iK(t)}. \tag{3.8}$$

While H_F does not depend on the initial and final kick times t_i and t_f, respectively, H^{FM}_{F,t_i} has a spurious dependence on the initial time t_i [109,112,113,190], resulting in artifactual symmetry breaking [110]. Despite this drawback, the decomposition (3.7) is useful for a general analysis of the high-frequency expansion like its convergence properties [95,96,114]. Besides, it is used to analyze the long-time behavior of the system, e.g., heating and an exact steady state, because $H^{\mathrm{FM}}_{F,t_i=0}$ is directly related with the Floquet operator $U(T,0)$ as $U(T,0) = \exp\left(-iTH^{\mathrm{FM}}_{F,t_i=0}\right)$.

3.1.2 High-frequency expansion of the effective Hamiltonian and the kick operator

Practically, it is not realistic to evaluate the effective Hamiltonian and the kick operator based on the decomposition (3.3) and (3.7), and one has to rely on some approximations. An efficient tool to compute the effective Hamiltonian in the high-frequency limit is the *high-frequency expansion* (HFE), which is a perturbative scheme in powers of ω^{-1} [27, 28]. Corresponding to the two decomposition (3.3) and (3.7), there are two types of the HFE. On one hand, the HFE based on Eq. (3.3) is called the *van Vleck high-frequency expansion* (vV HFE) or simply the *high-frequency expansion* [109, 111–113]. On the other hand, the HFE based on Eq. (3.7) is called the *Floquet-Magnus high-frequency expansion* (FM HFE) or simply the *Floquet-Magnus expansion* [96, 114]. The vV HFE is used for the analytical and numerical calculation with low-order truncation because it does not have the spurious dependence on the initial time which the FM HFE has. The FM HFE is used for a general analysis of the convergence properties because its general term is known.

First few terms of the van Vleck high-frequency expansion

Let us express $H(t)$ in their Fourier harmonics

$$H(t) = \sum_{m=-\infty}^{\infty} H_m \mathrm{e}^{-im\omega t}, \tag{3.9}$$

$$H_m = \frac{1}{T}\int_0^T dt H(t)\mathrm{e}^{im\omega t}, \tag{3.10}$$

and formally expand H_F and $K(t)$ in powers of ω^{-1}:

$$H_F = \sum_{m=0}^{\infty} H_F^{(m)}, \quad K(t) = \sum_{m=0}^{\infty} K_F^{(m)}(t). \tag{3.11}$$

Here, $H_F^{(m)}$ and $K_F^{(m)}(t)$ are of the order of $\mathcal{O}(\omega^{-m})$. To be concrete, the three leading terms of $H_F^{(m)}$ are given as follows [109, 110]:

$$H_F^{(0)} = H_0, \tag{3.12}$$

$$H_F^{(1)} = \sum_{m\neq 0} \frac{[H_{-m}, H_m]}{2m\omega}, \tag{3.13}$$

$$H_F^{(2)} = \sum_{m\neq 0} \left\{ \frac{[H_{-m}, [H_0, H_m]]}{2(m\omega)^2} + \sum_{m'\neq 0,m} \frac{[H_{-m'}, [H_{m'-m}, H_m]]}{3mm'\omega^2} \right\}. \tag{3.14}$$

The three leading terms of $K_F^{(m)}(t)$ are also given by

$$K_F^{(0)}(t) = 0, \tag{3.15}$$

$$K_F^{(1)}(t) = -i\sum_{m\neq 0} \frac{H_{-m}\mathrm{e}^{im\omega t}}{m\omega}, \tag{3.16}$$

$$K_F^{(2)}(t) = i\sum_{m\neq 0}\left\{\frac{[H_0, H_{-m}]\,\mathrm{e}^{im\omega t}}{(m\omega)^2} + \sum_{m'\neq 0,m}\frac{[H_{m'}, H_{-m}]\,\mathrm{e}^{i(m-m')\omega t}}{2m(m-m')\omega^2}\right\}. \tag{3.17}$$

Equations (3.12) and (3.15) indicate that, in the lowest order, the dynamics is generated by the time-averaged Hamiltonian: $U(t,0) \approx \exp(-iH_0 t)$. This result is consistent with our intuition: the system cannot follow a fast drive and hence feels the time average H_0. The derivation of the vV HFE based on van Vleck's degenerate perturbation theory is given in Ref. [110].

By substituting the truncated series into Eq. (3.11), we can evaluate the time evolution (3.3). In particular, if we ignore the micromotion and focus on the averaged dynamics, we can approximate it by the *static* effective Hamiltonian: $U(t,0) \approx \exp(-iH_F t)$, where the analysis of the *non-equilibrium* problem is now reduced to a *static* one. Conversely, by tailoring the time-dependent Hamiltonian $H(t)$, one can realize the dynamics of a static Hamiltonian H_F with desired properties. This form of quantum engineering, usually termed *Floquet engineering*, now recognized as a versatile tool for controlling quantum systems including the dynamic control of the superfluid-Mott insulator transition [32–34], the creation of artificial gauge fields [35–38, 191],* the implementation of kinetic frustration and topological phases [17,19,20,56,85,193–196], and the control of magnetization and spin chirality [71–74, 76–78].

General term of the Floquet-Magnus high-frequency expansion

Let $H_{F,t_0}^{(m)}$ be the mth-order term of the FM HFE of H_{F,t_0}^{FM}:

$$H_{F,t_0}^{\mathrm{FM}} = \sum_{m=0}^{\infty} H_{F,t_0}^{(m)}, \tag{3.18}$$

where $H_{F,t_0}^{(m)}$ is of the order of $\mathcal{O}(\omega^{-m})$ and t_0 is the initial time. Unlike the vV HFE, the general term for the FM HFE of H_{F,t_0}^{FM} is known, which is given as follows [189, 197]:

$$H_{F,t_0}^{(0)} = \int_{t_0}^{t_0+T} dt\; H(t), \tag{3.19}$$

$$H_{F,t_0}^{(m)} = \sum_{\sigma\in S_m}\frac{(-1)^{m-\Theta_\sigma}\Theta_\sigma!(m-\Theta_\sigma)!}{i^m(m+1)^2 m! T} \times \int_{t_0}^{t_0+T} dt_{m+1}\cdots\int_{t_0}^{t_0+t_2} dt_1\left[H'_{m+1},[H'_m,\cdots[H'_2,H'_1]]\right] \quad \text{for} \quad m\geq 1, \tag{3.20}$$

where S_m is the permutation group of order m, $H'_i := H(t_{\sigma(i)})$, and Θ_σ is defined by $\Theta_\sigma := \sum_{i=1}^{m}\theta\left[\sigma(i+1)-\sigma(i)\right]$ with $\theta(x)$ being the Heaviside unit step function. Using this general term, the convergence property of the HFE is analyzed in both few-body [114] and many-body [95, 96] systems. Note that the convergence property does not change for two HFEs because of the unitary equivalence (3.8) between H_F and H_{F,t_0}^{FM}.

*Though it is not explicitly mentioned frequently, an artificial gauge field is an example of Floquet engineering. In fact, the Rabi frequency of an artificial gauge field created by the two Raman beams in a Λ scheme is proportional to the inverse frequency of the Raman beams, which can be regarded as the first correction term $H_F^{(1)}$ of the vV HFE (3.11). See Refs. [27, 192] for further discussions.

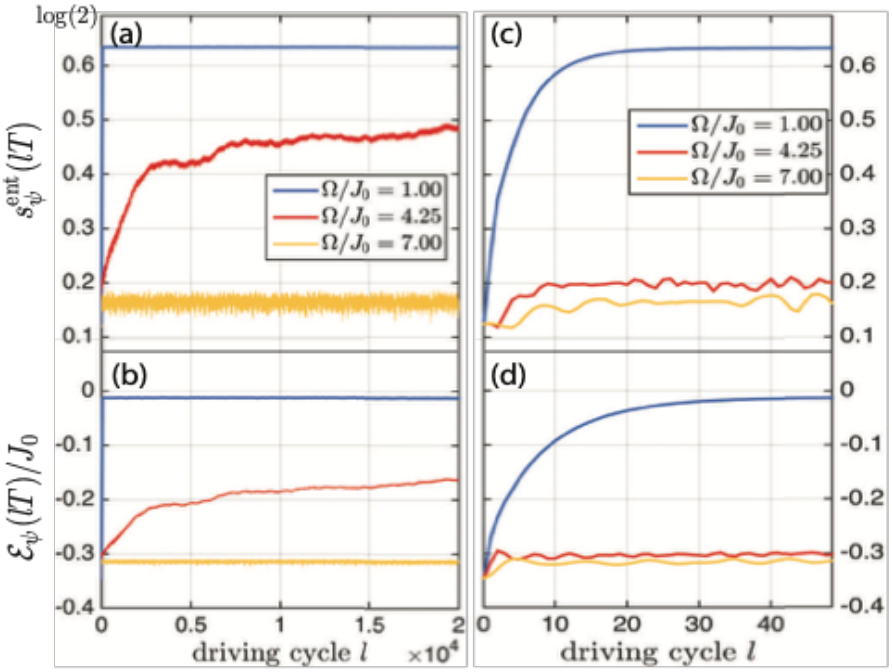

Figure 3.1: Short- and long-time stroboscopic dynamics of (a) and (c) the entropy density and (b) and (d) energy density of driven hard-core bosons on a one-dimension lattice with two bands, where Ω and J_0 denote the frequency of the drive and the average hopping amplitude to nearest-neighbor sites, respectively. For a low-frequency drive ($\Omega/J_0 = 1.00$), the system quickly heats up to the infinite temperature state with the maximum energy and entropy densities. On the other hand, for relatively high-frequency drives ($\Omega/J_0 = 4.25, 7.00$), the system relaxes to a Floquet prethermal states with finite energy and entropy densities, which are well described by the truncated HFE. Reproduced from Fig. 2 of Ref. [97]. © 2016 by the American Physical Society.

Convergence property of the high-frequency expansion

Mathematically, the FM HFE is guaranteed to converge if $H(t)$ satisfies

$$\int_0^T dt \|H(t)\| \leq \zeta, \tag{3.21}$$

where $\|\cdot\|$ is the operator norm and ζ is a universal constant of the order of one [114, 189]. However, one cannot apply this inequality to *many-body* Floquet systems because the left-hand side of Eq. (3.21) diverges in the thermodynamic limit. Quantum many-body systems, in general, have a large number of excited states and hence can absorb energy from an external drive without limit, leading to eventual heating to a featureless infinite-temperature state after a sufficiently long time [94, 96, 198–201]. Based on this fact and the Floquet eigenstate thermalization hypothesis [94, 198–201], which is a generalization of the eigenstate thermalization hypothesis (ETH) [202–204] to Floquet systems, it is widely believed that the HFE is a divergent series for a generic quantum many-body system, though several exceptions exist including an integrable system and a many-body localized system [94, 200, 205–208].

Nevertheless, the HFE provides a suitable approximation when ω is sufficiently larger than a typical single-particle energy scale of the system, at least within a time domain before the system heats up. For locally interacting systems with a finite single-particle energy, e.g. lo-

cally interacting spins, fermions, and hard-core bosons, it is rigorously shown that the energy absorption rate dE/dt is exponentially small up to a certain time [95, 96, 98, 209]:

$$\frac{1}{N}\frac{dE}{dt} \leq \frac{N_V}{N} \exp\left[-\mathcal{O}\left(\frac{\omega}{g}\right)\right], \tag{3.22}$$

where g, N, and N_V are the maximum energy scale per site, the number of sites, and the number of sites under the drive, respectively. This time domain, usually termed as the *Floquet prethermal regime*, is exponentially long with respect to ω and the truncated FM HFE $H_{\mathrm{TR}}^{(m_0)} := \sum_{m=0}^{m_0} H_{F,t_0}^{(m_0)}$ is almost conserved within the Floquet prethermal regime:

$$\|U^\dagger(t,0)H_{\mathrm{TR}}^{(m_0)}U(t,0) - H_{\mathrm{TR}}^{(m_0)}\| \leq 16g^2k2^{-m_0}N_V t, \tag{3.23}$$

where k and $m_0 \approx \omega/gk$ are the number of sites associated with the interaction and the optimal order of the truncation, respectively. The bound (3.22) physically implies that, even though a many-body system can absorb a large amount of energy, this process must be accompanied by a large number of single-particle excitations and hence is exponentially suppressed. Because of the quasi-conserved quantity $H_{\mathrm{TR}}^{(m_0)}$ derived from Eq. (3.23), a generic (non-integrable) many-body system approaches the Floquet-Gibbs state $\exp(-\beta H_{\mathrm{TR}}^{(m_0)})$ after the initial relaxation. This transient state is called the *Floquet prethermal state* in analogy with the prethermal state in integrable systems under a sudden quench [210–213]. The existence of the Floquet prethermal state in the Floquet prethermal regime is numerically verified in quantum systems with interacting spins and hard-core bosons [95–97]. For example, in Ref. [97], driven hard-core bosons on a one-dimension lattice with two bands is studied. As shown in Fig. 3.1, for relatively high-frequency drives (red and yellow curves), the system thermalizes to a Floquet prethermal state with finite energy and entropy densities, which is well described by the truncated FM HFE. Furthermore, the existence of the Floquet prethermal state is demonstrated in various experiments using ultracold bosonic and fermionic gases [27, 28]. In ultracold atomic gases, Floquet engineering using a Floquet prethermal state is commonly used for realizing exotic topological band structures [20, 37, 214, 215], kinetic frustration [193–195], and artificial gauge fields [36, 38, 216, 217]. We finally note that, while the presence of Floquet prethermal states is rigorously proven, little is known on the exact steady state that appears after the Floquet prethermal regime. While the system should heat up to an infinite temperature state if the Floquet ETH holds, there might be another possibility [198] and the precise condition of the Floquet ETH is not known so far. It is also an open problem to understand the heating dynamics from a Floquet prethermal state to an infinite temperature state, for example whether it is a crossover or a non-equilibrium phase transition.

3.2 Floquet engineering of topological quantum phenomena

When a Floquet system is defined on a translationally invariant lattice, its Floquet operator is decomposed according to the momentum $\boldsymbol{k}$: $U(T,0) = \sum_{\boldsymbol{k}} U(\boldsymbol{k})$, where $U(\boldsymbol{k})$ is called the *Floquet-Bloch operator* or the *Floquet unitary*. There are two ways to assign nontrivial topology in Floquet systems: (i) using the entire time evolution $\{U(t,0)|0 \leq t \leq T\}$, (ii) using

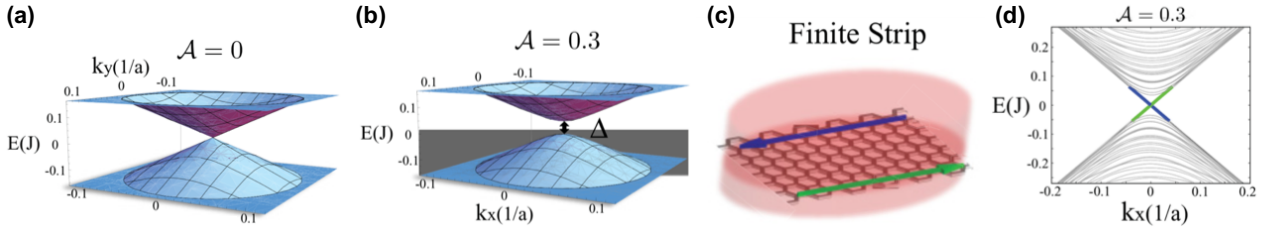

Figure 3.2: Quasienergy spectra of H_F for a single spin state near one of the Dirac points in the torus geometry for driving strength $\mathcal{A} = 0$ (a) and $\mathcal{A} = 0.3$ (b). A finite gap Δ opens at the Dirac point in Fig. (b) through the external drive. (c) Schematic illustration of gapless chiral edge states in the Floquet TI in a laser-irradiated graphene. (d) The spectrum of H_F for a single spin state near one of the Dirac points in the strip geometry. The parameters are chosen as $\omega = 7.5J$ and $\mathcal{A} = 0.3$. The blue and green curves correspond to the edge states in the upper and lower edges in Fig. (c). Reproduced from Fig. 3 of Ref. [86]. © 2011 by the American Physical Society.

the Floquet unitary $U(T, 0)$. The former gives anomalous topological insulators while the latter gives Floquet topological insulators and topological pumps including the Thouless pump.

3.2.1 Floquet topological insulators

Consider a graphene irradiated by a circularly polarized light with an electric field $\boldsymbol{E}(t) := \partial_t \boldsymbol{A}(t)$, where $\boldsymbol{A}(t) := A\,(\sin(\omega t), \cos(\omega t), 0)^{\mathrm{tr}}$ is the vector potential. Through the gauge field, the hopping amplitude of electrons acquires the Peierls phase, where the tight-binding Hamiltonian is given as follows [86]:

$$H(t) = -t \sum_{\langle \boldsymbol{r}, \boldsymbol{r}' \rangle, s} \mathrm{e}^{ie\boldsymbol{A}(t)\cdot(\boldsymbol{r}-\boldsymbol{r}')} c^{\dagger}_{\boldsymbol{r},s} c_{\boldsymbol{r}',s}. \tag{3.24}$$

Here, t and $c_{\boldsymbol{r},s}$ are the bare hopping amplitude and the annihilation operator of an electron at site $\boldsymbol{r}$ with spin $s =\uparrow, \downarrow$, respectively. For a large driving frequency ω ($\gg t$), we can perform the vV HFE to obtain the effective Hamiltonian near the Dirac point:

$$H_F = H_0 + \frac{[H_{-1}, H_1]}{\omega} \approx \sum_{\boldsymbol{k}} \left[v_G(\sigma_y k_x - \sigma_x k_y \tau_z) + \frac{(v_G \mathcal{A})^2}{\omega} \sigma_z \tau_z \right], \tag{3.25}$$

where $v_G = 3t/2$ and $\mathcal{A} := eAa$ are the velocity of the Dirac electron and the dimensionless parameter of the light intensity, respectively with a being the lattice constant of the graphene. Here, k_x and k_y are the momenta measured from the Dirac point and σ_i (τ_i) is the Pauli matrices representing the sublattice (valley) degrees of freedom.

By a periodic drive, the gap $\Delta := 2v_G^2 \mathcal{A}^2/\omega$ opens at the Dirac point (see Figs. 3.2 (a) and (b)). Moreover, the resulting effective Hamiltonian H_F describes a Chern insulator with Chern number $Ch_1 = +1$. This is an example of the *Floquet topological insulators*, topological insulators induced by periodic drives [17, 18, 56, 86, 218]. Because of the nonzero Chern number, the quasienergy band features the chiral dispersions as shown in Fig. 3.2 (d) representing chiral edge states (see Fig. 3.2 (c)).

Experimentally, the topological band structures of Floquet topological insulators were observed in ultracold atomic gases by sophisticated band spectroscopy [20, 37, 214, 215, 219, 220]

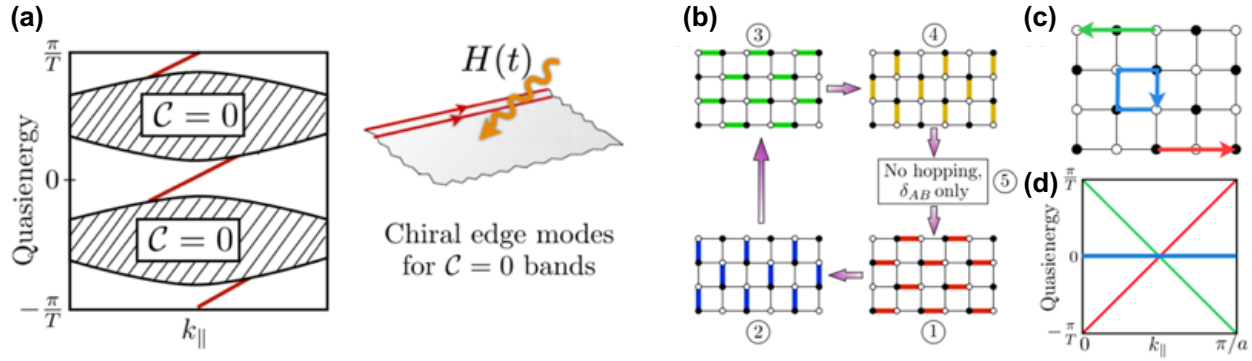

Figure 3.3: (a) (Left) Schematic illustration of quasienergy bands of an anomalous topological insulator ($\mathcal{C}$ is the Chern number). Chiral edge bands shown as the red curves appear around $\epsilon = \pi/T$, where $k_\parallel$ is the momentum along the edge in the right figure. (Right) anomalous edge states in a two-dimensional system with time-dependent Hamiltonian $H(t)$. (b) Five-step protocol of the model defined in Eqs. (3.26) and (3.27). (c) Motion of a particle in one cycle for the parameters $JT/5 = \pi/2$ and $\delta_{AB} = 0$. When a particle starts from a bulk site, it returns to its initial site (blue loop), while particles starting from edge sites propagates along the boundary (red and green arrows) (d) Quasienergy spectra of the bulk (blue) and the edge (red and green) states for parameters $JT/5 = \pi/2$ and $\delta_{AB} = 0$. Reproduced from Figs. 1 and 2 of Ref. [225]. © 2013 by the American Physical Society.

and in solid-state systems by angle-resolved photoemission spectroscopy [19, 21]. In ultracold atomic gases, skipping motions of the chiral edge states of quantum Hall states induced by artificial gauge fields have been observed [219, 220] using the technique of *synthetic dimensions* [221]. Very recently, following the original proposals [17, 86], the anomalous Hall effect has been observed in a laser-irradiated monolayer graphene, where the Hall conductance approaches the quantized value $e^2/2\pi$ when the Fermi level lies within the band gap [22]. We note that while a Floquet topological insulator can be realized as an almost isolated system in ultracold atomic gases, a coupling with an environment is not negligible in a solid-state system. Furthermore, one must introduce dissipation to prevent heating and stabilize Floquet topological insulators. Floquet topological insulators under dissipative environments, usually termed as dissipative topological insulators, have been studied in Refs. [59, 60, 222–224]. Finally, it is worthwhile to mention that the realizable band structures derived through the HFE are the same as those in static systems because H_F is continuously deformed into a static Hamiltonian H_0 by taking the high-frequency limit $\omega^{-1} \to 0$.

3.2.2 Anomalous topological insulators and their classification

Anomalous topological insulators are topological phases of matter unique to Floquet systems that have no counterparts in static systems [86,87,225]. In particular, in driven two-dimensional systems, robust chiral edge states can appear even though the Chern numbers of all the bulk quasienergy bands vanish [86, 225] (see Fig. 3.3 (a)).

Here, we consider the tight-binding model on a bipartite square lattice introduced in Ref. [225]. The hopping amplitudes are varied in a spatially homogeneous but time-periodic

manner as shown in Fig. 3.3 (b). The Hamiltonian of this system is given by

$$H = \sum_{\boldsymbol{k}} \left(c^\dagger_{\boldsymbol{k},A}, c^\dagger_{\boldsymbol{k},B} \right) h(\boldsymbol{k},t) \begin{pmatrix} c_{\boldsymbol{k},A} \\ c_{\boldsymbol{k},B} \end{pmatrix}, \tag{3.26}$$

$$h(\boldsymbol{k},t) = \begin{cases} -J(\sigma_+ \mathrm{e}^{i\boldsymbol{b}_1\cdot\boldsymbol{k}} + \mathrm{h.c.}) + \delta_{AB}\sigma_z & t \in [0, T/5] \mod T; \\ -J(\sigma_+ \mathrm{e}^{i\boldsymbol{b}_2\cdot\boldsymbol{k}} + \mathrm{h.c.}) + \delta_{AB}\sigma_z & t \in [T/5, 2T/5] \mod T; \\ -J(\sigma_+ \mathrm{e}^{i\boldsymbol{b}_3\cdot\boldsymbol{k}} + \mathrm{h.c.}) + \delta_{AB}\sigma_z & t \in [2T/5, 3T/5] \mod T; \\ -J(\sigma_+ \mathrm{e}^{i\boldsymbol{b}_4\cdot\boldsymbol{k}} + \mathrm{h.c.}) + \delta_{AB}\sigma_z & t \in [3T/5, 4T/5] \mod T; \\ \delta_{AB}\sigma_z & t \in [4T/5, T] \mod T, \end{cases} \tag{3.27}$$

where $c_{\boldsymbol{k},X}$ is the annihilation operator of a particle on sublattice $X = A, B$ with momentum $\boldsymbol{k}$ and $\boldsymbol{b}_1 = -\boldsymbol{b}_3 = (a, 0)$ and $\boldsymbol{b}_2 = -\boldsymbol{b}_4 = (0, a)$, with a being the lattice constant. Here, δ_{AB} describes the potential difference between the sublattices.

For the parameter values $JT/5 = \pi/2$ and $\delta_{AB} = 0$, we can rigorously prove the existence of the edge states that propagate along the boundary. For this parameter set, a particle moves with probability 1 between neighboring sites during each hopping step of the cycle. A particle initially located at a bulk site makes a loop around a plaquette and returns to its initial position after one cycle as shown as the blue trajectory in Fig. 3.3 (c). Hence, the bulk Floquet operator is trivial: $U(T, 0) = 1$, which leads to the flat bulk bands as shown in Fig. 3.3 (d). On the other hand, a particle initially located at an edge site moves along the edge with two sites after one period, resulting in the gapless chiral bands in the quasienergy spectra (red and green trajectories in Fig. 3.3 (c)). When J and δ_{AB} are slightly modified, the gapless chiral spectra around $\epsilon = \pi/T$ survive and the flat bulk bands split into two bands with the vanishing Chern number. The resulting phase is called an *anomalous* topological insulator in the sense that it has nontrivial edge states, although all the bulk Chern numbers vanish.

Let us decompose the time evolution operator $U(t, 0)$ according to the momentum $\boldsymbol{k}$: $U(t, 0) = \sum_{\boldsymbol{k}} U(\boldsymbol{k}, t)$. When $U(\boldsymbol{k}, T)$ is a trivial Floquet unitary, the topological characterization of the anomalous TIs in two dimensions is given by the three-dimensional winding number ν of the map $(\boldsymbol{k}, t)$ $(\in \mathbb{T}^3) \mapsto U(\boldsymbol{k}, t)$ $(\in \mathrm{SU}(2))$ [225]:

$$\nu = \frac{1}{8\pi^2} \int dt d\boldsymbol{k} \mathrm{Tr} \left[R_t \left(R_{k_x} R_{k_y} - R_{k_x} R_{k_y} \right) \right], \tag{3.28}$$

where $R_i = U^\dagger(\boldsymbol{k}, t)\partial_i U(\boldsymbol{k}, t)$. Even when $U(\boldsymbol{k}, T)$ is not a trivial Floquet unitary, $\tilde{U}(\boldsymbol{k}, t) := \mathrm{e}^{iH_F t} U(\boldsymbol{k}, t)$ is and Eq. (3.28) with the replacement of U with $\tilde{U}$ gives the topological number of the anomalous TIs. The number of the edge states coincides with $|\nu|$ with their chirality determined from its sign $\mathrm{sgn}(\nu)$, which is the bulk-edge correspondence for anomalous topological insulators. Recently, anomalous edge states have been observed in a two-dimensional designer surface plasmon platform and a photonic crystal [226–228].

Similarly to static systems, symmetries, such as the CS and the PHS, play important roles in protecting anomalous edge states [87, 229–232]. The anomalous topological insulators protected by symmetries are, in general, classified by the map $(\boldsymbol{k}, t) \mapsto U(\boldsymbol{k}, t)$ under certain symmetry constraint. Their complete classification is performed through the "Hermitianization" $H_U(\boldsymbol{k}, t)$

Table 3.1: Tenfold-way topological classification of anomalous topological insulators for spatial dimensionality $d = 0, 1, \cdots, 7$ [146]. Notations are the same as in Tab. 2.1.

s	class	Θ	C	Γ	$d=0$	$d=1$	$d=2$	$d=3$	$d=4$	$d=5$	$d=6$	$d=7$
0	A	0	0	0	$\mathbb{Z}\oplus\mathbb{Z}$	0	$\mathbb{Z}\oplus\mathbb{Z}$	0	$\mathbb{Z}\oplus\mathbb{Z}$	0	$\mathbb{Z}\oplus\mathbb{Z}$	0
1	AIII	0	0	1	0	$\mathbb{Z}\oplus\mathbb{Z}$	0	$\mathbb{Z}\oplus\mathbb{Z}$	0	$\mathbb{Z}\oplus\mathbb{Z}$	0	$\mathbb{Z}\oplus\mathbb{Z}$
0	AI	1	0	0	$\mathbb{Z}\oplus\mathbb{Z}$	0	0	0	$2\mathbb{Z}\oplus2\mathbb{Z}$	0	$\mathbb{Z}_2\oplus\mathbb{Z}_2$	$\mathbb{Z}_2\oplus\mathbb{Z}_2$
1	BDI	1	1	1	$\mathbb{Z}_2\oplus\mathbb{Z}_2$	$\mathbb{Z}\oplus\mathbb{Z}$	0	0	0	$2\mathbb{Z}\oplus2\mathbb{Z}$	0	$\mathbb{Z}_2\oplus\mathbb{Z}_2$
2	D	0	1	0	$\mathbb{Z}_2\oplus\mathbb{Z}_2$	$\mathbb{Z}_2\oplus\mathbb{Z}_2$	$\mathbb{Z}\oplus\mathbb{Z}$	0	0	0	$2\mathbb{Z}\oplus2\mathbb{Z}$	0
3	DIII	-1	1	1	0	$\mathbb{Z}_2\oplus\mathbb{Z}_2$	$\mathbb{Z}_2\oplus\mathbb{Z}_2$	$\mathbb{Z}\oplus\mathbb{Z}$	0	0	0	$2\mathbb{Z}\oplus2\mathbb{Z}$
4	AII	-1	0	0	$2\mathbb{Z}\oplus2\mathbb{Z}$	0	$\mathbb{Z}_2\oplus\mathbb{Z}_2$	$\mathbb{Z}_2\oplus\mathbb{Z}_2$	$\mathbb{Z}\oplus\mathbb{Z}$	0	0	0
5	CII	-1	-1	1	0	$2\mathbb{Z}\oplus2\mathbb{Z}$	0	$\mathbb{Z}_2\oplus\mathbb{Z}_2$	$\mathbb{Z}_2\oplus\mathbb{Z}_2$	$\mathbb{Z}\oplus\mathbb{Z}$	0	0
6	C	0	-1	0	0	0	$2\mathbb{Z}\oplus2\mathbb{Z}$	0	$\mathbb{Z}_2\oplus\mathbb{Z}_2$	$\mathbb{Z}_2\oplus\mathbb{Z}_2$	$\mathbb{Z}\oplus\mathbb{Z}$	0
7	CI	1	-1	1	0	0	0	$2\mathbb{Z}\oplus2\mathbb{Z}$	0	$\mathbb{Z}_2\oplus\mathbb{Z}_2$	$\mathbb{Z}_2\oplus\mathbb{Z}_2$	$\mathbb{Z}\oplus\mathbb{Z}$

of the unitary operator $U(\boldsymbol{k}, t)$ [146]:

$$H_U(\boldsymbol{k}, t) := \begin{pmatrix} 0 & U(\boldsymbol{k}, t) \\ U^\dagger(\boldsymbol{k}, t) & 0 \end{pmatrix}. \tag{3.29}$$

We note that the Hamiltonian $H_U(\boldsymbol{k}, t)$ is a gapped Hamiltonian with flat dispersions because we have $[H_U(\boldsymbol{k}, t)]^2 = 1$. From the Hermitianization, the classification of $U(\boldsymbol{k}, t)$ reduces to that of the Hamiltonian $H_U(\boldsymbol{k}, t)$ with the additional CS. As shown in Table 3.1, the resulting classification is analogous to the original periodic table in Table 2.1, but the topological number is doubled. This doubling reflects the usual and anomalous edge states near $\epsilon = 0$ and $\epsilon = \pi/T$, respectively. For example, the topological number in class A in two dimensions is given by $\mathbb{Z}\oplus\mathbb{Z}$, where the first (second) $\mathbb{Z}$ represents the usual (anomalous) edge states.

3.2.3 Adiabatic topological pump revisited from the Floquet viewpoint

Interestingly, an adiabatic pump without any symmetry features a topologically nontrivial band structure in its quasienergy that is not achievable in a static system. To see this, consider the Rice-Mele model analyzed in Sec. 2.3. From the adiabatic theorem, an occupied state with momentum k returns to the same state within one cycle; thus the Floquet operator is decomposed according to the momentum k and the Bloch-band index α:

$$U(T, 0) = \sum_{k,\alpha} U_{F,\alpha}(k). \tag{3.30}$$

Then, the pumped fermion charge ν_{1d} in Eq. (2.34) is rewritten in terms of $U_{F,\alpha}(k)$ as follows [85]:

$$\nu_{1d} = \sum_{\alpha:\mathrm{occ}} \int_0^{2\pi} \frac{dk}{2\pi} \mathrm{Tr}[U_{F,\alpha}^\dagger(k) i\partial_k U_{F,\alpha}(k)], \tag{3.31}$$

where the sum $\sum_{\alpha:\mathrm{occ}}$ is taken over the occupied bands. Since the Thouless pump does not require any symmetry, the quasienergy has no accidental degeneracy and hence $U_\alpha(k)$ acts on

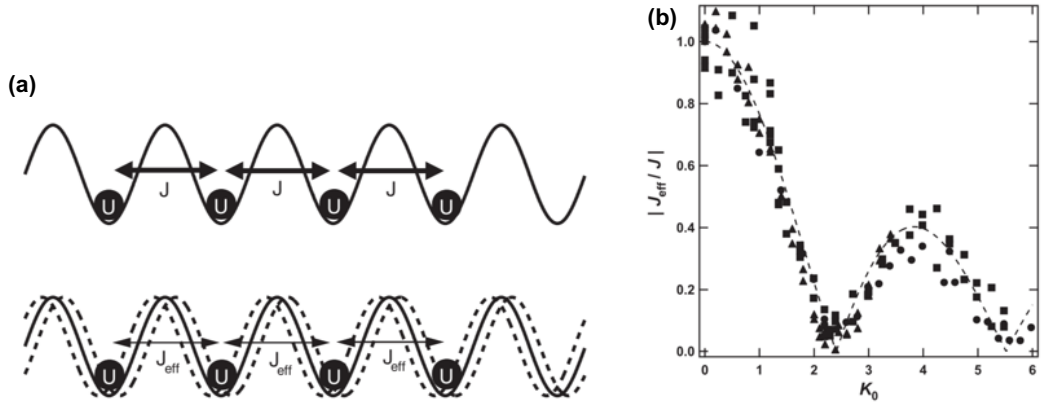

Figure 3.4: (a) Schematic illustration of a shaken optical lattice. By shaking the lattice, the hopping amplitude J is renormalized to $J_{\rm eff}$ while the on-site interaction U remains unchanged. (b) Dynamical suppression of the hopping amplitude in a shaken optical lattice. The horizontal axis $K_0 := K/\omega$ is the dimensionless driving strength and the vertical axis is the ratio $|J_{\rm eff}/J|$ between the renormalized and bare hopping amplitudes. The dashed curve shows the theoretical curve and the different markers correspond to different depths of the optical lattice and driving frequencies. Reproduced from Figs. 1 and 2 of Ref. [237]. © 2007 by the American Physical Society.

a single band. Therefore, $U_{F,\alpha}(k)$ is expressed in terms of the quasienergy $\epsilon_\alpha(k)$ as $U_{F,\alpha}(k) = \exp\left[-i\epsilon_\alpha(k)T\right]$; then, ν_{1d} is rewritten as follows:

$$\nu_{1d} = T\sum_{\alpha:\mathrm{occ}}\int_0^{2\pi}\frac{dk}{2\pi}\partial_k\epsilon_\alpha(k). \tag{3.32}$$

The right-hand side is the total winding number of the quasienergy bands as k runs over the Brillouin zone.

For a unit winding $\nu_{1d} = 1$, $\epsilon_\alpha(k)$ is topologically equivalent to $\epsilon_\alpha(k) = k/T$, i.e., the band of a single chiral fermion. It is known as the one-dimensional Nielsen-Ninomiya theorem that a single chiral fermion is impossible to realize in a one-dimensional static lattice system [90, 91]. In this sense, Floquet systems can realize topological band structures that are not achievable in static systems utilizing the periodicity of the quasienergy spectrum. Other than a single chiral fermion, it is known that a pair of helical fermions is known to be impossible to realize in a lattice system with the TRS, while it can be realized as a quasienergy band in a periodically driven lattice system with the TRS [89, 184]. The impossibility of pure lattice realizations of surface states is known to be deeply connected with their gapless nature protected under a symmetry via quantum anomalies [233–235].

3.3 Floquet engineering of ordered states

In the above examples, we have treated Floquet engineering of a topological phase of non-interacting particles, which is essentially a single-particle problem. Floquet engineering is also applied to many-body systems to control hopping amplitudes and interactions, where one can dynamically manipulate order parameters and even induce phase transitions [32–34, 71–74, 76–78, 80, 193–195, 236–238].

3.3.1 Bose-Einstein condensates

Consider the Bose-Hubbard model on a one-dimensional shaken optical lattice with L sites (see Fig. 3.4 (a)):

$$H(t) = -J\sum_{j=1}^{L}(c_{j+1}^{\dagger}c_j + c_j^{\dagger}c_{j+1}) + \frac{U}{2}\sum_{j=1}^{L} n_j(n_j-1) + K\cos(\omega t)\sum_{j=1}^{L} n_j, \tag{3.33}$$

where $c_j, n_j := c_j^{\dagger}c_j, K$, and ω are the annihilation operator of the boson at site j, the number operator, the strength of the shaking, and the shaking frequency, respectively. The first two terms on the right-hand side of Eq. (3.33) describe the Bose-Hubbard model with hopping amplitude J and on-site interaction U, while the third term represents the potential arising from the shaking. Transforming into the co-moving frame of the shaking and performing the vV HFE up to the lowest order, we obtain the effective Hamiltonian $H_F = H_F^{(0)}$. The resulting effective Hamiltonian $H_F^{(0)}$ turns out to be the same as the Bose-Hubbard model on a static lattice but with renormalized hopping:

$$H_F = -J\mathcal{J}_0(K/\omega)\sum_{j=1}^{L}(c_{j+1}^{\dagger}c_j + c_j^{\dagger}c_{j+1}) + \frac{U}{2}\sum_{j=1}^{L} n_j(n_j-1), \tag{3.34}$$

where $\mathcal{J}_0(x)$ is the zeroth-order Bessel function [32,33]. Since we have $|\mathcal{J}_0(x)| \leq 1$, the hopping is suppressed and even vanishes with suitable driving strength K, leading to the counterintuitive localization induced by a periodic drive, which is known as the *dynamical localization* [10]. The dynamical localization is observed in Bose-Einstein condensates of ^{87}Rb through measurements of the ballistic spread of initially localized condensates [34, 236, 237]. In these experiments, the expansion of the condensates is reduced and even completely suppressed in the suitable driving strengths $K \approx 2.4\omega, 5.5\omega$ as shown in Fig. 3.4 (b). Moreover, in Ref. [34], the superfluid-Mott insulator transition is induced by adiabatically changing the driving strength.

It is worth mentioning that Floquet engineering of Bose-Einstein condensates is applied for realizing *classical* frustrated magnets. Since the order-parameter manifold of a superfluid and that of a classical XY model are both the circle S^1, one can utilize an ultracold atomic gas in a superfluid regime for simulating a classical XY model. Moreover, using its great controllability, one can change various parameters in the model including spacial dimensionality, lattice structures, anisotropies, and even the *sign* of an interaction, which are hard to control in a usual solid-state setup [193–195]. Finally, we note that the dynamical localization is also observed in solid-state systems [43, 44, 49], where the insulator-metal transition is induced.

3.3.2 Quantum Magnets

Controlling magnetic materials by laser attracts growing interest in recent years since it could offer their ultrafast and non-contact manipulation [46, 47]. Using a periodic drive by laser as a tool of Floquet engineering, one can dynamically manipulate their magnetic orders [72, 73] and even control their intrinsic interactions, such as the exchange interaction [74, 75, 79] and the Dzyaloshinskii-Moriya (DM) interaction [76, 80–82].

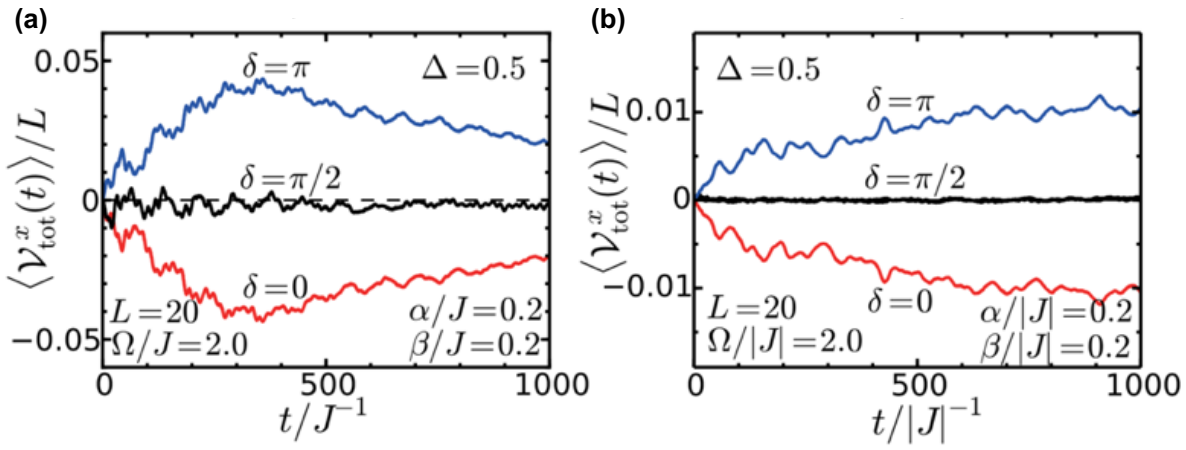

Figure 3.5: (a) Expectation value of the vector chirality $\mathcal{V}^x_{\rm tot}$ as a function of time in the antiferromagnetic XXZ chain (3.40), where $\delta = 0, \pi/2$, and π correspond to the right-circularly, linearly, and left-circularly polarized lasers, respectively. (b) The same as in (a) but with a ferromagnetic interaction. Reproduced from Fig. 3 of Ref. [76]. © 2016 by the American Physical Society.

Laser-driven multiferroic spin chain

Multiferroics are materials that exhibit both ferromagnetism and ferroelectricity [239–241]. Because of the coupling between the spin degrees of freedom and the polarization, multiferroic materials have potential applications to next-generation spintronics [242]. In Ref. [76], it was shown that, by irradiation of circularly polarized lasers, a synthetic DM interaction [99, 100] emerges with controlled magnitude and orientation, leading to a spiral magnetic order. Moreover, by spatially modulating the laser intensity, a spin current can be generated.

Consider a multiferroic spin chain with L spins irradiated by the laser field whose electric and magnetic fields are given by

$$\boldsymbol{E}(t) = E_0 \left(\cos(\omega t + \delta), -\sin(\omega t), 0\right)^{\rm tr}, \tag{3.35}$$

$$\boldsymbol{B}(t) = \frac{E_0}{c} \left(-\sin(\omega t), -\cos(\omega t + \delta), 0\right)^{\rm tr}. \tag{3.36}$$

Here, $\delta = 0, \pi/2$, and π correspond to the right-circularly, linearly, and left-circularly polarized lasers, respectively. The overall Hamiltonian $H(t)$ is given by

$$H(t) = H_0 - \boldsymbol{P} \cdot \boldsymbol{E}(t) - g\mu_B \boldsymbol{S} \cdot \boldsymbol{B}(t), \tag{3.37}$$

where the first, second, and third terms on the right-hand side represent the bare Hamiltonian, the magnetoelectric coupling, and the Zeeman coupling, respectively. Here, g and μ_B are Lande's g factor and the Bohr magneton, respectively. Here, $\boldsymbol{P}$ and $\boldsymbol{S} = \sum_{j=1}^{L} \boldsymbol{S}_j$ are the total polarization and the total magnetization, respectively, where $\boldsymbol{S}_j$ is the spin at site j. We assume that the magnetoelectric coupling is the antisymmetric magnetostriction type, which is written in the following form:

$$\boldsymbol{P} = g_{\rm me} \sum_{j=1}^{L} \boldsymbol{e}_1 \times (\boldsymbol{S}_j \times \boldsymbol{S}_{j+1}), \tag{3.38}$$

where $g_{\rm me}$ represents the strength of the magnetoelectric coupling and $\boldsymbol{e}_1 = (1,0,0)^{\rm tr}$ is the unit vector along the chain axis. This magnetoelectric coupling is responsible for electric polarization in various spirally ordered multiferroic magnets [243–246]. From the first-order vV HFE, the effective Hamiltonian H_F is given by

$$H_F = H_0 + \sum_{j=1}^{L} \frac{\alpha\beta\cos\delta}{2\omega}\mathcal{V}_{j,x} + \sum_{j=1}^{L} \frac{\beta^2\cos\delta}{2\omega} S_{j,z}, \tag{3.39}$$

where $\alpha := g_{\rm me}E_0$ and $\beta := (g\mu_B E_0)/c$ are the normalized electric and magnetic energies, respectively. Here, $\mathcal{V}_{j,x} := \boldsymbol{e}_1 \cdot (\boldsymbol{S}_j \times \boldsymbol{S}_{j+1})$ is the vector chirality along the x direction and the second term on the right-hand side of Eq. (3.39) describes the synthetic DM interaction along the x direction. From the effective Hamiltonian (3.39), we expect the generation of the vector chirality as time elapses. In Figs. 3.5 (a) and (b), the time evolution of the total vector chirality $\mathcal{V}^x_{\rm tot} := \sum_j \mathcal{V}_{j,x}$ for two different choices of H_0 is shown. In Fig. 3.5 (a), H_0 is taken as the antiferromagnetic XXZ chain

$$H_0 = J\sum_{j=1}^{L} \left(\boldsymbol{S}_j \cdot \boldsymbol{S}_{j+1} - \Delta S_{j,x}S_{j+1,x}\right), \tag{3.40}$$

where $J > 0$ and Δ are the antiferromagnetic coupling constant and the anisotropy parameter, respectively, while Fig. 3.5 (b) is obtained from the same H_0 but the ferromagnetic interaction, i.e., $J < 0$. The time evolution is calculated by solving the Schrödinger equation by the fourth-order Runge-Kutta method and the initial state is chosen as the ground state of H_0. In both cases, the finite vector chirality is produced with its value controlled by the helicity parameter δ, which is consistent with the effective Hamiltonian (3.39). However, after a sufficiently long time, $|\mathcal{V}^x_{\rm tot}|$ decreases because of the heating. When the laser intensity is spatially modulated, the spatial gradient of $\mathcal{V}_{j,x}$ is induced. From the Heisenberg equation

$$i\frac{dS_{j,x}}{dt} \approx [S_{j,x}, H_0] = iJ\left(\mathcal{V}_{j-1,x} - \mathcal{V}_{j,x}\right), \tag{3.41}$$

a spin current proportional to the spatial gradient is generated.

3.4 Floquet engineering of classical systems

Periodically driven classical systems have a long history of study, where a number of interesting phenomena have been found including dynamical localization [9], stochastic resonance [11, 12], and dynamical stabilization [13–15]. Motivated by recent experimental and theoretical progress on Floquet engineering of quantum systems, this field attracts renewed interest. In this section, we first review a well-known example of the dynamical stabilization, i.e., a Kapitza pendulum, and then turn to the recent studies on the Floquet prethermalization in classical systems [115–117].

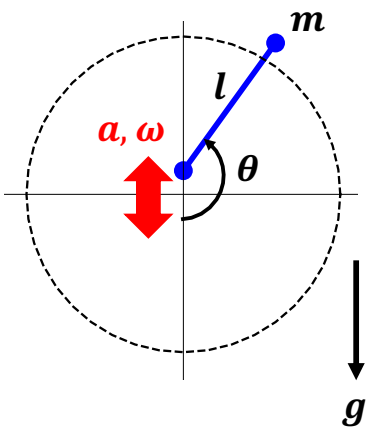

Figure 3.6: Schematic illustration of the Kapitza pendulum, where the suspension point oscillates in the vertical direction with amplitude a and frequency ω. Here, θ, l, and g are the angle measured from the downward position, the length of the pendulum, and the gravitational constant, respectively.

3.4.1 Kapitza pendulum and dynamical stabilization

The Kapitza pendulum is a prototypical example of dynamical stabilization, a counterintuitive stabilization of a system by a periodic drive. It is a classical rigid pendulum with an oscillating point of suspension (see Fig. 3.6), where θ is the angle measured from the downward position and $\omega_0 = \sqrt{g/l}$ is the frequency of the normal mode near $\theta = 0$ (g and l are the gravitational constant and the length of the pendulum, respectively). The point of suspension (x_c, y_c) oscillates vertically with amplitude a and frequency ω: $y_c = -a\cos(\omega t)$. Its equation of motion (EOM) reads [13, 27, 198]

$$\ddot{\theta} = -\omega_0^2 \sin\theta - \frac{a}{l}\omega^2 \cos(\omega t)\sin\theta. \tag{3.42}$$

While the first term on the right-hand side describes the gravitational force, the second one is the inertial force arising from the oscillation of the suspending point. In what follows, we will derive the stability of the inverted point $\theta = \pi$ based on the following two ways: (i) a heuristic derivation using a multi-scale perturbation analysis [13, 247], (ii) a modern derivation based on the vV HFE [117, 198].

Derivation of the stability based on the multi-scale perturbation analysis

In the multi-scale perturbation analysis, which is a kind of the singular perturbation theory [248, 249], the classical variable is decomposed into a slow dynamics and a rapid motion around it. For the case of the Kapitza pendulum, when the driving frequency is large ($\omega_0 \ll \omega$), the angle θ can be regarded as a sum $\theta = \theta_s + \xi$ of the slow variable θ_s and the rapid and small oscillation $\xi \ll 1$. Then, up to the first order of ξ, the equation of motion (3.42) is given by

$$\ddot{\theta}_s + \ddot{\xi} = -\omega_0^2 \sin\theta_s - \omega_0^2 \cos\theta_s \xi - \frac{a}{l}\omega^2 \cos(\omega t)\sin\theta_s - \frac{a}{l}\omega^2 \cos(\omega t)\cos\theta_s \xi. \tag{3.43}$$

Because of the smallness of the oscillation, i.e., $\ddot{\xi} \ll 1$, we have

$$\ddot{\xi} = -\omega_0^2 \cos\theta_s \xi - \frac{a}{l}\omega^2 \cos(\omega t)\sin\theta_s - \frac{a}{l}\omega^2 \cos(\omega t)\cos\theta_s \xi \approx -\frac{a}{l}\omega^2 \cos(\omega t)\sin\theta_s, \tag{3.44}$$

which gives

$$\xi = \frac{a}{l}\cos(\omega t)\sin\theta_s. \tag{3.45}$$

Substituting this into Eq. (3.43), we obtain

$$\ddot{\theta_s} = -\omega_0^2 \sin\theta_s - \frac{a}{l}\omega^2 \cos(\omega t)\sin\theta_s - \left(\frac{a}{l}\right)^2 \omega^2 \cos^2(\omega t)\cos\theta_s \sin\theta_s. \tag{3.46}$$

Since θ_s is a slow variable, $\cos^2(\omega t)$ can be replaced by its average $1/2$ over one cycle $[0, T]$; thus we obtain the equation of motion for θ_s:

$$\ddot{\theta}_s = -\omega_0^2 \sin\theta_s - \left(\frac{a\omega}{2l}\right)^2 \sin 2\theta_s. \tag{3.47}$$

This is the EOM of the Hamiltonian $H_F = p^2/2 + V_F(\theta_s)$, where p is the conjugate momentum of θ_s and $V_F(\theta_s)$ is the effective potential defined by

$$V_F(\theta_s) = -\omega_0^2 \cos\theta_s + \left(\frac{a\omega \sin\theta_s}{2l}\right)^2. \tag{3.48}$$

Thus, the highest point $\theta = \pi$ becomes stable above the critical frequency $\omega_c := \sqrt{2}l\omega_0/a$ and the pendulum exhibits an oscillation around this inverted position. This is an example of the *dynamical stabilization*. The dynamical stabilization is employed in many areas of physics [14–16, 250–252] including beam focusing in a synchrotron known as the alternating-gradient focusing [15, 16] and trapping ions in the Paul trap [14]. While the dynamical stabilization is mostly discussed in few-body systems, its many-body generalization is recently discussed [253–255] and moreover demonstrated experimentally [256].

Derivation of the stability based on the van Vleck high-frequency expansion

From the viewpoint of Floquet engineering, the stability of the inverted point can be explained from the static effective potential derived from the vV HFE [13, 27, 198]. It is clarified in Ref. [117] that, for a classical Hamilton system, the vV HFE of an effective Hamiltonian is obtained by formally replacing the commutator $(1/i)[\cdot, \cdot]$ appearing in the vV HFE in the quantum case (3.14) by the Poisson bracket $\{\cdot, \cdot\}$. The time-dependent Hamiltonian with EOM (3.42) is given by

$$H(t) = \frac{p^2}{2} - \left[\omega_0^2 + \frac{a}{l}\omega^2 \cos(\omega t)\right]\cos\theta_s, \tag{3.49}$$

for which the first few terms of the vV HFE is given as follows [198]:

$$H_F^{(0)} = \frac{p^2}{2} - \omega_0^2 \cos\theta_s, \quad H_F^{(1)} = 0, \quad H_F^{(2)} = \frac{a}{l}p^2 \cos\theta_s + \omega_0^2 \left(\frac{a \sin\theta_s \omega^2}{2l\omega_0^2} - \frac{a}{l}\right)\sin^2\theta_s. \tag{3.50}$$

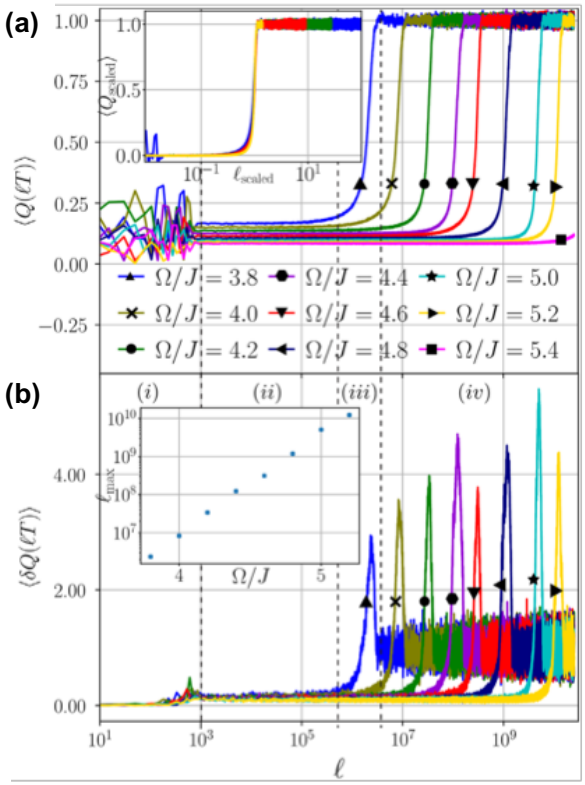

Figure 3.7: (a) Energy $\langle Q(lT)\rangle$ as a function of the number l of driving cycles, where the angle bracket $\langle\cdot\rangle$ denotes the ensemble average over the different initial states. Different colors correspond to different driving frequencies Ω. Inset: rescaled energy curves with horizontal axis $l/l_{\max}$. (b) Variance $\langle \delta Q(lT)\rangle$ of $Q(lT)$ as a function of l. Inset: the peak position $l_{\max}$ of $\langle \delta Q(lT)\rangle$ as a function of Ω. Reproduced from Fig. 1 of Ref. [116]. © 2019 by the American Physical Society.

By taking the limits $a \to 0$ and $\omega \to \infty$ while keeping the value $a\omega^2/(l\omega_0^2)$ fixed, we obtain the effective Hamiltonian

$$H_F = H_F^{(0)} + H_F^{(1)} + H_F^{(2)} = \frac{p^2}{2} + V_F(\theta_s), \tag{3.51}$$

where $V_F(\theta_s)$ is the effective potential defined in Eq. (3.48).

3.4.2 Floquet prethermalization in classical spin systems

It has recently been shown that an isolated interacting classical system under a fast drive also exhibits the Floquet prethremalization similarly to a quantum system [115–117]. In Ref. [116], the authors consider a classical Ising chain described by the time-dependent Hamiltonian

$$H(t) = \begin{cases} \sum_{j=1}^{N} JS_{j,z}S_{j+1,z} + hS_{j,z} & t \in [0, T/2] \mod T; \\ \sum_{j=1}^{N} gS_{j,x} & t \in [T/2, T] \mod T, \end{cases} \tag{3.52}$$

where J denotes the nearest-neighbour interaction strength, while h and g are the magnetic field strengths along the z and x-directions, respectively. Here, $S_j = (S_{j,x}, S_{j,y}, S_{j,z})$ is the spin variable at site j with unit magnitude: $|S_j| = 1$, and its equation of motion is given by the

Hamilton equation: $\dot{S}_{j,i} = \{S_{j,i}, H(t)\}$. The initial state is taken to be the ground state of the time-averaged Hamiltonian

$$H_{\text{ave}} = \frac{1}{2}\sum_{j=1}^{N} \left(JS_{j,z}S_{j+1,z} + hS_{j,x} + gS_{j,x}\right), \tag{3.53}$$

where a small randomness is introduced in the initial state to break its translational symmetry. The normalized energy $\langle Q(lT)\rangle$ after l periods defined by

$$\langle Q(lT)\rangle := \frac{\langle H_{\text{ave}}(S_j(lT))\rangle - E_{GS}}{\langle H_{\text{ave}}\rangle_{\beta=0} - E_{GS}} \tag{3.54}$$

is plotted in Fig. 3.7 (a), where $\langle H_{\text{ave}}\rangle_{\beta=0}$ and E_{GS} are the energies at the infinite-temperature state and that of the ground state, respectively. Here, the angle bracket $\langle\cdot\rangle$ denotes the average over the randomness in the initial state. Figure 3.7 (b) shows the variance $\langle \delta Q(lT)\rangle$ of $Q(lT)$, whose peak position $l = l_{\max}$ indicates the onset of heating.

As shown in Fig. 3.7 (a), after the initial relaxation ($l \lesssim 10^3$), a long-time plateau appears with constant $\langle Q(lT)\rangle$, and finally the system goes to the infinite-temperature state with maximum energy $Q(lT) = 1$. The onset $l_{\max}$ of heating grows exponentially with respect to ω as shown in the inset of Fig. 3.7 (b). These numerical findings indicate the presence of the Floquet prethermal regime before heating up that is exponentially long with respect to the driving frequency. It was later analytically proved that the energy absorption in a periodically driven classical spin system is exponentially slow with respect to the driving frequency and that the Floquet prethermal state is well approximated by the Gibbs ensemble with respect to the effective Hamiltonian obtained from a truncation of the FM HFE [117].

Chapter 4

Brief review on classical stochastic systems

In this chapter, we briefly review classical stochastic systems focusing on the relation between their equations of motion and master equations. We start from one of the simplest models of stochastic systems, i.e., a Brownian particle, and then consider a general stochastic system described by a stochastic differential equation. Finally, we review the stochastic Landau-Lifshitz-Gilbert equation, which is commonly used for describing a micromagnet coupled with a finite-temperature thermal bath.

4.1 Langevin equation

The Langevin equation is a well-known example of stochastic differential equations [118, 257]. Its study has fostered many fundamental developments of non-equilibrium statistical mechanics [119, 258] and profound applications in mathematics [259] and even in finance [260].

4.1.1 Langevin equation

A Brownian motion was first discovered in the study of a particle suspended in a fluid. Because of incessant collisions with the surrounding molecules in the fluid, a particle undergoes a random motion, which is modeled by the *Langevin equation*:

$$m\frac{d^2x}{dt^2} = -\gamma\frac{dx}{dt} + \eta(t), \tag{4.1}$$

where x, m and γ are the position, the mass, and the flow viscosity of the particle, respectively. For simplicity, we here consider a one-dimensional model, although generalizations to higher dimensions are straightforward. The first term on the right-hand side of Eq. (4.1) describes the frictional force and the second one is the random noise modeling collisions with the surrounding molecules. If the relaxation timescale of the surrounding molecules is short enough, it is natural to assume that $\eta(t)$ is a Gaussian white noise:

$$\begin{aligned} \langle \eta(t) \rangle &= 0, \\ \langle \eta(t)\eta(t') \rangle &= \Gamma_n \delta(t - t'), \end{aligned} \tag{4.2}$$

where Γ_n represents the strength of the noise, $\delta(t)$ is the Dirac delta function, and the angle bracket $\langle\cdot\rangle$ denotes the ensemble average over different noise realizations. The square mean velocity $\langle v^2(t)\rangle$ satisfies

$$\langle v^2(t)\rangle = \langle v^2(0)\rangle \mathrm{e}^{-\frac{\Gamma_n t}{2m\gamma}} + \frac{\Gamma_n}{2m\gamma}(1 - \mathrm{e}^{-\frac{\Gamma_n t}{2m\gamma}}). \tag{4.3}$$

In the long-time limit, $\langle v^2(t)\rangle = T_{\mathrm{te}}/m$ follows from the equipartition theorem, with T_{te} being the temperature of the surrounding molecules. Then, we obtain the *fluctuation-dissipation theorem*:

$$\Gamma_n = 2\gamma T_{\mathrm{te}}, \tag{4.4}$$

which dictates that the pair of the friction and random forces acts as a thermostat for a Langevin system so that the temperature is well defined in the Langevin equation (4.1). As we can see from Eq. (4.1), the velocity relax quickly for a sufficiently large friction $m/\gamma \to 0$. In this limit, which is knowns as the overdamped limit, Eq. (4.1) reduces to the *overdamped Langevin equation*:

$$\frac{dx}{dt} = h(t), \tag{4.5}$$

where $h := \eta/\gamma$.

4.1.2 Master equation: the Fokker-Planck equation

Because of the random nature of the equation, it is natural to consider the probability distribution $P(x,t)$ for the Langevin equation (4.1). The equation governing the time evolution of $P(x,t)$ is generally called a *master equation*. For example, the master equation for the overdamped Langevin equation (4.5) is given by the diffusion equation:

$$\partial_t P(x,t) = D\partial_x^2 P(x,t), \tag{4.6}$$

where $D := 2T_{\mathrm{te}}/\gamma$ is the diffusion constant. The derivation of Eq. (4.6) is given in Sec. 4.2.

4.2 General classical stochastic systems

4.2.1 Equation of motion

Let $\boldsymbol{\phi}(t) = [\phi_1(t), \phi_2(t), \cdots, \phi_N(t)]$ be a set of classical variables describing the system, e.g., the positions of particles for the Langevin equation. A classical system under a stochastic force is usually modeled by the stochastic differential equation [119, 261]:

$$\dot{\phi}_i(t) = f_i(\boldsymbol{\phi}) + \sum_{j=1}^{N} g_{ij}(\boldsymbol{\phi})\, h_j(t), \tag{4.7}$$

where $\dot{y} := dy/dt$ is the time derivative and h_j is a Gaussian random variables satisfying

$$\begin{aligned} \langle h_i(t) \rangle &= 0, \\ \langle h_i(t) h_j(t') \rangle &= 2D\delta_{ij}\delta(t-t'), \end{aligned} \tag{4.8}$$

with D being the diffusion constant. We note that when we consider the equation of motion for a classical field $\boldsymbol{\phi}_{\boldsymbol{r}} = [\phi_{\boldsymbol{r},1}(t), \phi_{\boldsymbol{r},2}(t), \cdots, \phi_{\boldsymbol{r},N_I}(t)]$, the subscript i in Eq. (4.7) represents a collection of the coordinate $\boldsymbol{r}$ and the internal degrees of freedom a. The equation of motion is written as follows:

$$\dot{\phi}_{\boldsymbol{r},a}(t) = f_{\boldsymbol{r},a}\left(\boldsymbol{\phi}\right) + \sum_{b=1}^{N_I} g_{\boldsymbol{r},ab}\left(\boldsymbol{\phi}\right) h_{\boldsymbol{r},b}(t). \tag{4.9}$$

Here we assume that the effect of the random field is local, i.e., the field $\boldsymbol{\phi}_{\boldsymbol{r}}$ at $\boldsymbol{r}$ is affected by the random field $\boldsymbol{h}_{\boldsymbol{r}}$ at the same position $\boldsymbol{r}$.

4.2.2 Discretization prescriptions

When $G(\boldsymbol{\phi})$ depends (does not depend) on $\boldsymbol{\phi}$, h_j is called a multiplicative (additive) noise. As in any stochastic differential equation with multiplicative noises, the discretization used to define the time evolution should be carefully taken into account to obtain reasonable physical results. For example, in the stochastic Landau-Lifshitz-Gilbert equation, the magnetization is preserved if and only if the Stratonovich prescription (see the next paragraph for the definition) is used [262].

This subtlety can be understood by looking at the integral

$$\int_{t_i}^{t_f} dt G(\boldsymbol{\phi})\boldsymbol{h}(t) = \int_{t_i}^{t_f} G(\boldsymbol{\phi}) d\boldsymbol{W}(t) = \lim_{N_d\to\infty} \sum_{n=0}^{N_d-1} G(\bar{\boldsymbol{\phi}}_n)\left[\boldsymbol{W}(t_{n+1}) - \boldsymbol{W}(t_n)\right], \tag{4.10}$$

where $\boldsymbol{W} := d\boldsymbol{h}/dt$ is the N-dimensional Wiener process and $t_i = t_0 < t_1 < t_2 \cdots < t_{N_d} = t_f$ are the times in the interval $[t_i, t_f]$. Here, $\bar{\boldsymbol{\phi}}_n$ is taken from the interval $[\boldsymbol{\phi}(t_{n-1}), \boldsymbol{\phi}(t_n)]$. Since the Wiener process is not continuous, the integral (4.10) depends on the choice of $\bar{\boldsymbol{\phi}}_n$. In the prescription called the α-prescription, one uses

$$\bar{\boldsymbol{\phi}}(t_n) := \alpha_d \boldsymbol{\phi}_n + (1-\alpha_d)\boldsymbol{\phi}_{n+1}, \quad g(\bar{\boldsymbol{\phi}}(t_n)) = g\left[\alpha_d \boldsymbol{\phi}_n + (1-\alpha_d)\boldsymbol{\phi}_{n+1}\right], \tag{4.11}$$

where $0 \le \alpha_d \le 1$ and $\boldsymbol{\phi}_i := \boldsymbol{\phi}(t_i)$.* The prescriptions with $\alpha_d = 0, 1/2$, and 1 correspond to the Itô, the Stratonovich, and the post-point prescription, respectively.

4.2.3 Master equation

Let $P(\boldsymbol{\phi}', t)$ is the probability density for finding the variable $\boldsymbol{\phi} = \boldsymbol{\phi}'$ at time t in the entire parameter space of $\boldsymbol{\phi}$. The master equation for Eq. (4.7), which is known as the *Fokker-Planck equation* (FP equation), is derived from the standard technique of the stochastic calculus

*Although the Greek letter α is commonly used to distinguish the α-prescriptions with different values of α, we do not use it to avoid possible confusion with the Gilbert damping α in the stochastic Landau-Lifshitz-Gilbert equation introduced in Sec. 4.3.

[122, 262–264]. To this end, we start from the identity:

$$P(\boldsymbol{\phi}, t+dt) = \int d\boldsymbol{\phi}_0 P(\boldsymbol{\phi}, t+dt|\boldsymbol{\phi}_0, t) P(\boldsymbol{\phi}_0, t), \tag{4.12}$$

where $P(\boldsymbol{\phi}, t+dt|\boldsymbol{\phi}_0, t)$ is the conditional probability of finding $\boldsymbol{\phi}$ at time $t+dt$, provided that $\boldsymbol{\phi} = \boldsymbol{\phi}_0$ at time t. Expanding $P(\boldsymbol{\phi}, t+dt|\boldsymbol{\phi}_0, t)$ in powers of $\Delta\boldsymbol{\phi} = \boldsymbol{\phi} - \boldsymbol{\phi}_0$, we obtain

$$P(\boldsymbol{\phi}, t+dt|\boldsymbol{\phi}_0, t) = \delta(\boldsymbol{\phi} - \boldsymbol{\phi}_0) - \frac{\partial \delta(\boldsymbol{\phi} - \boldsymbol{\phi}_0)}{\partial \phi_i} \langle \Delta\phi_i \rangle + \frac{1}{2} \frac{\partial^2 \delta(\boldsymbol{\phi} - \boldsymbol{\phi}_0)}{\partial \phi_i \partial \phi_j} \langle \Delta\phi_i \Delta\phi_j \rangle. \tag{4.13}$$

Here, we omit the summation of the repeated indices i and j. For deriving the master equation, we evaluate the right-hand side in the order of dt. From Eq. (4.7), we have

$$\Delta\phi_i = f_i(\boldsymbol{\phi}_0) dt + g_{ij} \left[\boldsymbol{\phi}_0 + \alpha_d \Delta\boldsymbol{\phi}(t+dt)\right] \int_t^{t+dt} dt' h_j(t'). \tag{4.14}$$

By using Eq. (4.8), we obtain

$$\langle \Delta\phi_i \rangle = f_i(\boldsymbol{\phi}_0) dt + 2D\alpha_d g_{kl}(\boldsymbol{\phi}_0) \frac{\partial g_{il}(\boldsymbol{\phi}_0)}{\partial \phi_k} dt, \tag{4.15}$$

$$\langle \Delta\phi_i \Delta\phi_j \rangle = 2D g_{ik}(\boldsymbol{\phi}_0) g_{jk}(\boldsymbol{\phi}_0) dt. \tag{4.16}$$

Combining Eqs. (4.12) and (4.13), we have

$$P(\boldsymbol{\phi}, t+dt) - P(\boldsymbol{\phi}, t) = -\frac{\partial}{\partial \phi_i} \left[\langle \Delta\phi_i \rangle P(\boldsymbol{\phi}, t)\right] + \frac{1}{2} \frac{\partial^2}{\partial \phi_i \phi_j} \left[\langle \Delta\phi_i \Delta\phi_j \rangle P(\boldsymbol{\phi}, t)\right], \tag{4.17}$$

from which the master equation is derived:

$$\frac{\partial P(\boldsymbol{\phi}, t)}{\partial t} = \frac{\partial}{\partial \phi_i} \left[\mathcal{F}_i(\boldsymbol{\phi}) P(\boldsymbol{\phi}, t)\right] + \frac{\partial^2}{\partial \phi_i \partial \phi_j} \left[\mathcal{D}_{ij}(\boldsymbol{\phi}) P(\boldsymbol{\phi}, t)\right]. \tag{4.18}$$

The first and second terms on the right-hand side represent the drift and diffusion of the probability, resprectively, and $\mathcal{F}_i$ and $\mathcal{D}_{ij}$ are defined are follows:

$$\mathcal{F}_i(\boldsymbol{\phi}) := -f_i(\boldsymbol{\phi}) - 2D\alpha_d g_{kl}(\boldsymbol{\phi}) \frac{\partial g_{il}(\boldsymbol{\phi})}{\partial \phi_k}, \tag{4.19}$$

$$\mathcal{D}_{ij}(\boldsymbol{\phi}) := D g_{ik}(\boldsymbol{\phi}) g_{jk}(\boldsymbol{\phi}). \tag{4.20}$$

The second term $2D\alpha_d g_{kl}(\boldsymbol{\phi}) \partial_{\phi_k} g_{il}(\boldsymbol{\phi})$ on the right-hand side of Eq. (4.19) is called the spurious drift terms. By introducing the current $J_i := -\mathcal{F}_i P - \partial(D_{ij}P)/(\partial\phi_j)$, we can rewrite Eq. (4.18) into the continuity equation for P: $\partial_t P + \partial_{\phi_i} J_i = 0$, which satisfies the conservation of the probability: $\int d\boldsymbol{\phi} P(\boldsymbol{\phi}, t) = 1$ at any time t.

For the case of the overdamped Langevin equation (4.5), we have $\phi_i = x$, $f_i = 0$, and $g_{ij} = 1$. The diffusion equation (4.6) follows from the general master equation (4.18) by substituting these relations to Eqs. (4.19) and (4.20).

4.3 Stochastic Landau-Lifshitz-Gilbert equation

The control of magnetic materials lies at the heart of the current information technologies and the development of spintronics [242, 265]. When a ferromagnet is used to store information, bits are encoded as the orientation of the local magnetization. It is practically important to understand the impact of the damping and thermal fluctuations through the interaction with an environment because they deteriorate the performance of magnetic recording devices. The Landau-Lifshitz-Gilbert (LLG) and stochastic LLG equations are commonly used for describing magnetic dynamics under these effects.

4.3.1 Equation of motion

Landau-Lifshitz-Gilbert equation

The Landau-Lifshitz-Gilbert (LLG) equation is a phenomenological equation of a ferromagnet, which is formally the torque equation with damping [120,121]. Let $\boldsymbol{m_r}$ and $\mathcal{H}(t)$ be the magnetic moment at site $\boldsymbol{r}$ on some lattice L and the Hamiltonian (energy) of the system, respectively. The LLG equation reads

$$\dot{\boldsymbol{m}}_{\boldsymbol{r}} = -\gamma \boldsymbol{m_r} \times \boldsymbol{H_r} + \frac{\alpha}{m_s} \boldsymbol{m_r} \times \dot{\boldsymbol{m}}_{\boldsymbol{r}}, \tag{4.21}$$

where $\boldsymbol{H_r} = -\delta\mathcal{H}/\delta\boldsymbol{m_r}$ is an effective magnetic field generated by the surrounding spins and external fields with $\mathcal{H}$ being the classical Hamiltonian of the system. Here, α, γ, and $m_s := |\boldsymbol{m_r}|$ are the Gilbart damping, the gyromagnetic ratio, and the magnitude of the magnetization, respectively. In what follows, we set $\gamma = 1$. We also set the magnitude $m_s = 1$ because m_s is preserved in Eq. (4.21): $d|\boldsymbol{m_r}|/dt = 0$ [262]. The first term on the right-hand side of Eq. (4.21) describes the precession around $\boldsymbol{H_r}$, while the second term, the so-called Gilbert term, describes damping toward the effective magnetic field $\boldsymbol{H_r}$. For a numerical simulation, we rewrite Eq. (4.21) as follows:

$$\dot{\boldsymbol{m}}_{\boldsymbol{r}} = -\boldsymbol{m_r} \times \boldsymbol{H_r} + \frac{\alpha}{m_s} \boldsymbol{m_r} \times \left[-\boldsymbol{m_r} \times \boldsymbol{H_r} + \frac{\alpha}{m_s} \boldsymbol{m_r} \times \dot{\boldsymbol{m}}_{\boldsymbol{r}} \right] \tag{4.22}$$

$$= -\boldsymbol{m_r} \times \left[\boldsymbol{H_r} + \frac{\alpha}{m_s} \boldsymbol{m_r} \times \boldsymbol{H_r} \right] - \alpha^2 \dot{\boldsymbol{m}}_{\boldsymbol{r}}, \tag{4.23}$$

$$\Rightarrow \quad \dot{\boldsymbol{m}}_{\boldsymbol{r}} = -\frac{\boldsymbol{m_r}}{1+\alpha^2} \times \left[\boldsymbol{H_r} + \frac{\alpha}{m_s} \boldsymbol{m_r} \times \boldsymbol{H_r} \right], \tag{4.24}$$

where we have used $\dot{\boldsymbol{m}}_{\boldsymbol{r}} \perp \boldsymbol{m_r}$ in deriving Eq. (4.23).

Stochastic Landau-Lifshitz-Gilbert equation

For a sufficiently small magnetic device, thermal fluctuations become relevant for determining the magnetization dynamics. In 1963, Brown proposed a simple generalization of the LLG equation (4.21), which is known as the stochastic LLG (sLLG) equation, in which thermal fluctuations are introduced as random magnetic fields [122]. The sLLG equation is widely used in the field of spintronics and proved to be a powerful approach to modeling ultrafast magnetization processes [46, 47] like the laser-induced demagnetization [53, 266, 267], non-thermal

magnetization control [268], and spin-current generation [269,270] in a ferromagnet. The sLLG equation reads

$$\dot{\boldsymbol{m}}_{\boldsymbol{r}} = -\gamma \boldsymbol{m}_{\boldsymbol{r}} \times [\boldsymbol{H}_{\boldsymbol{r}} + \boldsymbol{h}_{\boldsymbol{r}}(t)] + \frac{\alpha}{m_s} \boldsymbol{m}_{\boldsymbol{r}} \times \dot{\boldsymbol{m}}_{\boldsymbol{r}}, \tag{4.25}$$

where $\boldsymbol{h}_{\boldsymbol{r}}(t) := [h_{\boldsymbol{r},1}(t), h_{\boldsymbol{r},2}(t), h_{\boldsymbol{r},3}(t)]$ is the random magnetic field at $\boldsymbol{r}$ satisfying

$$\langle h_{\boldsymbol{r},a}(t) h_{\boldsymbol{r}',b}(t') \rangle = 2D\delta_{ab}\delta_{\boldsymbol{r},\boldsymbol{r}'}\delta(t-t'). \tag{4.26}$$

Here, $D = 2k_B T_{\rm te}\alpha$ is the diffusion constant which satisfies the fluctuation-dissipation theorem, where $T_{\rm te}$ is the temperature of the environment. We can rewrite Eq. (4.25) in the form of Eq. (4.9) in a manner similar to what we have done in deriving Eq. (4.24) from Eq. (4.21):

$$\dot{\boldsymbol{m}}_{\boldsymbol{r}} = -\frac{\boldsymbol{m}_{\boldsymbol{r}}}{1+\alpha^2} \times \left\{ \boldsymbol{H}_{\boldsymbol{r}} + \boldsymbol{h}_{\boldsymbol{r}}(t) + \frac{\alpha}{m_s} \boldsymbol{m}_{\boldsymbol{r}} \times [\boldsymbol{H}_{\boldsymbol{r}} + \boldsymbol{h}_{\boldsymbol{r}}(t)] \right\}. \tag{4.27}$$

4.3.2 Master equation

Comparing Eqs. (4.7) and (4.27), we obtain the drift and diffusion field:

$$\begin{aligned} \boldsymbol{f}_{\boldsymbol{r}} &= -\frac{\boldsymbol{m}}{1+\alpha^2} \times \left(\boldsymbol{H}_{\boldsymbol{r}} + \frac{\alpha}{m_s} \boldsymbol{m}_{\boldsymbol{r}} \times \boldsymbol{H}_{\boldsymbol{r}} \right) + \frac{2D}{1+\alpha^2} \boldsymbol{m}_{\boldsymbol{r}}, \\ g_{\boldsymbol{r},ab} &= \frac{1}{1+\alpha^2} \epsilon_{abc} m_{\boldsymbol{r},c} + \frac{\alpha m_s}{1+\alpha^2} \left(\delta_{ab} - \frac{m_{\boldsymbol{r},a} m_{\boldsymbol{r},b}}{(m_s)^2} \right), \end{aligned} \tag{4.28}$$

where ϵ_{abc} is the totally antisymmetric tensor of rank three. We obtain the FP equation for the sLLG equation by substituting these equations into Eqs (4.18) and (4.20). For example, in the case of a single spin, where $\boldsymbol{m}_{\boldsymbol{r}} = \boldsymbol{m}$ and $\boldsymbol{H}_{\boldsymbol{r}} = \boldsymbol{H}$, we have

$$\begin{aligned} \frac{\partial P(\boldsymbol{m},t)}{\partial t} + \mathrm{div} \Bigg\{ -\frac{\boldsymbol{m}}{1+\alpha^2} \times \left(\boldsymbol{H} + \frac{\alpha}{m_s} \boldsymbol{m} \times \boldsymbol{H} \right) P(\boldsymbol{m},t) \\ + \frac{D}{1+\alpha^2} \boldsymbol{m} \times [\boldsymbol{m} \times \mathrm{grad} P(\boldsymbol{m},t)] \Bigg\} = 0. \end{aligned} \tag{4.29}$$

Chapter 5

Floquet chiral magnetic effect

As we have reviewed in Sec. 3.2, a wide variety of band structures prohibited in static lattice systems under given symmetries can be realized as gapless quasienergy spectra in adiabatic and non-adiabatic pumps [84, 85, 89, 185, 271]. Examples include a single chiral fermion in a one-dimensional lattice without symmetries [85]. While such realizations by Floquet systems have been studied in the context of adiabatic pumps in one-dimensional lattices [18,89,178,184], little is known on their higher-dimensional analogs [128, 185, 271], in particular the realizations by non-adiabatic pumps. One notable example of such prohibited band structures in higher dimensionalities is a single Weyl fermion on a three-dimensional lattice, which is prohibited by the Nielsen-Ninomiya theorem [90, 91].

In this chapter, we demonstrate that a single Weyl fermion can be realized on a periodically driven lattice, thereby overcoming the above limitations. Our model is a three-dimensional generalization of the Thouless pump and features a single Weyl fermion in the quasienergy spectrum of its Floquet unitary operator. We study the dynamics of a spin-polarized thermal gas under our driving protocol and show that the pumped fermion charge and hence the current flow along its spin polarization as a consequence of the spin-momentum locking of Weyl fermions. Moreover, when a synthetic magnetic field is applied, the pumped charge flows opposite to the magnetic field even if an initial state is not spin polarized, offering a Floquet realization of the chiral magnetic effect (CME). In particular, at half-filling, this pumped charge can take a quantized value that is independent of the detail of the model. Our proposal can be implemented by using ultracold atomic gases, where the Thouless pump has already been experimentally realized [40, 41]. Finally, by generalizing the above idea to include symmetries, we provide a topological classification of Floquet unitary operators in the AZ symmetry classes, which is found to coincide with that of gapless surface states of static TIs and TSCs. By constructing concrete models in each symmetry class and dimensionality, we show that all gapless surface states of TIs and TSCs can emerge in bulk quasienergy spectra in Floquet systems.

5.1 Definition of the model

We consider spin-half fermions on a cubic lattice L_C with a sublattice structure in the third direction:

$$L_C := \left\{ \left(m_1, m_2, \frac{m_3}{2} \right) \middle| \, m_1, m_2, m_3 \in \mathbb{Z} \right\}, \tag{5.1}$$

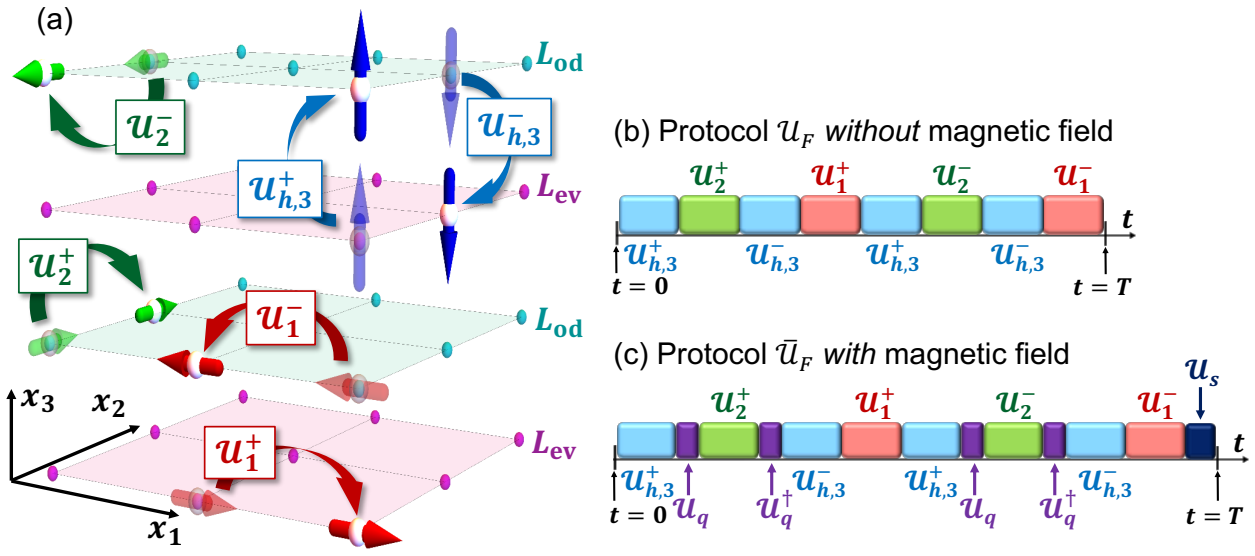

Figure 5.1: (a) Schematic illustration of the fermion pumps $\mathcal{U}_1^\pm$ (red arrows), $\mathcal{U}_2^\pm$ (green arrows), and $\mathcal{U}_{h,3}^\pm$ (blue arrows) defined in Eqs. (5.3) and (5.5), on the three-dimensional lattice L_C, where $L_{\rm ev}$ and $L_{\rm od}$ denote the sublattices of L_C. The directions of the arrows describe the spin directions of fermions. (b), (c) Driving protocols $\mathcal{U}_F$ of the pump (b) without and (c) with a magnetic field, where $\mathcal{U}_q := \exp(-i2\pi\phi x_1 x_2)$ and $\mathcal{U}_s := \exp(-i\tau_s H_s)$ are the time evolution operator induced by a sudden switch-on and -off of a quadrupole potential and that induced by laser-assisted hoppings with Hamiltonian (5.45), respectively.

where the sublattices $L_{\rm ev}$ and $L_{\rm od}$ are defined as follows:

$$L_{\rm ev} := \{(m_1, m_2, m_3) | m_1, m_2, m_3 \in \mathbb{Z}\}, \quad L_{\rm od} := \left\{ \left(m_1, m_2, m_3 + \frac{1}{2}\right) \middle| m_1, m_2, m_3 \in \mathbb{Z} \right\}. \tag{5.2}$$

The lattice constant $a_{\rm lat}$ is set to be unity: $a_{\rm lat} = 1$. Although we do not make any distinction between the sites on $L_{\rm ev}$ and those on $L_{\rm od}$, they can be distinguished by, e.g., introducing the potential difference. The main ingredient of our model is spin-selective Thouless pumps [18, 89, 178] whose time evolution (unitary) operators $\mathcal{U}_j^\pm$ $(j = 1, 2)$ are given by

$$\mathcal{U}_j^\pm := \sum_{\boldsymbol{x}} \sum_{\alpha,\beta=\uparrow,\downarrow} \left[(P_j^\pm)^{\alpha\beta} c^\dagger_{\boldsymbol{x}\pm\boldsymbol{e}_j,\alpha} c_{\boldsymbol{x},\beta} + (P_j^\mp)^{\alpha\beta} c^\dagger_{\boldsymbol{x},\alpha} c_{\boldsymbol{x},\beta} \right] = \sum_{\boldsymbol{k}} c^\dagger_{\boldsymbol{k}} V_j^\pm(k_j) c_{\boldsymbol{k}}, \tag{5.3}$$

where $\boldsymbol{x} = (x_1, x_2, x_3)$ and $\boldsymbol{k} = (k_1, k_2, k_3)$ denote the lattice site and the crystal momentum, respectively, $\boldsymbol{e}_j$ is a unit vector in the x_j direction, and $c_{\boldsymbol{x}} = (c_{\boldsymbol{x},\uparrow}, c_{\boldsymbol{x},\downarrow})$ is the annihilation operator of a fermion with spin α ($\uparrow$ or $\downarrow$) at site $\boldsymbol{x}$. The matrix $P_j^\pm := (\sigma_0 \pm \sigma_j)/2$ is a projection operator on a spin state $\sigma_j = \pm 1$, with σ_0 and σ_j $(j = 1, 2, 3)$ being the 2×2 identity matrix and the Pauli matrices, respectively. Here, the Floquet-Bloch operators $V_j^\pm(k_j)$

are the 4×4 matrices defined by

$$V_j^{\pm}(k_j) := \begin{pmatrix} P_j^{\pm} e^{\mp ik_j} + P_j^{\mp} & 0 \\ 0 & P_j^{\pm} e^{\mp ik_j} + P_j^{\mp} \end{pmatrix} = \begin{pmatrix} U_j^{\pm}(k_j) & 0 \\ 0 & U_j^{\pm}(k_j) \end{pmatrix}, \tag{5.4}$$

where $U_j^{\pm}(k_j) := P_j^{\pm} e^{\mp ik_j} + P_j^{\mp}$ and the basis set for the four bands is taken as $(|\uparrow, A\rangle, |\uparrow, B\rangle, |\downarrow, A\rangle, |\downarrow, B\rangle)$. From the projective nature of $P_j^{\pm}$, under the pump $\mathcal{U}_j^{+}$ ($\mathcal{U}_j^{-}$), fermions in a spin state $\sigma_j = +1$ (-1) are displaced by one lattice site in the positive (negative) x_j direction, while fermions in a spin state $\sigma_1 = -1$ $(+1)$ are not, thereby achieving spin-selective transport (see red and green arrows in Fig. 5.1 (a)). We also introduce spin-selective Thouless pumps $\mathcal{U}_{h,3}^{\pm}$ which displace fermions by a half lattice site in the x_3 direction (see blue arrows in Fig. 5.1 (a)):

$$\mathcal{U}_{h,3}^{\pm} := \sum_{\boldsymbol{x}} \sum_{\alpha,\beta=\uparrow,\downarrow} \left[(P_j^{\pm})^{\alpha\beta} c^{\dagger}_{\boldsymbol{x}\pm\frac{\boldsymbol{e}_3}{2},\alpha} c_{\boldsymbol{x},\beta} + (P_j^{\mp})^{\alpha\beta} c^{\dagger}_{\boldsymbol{x},\alpha} c_{\boldsymbol{x},\beta} \right] = \sum_{\boldsymbol{k}} c^{\dagger}_{\boldsymbol{k}} V_{h,3}^{\pm}(k_3) c_{\boldsymbol{k}}, \tag{5.5}$$

where their Floquet-Bloch operators $V_{h,3}^{\pm}(k_3)$ are defined as follows:

$$V_{h,3}^{+}(k_3) = \begin{pmatrix} P_{3,-} & P_{3,+} e^{-ik_3} \\ P_{3,+} & P_{3,-} \end{pmatrix}, \quad V_{h,3}^{-}(k_3) = \begin{pmatrix} P_{3,+} & P_{3,-} \\ P_{3,-} e^{ik_3} & P_{3,+} \end{pmatrix}. \tag{5.6}$$

The driving protocol of our topological pump is constituted of eight successive applications of $\mathcal{U}_1^{\pm}$,$\mathcal{U}_2^{\pm}$, and $\mathcal{U}_{h,3}^{\pm}$ as shown in Fig. 5.1 (b), where the total time-evolution operator $\mathcal{U}_F^{\mathrm{wh}}$ for the whole four bands over one cycle is given by

$$\mathcal{U}_F^{\mathrm{wh}} := \mathcal{U}_1^{-}\mathcal{U}_{h,3}^{-}\mathcal{U}_2^{-}\mathcal{U}_{h,3}^{+}\mathcal{U}_1^{+}\mathcal{U}_{h,3}^{-}\mathcal{U}_2^{+}\mathcal{U}_{h,3}^{+} = \sum_{\boldsymbol{k}} c^{\dagger}_{\boldsymbol{k}} V^{\mathrm{wh}}(\boldsymbol{k}) c_{\boldsymbol{k}}, \tag{5.7}$$

$$V^{\mathrm{wh}}(\boldsymbol{k}) = V_1^{-}(k_1) V_{h,3}^{-}(k_3) V_2^{-}(k_2) V_{h,3}^{+}(k_3) V_1^{+}(k_1) V_{h,3}^{-}(k_3) V_2^{+}(k_2) V_{h,3}^{+}(k_3). \tag{5.8}$$

Then, the Floquet-Bloch operator $V^{\mathrm{wh}}(\boldsymbol{k})$ is decomposed into the two 2×2 matrices:

$$V^{\mathrm{wh}}(\boldsymbol{k}) = U^{L}(\boldsymbol{k}) \oplus U^{H}(\boldsymbol{k}), \tag{5.9}$$

$$U^{L}(\boldsymbol{k}) := U_1^{-}(k_1) U_{h,3}^{-}(k_3) U_2^{-}(k_2) U_{h,3}^{+}(k_3) U_1^{+}(k_1) U_{h,3}^{-}(k_3) U_2^{+}(k_2) U_{h,3}^{+}(k_3), \tag{5.10}$$

$$U^{H}(\boldsymbol{k}) := U^{L}(k_1, k_2, k_3 - 2\pi), \tag{5.11}$$

where $U_{h,3}(k) := U_3(k/2)$ represents the half-site translation along the x_3 direction. We refer to the bands which $U^{L}(\boldsymbol{k})$ ($U^{H}(\boldsymbol{k})$) acts on as the "lower" ("higher") Floquet bands. Equation (5.11) can be understood from the sublattice structure along the x_3 direction as follows. Our model can continuously be deformed to a model without the sublattice difference, where the Brillouin zone is extended from $\{(k_1, k_2, k_3) | -\pi \le k_j \le \pi\}$ to $\{(k_1, k_2, k_3) | -\pi \le k_1, k_2, k_3/2 \le \pi\}$. Equation (5.9) indicates that the "lower" Floquet bands correspond to the small-k_3 region $-\pi \le k_3 \le \pi$, while the "higher" ones correspond to the folded region $\pi < |k_3| \le 2\pi$.

We hereafter focus only on the "lower" Floquet bands and the unitary operator $U(\boldsymbol{k}) := U^{L}(\boldsymbol{k})$. As we will see below, the Floquet-Bloch operator $U(\boldsymbol{k})$ is a topologically nontrivial map and features a single Weyl fermion within its quasienergy spectrum. It is worth mentioning that such a nontrivial map is obtained from the *smash product*, which is a mathematical method of constructing topologically nontrivial maps from a manifold like a torus [272]. See App. A.1 for

the detail on the construction. A straightforward calculation shows that $U(\boldsymbol{k})$ stays a constant value $-\sigma_0$ if $\boldsymbol{k}$ belongs to the boundary of the Brillouin zone $\mathbb{T}^3 := [-\pi, \pi]^3$ and hence satisfies the periodic boundary condition on $\mathbb{T}^3$ (see App. A.2 for the derivation).

5.1.1 Topological number of the Floquet-Bloch operator

The Floquet-Bloch operator $U(\boldsymbol{k})$ in Eq. (5.10) formally defines a map from $\mathbb{T}^3$, the Brillouin zone, to $\mathrm{U}(n)$, which is a space of unitary operators with size n. Its topological characterization is given by the three-dimensional winding number W on $\mathrm{U}(n)$:

$$W := -\int \frac{d\boldsymbol{k}}{24\pi^2} \sum_{i,j,k=1}^{3} \epsilon^{ijk} \mathrm{Tr}\left[R_i R_j R_k\right], \tag{5.12}$$

where $R_i := U^\dagger(\boldsymbol{k})\partial_{k_i} U(\boldsymbol{k})$ [273]. To examine the nontrivial topology of $U(\boldsymbol{k})$, we parametrize the element U in $\mathrm{SU}(2)$ in terms of $\boldsymbol{u} = (u_1, u_2, u_3, u_4) \in S^3$ as follows:

$$U = u_4\sigma_0 + i\left(u_1\sigma_1 + u_2\sigma_2 + u_3\sigma_3\right), \quad \sum_{k=0}^{3}(u_k)^2 = 1. \tag{5.13}$$

If we parametrize $U(\boldsymbol{k})$ as

$$U(\boldsymbol{k}) = u_4(\boldsymbol{k})\sigma_0 + i\left(u_1(\boldsymbol{k})\sigma_1 + u_2(\boldsymbol{k})\sigma_2 + u_3(\boldsymbol{k})\sigma_3\right), \tag{5.14}$$

$\boldsymbol{u}(\boldsymbol{k}) = (u_1(\boldsymbol{k}), u_2(\boldsymbol{k}), u_3(\boldsymbol{k}), u_4(\boldsymbol{k}))$ defines a map from $\mathbb{T}^3$ to S^3, where the explicit form of $\boldsymbol{u}(\boldsymbol{k})$ is given by

$$\begin{cases} u_1(\boldsymbol{k}) = -\sin(k_1)\cos^2\left(\frac{k_2}{2}\right)\cos^2\left(\frac{k_3}{2}\right); \\ u_2(\boldsymbol{k}) = -\cos^2\left(\frac{k_1}{2}\right)\sin(k_2)\cos\left(\frac{k_3}{2}\right) + \frac{1}{2}\sin(k_1)\cos^2\left(\frac{k_2}{2}\right)\sin(k_3); \\ u_3(\boldsymbol{k}) = -\frac{1}{2}\sin(k_1)\sin(k_2)\cos\left(\frac{k_3}{2}\right) - \cos^2\left(\frac{k_1}{2}\right)\cos^2\left(\frac{k_2}{2}\right)\sin(k_3); \\ u_4(\boldsymbol{k}) = 2\cos^2\left(\frac{k_1}{2}\right)\cos^2\left(\frac{k_2}{2}\right)\cos^2\left(\frac{k_3}{2}\right) - 1. \end{cases} \tag{5.15}$$

From Eqs. (5.12) and (5.14), W is expressed as the three-dimensional winding number on S^3 [273]:

$$W = \int \frac{d\boldsymbol{k}}{2\pi^2} \sum_{i,j,k,l=1}^{4} \epsilon_{ijkl} u_i(\boldsymbol{k}) \frac{\partial u_j(\boldsymbol{k})}{\partial k_1} \frac{\partial u_k(\boldsymbol{k})}{\partial k_2} \frac{\partial u_l(\boldsymbol{k})}{\partial k_3}. \tag{5.16}$$

Substituting Eq. (5.15) into Eq. (5.16), we obtain the unit winding number:

$$W = 1. \tag{5.17}$$

It is worth mentioning that the winding number (5.12) is a three-dimensional generalization of the one-dimensional winding number (3.31), which is used for a topological characterization of the Thouless pump [85]. In this sense, our model can be regarded as a three-dimensional analog of the Thouless pump. While the existence of topologically nontrivial pumps characterized the three-dimensional winding number (5.12) has already been discussed in a previous study [85],

its physical consequence and concrete model had remained elusive.

Although $U(\boldsymbol{k})$ has the nontrivial winding number W, the other Floquet-Bloch operator $U^H(\boldsymbol{k})$ acting on the "higher" Floquet bands has the opposite winding number $W = -1$, and hence the total winding number vanishes: $W = 0$. This is the same as what we have in the Thouless pump in the Rice-Mele model (see Sec. 2.3). We have two Floquet-Bloch bands corresponding to the particle and hole bands of an initial Hamiltonian, which we label as $\gamma = 1$ and 2, respectively. Their one-dimensional winding numbers ν_γ are written in terms of their quasienergies $\epsilon_\gamma(k)$ as follows:

$$\nu_\gamma = \int_{-\pi}^{\pi} \frac{dk}{2\pi} \frac{\partial \epsilon_\gamma(k)}{\partial k}. \tag{5.18}$$

When the Floquet-Bloch band $\gamma = 1$ has a nontrivial winding number $\nu_{\gamma=1}$, a chiral current flows under the pump when we start from the ground state of the initial Hamiltonian. On the other hand, the winding number of the other Floquet-Bloch band should have the opposite winding number $\nu_{\gamma=2} = -\nu_{\gamma=1}$. Thus, the current with the same strength flows in the opposite direction under the pump if only the hole band is initially occupied. Therefore, the total winding number vanishes: $\nu_{\gamma=2} + \nu_{\gamma=1} = 0$. Similar things happen in static and anomalous TIs and TSCs: edge states with the opposite topological numbers should appear in pairs on the surfaces facing with each other [83,84,225]. One cannot isolate one of them with finite numbers of bands.

5.2 Dispersion and dynamics without a magnetic field

5.2.1 Single Weyl fermion in the quasienergy spectrum

Let $h_{\text{eff}}(\boldsymbol{k})$ be the effective Bloch Hamiltonian of $U(\boldsymbol{k})$ defined by

$$U(\boldsymbol{k}) =: \exp\left[-ih_{\text{eff}}(\boldsymbol{k})T\right], \tag{5.19}$$

with T being the period of the drive. In what follows, we set it to be unity: $T = 1$. Since $U(\boldsymbol{k})$ is an element of SU(2), its eigenvalues $\exp\left[\pm i\epsilon(\boldsymbol{k})T\right]$ satisfy

$$\cos\left[\epsilon(\boldsymbol{k})T\right] = \frac{\mathrm{Tr}\left[U(\boldsymbol{k})\right]}{2} = u_4(\boldsymbol{k}). \tag{5.20}$$

Therefore, the quasienergy $\epsilon(\boldsymbol{k})$ is obtained from Eq. (5.15) as

$$\epsilon(\boldsymbol{k}) = \frac{1}{T}\cos^{-1}\left[2\cos^2\left(\frac{k_1}{2}\right)\cos^2\left(\frac{k_2}{2}\right)\cos^2\left(\frac{k_3}{2}\right) - 1\right]. \tag{5.21}$$

The quasienergy spectra along the loop connecting $\Gamma = (0,0,0)$, $\mathrm{M} = (0,\pi,\pi)$, and $\mathrm{K} = (\pi,\pi,\pi)$ are shown in Fig. 5.2 (a). One can see that $h_{\text{eff}}(\boldsymbol{k})$ vanishes only at the Γ point, around which the dispersion relation is linear. Since $U(\boldsymbol{k})$ can be expanded around the Γ point as

$$U(\boldsymbol{k}) \approx \sigma_0 - i\boldsymbol{k}\cdot\boldsymbol{\sigma}, \tag{5.22}$$

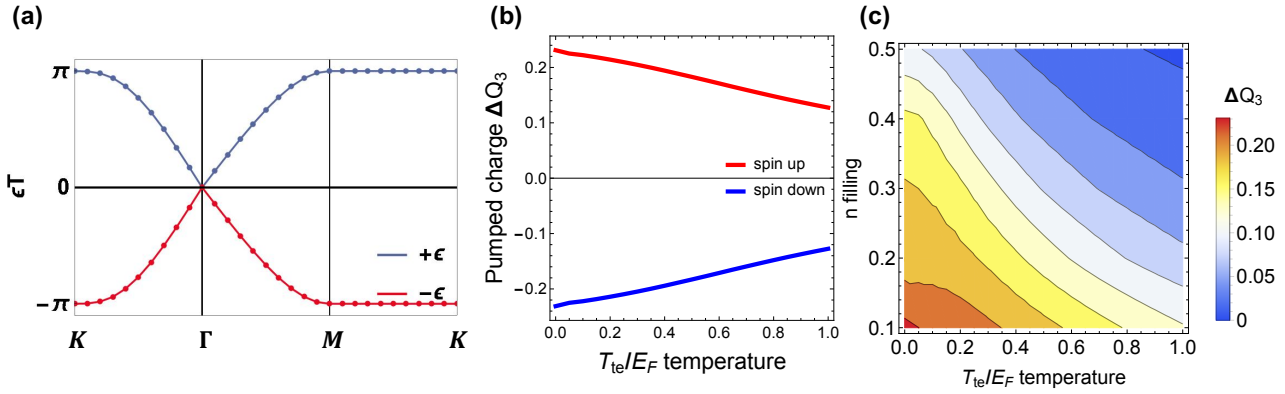

Figure 5.2: (a) Quasienergy spectra $\epsilon(\boldsymbol{k})$ (blue) and $-\epsilon(\boldsymbol{k})$ (red) of the Floquet-Bloch operator $U(\boldsymbol{k})$ in Eq. (5.10) along the loop connecting the points $\mathrm{K} = (\pi, \pi, \pi)$, $\mathrm{M} = (0, \pi, \pi)$, and $\Gamma = (0, 0, 0)$ within the Brillouin zone $\mathbb{T}^3 = \{(k_1, k_2, k_3) | -\pi \leq k_j \leq \pi\}$ of the cubic lattice L_C. The quasienergy spectra extend over $-\pi \leq \epsilon(\boldsymbol{k}) \leq \pi$. (b) Pumped fermion charge ΔQ_3 as a function of temperature T_{te} for the spin-polarized thermal state (5.25) with the band filling $n = 0.1$, where E_F is the Fermi energy. In the red (blue) curve, the initial state is fully polarized with spin-up (spin-down) fermions. (c) Pumped fermion charge ΔQ_3 as a function of temperature T_{te} and the band-filling n. The initial state is the thermal state (5.25) polarized with spin-up. The pumped charge ΔQ_3 becomes large at low temperature and low band-filling.

from Eq. (5.10) together with the relation $U_j^{\pm}(k) \approx \sigma_0 \mp i P_j^{\pm} k$ for $k \approx 0$, the effective Hamiltonian can be written as

$$h_{\mathrm{eff}}(\boldsymbol{k}) \approx \frac{\boldsymbol{k} \cdot \boldsymbol{\sigma}}{T}, \tag{5.23}$$

which clearly indicates the presence of a single left-handed Weyl fermion at $\boldsymbol{k} = 0$.

A few remarks are in order. First, the quasienergies are constant between the M and K points, since we have $U(\boldsymbol{k}) = -\sigma_0$ on the boundary of $\mathbb{T}^3$. Secondly, our model should be distinguished in topology from the previous proposals for realizing Floquet-Weyl semimetals [64, 274–282], where the Weyl points always appear in pairs *within a single band* in accordance with the Nielsen-Ninomiya theorem. Finally, the presence and stability of the single Weyl fermion is ensured from the nontrivial three-dimensional winding number (5.12) and hence not restricted to our model. In fact, the stability of the single Weyl fermion is shown in another model using an adiabatic pump [283].

5.2.2 Topological pump with spin-momentum locking

We now show that the dynamics under the driving protocol $\mathcal{U}_F$ reflects the spin-momentum locking of Weyl fermions. The time evolution of the system is governed by the discrete-time von-Neumann equation:

$$\rho_{t+T} = \mathcal{U}_F \rho_t \mathcal{U}_F^{\dagger}, \tag{5.24}$$

where ρ_t is a many-body density matrix at time t. It is worth mentioning that we do not have the notion of the "ground state" in a Floquet system because of the periodicity of quasienergies,

and therefore there is no *a priori* guiding principle for choosing an initial state unlike in an adiabatic pump. As an initial state ρ_0, we here take a thermal state of fermions on the lattice L_C:

$$\rho_0 = \sum_{\boldsymbol{q},\alpha} f_{\mathrm{FD},\alpha}(\boldsymbol{q}) \left|\boldsymbol{q},\alpha\right\rangle_0 \left\langle \boldsymbol{q},\alpha\right|_0, \tag{5.25}$$

which can easily be implemented in ultracold atomic gases. Here, $\left|\boldsymbol{q},\alpha\right\rangle_0$ is the eigenstate with momentum $\boldsymbol{q}$ ($\in [-\pi,\pi]^2 \times [-2\pi, 2\pi]$) and spin $\alpha = \uparrow, \downarrow$:

$$\left|\boldsymbol{q},\alpha\right\rangle_0 = \sum_{\boldsymbol{x}} \mathrm{e}^{-i\boldsymbol{k}\cdot\boldsymbol{x}} \left|\boldsymbol{x}\right\rangle \otimes \left|\alpha\right\rangle, \tag{5.26}$$

where $|\boldsymbol{x}\rangle \otimes |\alpha\rangle$ represents the localized state at site $\boldsymbol{x}$ with spin α. The population of eigenstates is determined from the Fermi distribution function $f_{\mathrm{FD},\alpha}(\boldsymbol{q})$:

$$f_{\mathrm{FD},\alpha}(\boldsymbol{q}) = \left[1 + \exp\left(\frac{\epsilon_0(\boldsymbol{q}) - E_F}{T_{\mathrm{te}}}\right)\right]^{-1}, \tag{5.27}$$

where T_{te} and E_F are the temperature and the Fermi energy, respectively, and

$$\epsilon_0(\boldsymbol{q}) := 2t_1(1-\cos q_1) + 2t_2(1-\cos q_2) + 2t_3\left[1 - \cos\left(\frac{q_2}{2}\right)\right] \tag{5.28}$$

is the dispersion relation of the tight-binding model on L_C with momentum $\boldsymbol{q}$, with t_i being the hopping amplitude in the x_i direction. We write the filling in the initial state as n:

$$n = \frac{\sum_{\boldsymbol{q},\alpha} f_{\mathrm{FD},\alpha}(\boldsymbol{q})}{\sum_{\boldsymbol{q},\alpha} 1}, \tag{5.29}$$

To analyze the dynamics under the pump, we calculate the pumped fermion charge $\boldsymbol{\Delta Q} := (\Delta Q_1, \Delta Q_2, \Delta Q_3)$, which is defined as the integral of the current $J_i(t)$ over one period:

$$\Delta Q_i := \int_0^T dt\ J_i(t), \tag{5.30}$$

$$J_i(t) := \sum_{k_i} \mathrm{Tr}\left[\rho_t \frac{\partial H(\boldsymbol{k},t)}{\partial k_i}\right], \tag{5.31}$$

where ρ_t and $H(\boldsymbol{k},t)$ are the density matrix and the instantaneous Hamiltonian, respectively, at time t. Then, $\boldsymbol{\Delta Q}$ is shown to be written as the average of the velocity $\nabla_{\boldsymbol{k}}\epsilon_\gamma$ with respect to the non-equilibrium distribution function $f_\gamma(\boldsymbol{k}) := \langle \boldsymbol{k},\gamma|\,\rho_0\,|\boldsymbol{k},\gamma\rangle$ (see App. A.3 for the derivation):

$$\boldsymbol{\Delta Q} := \frac{1}{N}\sum_{\boldsymbol{k},\gamma} f_\gamma(\boldsymbol{k}) \nabla_{\boldsymbol{k}}\epsilon_\gamma, \tag{5.32}$$

where γ is the label to distinguish the Floquet bands and $N = \sum_{\boldsymbol{k},\gamma} f_\gamma(\boldsymbol{k})$ is the particle number. Note that the non-equilibrium distribution function $f_\gamma(\boldsymbol{k})$ is determined from $f_{\mathrm{FD},\alpha}(\boldsymbol{k})$ and the

overlap between $|\boldsymbol{q},\alpha\rangle_0$ and $|\boldsymbol{k},\gamma\rangle$ as follows:

$$f_\gamma(\boldsymbol{k}) = \sum_{\boldsymbol{q},\alpha} f_{\mathrm{FD},\alpha}(\boldsymbol{q}) |\langle \boldsymbol{k},\gamma|\boldsymbol{q},\alpha\rangle_0|^2 = \sum_{\alpha} f_{\mathrm{FD},\alpha}(\boldsymbol{k}) |\langle u_\gamma(\boldsymbol{k})|\alpha\rangle|^2, \tag{5.33}$$

where $u_\gamma(\boldsymbol{k})$ is the Floquet-Bloch state with momentum $\boldsymbol{k}$ and band γ. One can see from Eq. (5.33) that one can effectively restrict oneself to the "lower" Floquet bands $|k_3| \le \pi$ when the band filling n satisfies $n \le 0.5$ and the Fermi gas is degenerate around $\boldsymbol{k} = 0$. To maximize the population $f_\gamma(\boldsymbol{k})$ in the "lower" Floquet bands, we assume $t_1, t_2 < t_3$ and henceforth set $t_1 = t_2 = t_0$ and $t_3 = 2t_0$.

To analyze the effect of the Weyl point $\boldsymbol{k} = 0$, we first consider the low-temperature and small band-filling case, where one can analytically calculate $\boldsymbol{\Delta Q}$. In this case, the initial state has a localized population near the Weyl point. The quasienergies ϵ_γ and the corresponding Floquet-Bloch states $|u_\gamma(\boldsymbol{k})\rangle$ are approximated near $\boldsymbol{k} = 0$ as

$$\begin{cases} \epsilon_{\gamma=1}(\boldsymbol{k}) = |\boldsymbol{k}|, & |u_{\gamma=1}(\boldsymbol{k})\rangle = \begin{pmatrix} \cos(\theta_k/2)\, \mathrm{e}^{-i\phi_k} \\ \sin(\theta_k/2) \end{pmatrix}; \\ \epsilon_{\gamma=2}(\boldsymbol{k}) = -|\boldsymbol{k}|, & |u_{\gamma=2}(\boldsymbol{k})\rangle = \begin{pmatrix} \sin(\theta_k/2)\, \mathrm{e}^{-i\phi_k} \\ -\cos(\theta_k/2) \end{pmatrix}, \end{cases} \tag{5.34}$$

where θ_k and ϕ_k are the polar and azimuth angles of the unit vector $\boldsymbol{k}/|\boldsymbol{k}|$:

$$\frac{\boldsymbol{k}}{|\boldsymbol{k}|} = (\sin\theta_k \cos\phi_k, \sin\theta_k \sin\phi_k, \cos\theta_k). \tag{5.35}$$

Then, we have

$$\sum_\gamma |u_\gamma(\boldsymbol{k})\rangle \nabla_{\boldsymbol{k}} \epsilon_\gamma \langle u_\gamma(\boldsymbol{k})| \approx \widehat{\boldsymbol{k}}(\widehat{\boldsymbol{k}}\cdot\boldsymbol{\sigma}), \tag{5.36}$$

where the pumped charge $\boldsymbol{\Delta Q}$ is calculated to be

$$\boldsymbol{\Delta Q} \approx \frac{1}{N}\sum_{\boldsymbol{k},\alpha} f_{\mathrm{FD},\alpha}(\boldsymbol{k}) \langle\alpha|\widehat{\boldsymbol{k}}(\widehat{\boldsymbol{k}}\cdot\boldsymbol{\sigma})|\alpha\rangle = \frac{\sum_{\boldsymbol{k}:\mathrm{FS}} \widehat{\boldsymbol{k}}(\widehat{\boldsymbol{k}}\cdot\boldsymbol{S}_{\boldsymbol{k}})}{\sum_{\boldsymbol{k}:\mathrm{FS}} 1}. \tag{5.37}$$

Here, $\sum_{\boldsymbol{k}:\mathrm{FS}}$ denotes the sum over the Fermi sphere and $\boldsymbol{S}_{\boldsymbol{k}} := \sum_\alpha f_{\mathrm{FD},\alpha}(\boldsymbol{k}) \langle\alpha|\boldsymbol{\sigma}|\alpha\rangle$ is the spin polarization at momentum $\boldsymbol{k}$. Thus, $\boldsymbol{\Delta Q}$ is the average of $\widehat{\boldsymbol{k}}(\widehat{\boldsymbol{k}}\cdot\boldsymbol{S}_{\boldsymbol{k}})$ over the Fermi sphere. For a spin-polarized initial state with spin state $|\alpha\rangle$, $\boldsymbol{S}_{\boldsymbol{k}}$ is parallel to $\langle\alpha|\boldsymbol{\sigma}|\alpha\rangle$. Therefore, $(\widehat{\boldsymbol{k}}\cdot\boldsymbol{S}_{\boldsymbol{k}})$ is maximized when $\widehat{\boldsymbol{k}} \parallel \langle\alpha|\boldsymbol{\sigma}|\alpha\rangle$, which gives $\boldsymbol{\Delta Q} \parallel \langle\alpha|\boldsymbol{\sigma}|\alpha\rangle$. Thus, the pumped charge and hence the current flow parallel to the spin polarization, which is a manifestation of the spin-momentum locking of a Weyl fermion.

To support the above analytical argument, we numerically calculate $\boldsymbol{\Delta Q}$ according to Eq. (5.32) for various temperature T_{te} and the band filling n. We assume that the spin is initially polarized in the S_3 direction and calculate the pumped fermion charge ΔQ_3 along the x_3 direction. In all the choices of the parameters, we confirm that the pumped charges ΔQ_1 and ΔQ_2 in the other directions vanish. In Fig. 5.2 (b), we plot ΔQ_3 as a function of temperature T_{te} for the small band filling $n = 0.1$. In the red (blue) curve, the initial state is fully polarized

with spin-up (spin-down). Depending on the direction of the spin polarization, the current with the same magnitude flows in the opposite, which is consistent with the above analytical argument. The pumped charge ΔQ_3 saturates in the low-temperature limit and survives even at high temperatures $T_{\rm te} \lesssim E_F$. In Fig. 5.2 (c), we present the temperature and the band-filling dependence of ΔQ_3 for an initial state polarized with spin-up. In a wide parameter region, ΔQ_3 takes a positive value, which results from the effect of the spin-momentum locking of the Weyl fermion.

5.3 Floquet chiral magnetic effect

5.3.1 Dispersion: chiral fermion under a magnetic field

When a magnetic field is applied, a Weyl fermion features chiral transport along the applied magnetic field, which is a phenomenon known as the CME [92, 93]. A magnetic field can be introduced in our model through the replacement of $\mathcal{U}_2^{\pm}$ in Eq. (5.10) with $\mathcal{U}_q^{\dagger}\mathcal{U}_2^{\pm}\mathcal{U}_q$ (see Fig. 5.1 (c)), where $\mathcal{U}_q := \exp(-i2\pi\phi x_1 x_2)$ is the time-evolution operator induced by a sudden switch-on and -off of a quadrupole potential [191, 284]. Since we have

$$\mathcal{U}_q^{\dagger}V_2^{\pm}(k_2)\mathcal{U}_q = V_2^{\pm}(k_2 - 2\pi\phi x_1), \quad \mathcal{U}_q^{\dagger}U_2^{\pm}(k_2)\mathcal{U}_q = U_2^{\pm}(k_2 - 2\pi\phi x_1), \tag{5.38}$$

the effective Hamiltonian near $\boldsymbol{k} = 0$ is given by

$$h_{\rm eff} = (\boldsymbol{k} + \boldsymbol{A}) \cdot \boldsymbol{\sigma}, \tag{5.39}$$

with $\boldsymbol{A} = (0, -2\pi\phi x_1, 0)$ being the vector potential of a uniform magnetic field $\boldsymbol{B} = (0, 0, -2\pi\phi)$ in the Landau gauge. Equation (5.39) describes a Weyl fermion under the magnetic field of strength $B_s = 2\pi\phi$ along the $(-z)$ direction.

To determine the quasienergy spectra, we first derive a Floquet analog of the Aubry-Andrei-Harper model as we derive the Harper Hamiltonian from the two-dimensional Hamiltonian of electrons under a magnetic field [285,286]. Let L_1 be the number of sites along the x_1 direction. The partial Fourier transform of $\mathcal{U}_q^{\dagger}\mathcal{U}_2^{\pm}\mathcal{U}_q$ and $\mathcal{U}_1^{\pm}$ in the x_2- and x_3-axes are given by

$$\mathcal{U}_q^{\dagger}\mathcal{U}_2^{\pm}\mathcal{U}_q = \sum_{k_2,k_3}\sum_{x_1=1}^{L_1} \bar{c}_{x_1}^{\dagger}U_2^{\pm}(k_2 - 2\pi\phi x_1)\bar{c}_{x_1}, \quad \mathcal{U}_1^{\pm} = \sum_{k_2,k_3}\sum_{x_1=1}^{L_1}\left(\bar{c}_{x_1\pm1}^{\dagger}P_1^{\pm}\bar{c}_{x_1} + \bar{c}_{x_1}^{\dagger}P_1^{\mp}\bar{c}_{x_1}\right), \tag{5.40}$$

where $\bar{c}_{x_1} := c_{x_1,k_2,k_3}$ is the annihilation operator of the fermion at site x_1 with fixed momenta k_2 and k_3. Then, defining $U^{\pm}(x_1)$ as $\bar{U}^{\pm}(x_1) := U_{h,3}^{-}(k_3)U_2^{\pm}(k_2 - 2\pi\phi x_1)U_{h,3}^{+}(k_3)$, we obtain

$$\mathcal{U}_{h,3}^{-}\mathcal{U}_q^{\dagger}\mathcal{U}_2^{\pm}\mathcal{U}_q\mathcal{U}_{h,3}^{+} = \sum_{k_2,k_3}\sum_{x_1=1}^{L_1}\bar{c}_{x_1}^{\dagger}\bar{U}^{\pm}(x_1)\bar{c}_{x_1}, \tag{5.41}$$

$$\mathcal{U}_F = \mathcal{U}_1^{-}\mathcal{U}_{h,3}^{-}\mathcal{U}_q^{\dagger}\mathcal{U}_2^{-}\mathcal{U}_q\mathcal{U}_{h,3}^{+}\mathcal{U}_1^{+}\mathcal{U}_{h,3}^{-}\mathcal{U}_q^{\dagger}\mathcal{U}_2^{+}\mathcal{U}_q\mathcal{U}_{h,3}^{+} =: \sum_{k_2,k_3}U'(k_2,k_3), \tag{5.42}$$

where the overall Floquet-Bloch operator $U'(k_2, k_3)$ is defined in Eq. (5.42) and given by

$$U'(k_2,k_3) = \sum_{x_1=1}^{L_1} \left(\bar{c}^\dagger_{x_1+1} \bar{u}_1 \bar{c}_{x_1} + \bar{c}^\dagger_{x_1} \bar{u}_0 \bar{c}_{x_1} + \bar{c}^\dagger_{x_1-1} \bar{u}_{-1} \bar{c}_{x_1} \right), \tag{5.43}$$

$$\begin{cases} \bar{u}_1 = P_1^+ \bar{U}^-(x_1+1) P_1^+ \bar{U}^+(x_1); \\ \bar{u}_0 = P_1^- \bar{U}^-(x_1+1) P_1^+ \bar{U}^+(x_1) + P_1^+ \bar{U}^-(x_1) P_1^- \bar{U}^+(x_1); \\ \bar{u}_{-1} = P_1^- \bar{U}^-(x_1) P_1^- \bar{U}^+(x_1). \end{cases} \tag{5.44}$$

However, the unitary operator $U'(k_2, k_3)$ with nonzero ϕ does not satisfy the periodic boundary condition along the k_3 direction, i.e, $U'(k_2, \pi) \neq U'(k_2, -\pi)$, because the "lower" and "higher" Floquet bands are coupled through the quadrupole fields. To completely decouple them even in the presence of the quadrupole fields, we introduce the additional time evolution $\mathcal{U}_s$ with duration τ_s under a static Hamiltonian H_s defined by

$$H_s = J_s \sum_{\boldsymbol{x}} (i c_{\boldsymbol{x}+\frac{\boldsymbol{e}_3}{2}} c_{\boldsymbol{x}} + \text{h.c.}), \tag{5.45}$$

which can be implemented by laser-assisted hopping [192]. By tuning $2J_s\tau_s = \pi\phi/2$, we obtain the whole time-evolution operator $\bar{U}(k_2, k_3)$ for the "lower" Floquet bands:

$$\bar{U}(k_2,k_3) = U_s(k_3) U'(k_2,k_3), \tag{5.46}$$

where $U_s(k_3) := \exp\left[-i(\pi\phi/2)\sin(k_3/2)\right]$ is the Floquet-Bloch operator acting on the "lower" Floquet bands. Through a straightforward calculation, we can show that $\bar{U}(k_2, k_3)$ satisfies the periodic boundary condition: $\bar{U}(k_2, \pi) = \bar{U}(k_2, -\pi)$. The unitary operator $\bar{U}(k_2, k_3)$ gives a Floquet analog of the Aubry-Andrei-Harper model [285, 286] with two parameters k_2 and k_3. When the periodic boundary condition is imposed in the x_1 direction, a change in the momentum $k_2 \to k_2 + \Delta k$ is compensated for by a shift of the position $x_1 \to x_1 + \Delta k/(2\pi\phi)$ along the x_1 direction, and therefore the spectrum of $\bar{U}(k_2, k_3)$ is independent of k_2.

Figures 5.3 (a) and (b) show the quasienergy spectra of $\bar{U}(0, k_3)$ for $\phi = 0$ and $\phi = 1/20$, respectively, where the color of the points represents the spin polarization $S_3 := \langle u_a(k_3)|\sigma_3|u_a(k_3)\rangle$ of eigenstate $|u_a(k_3)\rangle$. The flux ϕ opens the Landau gap with size $2\omega_L := 2\sqrt{2B_s} \approx 1.6$ near the Weyl point $k_3 = 0$, and a spin-polarized chiral fermion emerges inside the gap. The energy spectrum of the Weyl Hamiltonian (5.39) under the magnetic field is given by

$$\epsilon_n(k_3) = \begin{cases} \sqrt{k_3^2 + n\omega_L^2} & n > 0; \\ k_3 & n = 0; \\ -\sqrt{k_3^2 + |n|\omega_L^2} & n < 0. \end{cases} \tag{5.47}$$

Figure 5.3 (c) shows an enlarged spectrum near the Weyl point at $k_3 = 0$ for $\phi = 1/20$, where we can see good agreement between the numerical result (points) and the analytical one (5.47) (black dashed curves).

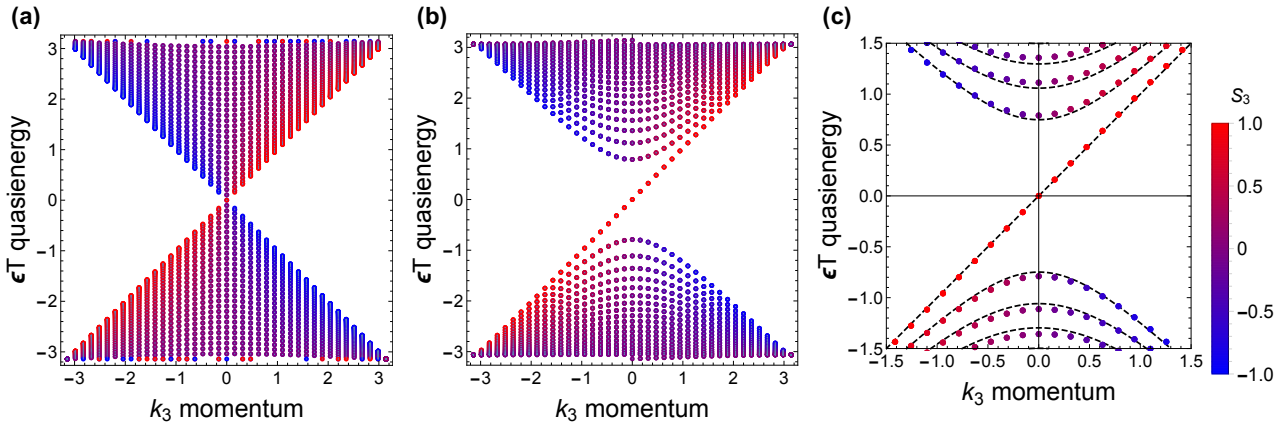

Figure 5.3: (a), (b) Quasienergy spectra of $\bar{U}(0, k_3)$ with flux (a) $\phi = 0$ and (b) $\phi = 1/20$, where the color of the points represents the expectation value S_3 of σ_3 for each eigenstate. (c) Quasienergy spectrum with $\phi = 1/20$ near the Weyl point at $k_3 = 0$. The dashed curves show the dispersion (5.47) of the Weyl Hamiltonian (5.39) under a magnetic field.

5.3.2 Chiral transport along the magnetic field

Because of the presence the chiral dispersion, a spin-polarized wave packet moves in the direction opposite to the applied magnetic field under the drive, which is a Floquet realization of the CME. To see this, we calculate the pumped fermion charge of a degenerate Fermi gas with a thermal initial state (5.25). Let us write the eigenstate of $\bar{U}(k_2, k_3)$ as $|k_3, k_2, b\rangle$, with b being the label of Landau levels. The time evolution is governed by the discrete-time von Neumann equation $\rho_{t+T} = \mathcal{U}_F \rho_t \mathcal{U}_F^\dagger$ and the pumped fermion charge ΔQ_3 antiparallel to the magnetic field is defined by

$$\Delta Q_3 = \frac{1}{N} \sum_{k_2,k_3,b} f_{k_2,b}(k_3) \frac{\partial \epsilon_b}{\partial k_3} = \frac{\sum_{k_2,b} \int_{-\pi}^{\pi} \frac{dk_3}{2\pi} f_{k_2,b}(k_3) \partial_{k_3} \epsilon_b}{\sum_{k_2,b} \int_{-\pi}^{\pi} \frac{dk_3}{2\pi} f_{k_2,b}(k_3)}, \tag{5.48}$$

where $f_{k_2,b}(k_3) := \langle k_3, k_2, b| \, \rho_0 \, |k_3, k_2, b\rangle$ is the non-equilibrium distribution function. One can see from Eq. (5.48) that ΔQ_3 is the sum of the weighted average of the winding-number density $\partial_{k_3} \epsilon_b$. Since the magnetic field is applied in the $(-z)$ direction: $\boldsymbol{B} := (0, 0, -2\pi\phi)$, we expect a net pumped charge along the $(+z)$ direction starting from an unpolarized spin state.

Figure 5.4 (a) shows the pumped fermion charge ΔQ_3 as a function of temperature $T_{\rm te}$ with the small band filling $n = 0.1$ and flux $\phi = 1/10$. The initial states are chosen as a fully polarized state with spin-up (red solid curve), that with spin-down (blue solid curve), or an unpolarized state with an equal mixture of the spin states (purple solid curve). For reference, we present the same calculation but without a magnetic field (red, blue, and purple dashed curves). For a wide range of temperature, the pumped charge of the down-spin state is suppressed because of the Landau gap, while it is enhanced for the up-spin state owing to the gapless chiral dispersion $\epsilon \propto k_3$. As a result, the net pumped charge ΔQ_3 for the unpolarized state takes a positive value in the presence of a magnetic field (purple solid curve) while it vanishes without a magnetic filed (purple dashed curve). Figure 5.4 (b) shows the temperature and the band-filling dependence of ΔQ_3 with flux $\phi = 1/10$ for an unpolarized initial state. In the entire parameter region, ΔQ_3 takes a positive value, which is a manifestation of the chiral

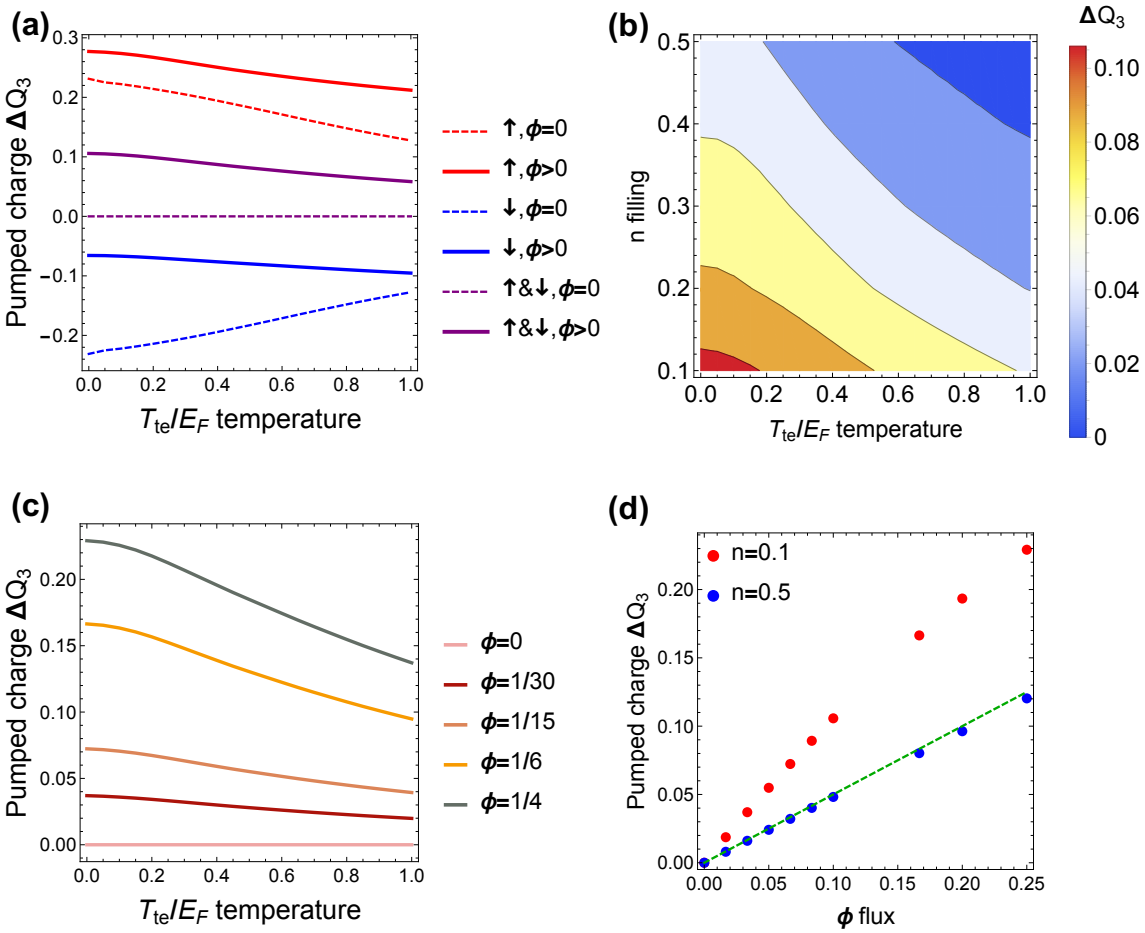

Figure 5.4: (a) Pumped fermion charge ΔQ_3 antiparallel to the magnetic field as a function of temperature $T_{\rm te}$ with the small band filling $n = 0.1$ and flux $\phi = 1/10$, where E_F is the Fermi energy. The red, blue, and purple solid curves correspond to the thermal state polarized with spin-up, that with spin-down, and the unpolarized initial states, respectively. The dashed curves show ΔQ_3 for the same initial states without a magnetic field. (b) Pumped fermion charge ΔQ_3 as a function of temperature $T_{\rm te}$ and the band filling n with the fixed flux $\phi = 1/10$. The initial state is an unpolarized state. (c) Pumped fermion charge ΔQ_3 as a function of temperature $T_{\rm te}$ for various values of flux ϕ. The band filling is fixed as $n = 0.1$ and the initial state is an unpolarized state. (d) Pumped fermion charge ΔQ_3 as a function of flux ϕ. The initial state is an unpolarized state and the temperature is fixed to be zero. The red (blue) points correspond to the band filling $n = 0.1$ ($n = 0.5$) and the green dashed line shows the analytical expression $\Delta Q_3 = \phi/2$ in Eq. (5.51).

transport of the CME. In Fig. 5.4 (c), we plot the temperature dependence of ΔQ_3 for several values of flux ϕ for the fixed band filling $n = 0.1$. The net pumped charge becomes larger for larger ϕ.

In Fig. 5.4 (d), we present the zero-temperature pumped fermion charge for an unpolarized initial state. The band filling is fixed at $n = 0.1$ ($n = 0.5$) for the red (blue) points. At half-filling $n = 0.5$, ΔQ_3 is close to $\phi/2$ (green dashed line), which actually has the topological origin explained as follows. In the limit $t_3 \gg t_1, t_2$, only the "lower" Floquet band is occupied at half-filling $n = 0.5$ and moreover the distribution $f_{{\rm FD},\alpha}(\boldsymbol{k})$ is uniform at the zero temperature.

Then, the non-equilibrium distribution function $f_{k_2,b}(k_3)$ also takes a constant value:

$$f_{k_2,b}(k_3) = \sum_{\boldsymbol{q},\alpha} f_{\mathrm{FD},\alpha}(\boldsymbol{q}) |\langle k_3, k_2, b|\boldsymbol{q},\alpha\rangle|^2 = \sum_{\boldsymbol{q},\alpha} |\langle k_3, k_2, b|\boldsymbol{q},\alpha\rangle|^2 = \langle k_3, k_2, b|k_3, k_2, b\rangle = 1. \tag{5.49}$$

Therefore, ΔQ_3 in Eq. (5.48) reduces to the sum of the one-dimensional winding number over all the bands divided by the number of bands:

$$\Delta Q_3 = \frac{\sum_{k_2,b} \int_{-\pi}^{\pi} \frac{dk_3}{2\pi} \frac{\partial \epsilon_b}{\partial k_3}}{\sum_{k_2,b} 1} = \frac{\sum_{k_2,b} \nu_b}{\sum_{k_2,b} 1}. \tag{5.50}$$

For each k_2, we have the $(2L_1)$-Landau bands and the (ϕL_1)-chiral bands through the magnetic flux ϕ. Each chiral band gives the winding number $\nu_b = +1$ and hence we have

$$\Delta Q_3 = \frac{\sum_{k_2} \phi L_1}{\sum_{k_2} (2L_1)} = \frac{\phi}{2}. \tag{5.51}$$

We emphasize that this quantized pumped charge vanishes in usual Floquet-Weyl semimetals obtained with topologically trivial $U(\boldsymbol{k})$ because left- and right-handed Weyl fermions appear with equal numbers *within a single band* in accordance with the Nielsen-Ninomiya theorem. The quasienergy band in our setup, in contrast, hosts a single-chirality Weyl fermion without a partner of opposite chirality within a single band, enabling us to realize the "maximally imbalanced" population where only one chiral component is occupied.

5.4 Experimental implementation

With high scalability and controllability [287], ultracold atomic gases are excellent candidates for implementing the Floquet CME. The crucial ingredients are the spin-selective Thouless pumps $\mathcal{U}_j^{\pm}$ and $\mathcal{U}_{h,3}^{\pm}$, which can be realized by a spin-dependent optical lattice [288–292] using ^{87}Rb or by laser-assisted tunneling [89,293] using ^{173}Yb. In both cases, the unitary operators $\mathcal{U}_q$ and $\mathcal{U}_s$ can be implemented by a sudden switch-on and -off of a quadrupole potential [191,284] and the laser-assisted hopping [192], respectively.

5.4.1 Setup with ^{87}Rb

Rubidium is the most-used atomic species in quantum simulation based on ultracold atomic gas. The spin-dependent transport using spin-dependent optical lattices have already been realized with ^{87}Rb [291, 292]. The two spin states $|\uparrow\rangle$ and $|\downarrow\rangle$ are chosen as $|\uparrow\rangle = |F = 2, m_F = -2\rangle$ and $|\downarrow\rangle = |F = 1, m_F = -1\rangle$. Consider a three-dimensional optical lattice produced by three orthogonal laser beams and their retroreflected ones. To suppress the natural hopping J, we apply an optical field gradient with a slope Δ, which is sufficiently small compared with the lattice depth V_0 but larger than J [35, 37]. The three pairs of counterpropagating plane waves are all linearly polarized, and we write the angle between the polarization vectors $\boldsymbol{e}_{1,+}^p$ and $\boldsymbol{e}_{1,-}^p$ of the beams along the x_1 axis as θ_1, that along the x_2 axis as θ_2, and that along the x_3 axis as θ_3. Those angles are dynamically controlled by electro-optical modulators by rotating the

polarization vector of the retroreflected laser beams. Then, the wave vectors $\boldsymbol{k}_{i,\alpha}$ ($i = 1, 2, 3$ and $\alpha = +, -$) and the polarization vectors $\boldsymbol{e}^p_{i,\alpha}$ ($i = 1, 2, 3$ and $\alpha = +, -$) of the six laser beams are given by

$$\boldsymbol{k}_{1,\pm} = \pm k\boldsymbol{e}_1, \quad \boldsymbol{k}_{2,\pm} = \pm k\boldsymbol{e}_2, , \quad \boldsymbol{k}_{3,\pm} = \pm k\boldsymbol{e}_3, \tag{5.52}$$

$$\boldsymbol{e}^p_{1,\pm}, = R_1\left(\frac{\pm\theta_1}{2}\right)\boldsymbol{e}_2, , \qquad \boldsymbol{e}^p_{2,\pm} = R_2\left(\frac{\pm\theta_2}{2}\right)\boldsymbol{e}_3, \qquad \boldsymbol{e}^p_{3,\pm} = R_3\left(\frac{\pm\theta_3}{2}\right)\boldsymbol{e}_1, \tag{5.53}$$

where $R_i(\theta)$ is the rotation matrix around the x_i axis through angle θ (see Figs. 5.5 (a), (b), and (c)). Then, the created optical potential $U_p(\boldsymbol{x})$ at the position $\boldsymbol{x}$ is given by

$$U_p(\boldsymbol{x}) = u_s|\left[\boldsymbol{e}^p(\boldsymbol{x})\right]^* \cdot \boldsymbol{e}^p(\boldsymbol{x})|\sigma_0 + u_v\boldsymbol{B}_{\rm eff}\cdot\boldsymbol{\sigma}, \tag{5.54}$$

$$\boldsymbol{B}_{\rm eff} = i\left[\boldsymbol{e}^p(\boldsymbol{x})\right]^* \times \boldsymbol{e}^p(\boldsymbol{x}), \tag{5.55}$$

$$\boldsymbol{e}^p(\boldsymbol{x}) = \sum_{i=1,2,3}\sum_{\alpha=\pm}\boldsymbol{e}^p_{i,\alpha}\exp(i\boldsymbol{k}_{i,\alpha}\cdot\boldsymbol{x} + \phi_i), \tag{5.56}$$

where u_s and u_v are the scalar potential and the vector potential, respectively [192]. Here, ϕ_i is the phase of an incoming wave along the x_i axis, which is phase-locked and controlled by an additional electro-optical modulator. We first consider the spin transport along the x_1-axis through the changes of θ_1 and ϕ_1. Suppose $u_s > u_v > 0$ and we initially set $\theta_1 = \theta_2 = \theta_3 = 0$ and $\phi_1 = \phi_2 = \phi_3 = \pi$. In this case, the atoms are trapped at $\boldsymbol{x} = a_{\rm lat}(m_1, m_2, m_3) \in L_C$, where $a_{\rm lat} = \pi/k$ is the lattice constant. As we change (θ_1, ϕ_1) from $(0, \pi)$ to $(\pi, 2\pi)$, atoms with spin states $\sigma_1 = 1$ are displaced by one lattice site in the positive x_1 direction, while those with spin states $\sigma_1 = -1$ are not, realizing spin-selective transport of atoms with $\sigma_1 = 1$. For the parameter change of (θ_1, ϕ_1) from $(0, \pi)$ to $(\pi, 0)$, atoms with spin states $\sigma_1 = -1$ are displaced by one lattice site in the negative x_1 direction, while those with spin states $\sigma_1 = 1$ are not, realizing a spin-selective transport of atoms with $\sigma_1 = -1$. The spin-selective transport along the x_2- and x_3-directions can be achieved by changing (θ_2, ϕ_2) and (θ_3, ϕ_3), respectively.

Although ^{87}Rb is a boson and hence the observed pumped charge ΔQ_3 is different from that shown in Sec. 5.2, we still expect a nonzero ΔQ_3 originating from the chiral dispersion in the quasienergy in Fig. 5.3 (b). Since the pumped charge ΔQ_3 is largely determined from the dispersion near the Weyl point $\boldsymbol{k} = 0$, a Bose-Einstein condensate of ^{87}Rb, whose momentum distribution are localized near $\boldsymbol{k} = 0$, are sufficient to observe the spin-dependent transport and the Floquet CME. In Fig. 5.5 (d), we calculate ΔQ_3 (blue points), where the initial state is taken as Bose-Einstein condensates at the momentum $\boldsymbol{k} = 0$. When the temperature is low enough, the initial-state density matrix ρ_0 is given by the mixture of the Bose-Einstein condensates with spin up and down with momentum $\boldsymbol{k} = 0$:

$$\rho_0 = \sum_{\alpha=\uparrow,\downarrow}|\boldsymbol{k} = 0, \alpha\rangle\langle\boldsymbol{k} = 0, \alpha|. \tag{5.57}$$

As shown as the blue points in Fig. 5.5 (d), ΔQ_3 exhibits the power-law behavior $\Delta Q_3 \propto \sqrt{\phi}$ for a small ϕ (green dashed curve).

To observe the Floquet CME, we measure the shift $\boldsymbol{X}_C$ in the center of mass within one cycle, which coincides with the pumped charge $\boldsymbol{\Delta Q}$ under a semiclassical approximation. For the observation, the timescale of the pump $\tau_{\rm pump}$ should be made much smaller than the decoherence

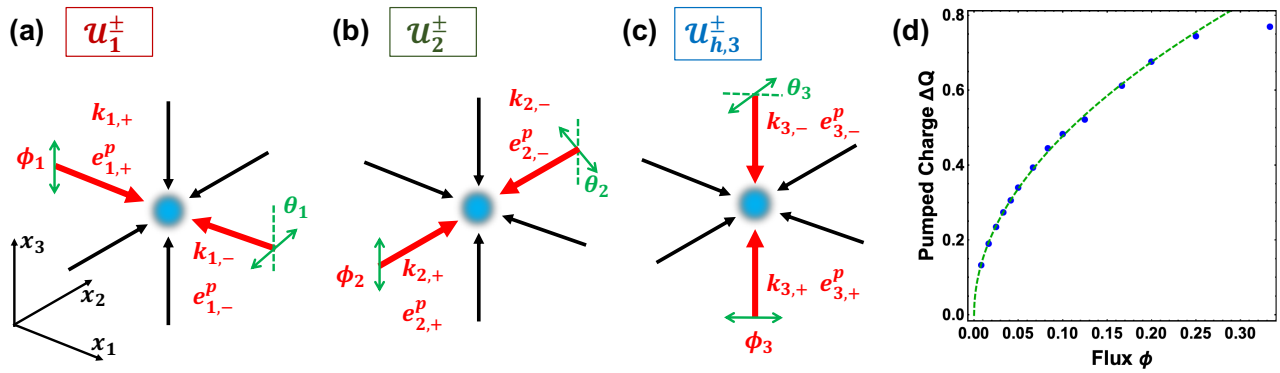

Figure 5.5: (a), (b), (c) Laser configurations of the spin-selective pumps (a) $\mathcal{U}_1^{\pm}$, (b) $\mathcal{U}_2^{\pm}$, and (c) $\mathcal{U}_{h,3}^{\pm}$, where $\boldsymbol{k}_{i,\alpha}$ and $\boldsymbol{e}_{i,\alpha}^{p}$ ($i = 1, 2, 3$ and $\alpha = +, -$) are the wave vectors and the polarization vectors of the six linearly polarized laser beams forming an optical lattice. The red and black arrows represent the wave vectors of the counterpropagating laser beams and green arrows are their polarization directions, and θ_i denotes the angle between $\boldsymbol{e}_{i,+}^{p}$ and $\boldsymbol{e}_{i,-}^{p}$, and ϕ_i denotes the locked phase of the incoming wave along the x_i axis. (d) Pumped fermion charge ΔQ_3 for a bosonic atomic gas, where the initial state is taken as a Bose-Einstein condensate at the momentum $\boldsymbol{k} = 0$.

time $\tau_{\rm de}$ of the spin. The timescale of the pump $\tau_{\rm pump}$ is determined from the adiabaticity condition for the lattice sliding, i.e., avoiding excitations to higher Bloch bands. This condition is satisfied for $\tau_{\rm pump} \geq 40$ μsec for the lattice depth $V_0 = 30E_r$, with E_r being the recoil energy [291, 292]. The dominant mechanism for decoherence may be the on-site interaction between particles [291], by which $\tau_{\rm de} = 200$ μsec for the lattice depth $V_0 = 25E_r$ with E_r being the recoil energy of ^{87}Rb with wavelength $\lambda = 785$ nm. When the single spin-selective Thouless pump operates within 40 μsec, atoms experience the interaction energy during the time $\tau_{d,s} = 40$ μsec $\times$ (w/λ) with w being the size of a wave packet localized at a site. Then, the total time $\tau_{d,\rm tot}$ during which the atoms experience the interaction is estimated to be $\tau_{d,\rm tot} = 8\tau_{d,s}$. Since $(w/\lambda) \approx \sqrt{V_0/E_r}$ for a deep optical lattice and the interaction energy $\propto \tau_{\rm de}^{-1}$ is proportional to $(V_0/E_r)^{\frac{4}{3}}$ [287], $\tau_{\rm de}/\tau_{d,\rm tot} = 8$ for the lattice depth $V_0/E_r = 20$. In this case, the optical field gradient with the on-site energy difference Δ with tens of kHz is sufficient to suppress the natural hopping $J = 0.02E_r \sim$ kHz. Thus, 8 cycles of the pumps can operate, which is sufficient to observe the displacement of the center of mass shown in Fig. 5.4 (d). Another limitation is the excitation to higher Bloch bands through a quadrupole field pulse. The weight $w_{\rm exc}$ of the excited states is given by $w_{\rm exc} \propto \phi(w/\lambda)^2$ [191] and hence it is negligible for a weak magnetic flux and a deep optical lattice.

5.4.2 Setup with ^{173}Yb

Motivated by the recent experiments on realizing synthetic gauge fields [219, 294] and the proposals for implementing helical hopping [89, 293], we consider yet another implementation scheme using fermionic alkaline-earth-like atoms ^{173}Yb and a laser-assisted hopping using the excited level ^{3}P$_1$. For the implementation, we rewrite $U(\boldsymbol{k})$ as the combination of helical pumps

as follows:

$$U(\boldsymbol{k}) = \widetilde{U}_1(k_1)\widetilde{U}_3\left(\frac{k_3}{2}\right)\widetilde{U}_2(k_2)\widetilde{U}_3\left(\frac{k_3}{2}\right)\widetilde{U}_1(k_1)\widetilde{U}_3\left(\frac{k_3}{2}\right)\widetilde{U}_2(k_2)\widetilde{U}_3\left(\frac{k_3}{2}\right), \tag{5.58}$$

where $\widetilde{U}_j(k) := \mathrm{e}^{-i\frac{\sigma_j}{2}k}$ is the helical pump. The two spin states are taken as $|m_F = -5/2\rangle$ and $|m_F = -1/2\rangle$ in the ground state manifold ${}^1\mathrm{S}_0$ with $F = I = 5/2$. The six-fold degeneracy between the spin states is lifted by a Zeeman splitting $\Delta_{B,3}$ induced by a uniform magnetic field in the x_3 direction. The natural hopping is suppressed by a magnetic field gradient $\delta B_3 = \Delta_1 x_1 + \Delta_2 x_2 + \Delta_3 x_3$, where Δ_1, Δ_2, and Δ_3 are the on-site energy difference along the x_1, x_2, and x_3 directions, respectively. For a lattice depth $V_0 = 20E_r$, where the natural hopping J is given by $J = 0.02E_r$, the Zeeman splitting $\Delta_{B,z}$ of the order of tens of kHz is sufficient for the suppression. A spin-flip hopping along the x_3 direction can be induced by Raman laser beams resonant to the energy difference Δ_3 [293]. The helical pump can be implemented by this spin-flip hopping followed by the π pulse [89]. The helical hoppings $\widetilde{U}_{1,2}(k_{1,2})$ in the other two directions can be implemented by a combination of the $\pi/2$ pulses and the helical pump because we have

$$\widetilde{U}_1(k_1) = \mathrm{e}^{-\frac{i\pi\sigma_2}{4}}\widetilde{U}_3(k_1)\mathrm{e}^{\frac{i\pi\sigma_2}{4}}, \quad \widetilde{U}_2(k_2) = \mathrm{e}^{\frac{i\pi\sigma_1}{4}}\widetilde{U}_3(k_2)\mathrm{e}^{-\frac{i\pi\sigma_1}{4}}. \tag{5.59}$$

One can selectively induce these three-directional hoppings by making Δ_1, Δ_2, and Δ_3 different from each other and three pairs of Raman laser beams. This can be done also by a pair of Raman laser beams and dynamically changing Δ_1, Δ_2, and Δ_3.

To observe the Floquet CME, the timescale of the pump τ_{pump} should be made much smaller than the lifetime τ_{life} of the Raman induced hopping. The timescale of a Raman-induced hopping Ω on a lattice system is of the order of kHz [219] when the one-photon detuning δ of the Raman process is taken to be of the order of 1 GHz [293,294]. In this case, the single pump operates within one millisecond, leading to tens of millisecond for one cycle of the pump. The lifetime $\tau_{\mathrm{life}} \sim \delta/(\gamma\Omega)$ resulting from heating with the Raman process is of the order of 1 sec for the lifetime of $\gamma = 850$ nsec [295], which is much longer than an alkali-metal system [294]. Therefore, at least a few tens of pumps can operate within the lifetime, which is sufficient for the observation of the Floquet CME.

5.5 Classification of gapless Floquet spectra

The emergence of a single Weyl fermion is a consequence of the nontrivial topology of the Floquet-Bloch operator $U(\boldsymbol{k})$. This phenomenon is generalized to a wider range of lattice-prohibited band structures under certain symmetries. In general, topologically nontrivial Floquet-Bloch operators as unitary maps from the Brillouin zone possess gapless quasienergy spectra, since a gapped Floquet operator can continuously be deformed into a trivial unitary, e.g., $U(\boldsymbol{k}) = \mathbf{1}_N$ [18,296], where $\mathbf{1}_N$ is the identity matrix with size N. Here, N denotes the number of bands. Let us take a Floquet-Bloch operator

$$U(\boldsymbol{k}) := \mathcal{T}_t \exp\left[-i\int_0^T dt h(\boldsymbol{k}, t)\right] \in U(N) \tag{5.60}$$

given by some unitary matrix. We consider three symmetries in the AZ classes [101, 102], i.e. the time-reversal symmetry Θ, the particle-hole symmetry C, and the chiral symmetry Γ:

$$\Theta h(\boldsymbol{k},t)\Theta^{-1} = h(-\boldsymbol{k},T-t), \quad Ch(\boldsymbol{k},t)C^{-1} = -h(-\boldsymbol{k},t), \quad \Gamma h(\boldsymbol{k},t)\Gamma^{-1} = -h(\boldsymbol{k},T-t). \tag{5.61}$$

In terms of the Floquet-Bloch operators, these symmetries are expressed as follows [18]:

$$\Theta U(\boldsymbol{k})\Theta^{-1} = U^\dagger(-\boldsymbol{k}), \quad CU(\boldsymbol{k})C^{-1} = U(-\boldsymbol{k}), \quad \Gamma U(\boldsymbol{k})\Gamma^{-1} = U^\dagger(\boldsymbol{k}), \tag{5.62}$$

which can be rewritten as the symmetries of the effective Bloch Hamiltonian $h_{\rm eff}(\boldsymbol{k})$:

$$\Theta h_{\rm eff}(\boldsymbol{k})\Theta^{-1} = h_{\rm eff}(-\boldsymbol{k}), \quad Ch_{\rm eff}(\boldsymbol{k})^{-1}C = -h_{\rm eff}(-\boldsymbol{k}), \quad \Gamma h_{\rm eff}(\boldsymbol{k})\Gamma^{-1} = -h_{\rm eff}(\boldsymbol{k}). \tag{5.63}$$

We allow any continuous deformation of Floquet-Bloch operators which respect the symmetry of the system, and classify their stable equivalence classes according to the K-theory [102, 103]. Note that we do *not* assume energy gaps of the quasienergy band.

We emphasize that the symmetry restrictions (5.62) on the Floquet-Bloch operator is different from those on adiabatic pumps. As we can see from Eqs. (2.35) and (5.63), the AZ symmetries are imposed on the instantaneous Bloch Hamiltonian $h(\boldsymbol{k},t)$ in adiabatic pumps while those are imposed on the effective Bloch Hamiltonian $h_{\rm eff}(\boldsymbol{k})$ of the Floquet-Bloch operators in our setup.

5.5.1 Floquet-Bloch operators without chiral symmetry

The classification of the unitary matrices can be performed in a manner similar to that of anomalous edge states in Sec. 3.2 [146, 297]. We construct from the Floquet-Bloch operator $U(\boldsymbol{k})$ a Hermitian matrix

$$H_U(\boldsymbol{k}) = \begin{pmatrix} 0 & U(\boldsymbol{k}) \\ U^\dagger(\boldsymbol{k}) & 0 \end{pmatrix} = \sigma_- \otimes U^\dagger(\boldsymbol{k}) + \sigma_+ \otimes U(\boldsymbol{k}), \tag{5.64}$$

where $\otimes$ denotes the tensor product. Since we have $[H_U(\boldsymbol{k})]^2 = \mathbf{1}_{2N}$, $H_U(\boldsymbol{k})$ is a gapped Hamiltonian with flat bands. This Hamiltonian has the following CS:

$$\Gamma_2 H_U(\boldsymbol{k})\Gamma_2^{-1} = -H_U(\boldsymbol{k}), \tag{5.65}$$

where the CS Γ_2 is defined by

$$\Gamma_2 = \begin{pmatrix} \mathbf{1}_N & 0 \\ 0 & -\mathbf{1}_N \end{pmatrix} = \sigma_3 \otimes \mathbf{1}_N. \tag{5.66}$$

Therefore, the classification of class-A (i.e., no symmetry) Floquet-Bloch operators in d dimensions is equivalent to that of class-AIII topological insulators in d dimensions. When the Floquet operator has the TRS $\Theta U(\boldsymbol{k})\Theta^{-1} = U^\dagger(-\boldsymbol{k})$ with $\epsilon_\Theta := \Theta^2 = \pm 1$, the Hamiltonian $H_U(\boldsymbol{k})$ has the following symmetries

$$\Theta_1 H_U(\boldsymbol{k})\Theta_1^{-1} = H_U(-\boldsymbol{k}), \quad \Theta_2 H_U(\boldsymbol{k})\Theta_2^{-1} = -H_U(-\boldsymbol{k}), \tag{5.67}$$

where

$$\Theta_1 := \begin{pmatrix} 0 & \Theta \\ \Theta & 0 \end{pmatrix} = \sigma_1 \otimes \Theta, \quad \Theta_2 := \epsilon_\Theta \begin{pmatrix} 0 & -\Theta \\ \Theta & 0 \end{pmatrix} = -i\epsilon_\Theta \sigma_2 \otimes \Theta. \tag{5.68}$$

These symmetries are regarded as effective TRS and PHS of $H_U(\boldsymbol{k})$. Since $\Theta_1^2 = \epsilon_\Theta$ and $\Theta_2^2 = -\epsilon_\Theta$, the classification of class-AI (class-AII) Floquet-Bloch operators in d dimensions corresponds to that of class-CI (class-DIII) topological superconductors in the same dimensionality. Similarly, when $U(\boldsymbol{k})$ has the PHS $CU(\boldsymbol{k})C^{-1} = U(-\boldsymbol{k})$ with $\epsilon_C := C^2 = \pm 1$, we can define

$$C_1 := \begin{pmatrix} C & 0 \\ 0 & C \end{pmatrix} = \sigma_0 \otimes C, \quad C_2 := \epsilon_C C_1 \Gamma_2 = \epsilon_C \begin{pmatrix} C & 0 \\ 0 & -C \end{pmatrix} = \epsilon_C \sigma_3 \otimes C, \tag{5.69}$$

so that

$$C_1 H_U(\boldsymbol{k}) C_1^{-1} = H_U(-\boldsymbol{k}), \quad C_2 H_U(\boldsymbol{k}) C_2^{-1} = -H_U(-\boldsymbol{k}), \tag{5.70}$$

with $C_1^2 = C_2^2 = \epsilon_C$. Therefore, the classification of class-D (class-C) Floquet-Bloch operators in d dimensions corresponds to that of class-BDI (class-CII) topological superconductors in the same dimensionality.

5.5.2 Floquet-Bloch operators with chiral symmetry

Next, we consider the cases where the Floquet-Bloch operator has the CS $\Gamma U(\boldsymbol{k})\Gamma^{-1} = U^\dagger(\boldsymbol{k})$. Then, the Hamiltonian $H_U(\boldsymbol{k})$ satisfies

$$\Gamma_1 H_U(\boldsymbol{k}) \Gamma_1^{-1} = -H_U(\boldsymbol{k}), \tag{5.71}$$

where Γ_1 is another CS of the Hamiltonian:

$$\Gamma_1 := \begin{pmatrix} 0 & -\Gamma \\ \Gamma & 0 \end{pmatrix} = -i\sigma_2 \otimes \Gamma. \tag{5.72}$$

By combining the two chiral symmetries (5.65) and (5.71), we have

$$\Gamma_1 \Gamma_2 H_U(\boldsymbol{k}) (\Gamma_1 \Gamma_2)^{-1} = H_U(\boldsymbol{k}), \tag{5.73}$$

and therefore the Hamiltonian $H_U(\boldsymbol{k})$ can be block-diagonalized simultaneously with $\Gamma_1\Gamma_2$. For the unitary matrix V defined by

$$V = \frac{1}{\sqrt{2}} \begin{pmatrix} \gamma\Gamma & -\gamma\Gamma \\ \mathbf{1}_N & \mathbf{1}_N \end{pmatrix}, \tag{5.74}$$

we obtain the block-diagonalized Hamiltonian and $\Gamma_1\Gamma_2$:

$$V^\dagger H_U(\boldsymbol{k}) V = \begin{pmatrix} \gamma\Gamma U(\boldsymbol{k}) & 0 \\ 0 & -\gamma\Gamma U(\boldsymbol{k}) \end{pmatrix} = \sigma_3 \otimes \gamma\Gamma U(\boldsymbol{k}), \tag{5.75}$$

$$V^\dagger \Gamma_1 \Gamma_2 V = \gamma^* \begin{pmatrix} \mathbf{1}_N & 0 \\ 0 & -\mathbf{1}_N \end{pmatrix} = \gamma^* \sigma_3 \otimes \mathbf{1}_N, \tag{5.76}$$

where $\Gamma_{1,2}$ have off-diagonal forms in this basis:

$$V^\dagger \Gamma_1 V = -i\gamma^* \sigma_2 \otimes \mathbf{1}_N, \quad V^\dagger \Gamma_2 V = -\sigma_1 \otimes \mathbf{1}_N. \tag{5.77}$$

When we assume that Θ and C commute with each other: $[\Theta, C] = 0$, $\Theta_{1,2}$ and $C_{1,2}$ are expressed in the new basis as follows:

$$V^\dagger \Theta_1 V = \epsilon_\Theta(\sigma_3 \mathrm{Re}\gamma - \sigma_2 \mathrm{Im}\gamma) \otimes C, \quad V^\dagger \Theta_2 V = -i(\sigma_2 \mathrm{Re}\gamma + \sigma_3 \mathrm{Im}\gamma) \otimes C, \tag{5.78}$$

$$V^\dagger C_1 V = \left(\sigma_3 \frac{1+\gamma^2}{2} + \sigma_1 \frac{1-\gamma^2}{2}\right) \otimes C, \quad V^\dagger C_2 V = \left(\sigma_0 \frac{-1+\gamma^2}{2} - \sigma_1 \frac{1+\gamma^2}{2}\right) \otimes C. \tag{5.79}$$

Thus, the classification of $H_U(\boldsymbol{k})$ reduces to that of $A(\boldsymbol{k}) := \gamma \Gamma U(\boldsymbol{k})$. Note that the Hermiticity of $A(\boldsymbol{k})$ follows from the CS of $U(\boldsymbol{k})$. If the Floquet-Bloch operator has the CS only (i.e., class AIII), $A(\boldsymbol{k})$ is a Hamiltonian without symmetry. Therefore, the classification of class-AIII Floquet-Bloch operators in d dimensions reduces to that of class-A topological insulators in the same dimensionality. For the remaining classes, where the Floquet-Bloch operators have TRS, PHS, and CS, we identify the symmetry of $A(\boldsymbol{k})$ by using $\gamma^2 = \Gamma^2 = \epsilon_\Theta \epsilon_C$. When $\gamma^2 = 1$, we find from Eqs. (5.78) and (5.79) that Θ_1 and C_1 are symmetries of $A(\boldsymbol{k})$ while Θ_2 and C_2 are not because Θ_2 and C_2 have off-diagonal forms. The symmetry conditions for Θ_1 and C_1 are expressed as

$$CA(\boldsymbol{k})C^{-1} = A(-\boldsymbol{k}), \tag{5.80}$$

and this is the TRS of $A(\boldsymbol{k})$. Therefore, the classification of class-BDI (class-CII) Floquet-Bloch operators in d dimensions is mapped to that of d-dimensional class-AI (class-AII) topological insulators. When $\gamma^2 = -1$, we find from Eqs. (5.78) and (5.79) that Θ_2 and C_2 are symmetries of $A(\boldsymbol{k})$ while Θ_1 and C_1 are not because Θ_1 and C_1 have off-diagonal forms. The symmetry conditions for Θ_2 and C_2 are expressed as

$$CA(\boldsymbol{k})C^{-1} = -A(-\boldsymbol{k}), \tag{5.81}$$

which is the PHS of $A(\boldsymbol{k})$. Thus we find that the classification of class-DIII (class-CI) Floquet-Bloch operators in d dimensions is equivalent to that of class-D (class-C) topological superconductors in the same dimensionality.

5.5.3 Periodic table for Floquet-Bloch operators

Let $K_{\mathbb{F}}^{\mathrm{FB}}(s, d)$ be the K-group of the Floquet-Bloch operators with dimensionality d and the AZ symmetry class $(\mathbb{F}, s)$. From the above discussion, we obtain the following results on the classification of Floquet-Bloch operators:

$$K_{\mathbb{F}}^{\mathrm{FB}}(s, d) = K_{\mathbb{F}}(s-1, d) = K_{\mathbb{F}}(s, d+1), \tag{5.82}$$

where $K_{\mathbb{F}}(s, d)$ is the K-group of static TIs and TSCs with dimensionality d and the AZ symmetry class $(\mathbb{F}, s)$. In the second equality in Eq. (5.82), we use the K-group isomorphism (2.22). Equation (5.82) shows the equivalence between the class of gapless bulk states in Floquet systems and that of surface gapless states of static TIs and TSCs. The final results are summarized in Table 5.1. These results strongly suggest that the gapless surface states of TIs and TSCs,

Table 5.1: Tenfold-way topological classification of Floquet-Bloch operators for spatial dimensionality $d = 0, 1, \cdots, 7$. The notations are the same as in Tab. 2.1. The Floquet single Weyl fermion in Eq. (5.10) corresponds to class A in $d = 3$.

s	class	Θ	C	Γ	$d=0$	$d=1$	$d=2$	$d=3$	$d=4$	$d=5$	$d=6$	$d=7$
0	A	0	0	0	0	$\mathbb{Z}$	0	$\mathbb{Z}$	0	$\mathbb{Z}$	0	$\mathbb{Z}$
1	AIII	0	0	1	$\mathbb{Z}$	0	$\mathbb{Z}$	0	$\mathbb{Z}$	0	$\mathbb{Z}$	0
0	AI	1	0	0	0	0	0	$2\mathbb{Z}$	0	$\mathbb{Z}_2$	$\mathbb{Z}_2$	$\mathbb{Z}$
1	BDI	1	1	1	$\mathbb{Z}$	0	0	0	$2\mathbb{Z}$	0	$\mathbb{Z}_2$	$\mathbb{Z}_2$
2	D	0	1	0	$\mathbb{Z}_2$	$\mathbb{Z}$	0	0	0	$2\mathbb{Z}$	0	$\mathbb{Z}_2$
3	DIII	-1	1	1	$\mathbb{Z}_2$	$\mathbb{Z}_2$	$\mathbb{Z}$	0	0	0	$2\mathbb{Z}$	0
4	AII	-1	0	0	0	$\mathbb{Z}_2$	$\mathbb{Z}_2$	$\mathbb{Z}$	0	0	0	$2\mathbb{Z}$
5	CII	-1	-1	1	$2\mathbb{Z}$	0	$\mathbb{Z}_2$	$\mathbb{Z}_2$	$\mathbb{Z}$	0	0	0
6	C	0	-1	0	0	$2\mathbb{Z}$	0	$\mathbb{Z}_2$	$\mathbb{Z}_2$	$\mathbb{Z}$	0	0
7	CI	1	-1	1	0	0	$2\mathbb{Z}$	0	$\mathbb{Z}_2$	$\mathbb{Z}_2$	$\mathbb{Z}$	0

which cannot have pure lattice realization without bulk, can be realized in bulk quasienergy spectra of periodically driven lattice systems. For example, the single Weyl fermion presented in Sec. 5.1 corresponds to a surface state of a four-dimensional topological insulator [128]. The correspondence with gapless surface states of TIs and TSCs can be understood from the symmetry constraints (5.63) on the effective Hamiltonian $h_{\rm eff}(\boldsymbol{k})$. For simplicity, consider the continuum Dirac Hamiltonian $h_{\rm eff}(\boldsymbol{k}) = \boldsymbol{k}\cdot\boldsymbol{\alpha}$, where $\boldsymbol{\alpha}$ is a set of anticommuting matrices. The stability condition of its gapless point $\boldsymbol{k} = 0$ is the same as that of surface states of TIs and TSCs with the same AZ symmetry class and dimensionality, leading to the same classification table. Using the periodicity of the quasienergy, this continuum Dirac Hamiltonian can be extrapolated to the boundary of the Brillouin zone such that the periodicity of the Brillouin zone is satisfied.

Some remarks are in order. To *prove* the correspondence between the gapless surface states of TIs and TSCs and the gapless spectra of Floquet-Bloch operators, we must find the time-dependent Hamiltonian that satisfies Eq. (5.61) in each symmetry class. While the classification in this section is performed by considering the symmetry conditions (5.62) *for Floquet-Bloch operators*, Eq. (5.62) does not necessary mean that Eq. (5.61) is satisfied. Therefore, the presence of concrete models are, in general, a nontrivial problem. In App. A.4, we show the above correspondence by constructing concrete models in all the symmetry classes and spatial dimensionalities up to three.

We note that the classification of gapless Floquet states in d dimensions coincides with that of anomalous edge (or surface) states of Floquet TIs and TSCs given by unitary loops in $(d+1)$ dimensions [146]. Indeed, it has been discussed that the gapless Floquet spectrum can be realized as the edge state of the anomalous TIs and TSCs [225]. We can interpret our result to be a generalization of this correspondence to all the Altland-Zirnbauer classes. The correspondence between the gapless topological singularities and topologically nontrivial unitaries has been discussed in the context of anomalous TIs and TSCs [146, 296].

Finally, we emphasize that the obtained classification is different from that of adiabatic pump in Sec. 2.3 (see Table 2.2 and Table 5.1). In fact, the K group $K_{\mathbb{F}}^{\rm AP}(s,d)$ of adiabatic pumps with dimensionality d and symmetry class $(\mathbb{F}, s)$ is related with that of the Floquet-Bloch

operators as follows:

$$K_{\mathbb{F}}^{\mathrm{FB}}(s,d) = K_{\mathbb{F}}^{\mathrm{AP}}(s-2,d). \tag{5.83}$$

While this difference does not gives rise to any distinction for the complex class $\mathbb{F} = \mathbb{C}$ because of the Bott periodicity, i.e., $K_{\mathbb{C}}^{\mathrm{AP}}(s-2,d) = K_{\mathbb{C}}^{\mathrm{AP}}(s,d)$, it gives different topological number for the real class $\mathbb{F} = \mathbb{R}$, which should lead to different transport phenomena. The difference in Eq. (5.83) arises from the following two reasons. First, the imposed symmetries (2.35) and (5.61) are different: while an instantaneous Bloch Hamiltonian $h(\boldsymbol{k}, t)$ has TRS, PHS, and CS in adiabatic pumps, the effective Bloch Hamiltonian $h_{\mathrm{eff}}(\boldsymbol{k})$ has these symmetries in our pump. Secondly, the adiabatic condition is not imposed on the topological pumps characterized by Floquet-Bloch operators. To see this, consider the class D in one dimension, where only the PHS is imposed. While the PHS gives the same symmetry constraint (see Eqs. (2.35) and (5.61)), adiabatic and non-adiabatic pumps have different topological numbers, $\mathbb{Z}_2$ and $\mathbb{Z}$, respectively. The former corresponds to the fermion-parity pump [103] while the latter counts the number of chiral Majorana fermions in its quasienergy spectra. Since the adiabaticity is no longer imposed in a non-adiabatic pump, the $\mathbb{Z}_2$ index is ill-defined.

Chapter 6

Floquet engineering of nonlinear systems

As we have seen in Chapter 3, Floquet engineering has various applications in quantum systems. The Floquet theorem and the high-frequency expansion (HFE) are commonly used techniques there because they allow us to map non-equilibrium systems to effective static ones, thereby greatly simplifying their analysis. It is therefore clearly important to extend these techniques to classical systems, in particular, to develop a general framework for performing the HFE of their equations of motion (EOMs). In fact, such a generalization potentially has a wide range of applications because classical EOMs appear not only in classical systems, e.g., a Langevin system in biology and chemistry [119], but also in quantum systems in symmetry-broken phases, e.g., Bose-Einstein condensates described by the Gross-Pitaevskii (GP) equation [298, 299]. Additionally, it is desirable to generalize it to including *open* classical systems because a coupling with an environment plays an important role in preventing the system from heating up against a persistent drive, as emphasized in the studies on open quantum systems [59,60,223,300–306].

However, the HFE of classical EOMs has so far been developed only for Hamilton systems [117, 198]. Although a heuristic approach based on the multi-scale perturbation analysis [248, 249] is found to be successful in specific examples [253, 254, 307–309], its calculation often becomes involved, which is usually the case with the singular perturbation theory. This makes the analysis of a general system difficult and little is known on the validity and convergence property of this perturbative expansion. One difficulty in treating classical systems is that the Floquet theorem can be applied only to linear differential equations like the Schrödinger equation [27, 30, 31], while classical EOMs are, in general, nonlinear. Another difficulty arises in an open classical system coupled to a thermal bath, where a thermal fluctuation arises in its EOM as a stochastic variable. Its randomness breaks the exact periodicity of the EOM; thus the Floquet theorem cannot be applied directly.

In this chapter, we develop the HFE for a general periodically driven classical system. Our idea is simple and general: using a master equation rather than the EOM itself. Since the master equation is linear in the probability distribution function and periodic with time, one can safely apply the Floquet theorem and perform the HFE. The effective EOM is obtained from the expanded master equation through the correspondence between an EOM and a master equation. Our method is applicable not only to isolated systems but also to open systems coupled to thermal reservoirs as far as they are described by stochastic differential equations. Furthemore, it can be used to a Markov process on a discrete state space like the asymmetric

simple exclusion process (ASEP) [310,311] and the abelian sandpile model [312,313]. Since the HFE is performed in a manner parallel to a quantum system, one can systematically analyze the higher-order terms and the convergence property of the FM HFE by adapting the techniques developed in quantum systems [95, 96]. These results are hard to obtain by the multi-scale perturbation theory because of the complexity of the calculation. From these analyses, we find that the FM HFE is, at least asymptotically, convergent for a high-frequency drive. Moreover, for a non-chaotic few-body system and a generic many-body systems, the HFE is found to well describe its steady state including a Floquet prethermal state of an isolated system and a non-equilibrium steady state (NESS) of a driven dissipative system. To support these analytical findings, we numerically test the validity of the HFE by two driven dissipative systems: (i) a Kapitza pendulum with friction and (ii) a laser-irradiated magnet described by the sLLG equation. Comparing the exact time-dependent EOMs and the effective EOMs obtained from the vV HFE, we confirm that the latter well approximate the former not only for a short time during an initial relaxation but also *for a long time until their NESSs*. This result is in stark contrast to closed quantum systems where the truncated HFE fails to capture eventual heating to infinite temperature [27, 94–98]. Finally, we present an application to spintronics, where we analyze a multiferroic spin chain irradiated by a circularly polarized laser. A spiral magnetic order appears in the NESS through a laser-driven DM interaction.

6.1 High-frequency expansion of a classical equation of motion

6.1.1 Equation of motion and master equation

Consider a classical system under a periodic drive with period T, which is described by a set of classical variables $\boldsymbol{\phi}(t) := [\phi_1(t), \phi_2(t), \cdots, \phi_N(t)]$. We assume that its EOM is given by a stochastic differential equation [314]:

$$\dot{\phi}_i(t) = f_i\left[\boldsymbol{\phi}(t), t\right] + \sum_{j=1}^{N} g_{ij}\left[\boldsymbol{\phi}(t), t\right] h_j(t), \tag{6.1}$$

where h_j is a Gaussian random variable with the Markovian nature (4.8). A Markov process on a discrete state space is discussed at the end of this subsection. This equation is a generalization of Eq. (4.7) in that the drift force $f_i\left(\boldsymbol{\phi}, t\right)$ and the diffusion matrix $g_{ij}\left(\boldsymbol{\phi}, t\right)$ become time-periodic with period T: $f_i\left(\boldsymbol{\phi}, t+T\right) = f_i\left(\boldsymbol{\phi}, t\right)$ and $g_{ij}\left(\boldsymbol{\phi}, t+T\right) = g_{ij}\left(\boldsymbol{\phi}, t\right)$. For a classical field $\boldsymbol{\phi}_{\boldsymbol{r}} = [\phi_{\boldsymbol{r},1}(t), \phi_{\boldsymbol{r},2}(t), \cdots, \phi_{\boldsymbol{r},N_I}(t)]$, its EOM is given by

$$\dot{\phi}_{\boldsymbol{r},a}(t) = f_{\boldsymbol{r},a}\left[\boldsymbol{\phi}(t), t\right] + \sum_{b=1}^{N_I} g_{\boldsymbol{r},ab}\left[\boldsymbol{\phi}(t), t\right] h_{\boldsymbol{r},b}(t), \tag{6.2}$$

where $\boldsymbol{r}$ is the coordinate and N_I is the number of the internal degrees of freedom. We here choose the Stratonovich prescription for the application to the sLLG equation in Sec. 6.4 though a generalization to the other prescriptions is straightforward [314].

Equations (6.1) and (6.2) with a finite diffusion constant $D > 0$ are commonly used to describe diffusive processes in nature, such as a Langevin motion [119] and the spin dynamics of

a micromagnet [122]. When $D = 0$, Eq. (6.1) gives a deterministic equation: $\dot{\phi}_i(t) = f_i[\boldsymbol{\phi}(t), t]$, which describes an open classical system at sufficiently low temperature or a closed classical system including a Hamilton system. It is worth mentioning that Eq. (6.1) can describe even *quantum* systems in symmetry-broken phases or the semiclassical limit. In the former case, $\boldsymbol{\phi}$ and Eq. (6.1) are the order parameter and its equation, e.g., the GP equation [298,299] and the Ginzburg-Landau equation [315], respectively. For the GP equation, the order parameter $\boldsymbol{\phi} = \{\psi_{\boldsymbol{r}}\}_{\boldsymbol{r}\in\mathbb{R}^d}$, with d being the spatial dimensionality, represents the macroscopic wavefunction, with its equation written into the form of Eq. (6.1) with $D = 0$:

$$\dot{\psi}_{\boldsymbol{r}} = -i\left[-\frac{\nabla_{\boldsymbol{r}}^2\psi_{\boldsymbol{r}}}{2m} + (\mu + g_c|\psi_{\boldsymbol{r}}|^2)\psi_{\boldsymbol{r}}\right]. \tag{6.3}$$

Here, m, μ and g_c are the mass of atoms, the chemical potential and the coupling constant, respectively. An example of the latter case is the Dicke model in the semiclassical limit, which describes two-level atoms coupled to a large number of photons in a cavity [316, 317]. In this limit, the system is described by the effective collective atomic pseudospin $\boldsymbol{J} := (J_x, J_y, J_z)$ ($\in \mathbb{R}^3$) and the coherent-state amplitude a ($\in \mathbb{C}$) of photons. Its EOM is derived from the Ehrenfest equation $d\langle A\rangle/dt = i\langle[H, A]\rangle$, which is given as follows:

$$\dot{\boldsymbol{J}} = (2\lambda \mathrm{Re}\,(a), 0, \omega_a) \times \boldsymbol{J}, \quad \dot{a} = -i\left(\omega_o a + \lambda J_x\right), \tag{6.4}$$

where ω_a, ω_o, and λ are the atomic frequency, the optical frequency, and the coupling constant between the photons and atoms, respectively.

The master equation corresponding to Eq. (6.1) is given by

$$\frac{\partial P(\boldsymbol{\phi}, t)}{\partial t} = \frac{\partial}{\partial \phi_i}\left[\mathcal{F}_i(\boldsymbol{\phi}, t)P(\boldsymbol{\phi}, t)\right] + \frac{\partial^2}{\partial\phi_i\partial\phi_j}\left[\mathcal{D}_{ij}(\boldsymbol{\phi}, t)P(\boldsymbol{\phi}, t)\right], \tag{6.5}$$

where $\mathcal{F}_i(\boldsymbol{\phi}, t)$ and $\mathcal{D}_{ij}(\boldsymbol{\phi}, t)$ are the drift field and the diffusion matrix, respectively, which are defined as follows:

$$\mathcal{F}_i(\boldsymbol{\phi}, t) := -f_i(\boldsymbol{\phi}, t) - Dg_{kl}(\boldsymbol{\phi}, t)\frac{\partial g_{il}(\boldsymbol{\phi}, t)}{\partial \phi_k}, \tag{6.6}$$

$$\mathcal{D}_{ij}(\boldsymbol{\phi}, t) := Dg_{ik}(\boldsymbol{\phi}, t)g_{jk}(\boldsymbol{\phi}, t). \tag{6.7}$$

Equations (6.6) and (6.7) give the relation between an EOM and a master equation. We note that the master equation (6.5) contains only up to the second-order derivative of $\boldsymbol{\phi}$ because the random variable h_j is Markovian and Gaussian. In other words, if the master equation contains higher-order derivative or becomes an integro-differential equation, the random noise must be either non-Markovian or non-Gaussian [318–322]. We will comment on this issue again in Sec. 6.1.2.

By introducing the vector fields $\boldsymbol{f} := (f_1, f_2, \cdots, f_N)$ and $\boldsymbol{h} := (h_1, h_2, \cdots, h_N)$, and the matrix-valued function $G := \{g_{ij}\}_{i,j=1}^N$, we can rewrite Eq. (6.1) in compact forms:

$$\dot{\boldsymbol{\phi}} = \boldsymbol{f}(\boldsymbol{\phi}, t) + G(\boldsymbol{\phi}, t)\boldsymbol{h}(t). \tag{6.8}$$

Similarly, if we introduce the vector field $\boldsymbol{\mathcal{F}} := (\mathcal{F}_1, \mathcal{F}_2, \cdots, \mathcal{F}_N)$ and the matrix-valued field

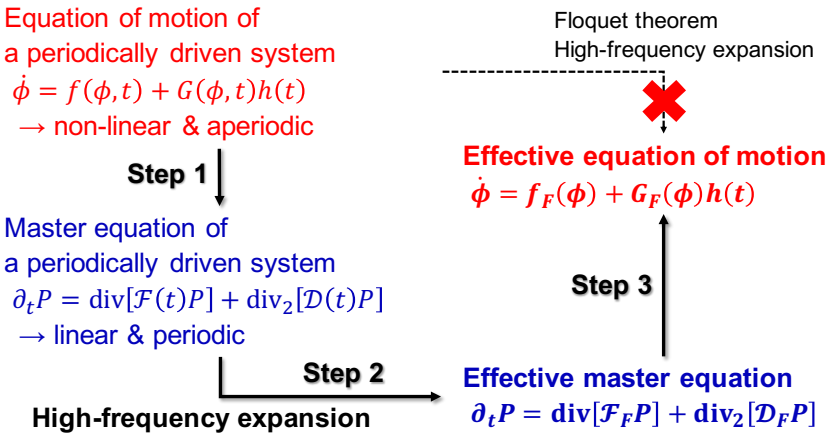

Figure 6.1: Procedure for performing the HFE of the classical EOM described by the stochastic differential equation (6.1). In the first step, we turn to the master equation (6.5) corresponding to Eq. (6.1), where we perform the HFE to obtain the effective master equation (6.24) in the second step. Finally, in the third step, we find a stochastic differential equation corresponding to Eq. (6.24).

$\mathcal{D} := \{\mathcal{D}_{ij}\}_{i,j=1}^{N}$, Eq. (6.5) can be rewritten in a compact form:

$$\partial_t P(\boldsymbol{\phi}, t) = \mathrm{div}\left(\boldsymbol{\mathcal{F}} P\right) + \mathrm{div}_2\left(\mathcal{D} P\right), \tag{6.9}$$

where the operator div_2 on a matrix $\mathcal{D}' = \{\mathcal{D}_{ij}(\boldsymbol{\phi})\}_{ij}$ is defined by $\mathrm{div}_2(\mathcal{D}') := (\partial^2 \mathcal{D}'_{ij})/(\partial\phi_i \partial\phi_j)$.

Finally, we comment on a Markov process on a discrete space. Its master equation is written in terms of the transition matrix $W_{ab}(t)$ as follows:

$$\frac{dp_a(t)}{dt} = \sum_b W_{ab}(t) p_b(t), \tag{6.10}$$

where $p_a(t)$ represents the probability of finding the system in state a at time t. Here, $W_{ab}(t)$ expresses the transition from the state b to the state a and satisfies the periodicity $W_{ab}(t+T) = W_{ab}(t)$. By introducing the vector $\boldsymbol{p}(t) := (p_1, p_2, \cdots, p_N)$ and the matrix $W := \{W_{ab}\}_{a,b=1}^{N}$ (N is the number of the states), we can rewrite Eq. (6.10) as follows:

$$\frac{d\boldsymbol{p}(t)}{dt} = W(t)\boldsymbol{p}(t). \tag{6.11}$$

6.1.2 High-frequency expansion of a master equation

As mentioned above, we cannot apply the Floquet theorem directly to classical EOMs because the original equation (6.1) is neither linear with respect to $\boldsymbol{\phi}$ nor time-periodic because of the presence of the random variable $h_j(t)$. However, we can apply it to its master equation (6.5) because it is linear with respect to P and time-periodic. Our strategy is summarized in Fig. 6.1. The HFE of an EOM is performed via that of the corresponding master equation.

By introducing the FP operator $\mathcal{L}_t$ defined by

$$\mathcal{L}_t(P) = \mathrm{div}\left[\boldsymbol{\mathcal{F}}(t) P\right] + \mathrm{div}_2\left[\mathcal{D}(t) P\right], \tag{6.12}$$

we can regard Eq. (6.5) as the "Schrödinger equation" driven by the non-Hermitian time-periodic "Hamiltonian" $H(t) := i\mathcal{L}_t$ [323]:

$$i\partial_t P = H(t)P, \tag{6.13}$$

where the probability distribution P plays the role of a wave function. In the case of a Markov process on a discrete space (6.11), $H(t)$ is related with the transition probability $W(t)$ as $H(t) := iW(t)$. We can formally solve Eq. (6.13) as $P(\boldsymbol{\phi}, t) = U(t, 0)P(\boldsymbol{\phi}, t = 0)$, where $U(t_2, t_1)$ is the time evolution operator from t_1 to t_2. From the Floquet-Lyapunov representation theorem [30, 31], $U(t_2, t_1)$ can be written in terms of the effective Hamiltonian H_F and the kick operators $\mathcal{G}_F(s)$ as follows [27, 110]:

$$U(t_2, t_1) := \mathcal{T}_t \exp\left[-i\int_{t_1}^{t_2} H(t)dt\right] = U_F^+(t_2)\mathrm{e}^{-i(t_2-t_1)H_F}U_F^-(t_1) = \mathrm{e}^{\mathcal{G}_F(t_2)}\mathrm{e}^{(t_2-t_1)\mathcal{L}_F}\mathrm{e}^{-\mathcal{G}_F(t_1)}, \tag{6.14}$$

where we introduce the effective FP operator $\mathcal{L}_F := -iH_F$ in the last equality. Note that the Floquet-Lyapunov representation theorem itself does not require the Hermiticity of $H(t)$ and hence can be applied to the above non-Hermitian Schrödinger equation.

For a fast drive, we can formally expand the effective FP operator $\mathcal{L}_F$ and the kick operator $\mathcal{G}_F$ in powers of ω^{-1} as follows:

$$\mathcal{L}_F = \sum_{m=0}^{\infty} \mathcal{L}_F^{(m)}, \quad \mathcal{G}_F(t) = \sum_{m=0}^{\infty} \mathcal{G}_F^{(m)}(t), \tag{6.15}$$

where $\mathcal{L}_F^{(m)} = \mathcal{O}(\omega^{-m})$ and $\mathcal{G}_F^{(m)}(t) = \mathcal{O}(\omega^{-m})$. Let us expand $\mathcal{L}_t$ and $H(t)$ in their Fourier harmonics as follows:

$$\mathcal{L}_t = \sum_m \mathcal{L}_m \mathrm{e}^{-im\omega t}, \quad H(t) = \sum_m H_m \mathrm{e}^{-im\omega t}, \tag{6.16}$$

where $\mathcal{L}_m = -iH_m$. Then, by substituting $\mathcal{L}_m = -iH_m$ in the vV HFE in quantum systems in Sec. 3.1, we obtain the HFEs of $\mathcal{L}_F$ and $\mathcal{G}_F(t)$. For example, the first three terms of $\mathcal{L}_F^{(m)}$ and those of $\mathcal{G}_F^{(m)}(t)$ are expressed to be

$$\mathcal{L}_F^{(0)} = -iH_F^{(0)} = \mathcal{L}_0, \tag{6.17}$$

$$\mathcal{L}_F^{(1)} = -iH_F^{(1)} = i\sum_{m\neq 0} \frac{[\mathcal{L}_{-m}, \mathcal{L}_m]}{2m\omega}, \tag{6.18}$$

$$\mathcal{L}_F^{(2)} = -iH_F^{(2)} = i^2 \sum_{m\neq 0} \left\{ \frac{[\mathcal{L}_{-m}, [\mathcal{L}_0, \mathcal{L}_m]]}{2(m\omega)^2} + \sum_{m'\neq 0,m} \frac{[\mathcal{L}_{-m'}, [\mathcal{L}_{m'-m}, \mathcal{L}_m]]}{3mm'\omega^2} \right\}, \tag{6.19}$$

$$\mathcal{G}_F^{(0)}(t) = 0, \tag{6.20}$$

$$\mathcal{G}_F^{(1)}(t) = -i\sum_{m\neq 0} \frac{\mathcal{L}_{-m}\mathrm{e}^{im\omega t}}{m\omega}, \tag{6.21}$$

$$\mathcal{G}_F^{(2)}(t) = i^2 \sum_{m\neq 0} \left\{ \frac{[\mathcal{L}_0, \mathcal{L}_{-m}]\, \mathrm{e}^{im\omega t}}{(m\omega)^2} + \sum_{m'\neq 0,m} \frac{[\mathcal{L}_{m'}, \mathcal{L}_{-m}]\, \mathrm{e}^{i(m-m')\omega t}}{2m(m-m')\omega^2} \right\}. \tag{6.22}$$

We note that the commutator $[\cdot,\cdot]$ is interpreted as that between operators:

$$[\mathcal{S}_1, \mathcal{S}_2](P) := \mathcal{S}_1[\mathcal{S}_2(P)] - \mathcal{S}_2[\mathcal{S}_1(P)]. \tag{6.23}$$

We further note that we have taken the convention $\int_0^T \mathcal{G}_F(t)dt = 0$ such that the effective FP operator becomes time-independent. If we focus on the averaged dynamics ignoring the kick operator $\mathcal{G}_F(t)$, the effective equation is given by the following static master equation:

$$\partial_t P = \mathcal{L}_F P \approx \sum_{m=0}^{m_0} \mathcal{L}_F^{(m)} P, \tag{6.24}$$

where m_0 is the truncation order. So far, we have focused only on the vV HFE. However, it is straightforward to generalize our analysis to other expansions like the FM HFE [114], the Brillouin-Wigner expansion [63], and the Floquet-Schriefer-Wolff transformation [74,77,78,324]. For example, for the FM HFE $\mathcal{L}_{F,t_0}^{(m)} := \sum_{m=0}^{\infty} \mathcal{L}_{F,t_0}^{(m)}$, the mth-order term $\mathcal{L}_{F,t_0}^{(m)}$ is given from Eqs. (3.19) and (3.20) as follows:

$$\mathcal{L}_{F,t_0}^{(0)} = \int_{t_0}^{t_0+T} dt\ \mathcal{L}_t, \tag{6.25}$$

$$\mathcal{L}_{F,t_0}^{(m)} = \sum_{\sigma\in S_m} \frac{(-1)^{m-\Theta_\sigma}\Theta_\sigma!(m-\Theta_\sigma)!}{(m+1)^2 m! T} \times \int_{t_0}^{t_0+T} dt_{m+1} \cdots \int_{t_0}^{t_0+t_2} dt_1 \left[\mathcal{L}'_{m+1}, [\mathcal{L}'_m, \cdots [\mathcal{L}'_2, \mathcal{L}'_1]]\right] \quad \text{for} \quad m \geq 1, \tag{6.26}$$

where $\mathcal{L}'_i := \mathcal{L}(t_{\sigma(i)})$.

To complete the procedure in Fig. 6.1, we must find an EOM whose master equation coincides with the truncated effective master equation obtained from the HFE (the step 3 in Fig. 6.1). For a Markov process on a discrete space, this can always be performed. However, this problem is, in general, nontrivial for a classical system described by a stochastic differential equation (6.1). If the effective master equation includes only up to the second-order derivative terms $\partial^2(\mathcal{D}_{ij}P)/(\partial\phi_i\partial\phi_j)$, we can find an EOM through Eqs. (6.6) and (6.7). This case includes several physically relevant situations, e.g., the cases where the diffusion is absent or time-independent. On the other hand, when the truncated HFE of a master equation contains derivatives higher than the second-order (e.g., $\partial^3(\widetilde{\mathcal{D}}_{ijk}P)/(\partial\phi_i\partial\phi_j\phi_k)$), the random variable h_j must be either non-Markovian or non-Gaussian [318–322]. It is unclear whether one can construct a modified stochastic differential equation even in this case, though several approximation schemes have been developed [261,325]. Finally, it is worth mentioning that an emergent non-Markov nature in the effective generator can also appear in a quantum system: the time evolution over one period of a time-periodic Lindblad equation is, in general, not generated by a Markovian generator but a generator with a memory kernel [326].

6.1.3 Deterministic system

We here consider the system without diffusions, i.e., $\mathcal{D} = 0$ and $h_j(t) = 0$. In this case, its EOM $\dot{\boldsymbol{\phi}} = \boldsymbol{f}(\boldsymbol{\phi}, t)$ can be regarded as a flow equation generated by $\boldsymbol{f}(\boldsymbol{\phi}, t)$. Let $\boldsymbol{f}_m$ be the mth-order Fourier harmonics of $\boldsymbol{f}(\boldsymbol{\phi}, t)$: $\boldsymbol{f}(\boldsymbol{\phi}, t) = \sum_m \boldsymbol{f}_m \mathrm{e}^{-im\omega t}$. Then, $\mathcal{L}_m$ is written as $\mathcal{L}_m(P) := -\mathrm{div}(\boldsymbol{f}_m P)$, and the commutator $[\mathcal{L}_m, \mathcal{L}_n]$ is given by

$$\begin{aligned}[\mathcal{L}_m, \mathcal{L}_n](P) &= \mathrm{div}\left[\boldsymbol{f}_m \mathrm{div}(\boldsymbol{f}_n P)\right] - \mathrm{div}\left[\boldsymbol{f}_n \mathrm{div}(\boldsymbol{f}_m P)\right] \\ &= \mathrm{div}\left\{\left[(\boldsymbol{f}_m \cdot \nabla)\boldsymbol{f}_n - (\boldsymbol{f}_n \cdot \nabla)\boldsymbol{f}_m\right] P\right\} = -\mathrm{div}\left(-\left[\boldsymbol{f}_m, \boldsymbol{f}_n\right]_{\mathrm{cl}} P\right). \end{aligned} \tag{6.27}$$

Here the commutator $[\boldsymbol{A}, \boldsymbol{B}]_{\mathrm{cl}}$ between two vector fields $\boldsymbol{A}$ and $\boldsymbol{B}$ is defined by

$$[\boldsymbol{A}, \boldsymbol{B}]_{\mathrm{cl},j} = (\boldsymbol{A} \cdot \nabla) B_j - (\boldsymbol{B} \cdot \nabla) A_j := A_i \frac{\partial B_j}{\partial \phi_i} - B_i \frac{\partial A_j}{\partial \phi_i}, \tag{6.28}$$

which is called the Lie bracket in mathematics. It is clear from Eq. (6.27) that the operators of the form $\mathcal{L} := \mathrm{div}(\boldsymbol{f}\cdot)$ is closed with respect to the commutator (6.23), and thereby the effective dynamics is described by the renormalized drift force $\boldsymbol{f}_F$. The mth-order vV HFE $\boldsymbol{f}_F^{(m)}$ of the drift field is obtained from $H_F^{(m)}$ by replacing the commutator $[H_m, H_n]$ between Hamiltonians with that $[\boldsymbol{f}_m, \boldsymbol{f}_n]_{\mathrm{cl}}$ between drift fields, followed by the multiplication by i^m. Then, the resulting effective EOM up to the second order in ω^{-1} is given by

$$\begin{aligned}\dot{\boldsymbol{\phi}} &= \boldsymbol{f}_F(\boldsymbol{\phi}) \\ &= \boldsymbol{f}_0(\boldsymbol{\phi}) + i\sum_{m\neq 0} \frac{[\boldsymbol{f}_{-m}, \boldsymbol{f}_m]_{\mathrm{cl}}}{2m\omega} - \sum_{m\neq 0}\left\{ \frac{[\boldsymbol{f}_{-m}, [\boldsymbol{f}_0, \boldsymbol{f}_m]_{\mathrm{cl}}]_{\mathrm{cl}}}{2(m\omega)^2} + \sum_{m'\neq 0,m} \frac{[\boldsymbol{f}_{-m'}, [\boldsymbol{f}_{m'-m}, \boldsymbol{f}_m]_{\mathrm{cl}}]_{\mathrm{cl}}}{3mm'\omega^2} \right\}. \end{aligned} \tag{6.29}$$

This result is consistent with the Magnus expansion of general non-autonomous (not necessarily time-periodic) ordinary differential equation $\dot{\boldsymbol{\phi}} = \boldsymbol{f}(\boldsymbol{\phi}, t)$ [189, 327–329].

As a special case, if the dynamics is governed by some classical Hamiltonian $H(t)$, the drift field $\boldsymbol{f}(t)$ and the commutator $[\cdot,\cdot]_{\mathrm{cl}}$ are replaced by the Hamilton flow and the Poisson bracket $-\{\cdot,\cdot\}$, respectively. The master equation (6.5) is nothing but the Liouville equation. Let $\boldsymbol{q}$ and $\boldsymbol{p}$ be a canonical conjugate pair. Then, the classical variable $\boldsymbol{\phi}$ and $\boldsymbol{f}_m$ are given by

$$\boldsymbol{\phi} = (\boldsymbol{q}, \boldsymbol{p}), \quad \boldsymbol{f}_m = \left(\frac{\partial H_m}{\partial \boldsymbol{p}}, -\frac{\partial H_m}{\partial \boldsymbol{q}}\right). \tag{6.30}$$

By a straightforward calculation, we obtain

$$[\boldsymbol{f}_m, \boldsymbol{f}_n]_{\mathrm{cl}} = -\left(\frac{\partial\{H_m, H_n\}}{\partial \boldsymbol{p}}, -\frac{\partial\{H_m, H_n\}}{\partial \boldsymbol{q}}\right). \tag{6.31}$$

The above results correctly reproduce the previous ones for periodically driven isolated Hamilton systems [27, 117, 198] and are consistent with the Magnus expansion of general time-dependent (not necessarily time-periodic) Hamilton systems [330–332].

6.1.4 Time-independent diffusion

We here assume that the diffusion matrix G and hence $\mathcal{D}$ are time-independent and $\mathcal{L}_m$ is given by

$$\mathcal{L}_0(P) := \mathrm{div}\left(\boldsymbol{\mathcal{F}}_0 P\right) + \mathrm{div}_2\left[\mathcal{D}P\right], \quad \mathcal{L}_m(P) := \mathrm{div}\left(\boldsymbol{\mathcal{F}}_m P\right) \quad \text{for} \quad m \neq 0, \tag{6.32}$$

where $\boldsymbol{\mathcal{F}}_m$ is the mth-order Fourier harmonics of $\boldsymbol{\mathcal{F}}(t)$. Under this assumption, one can always find the effective EOM corresponding to the effective FP operator $\mathcal{L}_F$ if we truncate at the second order.

First-order perturbation

From Eq. (6.22), the first-order vV HFE is obtained to be

$$\mathcal{L}_F^{(1)} := i\sum_{m\neq 0}\frac{[\mathcal{L}_{-m}, \mathcal{L}_m]}{2m\omega} = \mathrm{div}\left[\boldsymbol{\mathcal{F}}_F^{(1)}\cdot\right], \tag{6.33}$$

$$\boldsymbol{\mathcal{F}}_F^{(1)} := \sum_{m\neq 0}\frac{i}{2m\omega}\left[\left(\boldsymbol{\mathcal{F}}_{-m}\cdot\nabla\right)\boldsymbol{\mathcal{F}}_m - \left(\boldsymbol{\mathcal{F}}_m\cdot\nabla\right)\boldsymbol{\mathcal{F}}_{-m}\right] = \sum_{m\neq 0}\frac{i}{2m\omega}\left[\left(\boldsymbol{f}_{-m}\cdot\nabla\right)\boldsymbol{f}_m - \left(\boldsymbol{f}_m\cdot\nabla\right)\boldsymbol{f}_{-m}\right], \tag{6.34}$$

where the effective FP operator is given by

$$\mathcal{L}_F(P) = \mathrm{div}\left[(\boldsymbol{\mathcal{F}}_0 + \boldsymbol{\mathcal{F}}_F^{(1)})P\right] + \mathrm{div}_2(\mathcal{D}P). \tag{6.35}$$

A crucial observation here is that only the drift field is normalized; then the EOM corresponding to the Fokker-Planch operator (6.35) is obtained to be

$$\dot{\boldsymbol{\phi}} = \boldsymbol{f}_F(\boldsymbol{\phi}) + G(\boldsymbol{\phi})h(t). \tag{6.36}$$

Here $\boldsymbol{f}_F$ is the renormalized drift term:

$$\boldsymbol{f}_F := \boldsymbol{f}_0 + \sum_{m\neq 0}\frac{i}{2m\omega}\left[(\boldsymbol{f}_m\cdot\nabla)\boldsymbol{f}_{-m} - (\boldsymbol{f}_{-m}\cdot\nabla)\boldsymbol{f}_m\right]. \tag{6.37}$$

The time evolution without the kick operator is obtained by solving Eq. (6.36). Notably, if $\boldsymbol{f}_F$ represents the potential force of some potential $V_F(\boldsymbol{\phi})$ and the environment satisfies the detailed-balance condition at temperature T_{te}, the NESS is a canonical distribution $P(\boldsymbol{\phi}) \propto \exp\left[-V_F(\boldsymbol{\phi})/T_{\mathrm{te}}\right]$ of the potential $V_F(\boldsymbol{\phi})$.

The time evolution with the kick operator is calculated from three steps corresponding to the three exponential operators $\exp\left[-\mathcal{G}_F(t_1)\right]$, $\exp\left[(t_2-t_1)\mathcal{L}_F\right]$, and $\exp\left[\mathcal{G}_F(t_2)\right]$, as shown in Eq. (6.14). Let us first consider the effect of the kick operators on the EOM. The kick operator $\mathcal{G}_F^{(1)}(s)$, with s $(= t_1, t_2)$ being either the initial- or final-kick time, is given from Eq. (6.22) as

$$\mathcal{G}_F^{(1)}(s) = -\frac{1}{\omega}\mathrm{div}\left[\boldsymbol{f}_{F,\mathrm{mic}}^{(1)}(\boldsymbol{\phi}, s)\ \cdot\ \right], \tag{6.38}$$

where $\boldsymbol{f}^{(1)}_{F,\mathrm{mic}}$ is the oscillating drift field:

$$\boldsymbol{f}^{(1)}_{F,\mathrm{mic}}(\boldsymbol{\phi}, s) = -i \sum_{m\neq 0} \frac{\boldsymbol{f}_{-m} \mathrm{e}^{i\omega s}}{2m}. \tag{6.39}$$

From Eq. (6.39) and the definition of an exponential operator, $\exp\left[\pm\mathcal{G}_F(s)\right] P_0(\boldsymbol{\phi})$ is formally the solution of the master equation

$$\frac{\partial P(\boldsymbol{\phi},\tau)}{\partial \tau} = \mp \mathrm{div}\left[\boldsymbol{f}^{(1)}_{F,\mathrm{mic}}(\boldsymbol{\phi}, s) P(\boldsymbol{\phi},\tau)\right], \quad P(\boldsymbol{\phi}, \tau = 0) = P_0(\boldsymbol{\phi}), \tag{6.40}$$

at time $\tau = 1/\omega$. Thus, the exponential $\exp\left[\pm\mathcal{G}_F(s)\right]$ has the following physical interpretation: it is the integration of the flow field $\boldsymbol{f}^{(1)}_{F,\mathrm{mic}}$ from $\tau = 0$ to $\tau = 1/\omega$, where τ is an auxiliary time for calculating the kicks and $1/\omega$ is the duration of the kick. Since the above equation does not contain the diffusion term, plugging $P_0(\boldsymbol{\phi}_{\mathrm{kick}}) = \delta(\boldsymbol{\phi}_{\mathrm{kick}} - \boldsymbol{\phi}_0)$ into Eq. (6.40), we rewrite it into the equation for $\boldsymbol{\phi}_{\mathrm{kick}}$:

$$\frac{d\boldsymbol{\phi}_{\mathrm{kick}}}{d\tau} = \pm \boldsymbol{f}^{(1)}_{F,\mathrm{mic}}(\boldsymbol{\phi}_{\mathrm{kick}}, s), \quad \boldsymbol{\phi}_{\mathrm{kick}}(\tau = 0) = \boldsymbol{\phi}_0. \tag{6.41}$$

Thus, $\boldsymbol{\phi}_0$ is mapped to the solution of Eq. (6.41) at time $\tau = 1/\omega$ by the kick operators $\exp\left[\pm\mathcal{G}_F(s)\right]$. Note that Eqs. (6.40) and (6.41) are autonomous equations, i.e., they do not explicitly depend on the time τ. Practically, because of the smallness of the integration time $1/\omega$, the solution $\boldsymbol{\phi}_{\mathrm{kick}}(\tau = 1/\omega)$ is well approximated by the Euler method:

$$\boldsymbol{\phi}_{\mathrm{kick}}\left(\tau = \frac{1}{\omega}\right) \approx \boldsymbol{\phi}_0 \pm \frac{\boldsymbol{f}^{(1)}_{F,\mathrm{mic}}(\boldsymbol{\phi}_0, s)}{\omega}. \tag{6.42}$$

From the above discussions, the time evolution operator $U(t_2, t_1) = \mathrm{e}^{\mathcal{G}_F(t_2)} \mathrm{e}^{(t_2 - t_1)\mathcal{L}_F} \mathrm{e}^{-\mathcal{G}_F(t_1)}$ is calculated as follows: Let $\boldsymbol{\phi}_0$ be the initial state of $\boldsymbol{\phi}$. First, to calculate the effect of the initial kick $\exp\left[-\mathcal{G}_F(t_1)\right]$, we integrate Eq. (6.41) with the minus sign on the right-hand side and $s = t_1$ for initial condition $\boldsymbol{\phi}_0$:

$$\frac{d\boldsymbol{\phi}_{\mathrm{kick}}}{d\tau} = -\boldsymbol{f}^{(1)}_{F,\mathrm{mic}}(\boldsymbol{\phi}_{\mathrm{kick}}, t_1), \quad \boldsymbol{\phi}_{\mathrm{kick}}(\tau = 0) = \boldsymbol{\phi}_0. \tag{6.43}$$

The solution at time $\tau = 1/\omega$ gives the state after the initial kick, which we write as $\boldsymbol{\phi}_1$: $\boldsymbol{\phi}_1 := \boldsymbol{\phi}_{\mathrm{kick}}(\tau = 1/\omega)$. Next, we evaluate the effective dynamics $\exp\left[(t_2 - t_1)\mathcal{L}_F\right]$ by integrating Eq. (6.37) from within time $(t_2 - t_1)$ with the initial state is taken as $\boldsymbol{\phi}_1$:

$$\frac{d\boldsymbol{\phi}}{dt} = \boldsymbol{f}_F(\boldsymbol{\phi}) + G(\boldsymbol{\phi}) h(t), \quad \boldsymbol{\phi}(t = 0) = \boldsymbol{\phi}_1. \tag{6.44}$$

The solution at $t = t_2 - t_1$ gives the state after the effective flow $\mathcal{L}_F$, which we write as $\boldsymbol{\phi}_2$: $\boldsymbol{\phi}_2 := \boldsymbol{\phi}(t = t_2 - t_1)$. Finally, we integrate Eq. (6.41) with the plus sign on the right-hand side and $s = t_2$ up to time $1/\omega$ for the initial condition $\boldsymbol{\phi}_2$, and calculate the final kick $\exp\left[\mathcal{G}_F(t_2)\right]$:

$$\frac{d\boldsymbol{\phi}_{\mathrm{kick}}}{d\tau} = \boldsymbol{f}^{(1)}_{F,\mathrm{mic}}(\boldsymbol{\phi}_{\mathrm{kick}}, t_2), \quad \boldsymbol{\phi}_{\mathrm{kick}}(\tau = 0) = \boldsymbol{\phi}_2. \tag{6.45}$$

Then, the solution $\boldsymbol{\phi}_3 = \boldsymbol{\phi}_{\rm kick}(\tau = 1/\omega)$ gives the state after the final kick, and hence the state applied by the three operators $\mathrm{e}^{-\mathcal{G}_F(t_1)}$, $\mathrm{e}^{(t_2-t_1)\mathcal{L}_F}$, and $\mathrm{e}^{\mathcal{G}_F(t_2)}$ to the initial state $\boldsymbol{\phi}_0$.

Second-order perturbation

In the calculation at the second order, there appears the commutator between $\mathcal{L}(P) = \mathrm{div}(\boldsymbol{\mathcal{F}}P) + \mathrm{div}_2(\mathcal{D}P)$ and $\mathcal{L}'(P) = \mathrm{div}(\boldsymbol{\mathcal{F}}'P)$, which is calculated as follows:

$$[\mathcal{L}, \mathcal{L}'](P) = \mathrm{div}\left[\boldsymbol{\mathcal{F}}\mathrm{div}(\boldsymbol{\mathcal{F}}'P)\right] - \mathrm{div}\left[\boldsymbol{\mathcal{F}}'\mathrm{div}(\boldsymbol{\mathcal{F}}P)\right] + \mathrm{div}_2\left[\mathcal{D}\mathrm{div}(\boldsymbol{\mathcal{F}}'P)\right] - \mathrm{div}\left[\boldsymbol{\mathcal{F}}'\mathrm{div}_2(\mathcal{D}P)\right] \tag{6.46}$$

$$=: \mathrm{div}\left[\mathrm{drf}(\boldsymbol{\mathcal{F}}, \boldsymbol{\mathcal{F}}', \mathcal{D})P\right] + \mathrm{div}_2\left[\mathrm{diff}(\boldsymbol{\mathcal{F}}', \mathcal{D})P\right], \tag{6.47}$$

where the corresponding drift field $\mathrm{drf}(\boldsymbol{\mathcal{F}}, \boldsymbol{\mathcal{F}}', \mathcal{D}) := \{\mathrm{drf}_i(\boldsymbol{\mathcal{F}}, \boldsymbol{\mathcal{F}}', \mathcal{D})\}_{i=1}^N$ and the diffusion matrix $\mathrm{diff}(\boldsymbol{\mathcal{F}}', \mathcal{D}) = \{\mathrm{diff}_{ij}(\boldsymbol{\mathcal{F}}', \mathcal{D})\}_{i,j=1}^N$ are given by

$$\mathrm{drf}_i(\boldsymbol{\mathcal{F}}, \boldsymbol{\mathcal{F}}', \mathcal{D}) = (\boldsymbol{\mathcal{F}} \cdot \nabla)\mathcal{F}'_i - (\boldsymbol{\mathcal{F}}' \cdot \nabla)\mathcal{F}_i - \frac{\partial^2 \mathcal{F}'_i}{\partial\phi_j \partial\phi_k}\mathcal{D}_{jk}, \tag{6.48}$$

$$\mathrm{diff}_{ij}(\boldsymbol{\mathcal{F}}', \mathcal{D}) = \frac{\partial \mathcal{F}'_i}{\partial\phi_k}\mathcal{D}_{kj} + \frac{\partial \mathcal{F}'_j}{\partial\phi_k}\mathcal{D}_{ki} - \mathcal{F}'_k\frac{\partial \mathcal{D}_{ij}}{\partial\phi_k}. \tag{6.49}$$

The second-order term $\mathcal{L}_F^{(2)}$ is given by

$$\mathcal{L}_F^{(2)}(P) = \mathrm{div}(\boldsymbol{\mathcal{F}}_F^{(2)}P) + \mathrm{div}_2(\mathcal{D}_F^{(2)}P), \tag{6.50}$$

$$\boldsymbol{\mathcal{F}}_F^{(2)} := \sum_{m\neq 0}\left\{\frac{\mathrm{drf}\left[\mathrm{drf}\left[\boldsymbol{\mathcal{F}}_0, \boldsymbol{\mathcal{F}}_m, \mathcal{D}\right], \boldsymbol{\mathcal{F}}_{-m}, \mathcal{D}\right]}{2(m\omega)^2} + \sum_{m'\neq 0,m}\frac{-\left[\boldsymbol{\mathcal{F}}_{-m'}, \left[\boldsymbol{\mathcal{F}}_{m-m'}, \boldsymbol{\mathcal{F}}_m\right]_{\rm cl}\right]_{\rm cl}}{3mm'\omega^2}\right\}, \tag{6.51}$$

$$\mathcal{D}_F^{(2)} := \sum_{m\neq 0}\frac{\mathrm{diff}\left[\boldsymbol{\mathcal{F}}_{-m}, \mathrm{diff}\left(\boldsymbol{\mathcal{F}}_m, \mathcal{D}\right)\right]}{2(m\omega)^2}, \tag{6.52}$$

which indicates that not only the drift vector but also the diffusion matrix is renormalized at the second order. The kick operator $\mathcal{G}_F^{(2)}$ is given by

$$\mathcal{G}_F^{(2)}(t) = \mathrm{div}(\boldsymbol{\mathcal{F}}_{F,\rm mic}^{(2)}\,\cdot) + \mathrm{div}_2(\mathcal{D}_{F,\rm mic}^{(2)}\,\cdot), \tag{6.53}$$

$$\boldsymbol{\mathcal{F}}_{F,\rm mic}^{(2)} = -\sum_{m\neq 0}\left\{\frac{\mathrm{drf}\left[\boldsymbol{\mathcal{F}}_0, \boldsymbol{\mathcal{F}}_{-m}, \mathcal{D}\right]\mathrm{e}^{im\omega t}}{(m\omega)^2} + \sum_{m'\neq 0,m}\frac{\left[\boldsymbol{\mathcal{F}}_{m'}, \boldsymbol{\mathcal{F}}_{-m}\right]_{\rm cl}\mathrm{e}^{i(m-m')\omega t}}{2m(m-m')\omega^2}\right\}, \tag{6.54}$$

$$\mathcal{D}_{F,\rm mic}^{(2)} = -\sum_{m\neq 0}\frac{\mathrm{diff}\left[\boldsymbol{\mathcal{F}}_{-m}, \mathcal{D}\right]\mathrm{e}^{im\omega t}}{(m\omega)^2}. \tag{6.55}$$

In this case, the renormalized drift field $\boldsymbol{f}_F$ and the diffusion matrix G_F are determined from Eqs. (6.6) and (6.7). For a semi-positive matrix $\mathcal{D}_F$, the diffusion matrix G_F is uniquely determined from Eq. (6.7) up to the multiplication of an orthogonal matrix O and $\boldsymbol{f}_F$ is determined from $\mathcal{F}_F$ and G_F as shown in Eq. (6.6). Note that the ambiguity with O does not matter to the statistics of the random field $\boldsymbol{h}(t)$ (see Eq. (4.8)).

6.2 Validity and convergence of the high-frequency expansion

Mathematically, the FM HFE of a master equation is guaranteed to converge if its FP operator $\mathcal{L}_t$ satisfies

$$\int_0^T dt \|\mathcal{L}_t\| \leq \zeta, \tag{6.56}$$

where $\|\cdot\|$ is the operator norm and $\zeta = \mathcal{O}(1)$ is a universal constant [189]. There are two problems on applying the bound (6.56) to classical systems. First, $\|\mathcal{L}_t\|$ and hence the left-hand side of Eq. (6.56) grows linearly with a system size for a many-body system. Secondly, $\mathcal{L}_t$ usually contains unbounded operators like a derivative operator ∂_{ϕ_i}. Although these two problems make it hard to discuss rigorously the validity and the convergence of the FM HFE in a general classical system, the HFE is found to be valid for non-chaotic few-body systems and generic many-body systems as we will see below.

Before analyzing general cases, we comment on some exceptional cases in classical systems where the second problem does not appear, where a rigorous discussion is available using the techniques developed in an isolated quantum system [95,96]. An important example is a Markov process on a discrete state space described by Eq. (6.10). Since the dimension of the state space is finite, the transition matrix $W(t)$ in Eq. (6.10) is a finite-dimensional matrix constituted from bounded operators. For the FM HFE $\Omega_F = \sum_{m=0}^{\infty} \Omega_F^{(m)}$ of $W(t)$ (the subscript t_0 representing the initial time is omitted for simplicity), we can show that $\Omega_F^{(m)}$ is, at least asymptotically, convergent up to the order $m_0 \sim \omega/(gk)$:

$$\|\Omega_F^{(m)} - \Omega_F^{(m_0)}\| \leq N\mathcal{O}\left[(2gkT)^m\right] \quad \text{for} \quad m \leq m_0, \tag{6.57}$$

and that the exact steady state Π_{SS} is well approximated by the steady state $\Pi_{\mathrm{SS}}^{(m_0)}$ obtained from the m_0th-order truncated FM HFE:

$$\frac{1}{N}\|\Pi_{\mathrm{SS}} - \Pi_{\mathrm{SS}}^{(m_0)}\| \leq \mathcal{O}\left[(g\tau)^2 k 2^{-m_0}\right]. \tag{6.58}$$

Here, g, N, τ, and k are the maximum transition rate per site, the number of sites, the relaxation timescale to the steady state, and the number of sites associated with the interaction, respectively. See App. B.1 for the detail of the statement and its derivation.

6.2.1 Few-body system

For a few-body systems, where the only second problem arises, the HFE is expected to be convergent for a non-chaotic system, typically for a weakly driven system under strong dissipation. In this system, $\mathcal{L}_t$ is expected to be a Lyapunov continuous:

$$|\mathcal{L}_t P_0 - \mathcal{L}_t P_0'| \leq C_t |P_0 - P_0'|, \tag{6.59}$$

where P_0 and P_0' are some probability distributions, and C_t is some constant independent of ω. Therefore, when ω is sufficiently large such that $\omega \geq (2\pi \max_{0\leq t\leq T} C_t)/\zeta$, we have

$$\int_0^T dt \|\mathcal{L}_t\| \leq T \max_{0\leq t\leq T} C_t \leq \zeta. \tag{6.60}$$

Thus, Eq. (6.56) is satisfied. The above discussions is consistent with the previous studies on the chaos and the bifurcation in periodically driven systems [333–336].

On the other band, the HFE is useless for predicting the long-time behavior of a chaotic system irrespective to whether it is convergent or not. Let $L_{\rm TR}^{(m_0)}$ and P_0 be the truncated FM HFE with truncation order m_0 and some initial probability distribution, respectively. Then, two probability distributions at time t with different truncation orders m_0' and $\widetilde{m}_0$, i.e., $\exp(L_{\rm TR}^{(m_0')}t)P_0$ and $\exp(L_{\rm TR}^{(\widetilde{m}_0)}t)P_0$, are quite different for large t because of the onset of chaotic nature. This indicates that the time evolution strongly depends on the truncation order m_0 and that the FM HFE is useless.

6.2.2 Many-body system: preliminaries and statements

In a general classical many-body system, there appear both problems; the extensiveness of $\|\mathcal{L}_t\|$ and the presence of unbounded operators. Although the first problem appears even in interacting quantum spin or fermionic systems, rigorous results on the energy absorption and the existence of the Floquet prethermal states are obtained by fully utilizing the boundedness of their local operators [95,96,98,209]. On the other hand, it is quite hard to obtain a similar bound on the classical systems because unbounded operators are notoriously difficult to handle even in mathematics. Nevertheless, as we will see below, we can estimate the higher-order terms in the FM HFE by combining the dimensional analysis with the techniques developed in quantum systems [95,96]. We note that such a general discussion is hard to obtain within the framework of the multi-scale perturbation theory [248, 249] because its calculation becomes involved even in low orders. From this analysis, we argue that the FM HFE is, at least asymptotically, convergent. Moreover, its truncated series is found to well describe the steady state for a generic many-body system, e.g., a prethermal state for an isolated system and a NESS for a driven dissipative system.

Consider a generic (non-integrable) many-body system, which is described by a classical field $\boldsymbol{\phi}_{\boldsymbol{r}}$ obeying the EOM (6.2). We assume that the drift field $\boldsymbol{f}_{\boldsymbol{r}}$ and the diffusion matrix $G_{\boldsymbol{r}}$ depend on the fields $\boldsymbol{\phi}_{\boldsymbol{r}'}$ on, at most, k neighboring sites of $\boldsymbol{r}$. That is, the interaction and diffusion are, at most, k-body. We introduce a dimensionless field $\widetilde{\boldsymbol{\phi}}_{\boldsymbol{r}} := (\boldsymbol{\phi}_{\boldsymbol{r},1}/\phi_{0,1}, \boldsymbol{\phi}_{\boldsymbol{r},2}/\phi_{0,2}, \cdots \boldsymbol{\phi}_{\boldsymbol{r},N_I}/\phi_{0,N_I})$, with $\phi_{0,i}$ being the typical magnitude of $\boldsymbol{\phi}_{\boldsymbol{r},i}$, and rescale the random fields $\widetilde{\boldsymbol{h}}_{\boldsymbol{r}} := \boldsymbol{h}_{\boldsymbol{r}}/\sqrt{D}$. For example, for the GP equation (6.3), the typical magnitude of $\psi_{\boldsymbol{r}}$ is $\sqrt{\rho_0}$, with ρ_0 being the average density of a condensate. Then, the rescaled EOM is given by $d\widetilde{\boldsymbol{\phi}}_{\boldsymbol{r}}/dt = \widetilde{\boldsymbol{f}}_{\boldsymbol{r}} + \widetilde{G}_{\boldsymbol{r}}\widetilde{\boldsymbol{h}}_{\boldsymbol{r}}$, where $\widetilde{\boldsymbol{f}}_{\boldsymbol{r}}$ and $\widetilde{G}_{\boldsymbol{r}}$ are the rescaled drift field and diffusion matrix, respectively. The corresponding master equation is given by

$$\frac{\partial P}{\partial t} = \sum_{\boldsymbol{r}} \left[\frac{\partial}{\partial \widetilde{\phi}_{\boldsymbol{r},a}} \left(\widetilde{\mathcal{F}}_{\boldsymbol{r},a} P \right) + \frac{\partial^2}{\partial \widetilde{\phi}_{\boldsymbol{r},a} \partial \widetilde{\phi}_{\boldsymbol{r},b}} \left(\widetilde{\mathcal{D}}_{ab} P \right) \right] =: \sum_{\boldsymbol{r}} \hat{L}_{\boldsymbol{r}}(t) P, \tag{6.61}$$

where the local operator $\hat{L}_{\boldsymbol{r}}(t)$ acts on, at most, k neighboring sites of $\boldsymbol{r}$. More generally, we

define the locality of the operator as follows: an operator $A := \sum_{\boldsymbol{r}} A_{\boldsymbol{r}}$ is said to be k_A-local if $A_{\boldsymbol{r}}$ depends on the fields on, at most, k_A neighboring sites of $\boldsymbol{r}$. According to this definition, the FP operator $\hat{L}(t) := \sum_{\boldsymbol{r}} \hat{L}_{\boldsymbol{r}}(t)$ is a k-local operator. Note that a similar discussion holds for a Markov process on a discrete space with a translationally invariance because its master equation takes the form of Eq. (6.61). Since $\widetilde{\phi}_{\boldsymbol{r}}$ is dimensionless, $\hat{L}_{\boldsymbol{r}}(t)$ has the physical dimension of frequency, where we write its typical magnitude as ω_0. Formally, the time evolution operator $U(t,0)$ of Eq. (6.61) is given by the Dyson series:

$$U(t,0) = \sum_{m=0}^{\infty} \frac{1}{m!} \int_0^t dt_1 \cdots \int_0^t dt_m \mathcal{T}_t \left[\hat{L}(t_1) \cdots \hat{L}(t_m) \right] = \mathcal{T}_t \exp\left[\int_0^t \hat{L}(t') dt' \right]. \tag{6.62}$$

Then, the exponent $\Omega(t)$ defined by $U(t,0) =: \exp[\Omega(t)]$ satisfies the following differential relation [189]:

$$\frac{d\Omega(t)}{dt} = \sum_{m=0}^{\infty} \frac{B_m}{m!} \mathrm{ad}^m_{\Omega(t)} \hat{L}(t), \tag{6.63}$$

where $\mathrm{ad}_{\Omega} \hat{L} := \left[\Omega, \hat{L} \right]$ and B_m is the mth Bernoulli number.

Let us formally expand the effective operator $\Omega_F := \Omega(T)$ in powers of ω^{-1} as follows:

$$\Omega_F = \sum_{m=0}^{\infty} \Omega_F^{(m)}, \tag{6.64}$$

where $\Omega_F^{(m)} = \mathcal{O}(\omega^{-m})$. The FM HFE of the effective FP operator $\hat{L}_F := \Omega_F / T$ is obtained by iteratively substituting Eq. (6.64) into Eq. (6.63) followed by the integration of t over one period. We denote the mth-order truncated series of Ω_F as $\Omega_{\mathrm{TR}}^{(m)}$ and the time evolution operator generated by it as $U^{(m)}(t)$:

$$\Omega_{\mathrm{TR}}^{(m)} := \sum_{m'=0}^{m} \Omega_F^{(m')}, \quad U^{(m)}(t) := \exp\left[\frac{t \Omega_{\mathrm{TR}}^{(m)}}{T} \right]. \tag{6.65}$$

If this formal expansion converges, the exact time evolution $U(t,0)$ is well approximated by $U^{(m)}(t)$. For a generic many-body system, because of the non-integrability of the system, the system equilibrates with some typical timescales, which we denote by τ. Then, the two steady states $P_{SS}^{(m)} := U^{(m)}(t) P_0$ and $P_{SS} := U(t,0) P_0$ with $t \gg \tau$ do not depend on an initial probability distribution P_0. We note that τ defines the timescale of the initial equilibration to the Floquet prethermalization for an isolated system and that of the relaxation to a NESS for a driven dissipative system.

In what follows, we will claim the following two statements based on the evaluation of $\Omega_F^{(m)}$. We assume that the driving frequency ω is much larger than $k\omega_0$. (i) The formal expansion (6.64), at least asymptotically, converges up to the order $m = m_0 \approx \omega/(k\omega_0)$:

$$\left| \Omega_{\mathrm{TR}}^{(m)} - \Omega_{\mathrm{TR}}^{(m_0)} \right| = \mathcal{O}\left[(k\omega_0/\omega)^{m_0+1} \right] \quad \text{for} \quad m \le m_0. \tag{6.66}$$

(ii) The exact steady state P_{SS} is well approximated by the steady state $P_{SS}^{(m_0)}$ obtained from

the truncated FM HFE (6.65):

$$P_{SS}^{(m_0)} \approx P_{SS}. \tag{6.67}$$

6.2.3 Many-body system: derivation

The mth-order term $\Omega_F^{(m)}$ with $m \geq 1$ is given from the FM HFE in Eq. (6.26) as follows:

$$\Omega_F^{(m)} = \sum_{\sigma \in S_m} \frac{(-1)^{m-\Theta_\sigma}\Theta_\sigma!(m-\Theta_\sigma)!}{(m+1)^2 m!} \int_0^T dt_{m+1} \cdots \int_0^{t_2} dt_1 \mathrm{ad}_{\hat{L}_{m+1}} \mathrm{ad}_{\hat{L}_m} \cdots \mathrm{ad}_{\hat{L}_2} \hat{L}_1, \tag{6.68}$$

where $\hat{L}_i := \hat{L}(t_{\sigma(i)})$ and the initial time t_0 in Eq. (6.26) is taken to be zero.

The typical magnitude of the commutator in Eq. (6.68) is estimated from the locality of $\hat{L}_{\boldsymbol{r}}$ as follows. Consider two operators $A = \sum_{\boldsymbol{r}} A_{\boldsymbol{r}}$ and $B = \sum_{\boldsymbol{r}} B_{\boldsymbol{r}}$, where $A_{\boldsymbol{r}}$ ($B_{\boldsymbol{r}}$) depends on the fields on, at most, k_A (k_B) neighboring sites and its typical magnitude is denoted as g_A (g_B). Their commutator $[A, B] =: \sum_{\boldsymbol{r}} C_{\boldsymbol{r}}$ is $(k_A + k_B)$-local and the typical magnitude of $C_{\boldsymbol{r}}$ is given by $(k_A + k_B) g_A g_B$. Therefore, the m-fold commutator in Eq. (6.68) is $(m+1)k$-local and its typical magnitude is estimated as follows:

$$\mathrm{ad}_{\hat{L}_{m+1}} \mathrm{ad}_{\hat{L}_m} \cdots \mathrm{ad}_{\hat{L}_2} \hat{L}_1 = \mathcal{O}\left[N(\omega_0 k)^{m+1}(m+1)!\right], \tag{6.69}$$

where N is the number of sites. Combining Eq. (6.69) with the inequality $(-1)^{m-\Theta_\sigma}\Theta_\sigma!(m-\Theta_\sigma)! \leq m!/2^m$, we obtain

$$|\Omega_F^{(m)}| \lesssim m! \times \frac{1}{(m+1)^2 m!} \times \frac{m!}{2^m} \times \frac{T^{m+1}}{(m+1)!} \times (\omega_0 k)^{m+1}(m+1)! N = \frac{N m!}{(m+1)^2} \left(\frac{\pi k \omega_0}{\omega}\right)^{m+1}. \tag{6.70}$$

This indicates that the mth-order term describes the collective motion of the fields on $(m+1)k$ sites excited by a drive and that such a process is suppressed exponentially up to the order $m = m_0 \approx \omega/(k\omega_0)$. By taking $m = m_0$, we obtain $\Omega_F^{(m)} \sim N\mathrm{e}^{-\zeta' m}$ with a constant number $\zeta' = \mathcal{O}(1)$, which completes the derivation of Eq. (6.66). Then, we obtain

$$|\Omega_{\mathrm{TR}}^{(m)} - \Omega_{\mathrm{TR}}^{(m_0)}| = \mathcal{O}\left(N\mathrm{e}^{-\zeta' m}\right) \quad \text{for} \quad m \leq m_0, \tag{6.71}$$

which indicates that the truncated series $\Omega_{\mathrm{TR}}^{(m)}$ seems to converge up to the order $m \leq m_0$.

Next, we evaluate the difference between $U^{-1}(T,0)\Omega_{\mathrm{TR}}^{(m_0)}U(T,0)$ and $\Omega_{\mathrm{TR}}^{(m_0)}$. Let us expand them in powers of ω^{-1} as follows:

$$U^{-1}(T,0)\Omega_{\mathrm{TR}}^{(m_0)}U(T,0) = \sum_{m=0}^{\infty} \frac{1}{m!} \int_0^T dt_1 \cdots \int_0^T dt_m \mathcal{T}_t \left[\mathrm{ad}_{L(t_1)} \cdots \mathrm{ad}_{L(t_m)} \Omega_{\mathrm{TR}}^{(m_0)}\right] =: \sum_{m=0}^{\infty} \mathcal{A}_m \Omega_{\mathrm{TR}}^{(m_0)}, \tag{6.72}$$

$$\Omega_{\mathrm{TR}}^{(m_0)} = \left[U^{(m_0)}(T)\right]^{-1} \Omega_{\mathrm{TR}}^{(m_0)} U^{(m_0)}(T) = \sum_{m=0}^{\infty} \sum_{r=0}^{m} \sum_{\{l_i\}_{i=1}^r} \frac{1}{r!} \mathrm{ad}_{\Omega_F^{(l_1)}} \cdots \mathrm{ad}_{\Omega_F^{(l_r)}} \Omega_{\mathrm{TR}}^{(m_0)} =: \sum_{m=0}^{\infty} \mathcal{A}'_m \Omega_{\mathrm{TR}}^{(m_0)}, \tag{6.73}$$

where $\sum_{\{l_i\}_{i=1}^r}$ denotes the sum over all the sets of integers $\{l_i\}_{i=1}^r$ that satisfy $\sum_{i=1}^r (l_i+1) = m$ and $0 \le l_i \le m_0$. In the FM HFE, $\Omega_F^{(m_0)}$ is chosen such that $\mathcal{A}'_m \Omega_{\rm TR}^{(m_0)}$ coincides with $\mathcal{A}_m \Omega_{\rm TR}^{(m_0)}$ for any $m \le m_0$; thus we have

$$U^{-1}(T,0)\Omega_{\rm TR}^{(m_0)}U(T,0) - \Omega_{\rm TR}^{(m_0)} = \sum_{m=m_0+1}^{\infty} \left(\mathcal{A}_m \Omega_{\rm TR}^{(m_0)} - \mathcal{A}'_m \Omega_{\rm TR}^{(m_0)} \right). \tag{6.74}$$

Using the argument for folded commutators around Eq. (6.69), we obtain

$$\left\| \mathcal{A}_m \Omega_{\rm TR}^{(m_0)} \right\| \lesssim \left(\frac{4\pi k \omega_0}{\omega} \right)^m \left\| \Omega_{\rm TR}^{(m_0)} \right\|, \quad \left\| \mathcal{A}'_m \Omega_{\rm TR}^{(m_0)} \right\| \lesssim \left(\frac{8\pi k \omega_0}{\omega} \right)^m \left\| \Omega_{\rm TR}^{(m_0)} \right\|. \tag{6.75}$$

Thus, we have

$$\left\| U^{-1}(T,0)\Omega_{\rm TR}^{(m_0)}U(T,0) - \Omega_{\rm TR}^{(m_0)} \right\| \lesssim \left(\frac{8\pi k \omega_0}{\omega} \right)^{m_0} \left\| \Omega_{\rm TR}^{(m_0)} \right\| \lesssim N \mathrm{e}^{-\zeta m_0}, \tag{6.76}$$

where we used Eq. (6.70) in the last relation. Finally, we obtain

$$\left\| U^{-1}(n_t T,0)\Omega_{\rm TR}^{(m_0)}U(n_t T,0) - \Omega_{\rm TR}^{(m_0)} \right\| \lesssim n_t \left\| U^{-1}(T,0)\Omega_{\rm TR}^{(m_0)}U(T,0) - \Omega_{\rm TR}^{(m_0)} \right\| \lesssim N n_t \mathrm{e}^{-\zeta m_0}, \tag{6.77}$$

where n_t is an integer and ζ is a constant number. Consider two autonomous equations

$$\frac{dP(s)}{ds} = \Omega_{\rm TR}^{(m_0)} P(s), \tag{6.78}$$

$$\frac{dP(s)}{ds} = U^{-1}(n_t T,0)\Omega_{\rm TR}^{(m_0)}U(n_t T,0) P(s), \tag{6.79}$$

with the same initial probability distribution P_0: $P(s=0) = P_0$, where s is an auxiliary time. For a sufficiently large frequency ω, the relaxation timescale τ satisfies

$$\omega\tau \ll \mathrm{e}^{\zeta m_0} \simeq \mathrm{e}^{\frac{\zeta\omega}{k\omega_0}}. \tag{6.80}$$

Then, from the bound (6.77), the solutions $U^{(m_0)}(s)P_0$ and $U^{-1}(n_t T,0)U^{(m_0)}(s)U(n_t T,0)P_0$ of Eqs. (6.78) and (6.79), respectively, at time $s \gtrsim \tau$ shows almost similar thermodynamic properties:

$$U^{(m_0)}(s)P_0 \simeq U^{-1}(n_t T,0)U^{(m_0)}(s)U(n_t T,0)P_0. \tag{6.81}$$

By applying $U(n_t T,0)$ to the both sides of Eq. (6.81) from the left, we have

$$U(n_t T,0)U^{(m_0)}(s)P_0 \simeq U^{(m_0)}(s)U(n_t T,0)P_0. \tag{6.82}$$

For a generic many-body system, the state after the relaxation $n_t T \gtrsim \tau$ ($s \gtrsim \tau$), $U(n_t T,0)$ $U^{(m_0)}(s)P_0$ ($U^{(m_0)}(s)U(n_t T,0)P_0$) approaches the steady state P_{SS} ($P_{SS}^{(m_0)}$) that is solely deter-

mined from $U(n_tT,0)$ ($U^{(m_0)}(s)$):

$$U(n_tT,0)U^{(m_0)}(n_tT)P_0 = U(n_tT,0)P_0 = P_{SS}, \tag{6.83}$$

$$U^{(m_0)}(n_tT)U(n_tT,0)P_0 = U^{(m_0)}(n_tT)P_0 = P_{SS}^{(m_0)}. \tag{6.84}$$

Combining Eqs. (6.82), (6.83), and (6.84), we obtain $P_{SS} = P_{SS}^{(m_0)}$, which completes the derivation of Eq. (6.67).

6.2.4 Many-body system: discussion

For an isolated Hamilton system, Eq. (6.77) indicates that the truncated effective Hamiltonian $H_{\rm TR}^{(m_0)} := i\Omega_{\rm TR}^{(m_0)}/T$ is a quasi-conserved quantity, where the transient state is given by the generalized Gibbs distribution $P_{SS} \propto \exp(-H_{\rm TR}^{(m_0)}/T_{\rm te})$, which is known as the Floquet-Gibbs state [117]. From Eq. (6.71), $H_{\rm TR}^{(m_0)}$ and the prethermal state are well approximated by a lower-order truncation $H_{\rm TR}^{(m)}$ and the Gibbs state of $H_{\rm TR}^{(m)}$, respectively. We note that while macroscopic properties are well approximated by the truncated FM HFE, local dynamics is not because of the onset of chaos [117].

Next, we consider an isolated system that is not a Hamilton system, such as a general dynamical system [337] and a stochastic process on a discrete space including the ASEP. For these systems, there is no *a priori* method to determine their steady state like the equipartition principle in a Hamilton system. Nevertheless, the above results tell us that the exact steady states are well approximated by the truncated FM HFE $\Omega_{\rm TR}^{(m_0)}$. We know from Eq. (6.71) that $\Omega_{\rm TR}^{(m_0)}$ is well approximated by the lower-order truncation $\Omega_{\rm TR}^{(m)}$ and hence we expect that the exact steady states are obtained from $\Omega_{\rm TR}^{(m)}$. If the FM HFE is divergent, the system is expected to finally become a featureless state with a chaotic nature, which is an analog of an infinite-temperature state. This implies that some transient state described by the truncated series $\Omega_{\rm TR}^{(m)}$ might exist in a general classical system, which is reminiscent of a Floquet prethermal state [95, 96, 98, 209].

In a driven dissipative system, the system relaxes into an NESS with time τ through the balance between the drive and damping. Therefore, the steady state P_{SS} is not a transient state but an NESS; thus the truncated HFE well captures the whole dynamics of the system up to the NESS. This point is numerically confirmed in Secs. 6.4 and 6.5 by an example of the sLLG equation. Thus, we can control the *exact* steady states of classical systems by Floquet engineering, avoiding the problem of heating in isolated systems.

Before ending this section, we comment on an application of the above results to *quantum* systems. While the above derivation is conducted with classical systems in mind, similar results are obtained for open quantum systems by replacing the classical master equation (6.5) with a Markovian quantum master equation [338–340]:

$$\frac{d\rho}{dt} = -i\left[H(t),\rho\right] + \sum_i \left(L_i(t)\rho L_i(t)^\dagger - \frac{1}{2}\left\{L_i(t)^\dagger L_i(t),\rho\right\}\right) =: \mathcal{L}_{\rm Lind}(t)\rho. \tag{6.85}$$

Here, the generator $\mathcal{L}_t$ of a classical master equation is replaced by the Lindbladian $\mathcal{L}_{\rm Lind}(t)$. Equation (6.85) gives the most general description with Markovian, completely-positive, and trace-preserving nature that is and consistent with quantum mechanics [341]. As a by product

of the above analysis, we can show that the HFE works even in quantum *many-body* system described by Eq. (6.85). More precisely, for the FM HFE $\Omega_F = \sum_{m=0}^{\infty} \Omega_F^{(m)}$ of $\mathcal{L}_{\rm Lind}(t)$, we can show the (asymptotic) convergence of $\Omega_F^{(m)}$ up to the order $m_0 \sim \omega/(gk)$:

$$\|\Omega_F^{(m)} - \Omega_F^{(m_0)}\| \leq N\mathcal{O}\left[(2gkT)^m\right] \quad \text{for} \quad m \leq m_0, \tag{6.86}$$

and the correspondence of the exact steady state $\rho_{\rm SS}$ is well approximated by the steady state $\rho_{\rm SS}^{(m_0)}$ obtained from the m_0th-order truncated FM HFE:

$$\frac{1}{N}\|\rho_{\rm SS} - \rho_{\rm SS}^{(m_0)}\| \leq \mathcal{O}\left[(g\tau)^2 k 2^{-m_0}\right]. \tag{6.87}$$

See App. B.1 for further discussions and the derivation of the above results.

A few remarks are in order. First, while the HFE of a Lindbladian is, so far, applied and confirmed to be valid numerically only in *few-body* systems [342–345], the above results hold for *many-body* systems. Secondly, the effective equation is not necessarily be the Lindblad equation (6.85) because the Floquet operator $U(T, 0)$ is, in general, not generated by a time-homogeneous Markovian generator. In fact, in an example of a single qubit coupled with an environment, the effective equation is found to be non-Markovian [326] by using the measures of non-Markovianity [346, 347]. Finally, while the FM HFE is shown to be asymptotically convergent from Eq. (6.86), it is unclear where it is absolutely convergent. The divergent nature of the HFE in an isolated system is closely related to a sharp resonance and energy absorption associated with it [94, 96, 198–201, 348, 349]. Since they are suppressed in the presence of dissipation, the FM HFE might be absolutely convergent. It is worth mentioning that, when the HFE is applied *only to the Hamiltonian part*, i.e., the first term on the right-hand side of Eq. (6.85), it diverges above an optimal truncation order [350].

6.3 Kapitza pendulum with friction

In this section, we take the Kapitza pendulum with friction as an example of a driven dissipative few-body system to test the validity of the HFE. Although this is a single-body problem, the convergence of the Flouquet-Magnus expansion is a nontrivial issue because the unbounded operator like ∂_ϕ is present and the driving strength is proportional to ω^2.

6.3.1 Setup

Let us introduce a friction term $-\gamma\dot{\theta}$ into the EOM (3.42) of the Kapitza pendulum to ensure that the system reaches to a stable point after a long time. The EOM with friction is given by

$$\ddot{\theta} = -\gamma\dot{\theta} - \left[\omega_0^2 + \frac{a}{l}\omega^2\cos(\omega t)\right]\sin\theta. \tag{6.88}$$

In what follows, we analyze this EOM using the HFE developed in Sec. 6.1 and confirm that it correctly reproduces the time evolution of the pendulum and the stability at the inverted point $\theta = \pi$. We note that the systems is no longer a Hamilton system because of the presence of the friction term, where the HFE previously developed for Hamilton systems cannot be applied.

6.3.2 Hih-frequency expansion and effective equation of motion

To apply the general formalism developed in Sec. 6.1, we rewrite Eq. (6.88) into a first-order ordinary differential equation with respect to θ and v (v is the angular velocity) as follows:

$$\begin{cases} \dot{\theta} = v, \\ \dot{v} = -\gamma v - \left[\omega_0^2 + \frac{a}{l}\omega^2 \cos(\omega t)\right] \sin\theta. \end{cases} \tag{6.89}$$

Comparing Eq. (6.89) with Eq. (6.1), we find that the classical variable $\boldsymbol{\phi}$ is a two-dimensional vector: $\boldsymbol{\phi} = (\theta, v)$. The Fourier components of the drift force $\boldsymbol{f}(\boldsymbol{\phi}, t) := \boldsymbol{f}_0 + \boldsymbol{f}_1 \mathrm{e}^{-i\omega t} + \boldsymbol{f}_{-1}\mathrm{e}^{i\omega t}$ are given by

$$\boldsymbol{f}_0(v,\theta) := \begin{pmatrix} f_{0,\theta} \\ f_{0,v} \end{pmatrix} = \begin{pmatrix} v \\ -\gamma v - \omega_0^2 \sin\theta \end{pmatrix}, \quad \boldsymbol{f}_{\pm 1}(v,\theta) := \begin{pmatrix} f_{\pm 1,\theta} \\ f_{\pm 1,v} \end{pmatrix} = \begin{pmatrix} 0 \\ -\frac{a\omega^2}{2l}\sin\theta \end{pmatrix}, \tag{6.90}$$

and the diffusion matrix g vanishes. From the vV HFE in Eq. (6.29), we obtain the effective drift fields $\boldsymbol{f}_F^{(1)}(v,\theta)$ and $\boldsymbol{f}_F^{(2)}(v,\theta)$:

$$\boldsymbol{f}_F^{(1)}(v,\theta) := \frac{i\left[\boldsymbol{f}_{-1}, \boldsymbol{f}_1\right]_{\mathrm{cl}}}{\omega} = 0, \tag{6.91}$$

$$\left[\boldsymbol{f}_0, \boldsymbol{f}_1\right]_{\mathrm{cl}} = f_{0,\theta}\frac{\partial \boldsymbol{f}_1}{\partial\theta} + f_{0,v}\frac{\partial \boldsymbol{f}_1}{\partial v} - f_{1,\theta}\frac{\partial \boldsymbol{f}_0}{\partial\theta} - f_{1,v}\frac{\partial \boldsymbol{f}_0}{\partial v} = \frac{a\omega^2}{2l}\begin{pmatrix} \sin\theta \\ -v\cos\theta - \gamma\sin\theta \end{pmatrix}, \tag{6.92}$$

$$\boldsymbol{f}_F^{(2)}(v,\theta) := -\frac{\left[\boldsymbol{f}_{-1}, \left[\boldsymbol{f}_0, \boldsymbol{f}_1\right]_{\mathrm{cl}}\right]_{\mathrm{cl}} + \left[\boldsymbol{f}_1, \left[\boldsymbol{f}_0, \boldsymbol{f}_{-1}\right]_{\mathrm{cl}}\right]_{\mathrm{cl}}}{2\omega^2} = \begin{pmatrix} 0 \\ -\left(\frac{a\omega}{2l}\right)^2 \sin(2\theta) \end{pmatrix}, \tag{6.93}$$

where the effective EOM is given as follows:

$$\begin{cases} \dot{\theta} = v, \\ \dot{v} = -\gamma v - \omega_0^2 \sin\theta - \left(\frac{a\omega}{2l}\right)^2 \sin(2\theta). \end{cases} \tag{6.94}$$

Comparing Eqs. (6.89) and (6.94), we find that the original static potential $-\omega_0^2\cos\theta$ is replaced by the effective potential

$$V_F(\theta) = -\omega_0^2\cos\theta - \left(\frac{a\omega}{2l}\right)^2 \sin^2\theta, \tag{6.95}$$

through the periodic drive. We note that $V_F(\theta)$ is independent of the friction strength γ and the same as the one obtained from the analysis without friction [13,198]. Because of the second term on the right-hand side of Eq. (6.95), the effective potential develops a new local minimum at $\theta = \pi$ above the critical driving frequency $\omega_c = (\sqrt{2}l\omega_0)/a$. Since $(\theta, v) = (0, 0)$ and $(\pi, 0)$ are both stationary solutions of Eq. (6.94), the system converges to either of these points after a sufficiently long time with the help of the friction $-\gamma v$. The steady state angle $\theta_{SS} := \theta(t \to \infty)$, in general, depends on θ_0, ω, $v(t = 0)$, and γ, as we will see below.

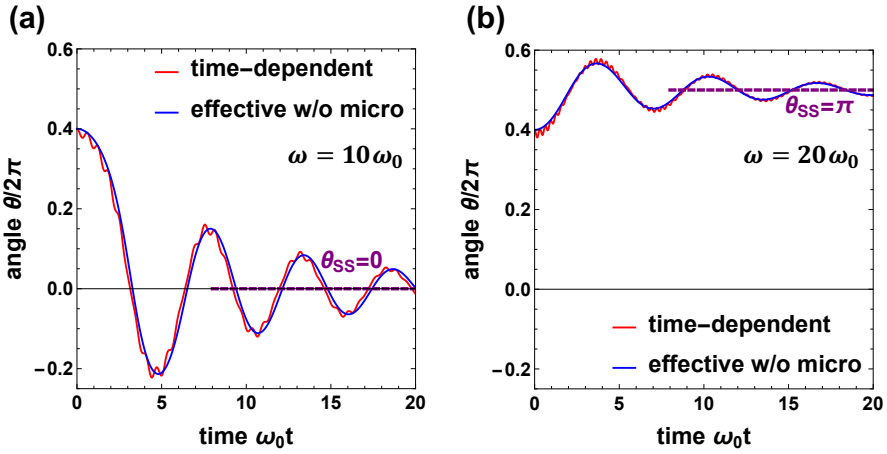

Figure 6.2: Time evolution of angle $\theta(t)$ for (a) slow ($\omega/\omega_0 = 10$) and (b) fast ($\omega/\omega_0 = 20$) drives, where the parameters are chosen as $a/l = 0.1$ and $\gamma/\omega_0 = 0.2$. The red and blue curves are obtained by solving the time-dependent EOM (6.89) and the effective EOM (6.94), respectively, which are in excellent agreement. Starting from the same initial state $\theta_0 = 0.8\pi$ with $v = 0$, the angle approaches 0 for the slow drive (a), while it approaches π for the fast drive (b). The purple dashed lines show the steady state angle θ_{SS}, which is either 0 or π.

6.3.3 Comparison between the time-periodic and effective equations of motion

In what follows, we compare Eqs. (6.89) and (6.94) through the dynamics $\theta(t)$ and the steady-state angle θ_{SS}. The parameters a/l and γ are fixed as $a/l = 0.1$ and $\gamma = 0.2\omega_0$, respectively. The time evolution of $\theta(t)$ for slow ($\omega/\omega_0 = 10$) and fast ($\omega/\omega_0 = 20$) drives are shown in Figs. 6.2 (a) and (b), respectively. The initial states are taken as $(\theta, v) = (0.8\pi, 0)$ in both cases. The red and blue curves are obtained from the time-dependent EOM (6.89) and the effective EOM (6.94), respectively, which are in excellent agreement. After a sufficiently long time, the pendulum approaches the lowest point $\theta = 0$ for the slow drive (a) below the critical frequency ω_c, while it approaches the inverted point $\theta = \pi$ for the fast drive (b).

In Fig. 6.3 (a), we present the steady state "phase diagram" of the pendulum for fixed parameters $v(t = 0) = 0$ and $\gamma = 0.2\omega_0$. We see that the inverted steady state with $\theta = \pi$ (shaded region in Fig. 6.3 (a)) is preferred for an initial angle close to π with a fast driving, while it approaches the lowest point $\theta = 0$ for the other parameter region. The boundary curve between $\theta_{SS} = 0$ and $\theta_{SS} = \pi$ for the effective EOM is determined from the effective potential (6.95) as follows:

$$\begin{cases} \omega > \omega_c; \\ |\theta - \pi| < \arccos\left[\left(\frac{\omega_c}{\omega}\right)^2\right]. \end{cases} \tag{6.96}$$

Although the effective EOM (6.94) (blue curve in Fig. 6.3 (a)) gives a boundary (6.96) close to that obtained from the time-dependent EOM (6.89) (red curve in Fig. 6.3 (a)), there is a slight deviation even in the high-frequency region, which might contradict the validity of the HFE. In particular, in the high-frequency limit, $\theta_{SS}/(2\pi)$ converges to 1/4 for the effective EOM (dashed black line in Fig. 6.3 (b)), while it converges to 0.267 for the EOM (dashed purple line

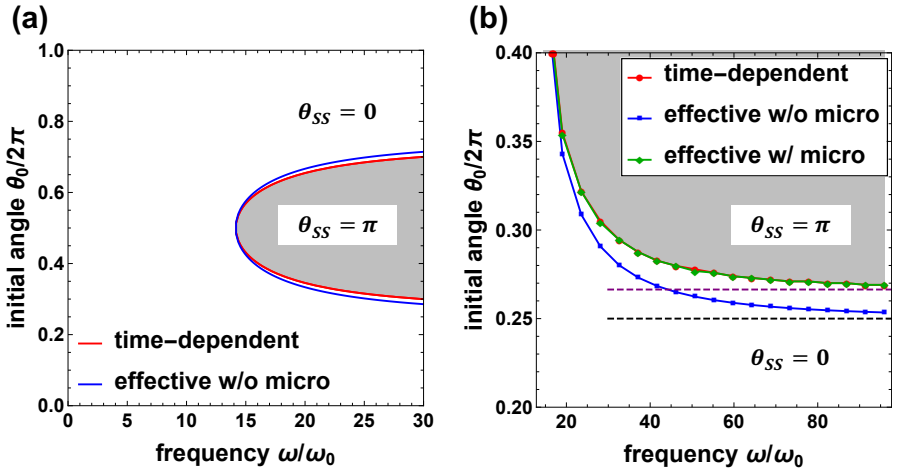

Figure 6.3: (a) Dependence of the steady-state angle θ_{SS} on the initial state $[\theta(0), v(0)] = (\theta_0, 0)$ and frequency ω, where a/l and γ/ω_0 are fixed in the same parameters as Fig. 6.2. In the shaded region, the angle approaches $\theta = \pi$ after sufficiently long time, while it approaches $\theta = 0$ in the other region. The red and blue curves show the boundary obtained from the time-dependent EOM (6.89) and that obtained from the effective EOM (6.94), respectively. (b) Boundary of the steady-state angle $\theta_{SS} = 0, \pi$ obtained from the time-dependent EOM (6.89) (red), the time-independent effective EOM (6.94) (blue), and the time-independent effective EOM (6.94) with the kick operator (green). The red and green curves overlap almost completely. The black and purple lines are guides to the eyes.

in Fig. 6.3 (b)). This deviation is, in fact, attributed to the ω-dependent coefficient in the drive: $\boldsymbol{f}_{\pm 1} \propto \omega^2$. Since we fix a/l rather than the coefficient $a\omega^2/(2l)$ of $\boldsymbol{f}_{\pm 1}$, the resulting potential, the second term on the right-hand side of Eq. (6.95), is proportional to ω^2. However, when we take into account the kick operator $\mathcal{G}_F(t)$ in Eq. (6.14), we obtain perfect agreement between the time-dependent EOM and the effective one, which are shown as the red and green curves in Fig. 6.3 (b), respectively. The above numerical results are consistent with the analytical argument in Sec. 6.2.

6.4 Stochastic Landau-Lifshitz-Gilbert equation

In this section, we treat a driven classical many-spin system described by the time-dependent sLLG equation. By calculating the time evolution of the magnetization and its time average at a NESS, we compare the time-dependent sLLG equation and the effective sLLG equation obtained from the HFE. Through a detailed comparison changing various parameters including the frequency, dissipation strength, and temperature, we confirm that the latter well approximates the former for a long time up to the NESS.

Consider the sLLG equation (4.27) with time-dependent Hamiltonian $\mathcal{H}(t)$:

$$\dot{\boldsymbol{m}}_{\boldsymbol{r}} = -\frac{\boldsymbol{m}_{\boldsymbol{r}}}{1+\alpha^2} \times \{\boldsymbol{H}_{\boldsymbol{r}}(t) + \boldsymbol{h}_{\boldsymbol{r}}(t) + \frac{\alpha}{m_s}\boldsymbol{m}_{\boldsymbol{r}} \times [\boldsymbol{H}_{\boldsymbol{r}}(t) + \boldsymbol{h}_{\boldsymbol{r}}(t)]\}, \tag{6.97}$$

where $\boldsymbol{H}_{\boldsymbol{r}}(t) = -(\delta\mathcal{H}(t))/(\delta\boldsymbol{m}_{\boldsymbol{r}})$ is an effective magnetic field generated by the surrounding spins and external driving fields. Comparing Eqs. (6.2) and (6.97), we find that $\boldsymbol{\phi}_{\boldsymbol{r}} = \boldsymbol{m}_{\boldsymbol{r}}$

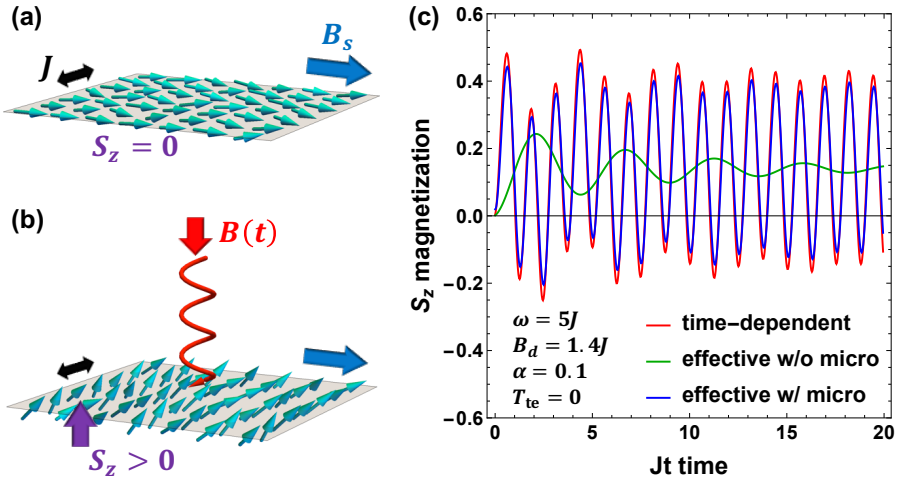

Figure 6.4: (a) Schematic illustration of a periodically driven two-dimensional ferromagnet with 100×100 spins. The nearest-neighbor spins are coupled with a ferromagnetic interaction of exchange interaction J and a static magnetic field of strength B_s is applied in the m_x direction. (b) When the system is irradiated by a circularly polarized magnetic field with strength B_d, the average magnetization S_z emerges. (c) Time evolution of the averaged magnetization S_z for the time-dependent sLLG equation (6.97) (red), the effective sLLG (6.109) with (blue) and without (green) the kick operator. The parameters are chosen as $J = 1, \omega = 5J, B_d = 1.4J, B_s = 1.4J, \alpha = 0.1$, and $T_{\rm te} = 0$.

represents the spin configuration, and $\boldsymbol{f}_{\boldsymbol{r}}$ and $\boldsymbol{g}_{\boldsymbol{r}}$ are given by

$$\boldsymbol{f}_{\boldsymbol{r}}(t) = -\frac{\boldsymbol{m}_{\boldsymbol{r}}}{1+\alpha^2} \times \left[\boldsymbol{H}_{\boldsymbol{r}}(t) + \frac{\alpha}{m_s} \boldsymbol{m}_{\boldsymbol{r}} \times \boldsymbol{H}_{\boldsymbol{r}}(t) \right] + \frac{2D}{1+\alpha^2} \boldsymbol{m}_{\boldsymbol{r}}, \tag{6.98}$$

$$g_{\boldsymbol{r},ab} = \frac{1}{1+\alpha^2} \epsilon_{abc} m_c + \frac{\alpha m_s}{1+\alpha^2} \left(\delta_{ab} - \frac{m_a m_b}{(m_s)^2} \right), \tag{6.99}$$

which describe the spin precession generated by $\boldsymbol{H}_{\boldsymbol{r}}$ and the spin diffusion induced by $\boldsymbol{h}_{\boldsymbol{r}}$.

As a concrete example, we consider a classical ferromagnetic Heisenberg model on a square lattice (see Fig. 6.4 (a)), whose Hamiltonian $\mathcal{H}(t)$ reads

$$\mathcal{H}(t) = -J \sum_{\langle \boldsymbol{r}, \boldsymbol{r}' \rangle} \boldsymbol{m}_{\boldsymbol{r}} \cdot \boldsymbol{m}_{\boldsymbol{r}'} - g\mu_B \sum_{\boldsymbol{r}} \boldsymbol{B}(t) \cdot \boldsymbol{m}_{\boldsymbol{r}}, \tag{6.100}$$

where $J > 0$ is the ferromagentic coupling constant and $\boldsymbol{B}(t)$ is an external magnetic field. The summation $\sum_{\langle \boldsymbol{r}, \boldsymbol{r}' \rangle}$ is taken over all the pairs of the nearest-neighbor sites. We measure the external magnetic field in units of $g\mu_B$ and thereby set it to be unity: $g\mu_B = 1$. We apply a circularly polarized driving magnetic field of strength B_d in the (m_x, m_y) plane (see Fig. 6.4 (b)). The total field $\boldsymbol{B}(t)$ is given by

$$\boldsymbol{B}(t) = (B_s + B_d \cos(\omega t), -B_d \sin(\omega t), 0)^{\rm tr}, \tag{6.101}$$

which is decomposed into the Fourier harmonics as follows:

$$\boldsymbol{B}(t) = \boldsymbol{B}_0 + \boldsymbol{B}_1 \mathrm{e}^{-i\omega t} + \boldsymbol{B}_{-1} \mathrm{e}^{i\omega t}, \quad \boldsymbol{B}_0 = (B_s, 0, 0)^{\rm tr}, \quad \boldsymbol{B}_{\pm 1} = \frac{B_d}{2} (1, \mp i, 0)^{\rm tr}. \tag{6.102}$$

6.4.1 High-frequency expansion and the effective sLLG equation

The Fourier harmonics $\boldsymbol{f}_{\pm 1}$ and the drift force $\boldsymbol{f}^{(1)}_{F,\boldsymbol{r}}$ obtained from the first-order vV HFE are given from Eqs. (6.37) and (6.99) as follows (see App. B.2 for the derivation):

$$\boldsymbol{f}_{\pm 1,\boldsymbol{r}} = -\frac{\boldsymbol{m}_{\boldsymbol{r}}}{1+\alpha^2} \times \left(\boldsymbol{B}_{\pm 1} + \frac{\alpha}{m_s} \boldsymbol{m}_{\boldsymbol{r}} \times \boldsymbol{B}_{\pm 1} \right), \tag{6.103}$$

$$\boldsymbol{f}^{(1)}_{F,\boldsymbol{r}} = \frac{i}{\omega} \left[\boldsymbol{f}_{1,\boldsymbol{r}} \cdot \frac{\partial \boldsymbol{f}_{-1,\boldsymbol{r}}}{\partial \boldsymbol{m}_{\boldsymbol{r}}} - \boldsymbol{f}_{-1,\boldsymbol{r}} \cdot \frac{\partial \boldsymbol{f}_{1,\boldsymbol{r}}}{\partial \boldsymbol{m}_{\boldsymbol{r}}} \right] = -\frac{\boldsymbol{m}_{\boldsymbol{r}}}{1+\alpha^2} \times \left(\boldsymbol{H}^{(1)}_{F,\boldsymbol{r}} + \frac{\alpha}{m_s} \boldsymbol{m}_{\boldsymbol{r}} \times \boldsymbol{H}^{(1)}_{F,\boldsymbol{r}} \right), \tag{6.104}$$

$$\boldsymbol{H}^{(1)}_{F,\boldsymbol{r}} = \frac{i\boldsymbol{B}_{-1} \times \boldsymbol{B}_{+1}}{(1+\alpha^2)\omega} - \alpha \frac{i\boldsymbol{B}_{-1} \times \boldsymbol{B}_{+1}}{(1+\alpha^2)\omega} \times \boldsymbol{m}_{\boldsymbol{r}}. \tag{6.105}$$

While the first term on the right-hand side of Eq. (6.105) describes the effective magnetic field

$$\boldsymbol{b}^{(1)} := \frac{i\boldsymbol{B}_{-1} \times \boldsymbol{B}_{+1}}{(1+\alpha^2)\omega} = \frac{(B_d)^2}{2\omega(1+\alpha^2)} \boldsymbol{e}_3, \tag{6.106}$$

with $\boldsymbol{e}_3 = (0,0,1)^{\mathrm{tr}}$ being the unit vector perpendicular to the plane, the second term describes the so-called spin-transfer torque [351–354]. The emergence of an effective magnetic field parallel to $i(\boldsymbol{B}_{-1} \times \boldsymbol{B}_{+1})$ can be qualitatively understood in an analogy with a quantum system. In the presence of the external drive $\hat{H}(t) = -\boldsymbol{B}(t) \cdot \hat{\boldsymbol{S}}$, the first-order vV HFE

$$\hat{H}^{(1)}_F := \frac{[\hat{H}_{-1}, \hat{H}_1]}{\omega} = \frac{i}{\omega} (\boldsymbol{B}_{-1} \times \boldsymbol{B}_{+1}) \cdot \hat{\boldsymbol{S}} \tag{6.107}$$

represents the effective magnetic field $i(\boldsymbol{B}_{-1} \times \boldsymbol{B}_{+1})/\omega$. However, we find from Eq. (6.106) that its magnitude decreases by a factor of $(1+\alpha^2)^{-1}$. Moreover, there appears the spin-transfer torque as a consequence of the coupling with the environment, which is absent in an isolated system. The drift field $\boldsymbol{f}^{(1)}_{\mathrm{mic},\boldsymbol{r}}$ corresponding to the kick operator $\mathcal{G}^{(1)}_F(t)$ is given by

$$\boldsymbol{f}^{(1)}_{\mathrm{mic},\boldsymbol{r}}(\boldsymbol{m}_{\boldsymbol{r}}, t) := -\frac{\boldsymbol{m}_{\boldsymbol{r}}}{1+\alpha^2} \times \left(\boldsymbol{H}^{(1)}_{\mathrm{mic}}(t) + \frac{\alpha}{m_s} \boldsymbol{m}_{\boldsymbol{r}} \times \boldsymbol{H}^{(1)}_{\mathrm{mic}}(t) \right), \tag{6.108}$$

where $\boldsymbol{H}^{(1)}_{\mathrm{mic}}(t) = i\left(\boldsymbol{B}_{-1}\mathrm{e}^{i\omega t} - \boldsymbol{B}_{+1}\mathrm{e}^{-i\omega t}\right)$ describes an oscillating magnetic field.

The second-order expansion term is much more complicated owing to the renormalization of the diffusion matrix G. The effective sLLG equation is obtained to be

$$\dot{\boldsymbol{m}}_{\boldsymbol{r}} = -\frac{\boldsymbol{m}_{\boldsymbol{r}}}{1+\alpha^2} \times \left[\boldsymbol{H}_{F,\boldsymbol{r}} + \sqrt{1+\chi_{\boldsymbol{r}}} \boldsymbol{h}_{\boldsymbol{r}} + \frac{\alpha}{m_s} \boldsymbol{m}_{\boldsymbol{r}} \times \left(\boldsymbol{H}_{F,\boldsymbol{r}} + \sqrt{1+\chi_{\boldsymbol{r}}} \boldsymbol{h}_{\boldsymbol{r}} \right) \right], \tag{6.109}$$

where $\boldsymbol{H}_{F,\boldsymbol{r}}$ and $\chi_{\boldsymbol{r}}(\boldsymbol{m}_{\boldsymbol{r}})$ are given as follows (see App. B.3 for the derivation):

$$\boldsymbol{H}_{F,\boldsymbol{r}} := \sum_{\boldsymbol{r}':\mathrm{n.n.}} (J\boldsymbol{m}_{\boldsymbol{r}'} + \boldsymbol{\delta J}_{\boldsymbol{r},\boldsymbol{r}'}) + \boldsymbol{B}_F + \boldsymbol{V}_F \times \boldsymbol{m}_{\boldsymbol{r}}, \tag{6.110}$$

$$\chi_{\boldsymbol{r}}(\boldsymbol{m}_{\boldsymbol{r}}) := -\left(\frac{\alpha B_d}{m_s \omega (1+\alpha^2)} \right)^2 \frac{3(m_s)^2 - (m_{\boldsymbol{r},z})^2}{2}. \tag{6.111}$$

Here the sum $\sum_{\boldsymbol{r}':\mathrm{n.n.}}$ is taken over the nearest-neighbor sites of $\boldsymbol{r}$. The total effective external

magnetic field $\boldsymbol{B}_F$, the spin-transfer torque $\boldsymbol{V}_F$, and the effective interaction are, respectively, given by

$$\boldsymbol{B}_F := \boldsymbol{B}_0 + \boldsymbol{b}^{(1)} + (1-\alpha^2)\boldsymbol{b}^{(2)} - \frac{\alpha m_s D}{2(1+\alpha^2)} \frac{\delta \chi_{\boldsymbol{r}}}{\delta \boldsymbol{m}_{\boldsymbol{r}}}, \tag{6.112}$$

$$\boldsymbol{V}_F := -\frac{\alpha}{m_s}\boldsymbol{b}^{(1)} - \frac{2\alpha}{m_s}\boldsymbol{b}^{(2)} + \frac{D}{2(1+\alpha^2)} \frac{\delta \chi_{\boldsymbol{r}}}{\delta \boldsymbol{m}_{\boldsymbol{r}}}, \tag{6.113}$$

$$\boldsymbol{\delta J}_{\boldsymbol{r},\boldsymbol{r}'} := J \left(\frac{\alpha B_d}{m_s \omega (1+\alpha^2)} \right)^2 m_{\boldsymbol{r}',z} \sum_{\boldsymbol{r}':n,n} \begin{pmatrix} m_{\boldsymbol{r}',x} \delta m_{\boldsymbol{r},\boldsymbol{r}',z} \\ m_{\boldsymbol{r}',y} \delta m_{\boldsymbol{r},\boldsymbol{r}',z} \\ -m_{\boldsymbol{r}',z} \delta m_{\boldsymbol{r},\boldsymbol{r}',x} - m_{\boldsymbol{r}',y} \delta m_{\boldsymbol{r},\boldsymbol{r}',y} \end{pmatrix}, \tag{6.114}$$

where $\delta \boldsymbol{m}_{\boldsymbol{r},\boldsymbol{r}'} := \boldsymbol{m}_{\boldsymbol{r}} - \boldsymbol{m}_{\boldsymbol{r}'}$ and $\boldsymbol{b}^{(2)}$ is defined by

$$\boldsymbol{b}^{(2)} := -\left(\frac{B_d}{2\omega(1+\alpha^2)} \right)^2 B_s \boldsymbol{e}_1. \tag{6.115}$$

6.4.2 Short-time dynamics

In Fig. 6.4 (c), we calculate the time evolution of the spatially averaged magnetization $S_z := (1/N)\sum_{\boldsymbol{r}} \boldsymbol{m}_{\boldsymbol{r}}$, with $N = 100\times100$ being the number of spins, using three different equations: (i) the time-dependent sLLG equation (6.97) (red curve), (ii) the effective sLLG equation (6.109) without the kick operator $\mathcal{G}_F$ (green curve), and (iii) the effective sLLG equation (6.109) with the kick operator $\mathcal{G}_F$ (blue curve). We use the Heun method for numerical integration of the sLLG equation with the linearization technique [355].

The initial state is taken as the fully polarized state along the m_x direction, i.e., $\boldsymbol{m}_{\boldsymbol{r}} = (1,0,0)^{\mathrm{tr}}$. The parameters are chosen as $J = 1, B_d = 1.4J, \omega = 5J, B_s = 1.4J, \alpha = 0.1$, and $T_{\mathrm{te}} = 0$. After a long time $t \gg (\alpha J)^{-1}$, the system approaches a NESS, where S_z oscillates with period T. Because of the effective magnetic field $\boldsymbol{b}_F^{(1)} (\parallel \boldsymbol{e}_3)$, the long-time average $\bar{S}_z$ of S_z becomes positive. As we can see from Fig. 6.4 (c), the effective sLLG equation with the kick operator (blue curve) shows good agreement with the time-dependent sLLG equation (red curve). Although the effective sLLG equation without the kick operator (green curve) fails to capture the oscillating behavior, it correctly reproduces the long-time average $\bar{S}_z$ for the NESS.

6.4.3 Non-equilibrium steady state

In Fig. 6.5, we show a comprehensive analysis on the dependence of the long-time average of the magnetization $\bar{S}_z$ on (a) the driving frequency ω, (b) the driving amplitude B_d, (c) the Gilbert damping α, and (d) temperature T_{te}. The curves with the three colors, red, green, and blue, are obtained from the three equations (i), (ii), and (iii), respectively. Except for the parameter changed in each panel, the parameters are fixed as $J = 1, \omega = 7J, B_d = J, B_s = 1.4J, \alpha = 0.1$, and $T_{\mathrm{te}} = 0.2J$. As shown in Fig. 6.5 (a), the average magnetization $\bar{S}_z (\propto \omega^{-1})$ is induced by the effective magnetic field $\boldsymbol{b}^{(1)} (\propto \omega^{-1})$ and the time-dependent sLLG equation (6.97) and the effective one (6.109) are in excellent agreement in the high-frequency regime $\omega/J > 5$. In Fig. 6.5 (b), the driving amplitude is varied from weakly driven ($B_d/J \approx 0$) to strongly driven ($B_d/J \lesssim 1$) regimes, where the effective sLLG equation with kick operators shows better agreement for strong drives. The effect of the Gilbert damping is shown in Fig. 6.5

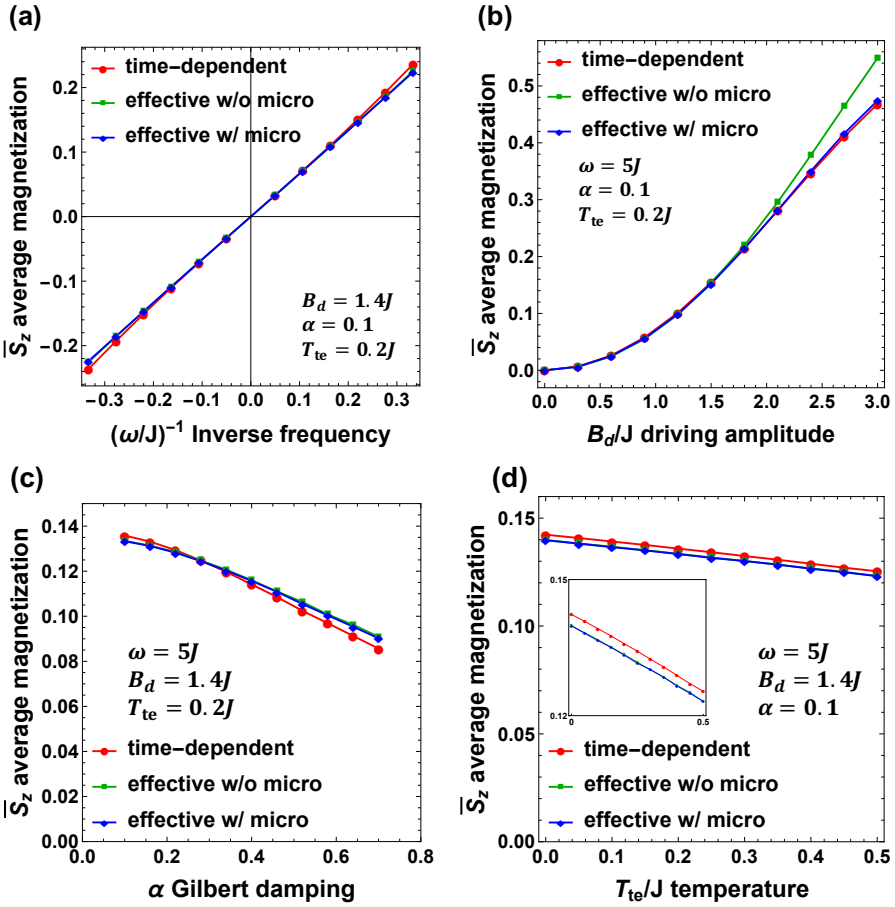

Figure 6.5: Long-time average $\bar{S}_z$ of the magnetization as functions of (a) the driving frequency ω, (b) the driving strength B_d, (c) the Gilbert damping α, and (d) temperature $T_{\rm te}$. The red, green, and blue points are obtained from the time-dependent sLLG equation (6.97), and the effective static sLLG equation (6.109) without the kick operators, and the effective sLLG (6.109) without them, respectively. The parameters are fixed as $J = 1, \omega = 5J, B_d = 1.4J, B_s = 1.4J, \alpha = 0.1$, and $T_{\rm te} = 0.2J$, except for the parameter that is varied in each panel. The inset in the panel (d) shows an enlarged image between $0.12 \leq \bar{S}_z \leq 0.15$.

(c), where the calculation is performed from weakly dissipative ($\alpha \approx 0$) to strongly dissipative ($\alpha \lesssim 1$) regimes. In Fig. 6.5 (d), where we vary temperature to simulate the sLLG equation with ($T_{\rm te} > 0$) and without ($T_{\rm te} = 0$) the random field $\boldsymbol{h}_{\boldsymbol{r}}$. Although a slight deviation is visible between the time-dependent and effective sLLG equation (see the inset), the latter correctly reproduces the temperature dependence of the former, i.e., the slope of the curve. From the above results, we can conclude that the effective sLLG equation obtained from the HFE well approximates the original one, irrespective of the magnitude of the dissipation and thermal fluctuation. These results are consistent with the analytical argument in Sec. 6.2.

6.5 Application to spintronics

In this section, we consider a multiferroic spin system described by the sLLG equation. Our setup is a classical analog of Ref. [76] reviewed in Sec. 3.3. While a vector spin chirality and a

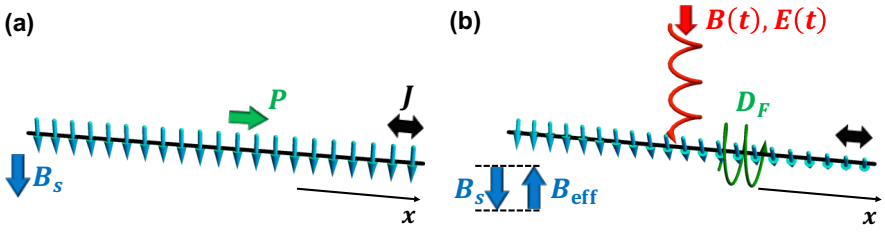

Figure 6.6: (a) Schematic illustration of a multiferroic spin chain. The nearest-neighbor spins are coupled with a ferromagnetic coupling of J and the magnetoelectric coupling of polarization $\boldsymbol{P}$, which is given by Eq. (6.117). The static field $\boldsymbol{B}_s$ is applied in the m_z direction. (b) Irradiation of the laser field with electric field $\boldsymbol{E}(t)$ and magnetic field $\boldsymbol{B}(t)$ induces the effective DM interaction $\boldsymbol{D}_F$ and the effective magnetic field $\boldsymbol{B}_F$, leading to a spiral spin texture and emergence of the vector chirality $\mathcal{V}_x^{\rm tot}$ along the x direction. The static field is tuned to cancel the effective field $\boldsymbol{B}_F$.

spin current have been shown to emerge in this study, they vanish after a long time through the heating effect. On the other hand, the system reaches the NESS with a finite vector chirality in our setup through the balance between the heating effect and the Gilbert damping.

6.5.1 Synthetic Dzyaloshinskii-Moriya interaction in a multiferroic spin chain

The Hamiltonian $\mathcal{H}_{\rm MF}(t)$ that we consider is given by that of a ferromagnet (6.100) with a magnetoelectric coupling:

$$\mathcal{H}_{\rm MF}(t) = \mathcal{H}(t) - \boldsymbol{P}\cdot\boldsymbol{E}(t). \tag{6.116}$$

Here, the second term represents the magnetoelectric coupling, which we consider having the same form as that considered in Sec. 3.3:

$$\boldsymbol{P} = \sum_{\langle \boldsymbol{r},\boldsymbol{r}'\rangle} \boldsymbol{P}_{\boldsymbol{r},\boldsymbol{r}'} = g_{\rm me} \sum_{\langle \boldsymbol{r},\boldsymbol{r}'\rangle} \boldsymbol{e}_{\boldsymbol{r},\boldsymbol{r}'} \times (\boldsymbol{m}_{\boldsymbol{r}} \times \boldsymbol{m}_{\boldsymbol{r}'}), \tag{6.117}$$

where $\boldsymbol{e}_{\boldsymbol{r},\boldsymbol{r}'} := (\boldsymbol{r}'-\boldsymbol{r})/|\boldsymbol{r}'-\boldsymbol{r}|$ is the unit vector connecting the nearest neighbor sites $\boldsymbol{r}$ and $\boldsymbol{r}'$, and $g_{\rm me}$ denotes the magnitude of the magnetoelectric coupling. Combining Eqs. (6.100) and (6.117), we obtain the explicit forms of $\mathcal{H}(t)$ and the effective field $\boldsymbol{H}_{\boldsymbol{r}}(t)$:

$$\mathcal{H}(t) = -\sum_{\langle \boldsymbol{r},\boldsymbol{r}'\rangle} [J\boldsymbol{m}_{\boldsymbol{r}}\cdot\boldsymbol{m}_{\boldsymbol{r}'} + \boldsymbol{D}_{\boldsymbol{r},\boldsymbol{r}'}(t)\cdot(\boldsymbol{m}_{\boldsymbol{r}}\times\boldsymbol{m}_{\boldsymbol{r}'})] - \sum_{\boldsymbol{r}} [\boldsymbol{B}_s + \boldsymbol{B}(t)]\cdot\boldsymbol{m}_{\boldsymbol{r}}, \tag{6.118}$$

$$\boldsymbol{H}_{\boldsymbol{r}}(t) = \sum_{\boldsymbol{r}':n.n.} (J\boldsymbol{m}_{\boldsymbol{r}'} + \boldsymbol{D}_{\boldsymbol{r},\boldsymbol{r}'}(t)\times\boldsymbol{m}_{\boldsymbol{r}'}) + \boldsymbol{B}_s + \boldsymbol{B}(t), \tag{6.119}$$

where $\boldsymbol{D}_{\boldsymbol{r},\boldsymbol{r}'}(t) := g_{\rm me}\boldsymbol{E}(t)\times\boldsymbol{e}_{\boldsymbol{r},\boldsymbol{r}'}$ is the DM coupling induced by the electric field.

To observe a spiral spin texture induced by a laser, consider a spin chain aligned along the x direction irradiated by the laser field traveling along the $(-z)$ direction (see Figs. 6.6 (a) and (b)). The electric field $\boldsymbol{E}(t)$ and magnetic field $\boldsymbol{B}(t)$ are given by

$$\boldsymbol{E}(t) = E_0\,(\sin(\omega t),\cos(\omega t),0)^{\rm tr}, \quad \boldsymbol{B}(t) = \frac{-\boldsymbol{e}_3}{c}\times\boldsymbol{E} = \frac{E_0}{c}\,(\cos(\omega t),-\sin(\omega t),0)^{\rm tr}. \tag{6.120}$$

Although a realistic multiferroic system has a strong three-dimensional nature [356, 357], we here analyze a spin chain for simplicity. From the first-order vV HFE, the effective static field $\boldsymbol{H}_{\boldsymbol{r},F}$ at site $\boldsymbol{r}$ is given from Eq. (6.37) by

$$\begin{aligned}\boldsymbol{H}_{\boldsymbol{r},F} :=& \sum_{\boldsymbol{r}':n.n.} [J\boldsymbol{m}_{\boldsymbol{r}'} + \boldsymbol{D}_{F,\boldsymbol{r},\boldsymbol{r}'} \times \boldsymbol{m}_{\boldsymbol{r}'}] + \boldsymbol{B}_s + \boldsymbol{B}_F \\ & - \alpha \boldsymbol{B}_F \times \boldsymbol{m}_{\boldsymbol{r}} - \sum_{\boldsymbol{r}':n.n.} \frac{\alpha \epsilon_B \epsilon_E}{2m_s(1+\alpha^2)\omega} \begin{pmatrix} m_s^2 + m_{\boldsymbol{r}',y}\delta m_{\boldsymbol{r},y} \\ -m_{\boldsymbol{r}',y}\delta m_{\boldsymbol{r},x} \\ 0 \end{pmatrix}, \end{aligned} \tag{6.121}$$

$$\boldsymbol{D}_{F,\boldsymbol{r},\boldsymbol{r}'} = \frac{\epsilon_E \epsilon_B}{2(1+\alpha^2)\omega} \boldsymbol{e}_{\boldsymbol{r},\boldsymbol{r}'} =: D_F \boldsymbol{e}_{\boldsymbol{r},\boldsymbol{r}'}, \quad \boldsymbol{B}_F = \frac{\epsilon_B^2}{2(1+\alpha^2)\omega} \boldsymbol{e}_3, \tag{6.122}$$

where $\epsilon_E := g_{\rm me} E_0$ and $\epsilon_B := (g\mu_B E_0)/c$ are the normalized electric and magnetic energies, respectively (see App. B.4 for the derivation). Equation (6.121) shows that a synthetic DM field $\boldsymbol{D}_{F,\boldsymbol{r},\boldsymbol{r}'}$ emerges from the combination of the magnetoelectric and Zeeman couplings, in addition to the effective magnetic field $\boldsymbol{B}_F$ that appeared in Sec. 6.4. The strongest magnetic field ϵ_B of terahertz lasers attains 1 - 10 T [358, 359] and the magnitude of $g_{\rm me}$ can be large in a gigahertz region [246, 360–362]. For standard magnets with $J = 0.1$ - 10 meV, both ϵ_E/J and ϵ_B/J can achieve values of 0.1 - 1.

For a weak dissipation $\alpha \ll 1$, $\boldsymbol{H}_{\boldsymbol{r},F}$ is approximated to be

$$\boldsymbol{H}_{\boldsymbol{r},F} \approx \sum_{\boldsymbol{r}':n.n.} [J\boldsymbol{m}_{\boldsymbol{r}'} + \boldsymbol{D}_{F,\boldsymbol{r},\boldsymbol{r}'} \times \boldsymbol{m}_{\boldsymbol{r}'}] + \boldsymbol{B}_s + \boldsymbol{B}_F, \tag{6.123}$$

which is the effective field in the sLLG equation with the static Hamiltonian

$$\mathcal{H}_F = -\sum_{j=1}^{L} [J\boldsymbol{m}_j \cdot \boldsymbol{m}_{j+1} + D_F \mathcal{V}_{j,x} + (\boldsymbol{B}_F + \boldsymbol{B}_s) \cdot \boldsymbol{m}_j]. \tag{6.124}$$

Here, $\mathcal{V}_{j,x} := \boldsymbol{e}_1 \cdot (\boldsymbol{m}_j \times \boldsymbol{m}_{j+1})$ is the vector chirality along the x axis. One can see from Eq. (6.124) that the system exhibits a spiral spin texture through the synthetic DM interaction, leading to the emergence of the vector chirality (see Fig. 6.6 (b)). To maximize the total vector chirality $\mathcal{V}_x^{\rm tot} := \sum_{j=1}^{L} \mathcal{V}_{j,x}$, we introduce a static field $\boldsymbol{B}_s$ along the z axis to cancel out $\boldsymbol{B}_F$, i.e., $\boldsymbol{B}_s + \boldsymbol{B}_F = 0$, which has not been considered in the previous study [76]. With the purely ferromagnetic and DM interactions in Eq. (6.124), a spin spiral state, which is known as the chiral soliton lattice, emerges whose vector chirality per site is given as follows [363, 364]:

$$\frac{\mathcal{V}_x^{\rm tot}}{L} := \frac{1}{L}\sum_j \mathcal{V}_{j,x} = \tan^{-1}\left(\frac{D_F}{J}\right) = \tan^{-1}\left[\frac{\epsilon_E \epsilon_B}{2(1+\alpha^2)\omega J}\right]. \tag{6.125}$$

6.5.2 Emergent vector chirality by laser irradiation

To demonstrate the emergent vector chirality $\mathcal{V}_x^{\rm tot}$ predicted from the effective theory (6.125), we perform a numerical simulation of the time-dependent sLLG equation (6.97) with time-dependent effective magnetic field $\boldsymbol{H}_{\boldsymbol{r}}(t)$ in Eq. (6.119). We fix the Zeeman coupling ϵ_B, Gilbert damping α, and temperature $T_{\rm te}$ as $\epsilon_B/J = 0.2$, $\alpha = 0.05$, and $T_{\rm te} = 0$, respectively.

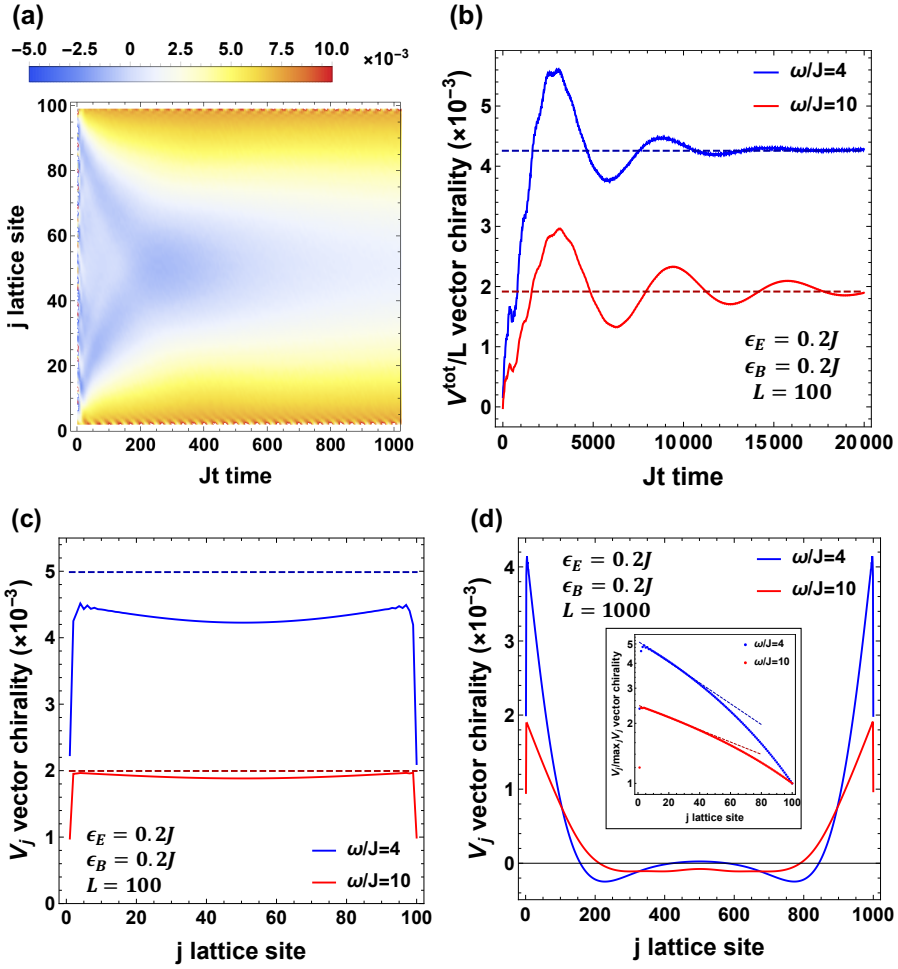

Figure 6.7: (a) Spatiotemporal dynamics of the vector chirality $(\mathcal{V}_{j-1}+\mathcal{V}_{j,x})/2$ with driving frequency $\omega/J = 4$. The vector chirality penetrates into the system from the edges $j = 0, L$, where it spreads uniformly over the system after a sufficiently long time. (b) Time evolution of the spatially averaged vector chirality $\mathcal{V}_x^{\rm tot}/L$ with different driving frequencies $\omega/J = 4$ (blue) and $\omega/J = 10$ (red). The dashed lines show the values at the NESSs. (c), (d) Spatial profile of $\mathcal{V}_{j,x}$ at the NESS for two system sizes ($L = 100$ for (c) and $L = 1000$ for (d)) in the NESSs. The inset in Fig. (d) shows the logarithmic plot of $\mathcal{V}_{j,x}/(\max_j \mathcal{V}_{j,x})$ for the first 100 sites $0 \leq j \leq 100$.

The initial state is set to be the polarized state $\boldsymbol{m}_r = (0, 0, -1)$, and the laser is turned on at $t = 0$. Since $\mathcal{V}_{j,x}$ emerges from the edges as we will see below, we solve the sLLG equation with the open boundary condition, i.e., $\boldsymbol{m}_0 = \boldsymbol{m}_{L+1} = \boldsymbol{0}$.

In Fig. 6.7 (a), the spatiotemporal dynamics of the vector chirality $(\mathcal{V}_{j-1} + \mathcal{V}_{j,x})/2$ is presented, while the time evolution of the spatially averaged vector chirality $\mathcal{V}_x^{\rm tot}/L$ is plotted in Fig. 6.7 (b). In the initial relaxation ($t \leq 200J^{-1}$), the vector chirality enters the system from the edges $j = 0, L$ and spreads uniformly over the system after a sufficiently long time ($t \sim 10^4 J^{-1}$). Through the balance between the drive and damping, the system reaches a NESS with constant $\mathcal{V}_x^{\rm tot}/L$ (dashed lines in Fig. 6.7 (b)). In Figs. 6.7 (c) and (d), we plot the spatial profiles of $\mathcal{V}_{j,x}$ at the NESSs for the chain lengths $L = 100$ and $L = 1000$, respectively. For a larger chain length ($L = 1000$) shown in Fig. 6.7 (d), the vector chirality in the NESSs is localized at the edges. For a smaller system ($L = 100$) shown in Fig. 6.7 (c), on the other hand, the

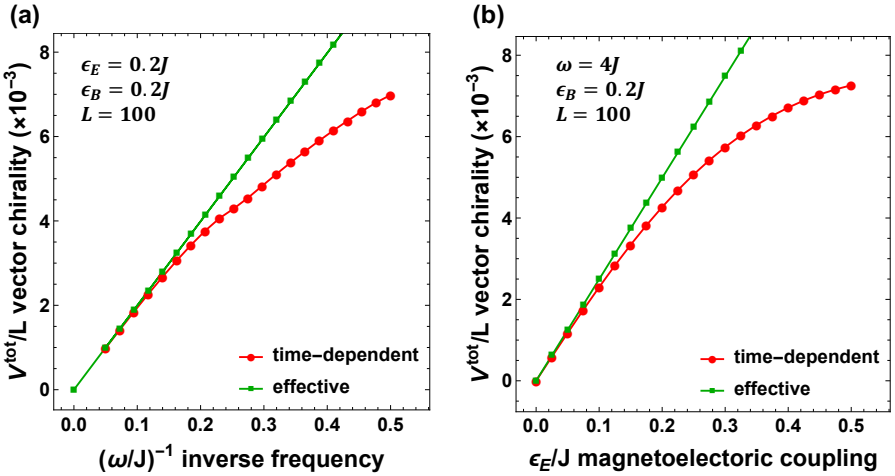

Figure 6.8: (a) Mean vector chirality $\mathcal{V}_x^{\rm tot}/L$ as a function of (a) the driving frequency ω and (b) the magnetoelectric coupling ϵ_E. The red curves are obtained from the solution of the sLLG equation with a time-dependent effective field (6.119) while green ones are drawn from Eq. (6.125) that is derived from the vV HFE.

vector chirality uniformly spreads over the system because of a rather long localization length (e.g., ~ 100 sites for $\omega/J = 4$). Note that the localization length becomes larger for larger ω as shown in the inset of Fig. 6.7 (d). This result implies that one can optically induce a tunable vector chirality in nanomagnets and disordered spin systems where impurities effectively play the role of boundaries.

Finally, we quantitatively check the validity of the effective theory by calculating the dependence of the mean vector chirality $\mathcal{V}_x^{\rm tot}/L$ at the NESS on the frequency ω and the magnetoelectric coupling ϵ_E. As shown in Fig. 6.8, the effective-theory results (6.125) (green curves) show excellent agreement with the vector chirality of the exact NESSs (red curves) in the high-frequency or weak magnetoelectric-coupling regions. In these regions, the synthetic DM interaction D_F is small and hence the HFE is expected to be good, which is consistent with the analytical argument in Sec. 6.2.

Chapter 7

Summary and outlook

7.1 Summary

In this thesis, we have applied Floquet engineering to topological quantum phenomena and nonlinear classical systems.

In Chapter 2, we have briefly reviewed topological quantum phenomena. Starting from a Chern insulator to illustrate basic concepts on topological phases of matter, we have discussed SPT phases, which are topological phases protected by symmetries, and their classification by means of the K theory [101, 102]. In SPT phases such as in the SSH model and the Kitaev chain [135], topological edge modes protected by symmetries emerge. They are immune to disorder that preserves the symmetries. Next, we have overviewed Weyl fermions and its exotic magnetic response, namely the CME [92, 93]. When a magnetic field is applied to a Weyl fermion, a chiral current flows parallel to the magnetic field as a consequence of quantum anomaly [162–165]. However, a pair of Weyl fermions with the opposite chirality must appear in a Weyl semimetal as a consequence of the Nielsen-Ninomiya theorem [90, 91], and therefore the chiral current vanishes. Finally, we have discussed adiabatic pumps and their classification by the K theory [103]. The classification of adiabatic pumps shows the same periodic structure as that of TIs and TSCs, which can be understood from the isomorphism in the K theory.

In Chapter 3, we have discussed some basic concepts of Floquet engineering and presented its applications for controlling topological band structures, superfluids, magnets, and classical systems. The Floquet theorem [30, 31] dictates that the time evolution of a periodically driven quantum system be, on average, generated by a time-periodic Hermitian operator, which is usually called an effective Hamiltonian. The effective Hamiltonian is systematically determined from the HFE, which is a perturbative expansion in powers of the inverse frequency [109, 110]. Although the HFE is a divergent series for a generic many-body system, its truncated series can describe the transient stationary state before heating up to an infinite-temperature state, which is known as the Floquet prethermal state [95, 96, 98, 209]. By means of Floquet engineering, exotic topological band structures have been realized that are difficult (e.g., the Haldane model) and even prohibited (e.g., a single chiral fermion) in a static lattice system [19, 20, 40, 41]. Floquet engineering is also applied to control symmetry-broken phases including superfluids and magnets, which have potential applications to quantum simulations and ultrafast spintronics. Floquet engineering in classical systems has a long history of study dating back to the study of the Kapitza pendulum [13], which is a prototypical example of dynamical stabilization. Recently, isolated classical Hamilton systems are found to approach the Floquet prethermal

states before heating up similarly to isolated quantum systems [115–117].

In Chapter 4, we have briefly reviewed classical stochastic systems described by stochastic differential equations. The time evolution of the probability distribution function is governed by a master equation, which is a linear equation with respect to the probability distribution function. For a Gaussian random variable with the Markovian nature, the master equation becomes a second-order differential equation, which is known as the FP equation. As a concrete example, we have discussed the sLLG equation [120,121], which is a phenomenological equation for a ferromagnet coupled with an environment. In the sLLG equation, a damping and a thermal fluctuation through the interaction with the environment are modeled as the Gilbert-damping term and a random magnetic field, respectively.

In Chapter 5, we have presented a periodically driven three-dimensional lattice system that exhibits a single Weyl fermion in its quasienergy spectrum. Although a single Weyl fermion is prohibited by the Nielsen-Ninomiya theorem in a static lattice system [90, 91], one can surpass this obstacle by using the topology unique to Floquet unitary operators, namely the $(2\pi/T)$-periodicity of the quasienergy. Our model provides the first example of non-adiabatic topological pumps characterized by Floquet unitary operators in higher spatial dimensions. Reflecting the spin-momentum locking of a Weyl fermion, a current flows parallel to the spin polarization under the drive. When a magnetic field is introduced in our driving protocol, a single chiral fermion emerges in the quasienergy spectrum. This leads to the chiral current parallel to the magnetic field, which is a Floquet analog of the CME. Through a detailed numerical analysis, we have confirmed that this chiral current survives over a wide range of parameters, e.g. the fermion density, temperature, and the strength of the magnetic field. In particular, at the half filling and zero temperature, this current takes a quantized value in half of the flux per site. Our model can be implemented in ultracold atomic gases by using the spin-dependent optical lattice or a laser-induced hopping. Generalizing the above discussion, we have given the topological classification of Floquet-Bloch operators in the AZ symmetry classes by means of the K theory. The obtained classification shows the same periodic structure as that of static TIs and TSCs [101, 102]. This result, together with the concrete models constructed in App. A.4, shows that all the gapless band structures in static TIs and TSCs can be realized as quasienergy band structures of periodically driven lattice systems.

In Chapter 6, we have developed the HFE of classical Floquet systems. Unfortunately, we cannot apply the Floquet theorem directly to classical systems owing to the nonlinearity of their EOMs and a random noise modeling a thermal fluctuation. The key idea is using, rather than the EOM itself, the master equation corresponding to the EOM of a system, to which we apply the Floquet theorem and perform the HFE. The HFE of the EOM is obtained from that of the master equation by using the correspondence between the EOM and the master equation. Our formalism is applicable to a wide variety of systems from purely classical to quantum ones in symmetry-broken phases and to both isolated and open ones at any temperature, as long as their EOMs are written as nonlinear (stochastic) ordinary differential equations or they are Markov processes on discrete spaces. By examining the generator of the time evolution, we find that the HFE is found to be convergent for a non-chaotic few-body system. Furthermore, by evaluating the higher-order terms of the expansion, we have found that it is, at least asymptotically, convergent and correctly reproduces the exact non-equilibrium steady state of a generic many-body system. These findings are numerically confirmed in a single-particle system and a many-body system by examples of the Kapitza pendulum with friction and driven magnets described by the sLLG equation, respectively. In both examples, the effective EOMs obtained from the

HFE well approximate the exact time evolution for a long time up to their NESS. This result is in stark contrast to closed systems where the truncated HFE fails to capture their steady states, i.e., infinite-temperature states after the Floquet prethermalization [95, 96, 98, 209]. Finally, we have presented an application to spintronics. We have demonstrated an optical creation of a spin vector chirality in a multiferroic spin chain by a circularly polarized laser, which could be used for ultrafast generation of a spin current.

7.2 Outlook

7.2.1 Floquet engineering of topological phenomena

First, while the topological classification of the Floquet-Bloch operators has been achieved and concrete models have been constructed, their physical implications are yet to be clarified. Remarkably, the obtained classification is found to be different from that of adiabatic pumps [103], indicating that non-adiabatic pumps and adiabatic ones may feature different dynamical responses, e.g., topologically protected transport phenomena and the robustness against disorder. It would be interesting to study them in detail based on the models presented in App. A.4 for exploring topological phenomena unique to Floquet systems.

Secondly, the effect of the particle correlation on our model should be investigated since it is relevant in solid-state systems and ultracold atomic gases, and hence is expected to affect the chiral current of the Floquet CME. Moreover, it is well-known that the strong correlation dramatically changes the topological classification both in static and Floquet systems, such as the reduction of a topological index [365, 366] and anomalous TIs and TSCs characterized by a rational topological index [367–369]. Therefore, the interaction effect may alter the topological classification on non-adiabatic pumps established in this theses, where exotic phases of matter might emerge.

7.2.2 Floquet engineering of nonlinear systems

First, it would be interesting to study application to Floquet engineering in solids. Although it is analyzed as isolated systems in most cases for simplicity [72–74, 76–78, 370, 371], a coupling with an environment is unavoidable in a realistic solid-state system. Furthermore, numerical simulations of many-body systems are limited to small system sizes because of the exponentially increasing dimension of the Hilbert spaces. Our approach allows us to simulate driven classical systems with considerably larger system sizes than quantum ones, and moreover, we can take into account the effect of dissipation and temperature at the same time. Non-equilibrium phase transitions and critical phenomena have been intensively studied in driven dissipative classical many-body systems [308, 372–375] and our theory can provide a reliable framework for predicting and even controlling them.

Secondly, a master equation offers a natural realization of the non-Hermitian Schrödinger equation as mentioned in Sec. 6.1. Recently, considerable efforts have been made to explore non-Hermitian physics both experimentally and theoretically using the state-of-art experimental techniques in atomic, molecular, and optical physics, in particular their topological aspects [376–389]. Remarkably, the topological classification of static non-Hermitian systems [5, 390, 391] is found to be significantly different from the Hermitian counterpart [102, 143, 392]. Besides, Hermitian Floquet systems host unique topological phenomena that have no counterparts in

static ones including anomalous TIs and TSCs [85, 87, 225] and gapless topological spectra [1, 85, 89]. Therefore, it is natural to expect that, through the interplay between the non-Hermiticity and a periodic drive, non-Hermitian Floquet systems also host unique topological phases, which are different from both Hermitian Floquet systems and non-Hermitian static systems. While non-Hermitian Floquet systems have been studied in the context of quantum walks [393–395], their realizations and properties of topological edge states in classical stochastic systems remain largely unexplored.

Finally, it would be interesting to clarify the role of the integrability of a system in the relaxation to a NESS. In the context of periodically driven isolated quantum systems, it is known that integrable systems show quite different relaxation dynamics from non-integrable ones. More precisely, the heating is suppressed for a high-frequency drive in an integrable system because of the presence of an infinite number of conserved quantities [94, 205, 208]. While a similar scenario may hold for a driven dissipative system, i.e., an integrable one and a non-integrable one exhibit different relaxation processes and approach different NESSs, no analytical and numerical studies have been done so far. The ASEP is appropriate to test this scenario both analytically and numerically. Its master equation can be mapped to a non-Hermitian XXZ chain, which can be solved by the Bethe-ansatz method [396,397]. Its integrability can be controlled by considering a step-wise driving protocol or by introducing an additional hopping term that breaks the integrability.

Appendix A

Details of mathematics and derivations in Chapter 5

In App. A.1, we provide the construction of the Floquet-Bloch operator $U(\boldsymbol{k})$ in Eq. (5.10), which has the nontrivial three-dimensional winding number on S^3. In App. A.2, we discuss the boundary condition of the Floquet-Bloch operator $U(\boldsymbol{k})$. In App. A.3, we derive the expression (5.32) of the pumped fermion charge. In App. A.4, we present concrete models with the Floquet-Bloch operators that feature lattice-prohibited band structures in all the symmetry classes and spatial dimensionalities up to three.

A.1 Construction of the Floquet-Bloch operator $U(k)$

A nontrivial map from $\mathbb{T}^3$ to S^3 is generally constructed from the smash product [272], which is a mathematical tool for constructing a manifold from two manifolds. Let X (Y) be a manifold and x_0 (y_0) be a point on X (Y). The smash product $X \wedge Y$ is defined as the product space $X \times Y$ with the space $(\{x_0\} \times Y) \cup (X \times \{y_0\})$ identified with a point on $X \times Y$. For example, the smash product $S^1 \wedge S^1$, with S^1 being a circle, is isomorphic to the two-dimensional sphere S^2. We parametrize these two circles as

$$S^1 = \{k| -\pi \leq k \leq \pi\}\,,\ S^1 = \{k'| -\pi \leq k' \leq \pi\}\,, \tag{A.1}$$

and take x_0 and y_0 as $k = \pm\pi$ and $k' = \pm\pi$, respectively. Then, the product space $S^1 \times S^1$ and its subspace,

$$(\{x_0\} \times Y) \cup (X \times \{y_0\}) = \{(\pm\pi, k')| -\pi \leq k' \leq \pi\} \cup \{(k, \pm\pi)| -\pi \leq k \leq \pi\}\,, \tag{A.2}$$

are identified with the Brillouin zone $\mathbb{T}^2 = [-\pi, \pi]^2$ of a square lattice and its boundary, respectively. As we can obtain S^2 from $\mathbb{T}^2$ by wrapping up the square $[-\pi, \pi]^2$, the smash product $S^1 \wedge S^1$, i.e., the square $[-\pi, \pi]^2$ with its boundary identified with a point, is isomorphic to S^2. The isomorphic mapping $f_{1,1}$ is given by

$$f_{1,1}(k, k') := \left[-2\cos^2\left(\frac{k}{2}\right)\cos^2\left(\frac{k'}{2}\right) + 1\right]\boldsymbol{e}_1 - \cos^2\left(\frac{k}{2}\right)\sin(k')\,\boldsymbol{e}_2 - \sin(k)\cos\left(\frac{k'}{2}\right)\boldsymbol{e}_3, \tag{A.3}$$

where $\boldsymbol{e}_1 = (1,0,0)^{\rm tr}$, $\boldsymbol{e}_2 = (0,1,0)^{\rm tr}$, and $\boldsymbol{e}_3 = (0,0,1)^{\rm tr}$ are the unit vectors in three orthogonal directions.

As we will show below, the nontrivial map $U(\boldsymbol{k})$ is constructed from the following isomorphism [272]:

$$S^1 \wedge S^1 \wedge S^1 \cong S^2 \wedge S^1 \cong S^3. \tag{A.4}$$

Let $\boldsymbol{\xi} = (\xi_1, \xi_2, \xi_3)^{\rm tr}$ be a unit vector on S^2, i.e., $\sum_{i=1}^3 (\xi_i)^2 = 1$, and $k_1 \in [-\pi, \pi] \cong S^1$. The isomorphic mapping $f\colon S^2 \times S^1 \to S^3$ of the second isomorphism in Eq. (A.4) is given by

$$f_{2,1}(\boldsymbol{\xi}, k_1) = \frac{\xi_1 - 1}{2} \sin(k_1)\, \boldsymbol{a}_1 + \cos\left(\frac{k_1}{2}\right)(\xi_3 \boldsymbol{a}_2 + \xi_2 \boldsymbol{a}_3) - \left[\sin^2\left(\frac{k_1}{2}\right) + \cos^2\left(\frac{k_1}{2}\right)\xi_1\right]\boldsymbol{a}_4, \tag{A.5}$$

where $\boldsymbol{a}_i$ $(i = 1,2,3,4)$ are unit vectors in four dimensions defined by

$$\boldsymbol{a}_1 = (1,0,0,0)^{\rm tr}, \quad \boldsymbol{a}_2 = (0,1,0,0)^{\rm tr}, \quad \boldsymbol{a}_3 = (0,0,1,0)^{\rm tr}, \quad \boldsymbol{a}_4 = (0,0,0,1)^{\rm tr}. \tag{A.6}$$

Then, the composition of $f_{1,1}$ and $f_{2,1}$ defined by

$$\widetilde{\boldsymbol{u}}(\boldsymbol{k}) = f_{2,1}\left[f_{1,1}(k_2, k_3), k_1\right] \tag{A.7}$$

gives an isomorphic mapping between $S^1 \wedge S^1 \wedge S^1$ and S^3. Since the isomorphic mapping $f_{2,1}\left[f_{1,1}(k_2,k_3), k_1\right]$ to S^3 naturally has a unit winding number and the domain of $S^1 \wedge S^1 \wedge S^1$ and that of $\mathbb{T}^3$ are both cubic $[-\pi,\pi]^3$, $\widetilde{\boldsymbol{u}}(\boldsymbol{k})$ has a unit winding number:

$$W = \int \frac{d\boldsymbol{k}}{2\pi^2} \sum_{i,j,k,l=1}^{4} \epsilon_{ijkl} \widetilde{u}_i(\boldsymbol{k}) \frac{\partial \widetilde{u}_j(\boldsymbol{k})}{\partial k_1} \frac{\partial \widetilde{u}_k(\boldsymbol{k})}{\partial k_2} \frac{\partial \widetilde{u}_l(\boldsymbol{k})}{\partial k_3} = 1. \tag{A.8}$$

We note that $\widetilde{\boldsymbol{u}}(\boldsymbol{k})$ stays constant on the boundary of the Brillouin zone $\mathbb{T}^3 = [-\pi,\pi]^3$:

$$\widetilde{\boldsymbol{u}}(\boldsymbol{k}) = (0,0,0,-1)\,. \tag{A.9}$$

We define a continuous deformation $\widetilde{\boldsymbol{u}}_s(\boldsymbol{k}) := R_{23}(sk_1/2)\widetilde{\boldsymbol{u}}(\boldsymbol{k})$ with a deformation parameter $s(\in [0,1])$, where $R_{23}(\theta)$ is a rotation matrix defined by

$$R_{23}(\theta) := \begin{pmatrix} 1 & 0 & 0 & 0 \\ 0 & \cos\theta & -\sin\theta & 0 \\ 0 & \sin\theta & \cos\theta & 0 \\ 0 & 0 & 0 & 1 \end{pmatrix}. \tag{A.10}$$

It follows from Eq. (A.9) that $\widetilde{\boldsymbol{u}}_s(\boldsymbol{k}) = (0,0,0,-1)$ on the boundary of $\mathbb{T}^3$ and hence $\widetilde{\boldsymbol{u}}_s(\boldsymbol{k})$ is continuous on $\mathbb{T}^3$. Furthermore, combining Eqs. (5.15), (A.3), and (A.5), we obtain

$$\widetilde{\boldsymbol{u}}_{s=0}(\boldsymbol{k}) = \widetilde{\boldsymbol{u}}(\boldsymbol{k}), \quad \widetilde{\boldsymbol{u}}_{s=1}(\boldsymbol{k}) = \boldsymbol{u}(\boldsymbol{k}), \tag{A.11}$$

where $\boldsymbol{u}(\boldsymbol{k}) = [u_1(\boldsymbol{k}), u_2(\boldsymbol{k}), u_3(\boldsymbol{k}), u_4(\boldsymbol{k})]$ is defined in Eq. (5.15). Therefore, $\boldsymbol{u}(\boldsymbol{k})$ is also an isomorphic mapping between $S^1 \wedge S^1 \wedge S^1$ and S^3 and has a unit winding number $W = 1$.

A.2 Boundary condition of the Floquet-Bloch operator $U(k)$

From the relation

$$U_j^{\pm}(k) = \mathrm{e}^{\frac{\mp ik}{2}} \left[P_j^{\pm} \mathrm{e}^{\frac{\mp ik}{2}} + P_j^{\mp} \mathrm{e}^{\frac{\pm ik}{2}} \right] = \mathrm{e}^{\frac{\mp ik}{2}} \widetilde{U}_j(k), \tag{A.12}$$

where $\widetilde{U}_j(k) := \mathrm{e}^{-i\frac{\sigma_j}{2}k}$, we have

$$U(\boldsymbol{k}) = \widetilde{U}_1(k_1)\widetilde{U}_3\left(\frac{k_3}{2}\right)\widetilde{U}_2(k_2)\widetilde{U}_3\left(\frac{k_3}{2}\right)\widetilde{U}_1(k_1)\widetilde{U}_3\left(\frac{k_3}{2}\right)\widetilde{U}_2(k_2)\widetilde{U}_3\left(\frac{k_3}{2}\right). \tag{A.13}$$

Using $\widetilde{U}_j(\pm\pi) = \mp i\sigma_j, \sigma_1\widetilde{U}_2(k)\sigma_1 = \widetilde{U}_2(-k)$ and $\sigma_1\widetilde{U}_3(k)\sigma_1 = \widetilde{U}_3(-k)$, we have

$$\begin{aligned} U(\pm\pi, k_2, k_3) =& -\sigma_1\widetilde{U}_3\left(\frac{k_3}{2}\right)\widetilde{U}_2(k_2)\widetilde{U}_3\left(\frac{k_3}{2}\right)\sigma_1\widetilde{U}_3\left(\frac{k_3}{2}\right)\widetilde{U}_2(k_2)\widetilde{U}_3\left(\frac{k_3}{2}\right) && \text{(A.14)} \\ =& -\widetilde{U}_3\left(-\frac{k_3}{2}\right)\widetilde{U}_2(-k_2)\widetilde{U}_3\left(-\frac{k_3}{2}\right)\widetilde{U}_3\left(\frac{k_3}{2}\right)\widetilde{U}_2(k_2)\widetilde{U}_3\left(\frac{k_3}{2}\right) = -\sigma_0. && \text{(A.15)} \end{aligned}$$

Similarly, we have

$$\begin{aligned} U(k_1, \pm\pi, k_3) =& -\widetilde{U}_1(k_1)\widetilde{U}_3\left(\frac{k_3}{2}\right)\sigma_2\widetilde{U}_3\left(\frac{k_3}{2}\right)\widetilde{U}_1(k_1)\widetilde{U}_3\left(\frac{k_3}{2}\right)\sigma_2\widetilde{U}_3\left(\frac{k_3}{2}\right) && \text{(A.16)} \\ =& -\widetilde{U}_1(k_1)\widetilde{U}_3\left(\frac{k_3}{2}\right)\widetilde{U}_3\left(\frac{-k_3}{2}\right)\widetilde{U}_1(-k_1)\widetilde{U}_3\left(\frac{-k_3}{2}\right)\widetilde{U}_3\left(\frac{k_3}{2}\right) = -\sigma_0, && \text{(A.17)} \end{aligned}$$

where we use $\sigma_2\widetilde{U}_1(k)\sigma_2 = \widetilde{U}_1(-k)$ and $\sigma_2\widetilde{U}_3(k)\sigma_2 = \widetilde{U}_3(-k)$ in the second and third lines, respectively. By a straightforward calculation of the product of 2×2 matrices, we have

$$\widetilde{U}_3\left(\pm\frac{\pi}{2}\right)\widetilde{U}_2(k_2)\widetilde{U}_3\left(\pm\frac{\pi}{2}\right) = \mp i\sigma_3\widetilde{U}_1(\pm k_2), \tag{A.18}$$

and thus we obtain

$$\begin{aligned} U(k_1, k_2, \pm\pi) =& \widetilde{U}_1(k_1)\left[\mp i\sigma_3\widetilde{U}_1(\pm k_2)\right]\widetilde{U}_1(k_1)\left[\mp i\sigma_3\widetilde{U}_1(\pm k_2)\right] && \text{(A.19)} \\ =& -\widetilde{U}_1(k_1)\widetilde{U}_1(\mp k_2)\widetilde{U}_1(-k_1)\widetilde{U}_1(\pm k_2) = -\sigma_0, && \text{(A.20)} \end{aligned}$$

which completes the derivation of the boundary condition $U(\boldsymbol{k}) = -\sigma_0$.

A.3 Derivation of Eq. (5.32)

For the time-evolution operator $U(k_i, t) := \mathcal{T}_t \mathrm{e}^{-i\int_0^t dt' H(k_i, t')}$ with fixed momentum k_i $(i = 1, 2, 3)$, we have

$$\frac{\partial U(k_i, T)}{\partial k_i} = -iU(k_i, T)\int_0^T dt\ U^{\dagger}(k_i, t)\frac{\partial H(k_i, t)}{\partial k_i}U(k_i, t). \tag{A.21}$$

From the solution of the Schödinger equation, we have

$$J(t) = \int_{-\pi}^{\pi} \frac{dk_i}{2\pi} \mathrm{Tr}\left[\rho_0 U^\dagger(k_i,t) \frac{\partial H(k_i,t)}{\partial k_i} U(k_i,t)\right], \tag{A.22}$$

and hence obtain

$$\begin{aligned}\Delta Q_i &= i\int_{-\pi}^{\pi} \frac{dk_i}{2\pi} \mathrm{Tr}\left[\rho_0 U^\dagger(k_i,T) \frac{\partial U(k_i,T)}{\partial k_i}\right] \\ &= \sum_{\gamma,k_i} f_\gamma(k_i) \frac{\partial \epsilon_\gamma(k_i)}{\partial k_i},\end{aligned} \tag{A.23}$$

where we use $f_\gamma(k_i) := \langle \gamma, k_i|\rho_0|\gamma, k_i\rangle$ and $U(k_i,T) = \sum_\gamma \mathrm{e}^{-i\epsilon_\gamma(k_i)T} |\gamma,k_i\rangle \langle\gamma,k_i|$ in the last line, with γ being the band label or quantum numbers other than k_i. Thus, the derivation has been completed.

A.4 Floquet-Bloch operators in the other symmetry classes

A.4.1 Topological invariant in each symmetry class

Before presenting concrete lattice models, we identify the topological invariants for Floquet-Bloch operators for given symmetry classes. For a Floquet-Bloch operator $U(\boldsymbol{k})$ in the symmetry class $(\mathbb{F}, s)$, its topological invariant is given by that of the Hermitian matrix $H_u(\boldsymbol{k})$ in the symmetry class $(\mathbb{F}, s-1)$, which is defined as follows:

$$H_u(\boldsymbol{k}) := \begin{cases} \gamma\Gamma U(\boldsymbol{k}) & \text{with CS } \Gamma; \\ \sigma_+ \otimes U(\boldsymbol{k}) + \sigma_- \otimes U^\dagger(\boldsymbol{k}) & \text{without CS } \Gamma. \end{cases} \tag{A.24}$$

Here, γ is a complex number defined by $\gamma^2 = \Gamma^2 = \pm 1$. We note that, without the CS, $H_u(\boldsymbol{k})$ is nothing but its "Q matrix" [101] since it has a flattened spectrum $[H_u(\boldsymbol{k})]^2 = 1$. As we can see from Tab. 5.1, there are fifteen nontrivial classes in spatial dimensionality $d = 1, 2, 3$, for which we identify their topological invariants one by one.

Class A $(\mathbb{F}, s, d) = (\mathbb{C}, 0, 1)$, class D $(\mathbb{F}, s, d) = (\mathbb{R}, 2, 1)$, and class CII $(\mathbb{F}, s, d) = (\mathbb{R}, 6, 1)$: one-dimensional winding number

Since the CS is absent in these classes, $H_u(\boldsymbol{k})$ is given by $H_u(\boldsymbol{k}) = \sigma_+ \otimes U(\boldsymbol{k}) + \sigma_- \otimes U^\dagger(\boldsymbol{k})$, where its topological invariant is given by the one-dimensional winding number

$$\nu_{1\mathrm{d}} := i\int_{-\pi}^{\pi} \frac{dk_1}{2\pi} \mathrm{Tr}\left[U^\dagger(k_1)\partial_{k_i} U(k_1)\right]. \tag{A.25}$$

Class AIII $(\mathbb{F}, s, d) = (\mathbb{C}, 1, 2)$**, class DIII** $(\mathbb{F}, s, d) = (\mathbb{R}, 3, 2)$**, and class CI** $(\mathbb{F}, s, d) = (\mathbb{R}, 7, 2)$**: Chern number**

Since the CS Γ is present these classes, we have $H_u(\boldsymbol{k}) = \gamma\Gamma U(\boldsymbol{k})$, where its topological number is the Chern number

$$Ch_1 := \int \frac{d\boldsymbol{k}}{2\pi} \left[\partial_{k_x}\mathcal{A}_{k_y}(\boldsymbol{k}) - \partial_{k_y}\mathcal{A}_{k_x}(\boldsymbol{k})\right]. \tag{A.26}$$

Here, $\mathcal{A}_{k_i}$ is the Berry connection of the Bloch states $|\alpha, \boldsymbol{k}\rangle$ of the lower bands of $H_u(\boldsymbol{k})$:

$$\mathcal{A}_{k_i} := -i \sum_{\alpha} \langle \alpha, \boldsymbol{k}| \, \partial_{k_i} \, |\alpha, \boldsymbol{k}\rangle . \tag{A.27}$$

Class A $(\mathbb{F}, s, d) = (\mathbb{C}, 0, 3)$**, class AI** $(\mathbb{F}, s, d) = (\mathbb{R}, 0, 3)$**, and class AII** $(\mathbb{F}, s, d) = (\mathbb{R}, 4, 3)$**: three-dimensional winding number**

Since the CS is absent in these classes, $H_u(\boldsymbol{k})$ is given by $H_u(\boldsymbol{k}) = \sigma_+ \otimes U(\boldsymbol{k}) + \sigma_- \otimes U^\dagger(\boldsymbol{k})$. Its topological invariant is given by the three-dimensional winding number

$$W := -\int \frac{d\boldsymbol{k}}{24\pi^2} \sum_{i,j,k=1}^{3} \epsilon^{ijk} \mathrm{Tr}\left[R_i R_j R_k\right], \tag{A.28}$$

with $R_i := U_{3d}^\dagger(\boldsymbol{k})\partial_{k_i}U(\boldsymbol{k})$.

Class DIII $(\mathbb{F}, s, d) = (\mathbb{R}, 3, 1)$**: Chern-Simons integral**

Since the CS Γ is present in this class, we have $H_u(\boldsymbol{k}) = \gamma\Gamma U(\boldsymbol{k})$, where its topological invariant is given by the Chern-Simons integral of the berry connection $\mathcal{A}_{k_1}$ defined in Eq. (A.27):

$$\nu_{\mathrm{CS}} := \exp\left(i \int_{-\pi}^{\pi} \frac{dk_1}{2\pi} \mathcal{A}_{k_1}\right). \tag{A.29}$$

Class CII $(\mathbb{F}, s, d) = (\mathbb{R}, 6, 3)$**:** $\mathbb{Z}_2$ **invariant**

Since the CS Γ is present in this class, we have $H_u(\boldsymbol{k}) = \gamma\Gamma U(\boldsymbol{k})$. Although the topological invariant ν_2 in this class does not have a closed integral expression, it can be defined operationally by the dimensional reduction [128, 392] or the Moore-Balents argument [398, 399].

Class AII $(\mathbb{F}, s, d) = (\mathbb{R}, 4, 1), (\mathbb{R}, 4, 2)$ **and class CII** $(\mathbb{F}, s, d) = (\mathbb{R}, 5, 2), (\mathbb{R}, 5, 3)$**:** $\mathbb{Z}_2$ **Parity**

The topological invariants in these classes are written as the product of the parities at TR time-reversal invariant momenta:

$$\nu_{\mathrm{par}} = \prod_{\boldsymbol{k}} \frac{\mathrm{Pf}\left[w(\boldsymbol{k})\right]}{\sqrt{\det\left[w(\boldsymbol{k})\right]}}, \tag{A.30}$$

where the product is taken over all the time-reversal invariant momenta. Here, $w(\boldsymbol{k})$ is the sewing matrix that satisfies

$$[w(\boldsymbol{k})]^{\rm tr} = -w(-\boldsymbol{k}). \tag{A.31}$$

Therefore, $w(\boldsymbol{k})$ becomes an antisymmetric matrix at time-reversal invariant momenta, where $\mathrm{Pf}\,[w(\boldsymbol{k})]$ denotes the Pfaffian of $w(\boldsymbol{k})$. Let $V_{\rm TRS}$ be the unitary matrix of Θ in class AII, i.e. $\Theta = V_{\rm TRS}\mathcal{K}$, and $|u(\boldsymbol{k})\rangle$ be the Bloch state of the lower band of $\gamma\Gamma U(\boldsymbol{k})$ for class CII. Then, $w(\boldsymbol{k})$ is defined as follows:

$$w(\boldsymbol{k}) := \begin{cases} V_{\rm TRS}^\dagger U(\boldsymbol{k}) & \text{class AII;} \\ \langle u(-\boldsymbol{k})|C|u(\boldsymbol{k})\rangle & \text{class CII.} \end{cases} \tag{A.32}$$

Note that Eq. (A.31) is automatically satisfied from the TRS $\Theta U(\boldsymbol{k})\Theta^\dagger = U^\dagger(-\boldsymbol{k})$ for class AII and from the Kramers theorem for the PHS C with $C^2 = -1$ for class CII.

For class AII, the corresponding Hamiltonian $H_u(\boldsymbol{k}) = \sigma_+ \otimes U(\boldsymbol{k}) + \sigma_- \otimes U^\dagger(\boldsymbol{k})$ have the TRS $\Theta_1 := \sigma_1 \otimes \Theta$. By the unitary matrix $\widetilde{V}$ defined by

$$V = \begin{pmatrix} V_{\rm TRS} & 0 \\ 0 & -\mathbf{1}_N \end{pmatrix}, \tag{A.33}$$

the TRS Θ_1 and $H_u(\boldsymbol{k})$ are transformed as follows:

$$\widetilde{V}^\dagger \Theta_1 \widetilde{V} = i\sigma_2 \otimes \mathbf{1}_N \mathcal{K}, \quad \widetilde{V}^\dagger H_u(\boldsymbol{k}) \widetilde{V} = -\sigma_+ \otimes w(\boldsymbol{k}) - \sigma_- \otimes w^\dagger(\boldsymbol{k}), \tag{A.34}$$

where $w(\boldsymbol{k})$ is defined in Eq. (A.32). From the topological invariants in class DIII [400,401], the topological invariant of $H_u(\boldsymbol{k})$ is given by Eq. (A.30) . For class CII, we have $H_u(\boldsymbol{k}) = \gamma\Gamma U(\boldsymbol{k})$, which is in class AII with the TRS C, i.e. $CH_u(\boldsymbol{k})C^\dagger = H_u(-\boldsymbol{k})$. Thus, its topological invariant is given by the $\mathbb{Z}_2$-parity in Eq. (A.30), where the with the sewing matrix is defined as Eq. (A.32) [131, 184, 402, 403].

The above results are summarized from the first to fourth columns of Tab. A.1.

A.4.2 General method for model construction

In what follows, we present concrete lattice models with topologically nontrivial Floquet-Bloch operators in all the spatial dimensionalities up to three and the symmetry classes except for class A.

Let $\widetilde{\sigma}_1, \widetilde{\sigma}_2, \widetilde{\sigma}_3$ be the matrices that satisfy the anticommutation relation

$$\widetilde{\sigma}_i \widetilde{\sigma}_j + \widetilde{\sigma}_j \widetilde{\sigma}_i = 2\delta_{ij} \widetilde{\sigma}_0, \tag{A.35}$$

where $\widetilde{\sigma}_0$ is the identity matrix. Then, we define the Floquet-Bloch operators $U_{1d}(k_1), U_{2d}(k_1, k_2)$, and $U_{3d}(k_1, k_2, k_3)$ as follows:

$$U_{3d}(k_1, k_2, k_3) := \mathrm{e}^{\frac{-ik_1\widetilde{\sigma}_1}{4}} \mathrm{e}^{\frac{-ik_2\widetilde{\sigma}_2}{4}} \mathrm{e}^{\frac{-ik_3\widetilde{\sigma}_3}{2}} \mathrm{e}^{\frac{-ik_2\widetilde{\sigma}_2}{4}} \mathrm{e}^{\frac{-ik_1\widetilde{\sigma}_1}{2}} \mathrm{e}^{\frac{-ik_2\widetilde{\sigma}_2}{4}} \mathrm{e}^{\frac{-ik_3\widetilde{\sigma}_3}{2}} \mathrm{e}^{\frac{-ik_2\widetilde{\sigma}_2}{4}} \mathrm{e}^{\frac{-ik_1\widetilde{\sigma}_1}{4}}, \tag{A.36}$$

$$U_{2d}(k_1, k_2) := U_{3d}(k_1, k_2, 0) = \mathrm{e}^{\frac{-ik_1\widetilde{\sigma}_1}{4}} \mathrm{e}^{\frac{-ik_2\widetilde{\sigma}_2}{2}} \mathrm{e}^{\frac{-ik_1\widetilde{\sigma}_1}{2}} \mathrm{e}^{\frac{-ik_2\widetilde{\sigma}_2}{2}} \mathrm{e}^{\frac{-ik_1\widetilde{\sigma}_1}{4}}, \tag{A.37}$$

$$U_{1d}(k_1) := U_{2d}(k_1, 0) = \exp\left(-ik_1\widetilde{\sigma}_1\right). \tag{A.38}$$

Table A.1: Topological invariants for nontrivial Floquet-Bloch operators for spatial dimensionality $d = 1, 2, 3$ in the symmetry class except for class A. The notations are the same as in Tab. 2.1 and the fourth column represents the pair of the topological index and the topological number $K^{\mathrm{FB}}(\mathbb{F}, s, d)$. The topological indices $\nu_{1d}, Ch_1, W, \nu_{\mathrm{CS}}$, and ν_{par} are the one-dimensional winding number (A.25), the Chern number (A.26), the three-dimensional winding number (A.28), the Chern-Simons invariant (A.29), and the $\mathbb{Z}_2$ parity (A.25), respectively. Although ν_2 is not expressed as a closed integral form, it can be defined operationally by the dimensional reduction or the Moore-Balents argument. The anticommuting matrices $\widetilde{\boldsymbol{\sigma}}$ are the basis of the Floquet-Bloch operators in Eqs. (A.36), (A.37), and (A.38).

class	s	d	invariant	Θ	C	Γ	$\widetilde{\boldsymbol{\sigma}}$
D	2	1	$(\nu_{1d}, \mathbb{Z})$	0	$\sigma_1\mathcal{K}$	0	(σ_2)
C	6	1	$(\nu_{1d}, 2\mathbb{Z})$	0	$i\sigma_0 \otimes \tau_2\mathcal{K}$	0	$(\sigma_2 \otimes \tau_1)$
AIII	1	2	$(Ch_1, \mathbb{Z})$	0	0	σ_3	(σ_1, σ_2)
DIII	3	2	$(Ch_1, \mathbb{Z})$	$i\sigma_2 \otimes \tau_0\mathcal{K}$	$\sigma_1 \otimes \tau_0\mathcal{K}$	$\sigma_3 \otimes \tau_0$	$(\sigma_1 \otimes \tau_0, \sigma_2 \otimes \tau_0)$
CI	7	2	$(Ch_1, 2\mathbb{Z})$	$\sigma_1 \otimes \tau_0\mathcal{K}$	$i\sigma_0 \otimes \tau_2\mathcal{K}$	$i\sigma_1 \otimes \tau_2$	$(\sigma_2 \otimes \tau_2, \sigma_3 \otimes \tau_0)$
AI	0	3	$(W, 2\mathbb{Z})$	$\sigma_1 \otimes \tau_0\mathcal{K}$	0	0	$(\sigma_1 \otimes \tau_2, \sigma_2 \otimes \tau_2, \sigma_3 \otimes \tau_0)$
AII	4	3	$(W, \mathbb{Z})$	$i\sigma_2 \otimes \tau_0\mathcal{K}$	0	0	$(\sigma_1 \otimes \tau_0, \sigma_2 \otimes \tau_0, \sigma_3 \otimes \tau_0)$
DIII	3	1	$(\nu_{\mathrm{CS}}, \mathbb{Z}_2)$	$i\sigma_2 \otimes \tau_0\mathcal{K}$	$\sigma_1 \otimes \tau_0\mathcal{K}$	$\sigma_3 \otimes \tau_0$	$(\sigma_1 \otimes \tau_0)$
C	6	3	$(\nu_2, \mathbb{Z}_2)$	0	$i\sigma_0 \otimes \tau_2\mathcal{K}$	0	$(\sigma_2 \otimes \tau_1, \sigma_3 \otimes \tau_0, \sigma_1 \otimes \tau_0)$
AII	4	1	$(\nu_{\mathrm{par}}, \mathbb{Z}_2)$	$i\sigma_2 \otimes \tau_0\mathcal{K}$	0	0	$(\sigma_1 \otimes \tau_0)$
AII	4	2	$(\nu_{\mathrm{par}}, \mathbb{Z}_2)$	$i\sigma_2 \otimes \tau_0\mathcal{K}$	0	0	$(\sigma_1 \otimes \tau_0, \sigma_2 \otimes \tau_0)$
CII	5	2	$(\nu_{\mathrm{par}}, \mathbb{Z}_2)$	$i\sigma_2 \otimes \tau_0\mathcal{K}$	$i\sigma_0 \otimes \tau_2\mathcal{K}$	$\sigma_2 \otimes \tau_2$	$(\sigma_1 \otimes \tau_0, \sigma_2 \otimes \tau_1)$
CII	5	3	$(\nu_{\mathrm{par}}, \mathbb{Z}_2)$	$i\sigma_2 \otimes \tau_0\mathcal{K}$	$i\sigma_0 \otimes \tau_2\mathcal{K}$	$\sigma_2 \otimes \tau_2$	$(\sigma_1 \otimes \tau_0, \sigma_2 \otimes \tau_1, \sigma_3 \otimes \tau_0)$

Using the anticommutation relation (A.35), $U_{3d}(k_1, k_2, k_3)$ can be rewritten in terms of $\widetilde{\sigma}_i$ as follows:

$$U_{3d}(k_1, k_2, k_3) = u_4(k_1, k_2, k_3)\widetilde{\sigma}_0 + i\left[u_1(k_1, k_2, k_3)\widetilde{\sigma}_1 + u_2(k_1, k_2, k_3)\widetilde{\sigma}_2 + u_3(k_1, k_2, k_3)\widetilde{\sigma}_3\right], \tag{A.39}$$

$$\begin{cases} u_1(k_1, k_2, k_3) := -\sin(k_1)\cos^2\left(\frac{k_2}{2}\right)\cos^2\left(\frac{k_3}{2}\right); \\ u_2(k_1, k_2, k_3) := -\sin(k_2)\cos\left(\frac{k_1}{2}\right)\cos^2\left(\frac{k_3}{2}\right); \\ u_3(k_1, k_2, k_3) := -\sin(k_3)\cos\left(\frac{k_1}{2}\right)\cos\left(\frac{k_2}{2}\right); \\ u_4(k_1, k_2, k_3) := 2\cos^2\left(\frac{k_1}{2}\right)\cos^2\left(\frac{k_2}{2}\right)\cos^2\left(\frac{k_3}{2}\right) - 1. \end{cases} \tag{A.40}$$

Note that $U_{3d}(k_1, k_2, k_3)$ satisfies the periodic boundary condition of the Brillouin zone because $U_{3d}(k_1, k_2, k_3) = -\widetilde{\sigma}_0$ on its boundary.

In what follows, we first find the Floquet-Bloch operators with the symmetry conditions (5.62), and then construct time-dependent Hamiltonians with the symmetry conditions (5.61). Let $\boldsymbol{k}$ be the d-dimensional momentum in the Brillouin zone $[-\pi, \pi]^d$ and $\widetilde{\boldsymbol{\sigma}} := (\widetilde{\sigma}_1, \cdots, \widetilde{\sigma}_d)$ be the first d elements in $\{\widetilde{\sigma}_1, \widetilde{\sigma}_2, \widetilde{\sigma}_3\}$. The Floquet-Bloch operators $U(\boldsymbol{k}) = U_{1d}(\boldsymbol{k}), U_{2d}(\boldsymbol{k})$, or $U_{3d}(\boldsymbol{k})$ satisfy the conditions of the TRS Θ *for Floquet-Bloch operators* in Eq. (5.62), i.e., $\Theta U(\boldsymbol{k})\Theta^{-1} = U^\dagger(-\boldsymbol{k})$, if $\widetilde{\boldsymbol{\sigma}}$ is odd under Θ: $\Theta\widetilde{\boldsymbol{\sigma}}\Theta^{-1} = -\widetilde{\boldsymbol{\sigma}}$. On the other hand, $\widetilde{\boldsymbol{\sigma}}$ must be

even under the PHS C and the CS Γ, i.e., $S\widetilde{\boldsymbol{\sigma}}S^{-1} = \widetilde{\boldsymbol{\sigma}}$ for $S = C, \Gamma$, such that $U(\boldsymbol{k})$ have the PHS C and CS Γ, respectively. To summarize, the TRS Θ, PHS C, or CS Γ *for Floquet-Bloch operators* in Eq. (5.62) are satisfied if $\widetilde{\boldsymbol{\sigma}}$ satisfies the following conditions:

$$\Theta\widetilde{\boldsymbol{\sigma}}\Theta^{-1} = -\widetilde{\boldsymbol{\sigma}}, \quad C\widetilde{\boldsymbol{\sigma}}C^{-1} = \widetilde{\boldsymbol{\sigma}}, \quad \Gamma\widetilde{\boldsymbol{\sigma}}\Gamma^{-1} = -\widetilde{\boldsymbol{\sigma}}. \tag{A.41}$$

It is worthwhile to mention that these relations are nothing but the symmetry conditions for the (static) Dirac Hamiltonian $H(\boldsymbol{k}) = \widetilde{\boldsymbol{\sigma}} \cdot \boldsymbol{k}$ in the same symmetry class.

The Floquet-Bloch operators $U_{1d}(\boldsymbol{k}), U_{2d}(\boldsymbol{k})$, and $U_{3d}(\boldsymbol{k})$, indeed, have the gapless spectra protected by symmetries. To see this, we first consider the case with three spatial dimensions. Let θ be the parameter defined by

$$\cos(v\theta) = u_4, \quad \sin(\theta v) = -v \tag{A.42}$$

for the three-dimensional vector $\boldsymbol{v} = (u_1, u_2, u_3)$, with $v := |\boldsymbol{v}| = \pm\sqrt{1-(u_4)^2}$ being its norm. Then, the exponential operator $\exp(-i\theta\boldsymbol{v}\cdot\widetilde{\boldsymbol{\sigma}})$ can be expanded as

$$\exp(-i\theta\boldsymbol{v}\cdot\widetilde{\boldsymbol{\sigma}}) = \cos(\theta v)\widetilde{\sigma}_0 - i\frac{\sin(\theta v)}{v}\boldsymbol{v}\cdot\widetilde{\boldsymbol{\sigma}} = u_4\widetilde{\sigma} + i\boldsymbol{v}\cdot\widetilde{\boldsymbol{\sigma}} = U_{3d}(\boldsymbol{k}). \tag{A.43}$$

Thus, the effective Hamiltonian is given by

$$h_{\text{eff}}(\boldsymbol{k}) = \theta\boldsymbol{v}\cdot\widetilde{\boldsymbol{\sigma}}, \tag{A.44}$$

where we set the driving period as unity: $T = 1$. Since we have

$$[h_{\text{eff}}(\boldsymbol{k})]^2 = (\theta v)^2\widetilde{\sigma}_0 = \left[\cos^{-1}(u_4)\right]^2\widetilde{\sigma}_0, \tag{A.45}$$

its quasienergies $\epsilon_{3d}(\boldsymbol{k})$ are given by

$$\epsilon_{3d}(\boldsymbol{k}) = \pm\cos^{-1}\left[u_4(\boldsymbol{k})\right] = \pm\cos^{-1}\left[2\cos^2\left(\frac{k_1}{2}\right)\cos^2\left(\frac{k_2}{2}\right)\cos^2\left(\frac{k_3}{2}\right) - 1\right]. \tag{A.46}$$

This dispersion has only one gapless point $\boldsymbol{k} = 0$, around which $h_{\text{eff}}(\boldsymbol{k})$ is expanded as

$$h_{\text{eff}}(\boldsymbol{k}) = \widetilde{\boldsymbol{\sigma}}\cdot\boldsymbol{k}. \tag{A.47}$$

It is clear that, for a given symmetry class $(\mathbb{F}, s)$, this gapless point is protected by its symmetries since the Dirac Hamiltonian $\widetilde{\boldsymbol{\sigma}}\cdot\boldsymbol{k}$ cannot be gapped out without breaking them. The same discussion holds in the lower dimensionalities $d = 1, 2$.

To show that $U(\boldsymbol{k})$ can be constructed with a time-dependent Hamiltonian $h(\boldsymbol{k}, t)$ that respects the TRS Θ, PHS C, or CS Γ *for time-dependent Hamiltonians* in Eq. (5.61), it is sufficient to prove that each helical pump $\exp(-iqk_i\widetilde{\sigma}_i)$ $(q = 1, 1/2, 1/4)$ can be implemented with a time-dependent Hamiltonian $h(\boldsymbol{k}, t)$ that satisfies Eq. (5.61). To see this, consider the

time-dependent Hamiltonian $h(k_i, t)$ defined by

$$h(k_i,t) := \begin{cases} -J\sigma_i' & 0 \le t \le T_h/3; \\ 2J(\sin(qk_i)\widetilde{\sigma}_i + \cos(qk_i)\sigma_i') & T_h/3 \le t \le 2T_h/3; \\ -J\sigma_i' & 2T_h/3 \le t \le T_h/3, \end{cases} \tag{A.48}$$

with σ_i' being the matrix that satisfies

$$(\sigma_i')^2 = 1, \quad \sigma_i'\widetilde{\sigma}_i + \widetilde{\sigma}_i\sigma_i' = 0. \tag{A.49}$$

We note that the first and third processes in $h(k_i, t)$ represent the rotation of the internal states, while the second one expresses a spin-dependent tunneling along the x_i direction with a sublattice structure. When $JT_h/3 = \pi/4$, from the straightforward calculation using Eq. (A.49), the time-evolution operator of $h(k_i, t)$ from $t = 0$ to $t = T_h$ is shown to coincide the helical pump $\exp(-iqk_i\widetilde{\sigma}_i)$:

$$\mathcal{T}_t \exp\left(-i\int_0^{T_h} dt h(k_i,t)\right) = \exp\left(\frac{i\pi\sigma_i'}{4}\right)\exp\left[\frac{-i\pi(\sin(qk_i)\widetilde{\sigma}_i + \cos(qk_i)\sigma_i')}{2}\right]\exp\left(\frac{i\pi\sigma_i'}{4}\right) \tag{A.50}$$

$$= \exp(-iqk_i\widetilde{\sigma}_i). \tag{A.51}$$

From Eq. (5.61), $h(k_i, t)$ has the TRS Θ, PHS C, or CS Γ if σ_i' satisfies $\Theta\sigma_i'\Theta^{-1} = \sigma_i'$, $C\sigma_i'C^{-1} = -\sigma_i'$, or $\Gamma\sigma_i'\Gamma^{-1} = -\sigma_i'$, respectively. Thus, the helical pumps in $U(\boldsymbol{k})$ can be implemented if there exists d matrices $\boldsymbol{\sigma}' := (\sigma_1', \cdots, \sigma_d')$ that satisfy

$$\Theta\boldsymbol{\sigma}'\Theta^{-1} = \boldsymbol{\sigma}', \quad C\boldsymbol{\sigma}'C^{-1} = -\boldsymbol{\sigma}', \quad \Gamma\boldsymbol{\sigma}'\Gamma^{-1} = -\boldsymbol{\sigma}'. \tag{A.52}$$

In summary, nontrivial Floquet-Bloch operators under given symmetries can be constructed by finding suitable matrices $\widetilde{\boldsymbol{\sigma}}$ and $\boldsymbol{\sigma}'$ that satisfy the symmetry constraints (A.41) and (A.52), respectively, and the anticommutation relation (A.49).

A.4.3 Concrete models in each symmetry class

Nontrivial Floquet-Bloch operators in class AIII can exist in $d = 2$. Let us take the CS Γ as $\Gamma = \sigma_3$. Then, $\widetilde{\boldsymbol{\sigma}} = (\sigma_1, \sigma_2)$ and $\boldsymbol{\sigma}' = (\sigma_2, \sigma_1)$ satisfy Eqs. (A.41) and (A.52), respectively. Its topological number is the Chern number (A.26) of the lower band of the Hermitian matrix $\gamma\Gamma U_{2d}(\boldsymbol{k})$. For the two-band model defined in Eq. (A.37), $\gamma\Gamma U_{2d}(\boldsymbol{k})$ is rewritten as $\gamma\Gamma U_{2d}(\boldsymbol{k}) := \boldsymbol{d}(k_1, k_2)\cdot\boldsymbol{\sigma}$, where $\boldsymbol{d}(k_1, k_2)$ is the three-dimensional vector with unit length defined by

$$\boldsymbol{d}(k_1,k_2) := [u_2(k_1,k_2,0), -u_1(k_1,k_2,0), u_4(k_1,k_2,0)]\,. \tag{A.53}$$

Then, the Chern number (A.26) reduces to the winding number of $\boldsymbol{d}(k_1, k_2)$ on S^2:

$$Ch_1 = \int \frac{d\boldsymbol{k}}{4\pi}\boldsymbol{d}\cdot\left(\frac{\partial\boldsymbol{d}}{\partial k_1}\times\frac{\partial\boldsymbol{d}}{\partial k_2}\right) = 1. \tag{A.54}$$

In general, a model with higher Chern number n ($\in \mathbb{Z}$) is obtained by replacing k_1 in $U_{2d}(\boldsymbol{k})$ with nk_1.

Nontrivial Floquet-Bloch operators in class AI can exist in $d = 3$. Let us take the TRS Θ as $\Theta = \sigma_1 \otimes \tau_0 \mathcal{K}$. Then, $\widetilde{\boldsymbol{\sigma}} = (\sigma_1 \otimes \tau_2, \sigma_2 \otimes \tau_2, \sigma_3 \otimes \tau_0)$ and $\boldsymbol{\sigma}' = (\sigma_0 \otimes \tau_1, \sigma_0 \otimes \tau_1, \sigma_1 \otimes \tau_0)$ satisfy Eqs. (A.41), (A.49), and (A.52), respectively. The topological number is given by the three-dimensional winding number W in Eq. (A.28). Substituting Eq. (A.36) into Eq. (A.28), together with $\widetilde{\boldsymbol{\sigma}} = (\sigma_1 \otimes \tau_2, \sigma_2 \otimes \tau_2, \sigma_3 \otimes \tau_0)$, we obtain $W = -2$. A higher winding number $2n$ ($\in 2\mathbb{Z}$) is obtained by replacing k_1 in $U_{3d}(\boldsymbol{k})$ by $-nk_1$.

Nontrivial Floquet-Bloch operators in class BDI do not exist in $d = 1, 2$, and 3.

Nontrivial Floquet-Bloch operators in class D can exist in $d = 1$. Its topological number is given by the one-dimensional winding number $\nu_{1\mathrm{d}}$ in Eq. (A.25). In this class, we cannot construct a nontrivial Floquet-Bloch operators by using Eqs. (A.36), (A.37), and (A.38) because Eq. (A.38) is generated by a traceless matrix $\widetilde{\sigma}_i$, where $\nu_{1\mathrm{d}}$ automatically vanishes. Therefore, we here must consider another protocol. Let us take the PHS in the Majorana basis $C = \sigma_3 \mathcal{K}$, where $\sigma_3 = 1$ (-1) corresponds to the real (imaginary) Majorana field. Consider two species of fermions labeled by $\alpha = 1, 2$ and we denote the real (imaginary) Majorana state with momentum k_1 and species α by $|k_1, R, \alpha\rangle$ ($|k_1, I, \alpha\rangle$). The PHS acts on the fermions with The driving protocol is given by the time-dependent Bloch Hamiltonian $h(k_1, t)$ defined by

$$h_D(k_1, t) = \begin{cases} J\,|k_1, I, 2\rangle\,\langle k_1, R, 1| + \mathrm{h.c} & 0 \le t \le T/2; \\ J\mathrm{e}^{-ik_1}\,|k_1, R, 1\rangle\,\langle k_1, I, 2| + \mathrm{h.c} & T/2 \le t \le T. \end{cases} \tag{A.55}$$

Since $|k_1, R, \alpha\rangle$ and $|k_1, I, \alpha\rangle$ are the eigenstates of C with the opposite parity, $h(k_1, t)$ has the PHS. When $JT/2 = \pi/2$, the entire Floquet operator is decomposed into the two Floquet operators that do not mix the species. The Floquet-Bloch operator $U_D(k_1)$ that acts on the species $\alpha = 1$ is given by

$$U_D(k_1) = \frac{\sigma_0 + \sigma_3}{2}\mathrm{e}^{-ik_1} + \frac{\sigma_0 - \sigma_3}{2}. \tag{A.56}$$

This operator, indeed, has the PHS, $CU(k_1)C^{-1} = U(-k_1)$, and a unit winding number $\nu_{1\mathrm{d}} = 1$. A higher winding number n is obtained by replacing k_1 with nk_1.

Nontrivial Floquet-Bloch operators in class DIII can exist in $d = 1, 2$. Let us take the TRS Θ and PHS C as $\Theta = i\sigma_2 \otimes \tau_0 \mathcal{K}$ and $C = \sigma_1 \otimes \tau_0 \mathcal{K}$, respectively. Then, $\widetilde{\boldsymbol{\sigma}} = (\sigma_1 \otimes \tau_0, \sigma_2 \otimes \tau_0)$ and $\boldsymbol{\sigma}' = (\sigma_2 \otimes \tau_2, \sigma_1 \otimes \tau_2)$ satisfy Eqs. (A.41), (A.49), and (A.52), respectively, and hence $U(\boldsymbol{k})$ has the TRS and PHS. For the one-dimensional model $U_{1d}(k_1)$, its topological number is determined from the Chern-Simons invariant ν_{CS} defined in Eq. (A.29). From a straightforward calculation, we obtain $\nu_{\mathrm{CS}} = -1$ for $U_{1d}(k_1)$ with $\widetilde{\sigma}_1 = \sigma_1 \otimes \tau_0$. For the two-dimensional model $U_{2d}(k_1, k_2)$, its topological number is given by the Chern number (A.26), which is obtained to be $Ch_1 = 1$.

Nontrivial Floquet-Bloch operators in class AII can exist in $d = 1, 2, 3$. Let us take the TRS Θ as $\Theta = i\sigma_2 \otimes \tau_0 \mathcal{K}$. Then, $\widetilde{\boldsymbol{\sigma}} = (\sigma_1 \otimes \tau_0, \sigma_2 \otimes \tau_0, \sigma_3 \otimes \tau_0)$ and $\boldsymbol{\sigma}' = (\sigma_2 \otimes \tau_2, \sigma_1 \otimes \tau_2, \sigma_1 \otimes \tau_2)$ satisfy Eqs. (A.41), (A.49), and (A.52), respectively, and hence $U(\boldsymbol{k})$ has the TRS. The topological invariant for the one- and two-dimensional models $U(\boldsymbol{k})$ are given by the $\mathbb{Z}_2$ parity (A.30). For the one-dimensional model, we have $\mathrm{Pf}\,[w(k_1)]\,/\sqrt{\det\,[w(k_1)]} = 1(-1)$ for $k_1 = 0$ ($k_1 = \pi$) and

hence $\nu_{\rm par} = -1$. For the two-dimensional model, we have

$$\frac{\mathrm{Pf}\,[w(\boldsymbol{k})]}{\sqrt{\det\,[w(\boldsymbol{k})]}} = \begin{cases} 1 & \boldsymbol{k} = (0,0); \\ -1 & \boldsymbol{k} = (\pi,0), (0,\pi), (\pi,\pi), \end{cases} \tag{A.57}$$

which gives $\nu_{\rm par} = -1$. Finally, consider the three-dimensional model $U_{3d}(k_1, k_2, k_3)$. Its topological number is the three-dimensional winding number W defined in Eq. (A.28). Substituting Eq. (A.36) into Eq. (A.28), together with $\widetilde{\boldsymbol{\sigma}} = (\sigma_1, \sigma_2, \sigma_3)$, we obtain $W = -1$.

Nontrivial Floquet-Bloch operators in class CII can exist in $d = 2, 3$. Let us take the TRS Θ and PHS C as $\Theta = i\sigma_2 \otimes \tau_0 \mathcal{K}$ and $C = i\sigma_0 \otimes \tau_2 \mathcal{K}$, respectively. Then, $\widetilde{\boldsymbol{\sigma}} = (\sigma_1 \otimes \tau_0, \sigma_2 \otimes \tau_1, \sigma_3 \otimes \tau_0)$ and $\boldsymbol{\sigma}' = (\sigma_3 \otimes \tau_2, \sigma_0 \otimes \tau_3, \sigma_1 \otimes \tau_2)$ satisfy Eqs. (A.41), (A.49), and (A.52), respectively, and hence $U(\boldsymbol{k})$ has the TRS and PHS. The topological numbers of the two- and three-dimensional models are both given by the $\mathbb{Z}_2$ parity (A.30) for the time-reversal invariant Hamiltonian $H_u(\boldsymbol{k}) = \gamma \Gamma U(\boldsymbol{k})$. By a straightforward calculation, we obtain

$$\frac{\mathrm{Pf}\,[w(\boldsymbol{k})]}{\sqrt{\det\,[w(\boldsymbol{k})]}} = \begin{cases} -1 & \boldsymbol{k} = (0,0); \\ 1 & \boldsymbol{k} = (\pi,0), (0,\pi), (\pi,\pi), \end{cases} \tag{A.58}$$

for the two-dimensional model and

$$\frac{\mathrm{Pf}\,[w(\boldsymbol{k})]}{\sqrt{\det\,[w(\boldsymbol{k})]}} = \begin{cases} -1 & \boldsymbol{k} = (0,0,0); \\ 1 & \text{other momenta}, \end{cases} \tag{A.59}$$

for the three-dimensional model. Thus, we obtain $\nu_{\rm par} = -1$ for both models.

Nontrivial Floquet-Bloch operators in class C can exist in $d = 1, 3$. Let us take the PHS C as $C = i\sigma_0 \otimes \tau_2 \mathcal{K}$. Then, $\widetilde{\boldsymbol{\sigma}} = (\sigma_2 \otimes \tau_1, \sigma_3 \otimes \tau_0, \sigma_1 \otimes \tau_0)$ and $\boldsymbol{\sigma}' = (\sigma_0 \otimes \tau_3, \sigma_1 \otimes \tau_2, \sigma_3 \otimes \tau_2)$ satisfy Eqs. (A.41), (A.49), and (A.52), respectively, and hence $U(\boldsymbol{k})$ has the PHS. The topological number of the one-dimensional model is given by the one-dimensional winding number $\nu_{\rm 1d}$ in Eq. (A.25). As a model with nontrivial winding number, we consider the pair of the driving protocol in class D and its time-reversal. The whole time-dependent Hamiltonian $h_C(k_1, t)$ is the direct product $h_C(k_1, t) = h(k_1, t) \oplus [-h(-k_1, t)]$, where $h(k_1, t)$ is defined by

$$h(k_1, t) = \begin{cases} J\,|k_1, R, 2\rangle\,\langle k_1, R, 1| + \mathrm{h.c} & 0 \le t \le T/2; \\ J\mathrm{e}^{-ik_1}\,|k_1, R, 1\rangle\,\langle k_1, R, 2| + \mathrm{h.c} & T/2 \le t \le T. \end{cases} \tag{A.60}$$

When $JT/2 = \pi/2$, the corresponding Floquet-Bloch operator $U_C(k_1)$ is given by

$$U_C(k_1) = U_D(k_1) \oplus U_D^\dagger(-k_1) = U_D(k_1) \oplus U_D(k_1), \tag{A.61}$$

where $U_D(k_1)$ is the Floquet-Bloch operator defined in Eq. (A.56). The Floquet-Bloch operator $U_C(k_1)$ indeed has the PHS, $CU_C(k_1)C^{-1} = U_C(-k_1)$, and a unit winding number $\nu_{\rm 1d} = 2$. Although we do not have a closed integral expression for the $\mathbb{Z}_2$ invariant for the three-dimensional model, we can compute it by means of the Moore-Balents argument [398, 399]. The Floquet-Bloch operator $U_{3d}(\boldsymbol{k})$ is given by Eq. (A.39), $k_3 > 0$ ($k_3 < 0$) corresponds to the

north (south) hemisphere of S^3. Let us define a modified model $\widetilde{U}_{3d}(\boldsymbol{k})$ by

$$\widetilde{U}_{3d}(\boldsymbol{k}) := \begin{cases} U_{3d}(\boldsymbol{k}) & \text{for} \quad k_3 \geq 0; \\ u_4(\boldsymbol{k})\widetilde{\sigma}_0 + u_1(\boldsymbol{k})\widetilde{\sigma}_1 + u_2(\boldsymbol{k})\widetilde{\sigma}_2 + u_3(\boldsymbol{k})e_3 & \text{for} \quad k_3 < 0, \end{cases} \tag{A.62}$$

where $e_3 := \sigma_1 \otimes \tau_1$ transforms under the TRS and the PHS as $\Theta e_3 \Theta^\dagger = e_3$ and $C e_3 C^\dagger = -e_3$, respectively. Note that its parities are the opposite to those of $\widetilde{\sigma}_3$ since $\Theta \widetilde{\sigma}_3 \Theta^\dagger = -\widetilde{\sigma}_3$ and $C\widetilde{\sigma}_3 C^\dagger = \widetilde{\sigma}_3$. Since we have from Eq. (A.40) that

$$u_4(\boldsymbol{k}_\parallel, k_3) = u_4(-\boldsymbol{k}_\parallel, k_3), \quad u_1(\boldsymbol{k}_\parallel, k_3) = -u_1(-\boldsymbol{k}_\parallel, k_3), \tag{A.63}$$

$$u_2(\boldsymbol{k}_\parallel, k_3) = -u_2(-\boldsymbol{k}_\parallel, k_3), \quad u_3(\boldsymbol{k}_\parallel, k_3) = u_3(-\boldsymbol{k}_\parallel, k_3), \tag{A.64}$$

with $\boldsymbol{k}_\parallel := (k_1, k_2)$ being the momenta other than k_3, $\widetilde{U}_{3d}(\boldsymbol{k})$ for $k_3 < 0$ defines a continuous deformation of $\widetilde{U}_{3d}(\boldsymbol{k}_\parallel, 0)$ into a trivial insulator that satisfies

$$\Theta \widetilde{U}_{3d}(\boldsymbol{k}_\parallel, k_3)\Theta^\dagger = \widetilde{U}_{3d}^\dagger(-\boldsymbol{k}_\parallel, k_3), \quad C\widetilde{U}_{3d}(\boldsymbol{k}_\parallel, k_3)C^\dagger = \widetilde{U}_{3d}(-\boldsymbol{k}_\parallel, k_3). \tag{A.65}$$

Thus, from the Moore-Balents argument, the $\mathbb{Z}_2$ topological number is given by the parity of the three-dimensional winding number $\widetilde{W}$ of the Hamiltonian $\widetilde{H}_u(\boldsymbol{k}) := \sigma_- \otimes \widetilde{U}_{3d}^\dagger(\boldsymbol{k}) + \sigma_+ \otimes \widetilde{U}_{3d}(\boldsymbol{k})$ in class AIII. Substituting Eq. (A.62) into Eq. (A.28), we obtain $\widetilde{W} = 1$ and hence $\nu_2 = (-1)^{\widetilde{W}} = -1$.

Nontrivial Floquet-Bloch operators in class CI can exist in $d = 2$. Let us take the TRS Θ and PHS C as $\Theta = \sigma_1 \otimes \tau_0 \mathcal{K}$ and $C = i\sigma_0 \otimes \tau_2 \mathcal{K}$, respectively. Then, $\widetilde{\boldsymbol{\sigma}} = (\sigma_2 \otimes \tau_2, \sigma_3 \otimes \tau_0)$ and $\boldsymbol{\sigma}' = (\sigma_0 \otimes \tau_1, \sigma_1 \otimes \tau_1)$ satisfy Eqs. (A.41), (A.49), and (A.52), respectively, and hence $U(\boldsymbol{k})$ has the TRS and PHS. The topological invariant is given by the Chern number (A.25) of the lower bands of the Hamiltonian $\gamma \Gamma U(\boldsymbol{k})$. For the two-dimensional model $U_{2d}(k_1, k_2)$, its topological number is given by the Chern number (A.26), which is obtained to be $Ch_1 = -2$. Note that the Chern number is alway an even integer because the model is constituted from two copies of a Chern insulator, which are related by the TRS.

The above results are summarized from the fifth to eighth columns of Table. A.1.

Appendix B

Details of derivations in Chapter 6

In App. B.1, we present rigorous discussions on a Markov chain on a discrete state space under a periodic drive and and a periodically driven Markovian quantum master equation, comparing it with the results on an isolated quantum system [95, 98]. In Apps. B.2, B.3, and B.4, we calculate the low-order terms of the vV HFE for the sLLG equations describing laser-driven magnets analyzed in Secs. 6.4 and 6.5.

B.1 Rigorous results on discrete systems

B.1.1 Markov chain on a discrete space

Consider a Markov chain on a lattice with N sites with the generator of its master equation being $\hat{L}(t)$:

$$\frac{\partial P}{\partial t} = \hat{L}(t)P, \tag{B.1}$$

where $\hat{L}(t)$ is periodic in time with period T: $\hat{L}(t) = \hat{L}(t+T)$. Here, $\hat{L}(t)$ and P are the transition matrix $W(t)$ and the probability distribution function $\boldsymbol{p}(t)$ in Eq. (6.11), respectively. We assume that the state space on a site is discrete, where P is a finite-dimensional vector. This is in stark contrast to the case with a continuum classical variable ϕ analyzed in Sec. 6.2, where P is an infinite-dimensional vector even in a single-particle system and hence a mathematically rigorous results are hard to obtain. It is worth mentioning that some of Markov processes have an exact correspondence with quantum spin systems; for example, $\hat{L}(t)$ for the ASEP is nothing but the Hamiltonian of the non-Hermitian XXZ chain [396, 397]. We assume that $\hat{L}(t)$ is written in the following form:

$$\hat{L}(t) = \sum_{X:|X|\leq k} l_X(t), \tag{B.2}$$

where $X = \left\{\boldsymbol{r}_1, \boldsymbol{r}_2, \cdots, \boldsymbol{r}_{|X|}\right\}$ and $l_X(t)$ are a set of sites with its number not more than k and an operator acting on the sites in X, respectively. This indicates that the transition process of a particle at some site depends on the state on, at most, k sites. We also assume that the

transition rate per site is bounded from above with g:

$$\sum_{X:X\in\boldsymbol{r}} \|l_X(t)\| \le g, \tag{B.3}$$

for any site $\boldsymbol{r}$. We define the effective generator L_F and Ω_F by $U(T,0) =: \exp(L_F T)$ and $\Omega_F := L_F T$, respectively. For the FM HFE $\Omega_F = \sum_{m=0}^{\infty} \Omega_F^{(m)}$, the mth-order term $\Omega_F^{(m)}$ is given by Eq. (6.68). For a global drive, using the same techniques as that used an isolated quantum system [95, 96], we can bound $\Omega_F^{(m)}$ from above as follows:

$$\|\Omega_F^{(m)}\| \le 2gTN\frac{(2gkT)^m m!}{(m+1)^2}, \tag{B.4}$$

which implies that $\Omega_F^{(m)}$ is, at least asymptotically, convergent up to the order $m_0 \sim \omega/(gk)$:

$$\|\Omega_F^{(m)} - \Omega_F^{(m_0)}\| \le N\mathcal{O}\left[(2gkT)^m\right] \quad \text{for} \quad m \le m_0. \tag{B.5}$$

Thus, the derivation of Eq. (6.57) has been completed. Furthermore, for $t = mT \in m\mathbb{Z}$ and $m_0 = \lfloor (8gkT)^{-1} - 1 \rfloor$, with $\lfloor\cdot\rfloor$ being the floor function, we can show the following bound for the truncated FM HFE $\Omega_{\rm TR}^{(m_0)} = \sum_{m=0}^{m_0} \Omega_F^{(m)}$:

$$\|U^{-1}(t,0)\Omega_{\rm TR}^{(m_0)}U(t,0) - \Omega_{\rm TR}^{(m_0)}\| \le 16g^2kTt2^{-m_0}N. \tag{B.6}$$

Equation (B.6) should be compered with the bound (3.23) on an isolated quantum system. In fact, Eq. (3.23) is obtained from Eq. (B.6) by replacing $\Omega_{\rm TR}^{(m_0)}$ and $U^{-1}(t,0)$ with $-iH_{\rm TR}^{(m_0)}T$ and $U^\dagger(t,0)$, respectively, because the bound (3.23) is obtained without using the Hermiticity of $H(t)$.

In the case of an isolated quantum mechanics, Eq. (3.23) shows that $H_{\rm TR}^{(m_0)}$ is a quasi-conserved quantity and that, together with the ETH [202–204], the Floquet prethermal state is given by the Gibbs state of $H_{\rm TR}^{(m_0)}$ if $H_0 \simeq H_{\rm TR}^{(m_0)}$ is non-integrable. On the other hand, one cannot determine the steady state from Eq. (B.6) because there is no guiding principle to determine the steady state for an open system. Therefore, we must analyze the steady-state properties in another way. Let us define $\bar{\Omega}_{\rm TR}^{(m_0)}$ by $\bar{\Omega}_{\rm TR}^{(m_0)} := U^{-1}(t,0)\Omega_{\rm TR}^{(m_0)}U(t,0)$ and consider the following two master equations:

$$\frac{\partial P}{dt} := \frac{\bar{\Omega}_{\rm TR}^{(m_0)}P}{T}, \tag{B.7}$$

$$\frac{\partial P}{dt} := \frac{\Omega_{\rm TR}^{(m_0)}P}{T}. \tag{B.8}$$

We denote the steady states of Eqs. (B.7) and (B.8) by $\bar{\Pi}_{\rm SS}^{(m_0)}$ and $\Pi_{\rm SS}^{(m_0)}$, respectively:

$$\bar{\Pi}_{\rm SS}^{(m_0)} := \exp\left(\bar{\Omega}_{\rm TR}^{(m_0)}\frac{\tau}{T}\right)P_0 = U^{-1}(t,0)\exp\left(\Omega_{\rm TR}^{(m_0)}\frac{\tau}{T}\right)U(t,0)P_0, \tag{B.9}$$

$$\Pi_{\rm SS}^{(m_0)} := \exp\left(\Pi_F^{(m_0)}\frac{\tau}{T}\right)P_0, \tag{B.10}$$

where P_0 and τ are an initial probability distribution and the relaxation timescale to the steady

states, respectively. For a non-integrable isolated system, a steady state is solely determined by conserved quantities like a Hamiltonian. As a counterpart, we here assume that the steady states $\Pi_{\rm SS}$ and $\Pi_{\rm SS}^{(m_0)}$ of the two master equations (B.1) and (B.8), respectively, are independent of the initial probability distributions. Assuming that τ is sufficiently shorter than $16g^2kT\tau^2 2^{m_0}$, we obtain from Eq. (B.6) that

$$\frac{1}{N}\|U^{-1}(\tau,0)\mathrm{e}^{\Omega_{\rm TR}^{(m_0)}\frac{\tau}{T}}U(\tau,0)P_0-\Pi_{\rm SS}^{(m_0)}\|=\frac{1}{N}\|\bar{\Pi}_{\rm SS}^{(m_0)}-\Pi_{\rm SS}^{(m_0)}\|\leq\mathcal{O}\left[(g\tau)^2k2^{-m_0}\right]. \tag{B.11}$$

Thus, we obtain

$$\begin{aligned}\frac{1}{N}\|\mathrm{e}^{\Omega_{\rm TR}^{(m_0)}\frac{\tau}{T}}U(\tau,0)P_0-U(\tau,0)\mathrm{e}^{\Omega_{\rm TR}^{(m_0)}\frac{\tau}{T}}P_0\|&\leq\frac{1}{N}\|U^{-1}(\tau,0)\Pi_{\rm SS}^{(m_0)}U(\tau,0)-\Pi_{\rm SS}^{(m_0)}\| &\text{(B.12)}\\ &\leq\mathcal{O}\left[(g\tau)^2k2^{-m_0}\right], &\text{(B.13)}\end{aligned}$$

because $U(t,0)$ is a probability matrix and hence its norm is less than one. Since $\Pi_{\rm SS}$ and $\Pi_{\rm SS}^{(m_0)}$ are independent of the initial probability distribution, we have

$$\Pi_{\rm SS}=U(\tau,0)\exp\left(\Omega_{\rm TR}^{(m_0)}\frac{\tau}{T}\right)P_0=U(\tau,0)P_0, \tag{B.14}$$

$$\Pi_{\rm SS}^{(m_0)}=\exp\left(\Omega_{\rm TR}^{(m_0)}\frac{\tau}{T}\right)U(\tau,0)P_0=\exp\left(\Omega_{\rm TR}^{(m_0)}\frac{\tau}{T}\right)P_0. \tag{B.15}$$

Therefore, we finally obtain

$$\frac{1}{N}\|\Pi_{\rm SS}-\Pi_{\rm SS}^{(m_0)}\|\leq\mathcal{O}\left[(g\tau)^2k2^{-m_0}\right], \tag{B.16}$$

which indicates the coincidence between the exact steady state $\Pi_{\rm SS}$ and the steady state $\Pi_{\rm SS}^{(m_0)}$ obtained from the FM HFE. This completes the derivation of Eq. (6.58). Furthermore, the difference between $\Pi_{\rm SS}^{(m_0)}$ and $\Pi_{\rm SS}^{(m)}$, which is obtained from the *lower-order* truncation ($m\leq m_0$), is of the order of $(2gkT)^m$ from Eq. (B.5), which gives

$$\frac{1}{N}\|\Pi_{\rm SS}-\Pi_{\rm SS}^{(m)}\|\leq\mathcal{O}\left[(g\tau)^2k2^{-m_0}+(2gkT)^m\right]. \tag{B.17}$$

Equation (B.17) indicates the coincidence between the exact steady state $\Pi_{\rm SS}$ and the steady state $\Pi_{\rm SS}^{(m_0)}$ obtained from the *low-order* FM HFE. From the above discussion, we can conclude that the FM HFE developed in Chapter 6 is valid for a Markov process on a discrete state space.

B.1.2 Markovian quantum master equation

Consider the Lindblad equation (6.85) with time-dependent Hamiltonian $H(t)$ and Lindblad operators $\{L_i\}_i$ which are defined on a lattice with N sites. The Lindblad equation $\dot{\rho}=\mathcal{L}_{\rm Lind}(t)\rho$ is regarded as a non-Hermitian Schrödinger equation. We assume that $H(t)$ and the dissipator are written in the form of Eq. (B.2) that satisfies Eq. (B.3):

$$H(t)=\sum_{X:|X|\leq k}l_{H,X}(t), \tag{B.18}$$

$$\sum_{X:X\in\boldsymbol{r}} \|l_{H,X}(t)\| \le g_H, \tag{B.19}$$

$$\sum_i \left(L_i(t)\rho L_i(t)^\dagger - \frac{1}{2}\left\{ L_i(t)^\dagger L_i(t), \rho \right\} \right) = \sum_{X:|X|\le k} l_{L,X}(t), \tag{B.20}$$

$$\sum_{X:X\in\boldsymbol{r}} \|l_{L,X}(t)\| \le g_L. \tag{B.21}$$

We further assume that the Hilbert space on each site is finite, where the density matrix ρ is spanned by tensor products of finite-dimensional matrices $\{M_{\boldsymbol{r}}\}_{\boldsymbol{r}}$ on each site $\boldsymbol{r}$. Then, $\mathcal{L}_{\rm Lind}(t)$ is local and bounded in that it can be written in the form of Eq. (B.2) that satisfies Eq. (B.3) for some k and g. We can derive Eqs. (6.86) and (6.87) in the same manner as we derive the similar results in Eqs. (6.57) and (6.58) for a Markov chain on a discrete space. One different point is the derivation of Eq. (B.13) where we use the bounded nature of the probability matrix $U(T,0)$. This should be replaced by $\|U(T,0)\| \le 1$, which is derived from the dissipative nature of the Lindblad equation as follows [404, 405]. Let $\|M\|_{\rm tr} := \sqrt{{\rm Tr}\,(M^\dagger M)}$ be the trace norm of a matrix M. For the density matrix ρ_t at time t, we obtain from Eq. (6.85) that

$$\frac{d}{dt}\|\rho_t\|_{\rm tr}^2 = {\rm Tr}\left[\rho_t^\dagger \left(\mathcal{L}_{\rm Lind}(t) + \mathcal{L}_{\rm Lind}^\dagger(t) \right) \rho_t \right] \tag{B.22}$$

$$= {\rm Tr}\left[\sum_i \left(L_i(t)\rho_t L_i(t)^\dagger - \frac{1}{2}\left\{ L_i(t)^\dagger L_i(t), \rho_t \right\} \right) \right] + \left(L_i(t) \to L_i^\dagger(t) \right) \tag{B.23}$$

$$= -\frac{1}{2}\sum_i \left(\| \left[\rho_t, L_i \right] \|_{\rm tr}^2 + \left\| \left[\rho_t, L_i^\dagger \right] \right\|_{\rm tr}^2 \right) \le 0. \tag{B.24}$$

Therefore, the trace norm $\|\rho_t\|_{\rm tr}$ is a monotonically decreasing function of t, which gives

$$\|U(T,0)\rho_0\|_{\rm tr} = \|\rho_T\|_{\rm tr} \le \|\rho_0\|_{\rm tr}, \tag{B.25}$$

and hence $\|U(T,0)\| \le 1$.

B.2 Two-dimensional ferromagnet: first order

For a systematic calculation of a commutator, we rewrite the FP operator in terms of the angular momentum operators. Let us define the angular momentum operators $L_{\boldsymbol{r},a}$ and the operators $K_{\boldsymbol{r},a}$ and $N_{\boldsymbol{r},a}$ by

$$L_{\boldsymbol{r},a} := -\epsilon_{abc} m_{\boldsymbol{r},b} \frac{\partial}{\partial m_{\boldsymbol{r},c}}, \quad K_{\boldsymbol{r},a} := \epsilon_{abc} L_{\boldsymbol{r},b} m_{\boldsymbol{r},c}, \quad N_{\boldsymbol{r},a} := L_{\boldsymbol{r},a} + \alpha K_{\boldsymbol{r},a}, \tag{B.26}$$

where α is the Gilbart damping in the sLLG equation. These operators satisfy the following commutation relations:

$$[L_{\boldsymbol{r},a}, L_{\boldsymbol{r}',b}] = \delta_{\boldsymbol{r},\boldsymbol{r}'}\epsilon_{abc} L_{\boldsymbol{r},c}, \quad [K_{\boldsymbol{r},a}, K_{\boldsymbol{r}',b}] = -\delta_{\boldsymbol{r},\boldsymbol{r}'}\epsilon_{abc} K_{\boldsymbol{r},c}, \quad [L_{\boldsymbol{r},a}, K_{\boldsymbol{r}',b}] = \delta_{\boldsymbol{r},\boldsymbol{r}'}\epsilon_{abc} L_{\boldsymbol{r},c}, \tag{B.27}$$

$$[N_{\boldsymbol{r},a}, N_{\boldsymbol{r}',b}] = \delta_{\boldsymbol{r},\boldsymbol{r}'} \left\{ \epsilon_{abc} N_{\boldsymbol{r},c} + \alpha \left(N_{\boldsymbol{r},a} m_{\boldsymbol{r},b} - m_{\boldsymbol{r},a} N_{\boldsymbol{r},b} \right) \right\}, \tag{B.28}$$

Consider the commutator between the operators $\mathcal{L}_\alpha := -\sum_{\boldsymbol{r}} \mathrm{div}[\boldsymbol{f}_{\boldsymbol{r},\alpha} \cdot\ ]$ and $\mathcal{L}_\beta := -\sum_{\boldsymbol{r}} \mathrm{div}[\boldsymbol{f}_{\boldsymbol{r},\beta} \cdot\ ]$, where $\boldsymbol{f}_{\boldsymbol{r},\gamma}$ $(\gamma = A, B)$ is given by

$$\boldsymbol{f}_{\boldsymbol{r},\gamma} = -\frac{\boldsymbol{m}_{\boldsymbol{r}}}{1+\alpha^2} \times \left(\boldsymbol{H}_{\boldsymbol{r},\gamma} + \frac{\alpha}{m_s} \boldsymbol{m}_{\boldsymbol{r}} \times \boldsymbol{H}_{\boldsymbol{r},\gamma} \right). \tag{B.29}$$

From the equation

$$\frac{\partial}{\partial m_a} \left(\epsilon_{abc} m_{\boldsymbol{r},b} \boldsymbol{H}_{\boldsymbol{r},c} \right) = -\epsilon_{abc} m_{\boldsymbol{r},a} \frac{\partial}{\partial m_{\boldsymbol{r},b}} \left(\boldsymbol{H}_{\boldsymbol{r},\gamma,c} \right) = \boldsymbol{L}_{\boldsymbol{r}} \cdot \boldsymbol{H}_{\boldsymbol{r},\gamma}, \tag{B.30}$$

we can rewrite $\mathcal{L}_\gamma$ in terms of $\boldsymbol{N}_{\boldsymbol{r}}$ as follows:

$$\mathcal{L}_\gamma = \sum_{\boldsymbol{r}} \left(\boldsymbol{L}_{\boldsymbol{r}} \cdot \bar{\boldsymbol{H}}_{\boldsymbol{r},\gamma} + \alpha\ \boldsymbol{K}_{\boldsymbol{r}} \cdot \bar{\boldsymbol{H}}_{\boldsymbol{r},\gamma} \right) = \sum_{\boldsymbol{r}} \boldsymbol{N}_{\boldsymbol{r}} \cdot \bar{\boldsymbol{H}}_{\boldsymbol{r},\gamma}, \tag{B.31}$$

where $\bar{\boldsymbol{H}}_{\boldsymbol{r},\gamma} = \boldsymbol{H}_{\boldsymbol{r},\gamma}/(1+\alpha^2)$. Using Eq. (B.28), we obtain

$$[\mathcal{L}_A, \mathcal{L}_B] = \sum_{\boldsymbol{r}} \boldsymbol{N}_{\boldsymbol{r}} \left[\bar{\boldsymbol{H}}_A, \bar{\boldsymbol{H}}_B \right]_{\boldsymbol{r},\mathrm{mag}}, \tag{B.32}$$

where the commutator $\left[\bar{\boldsymbol{H}}_A, \bar{\boldsymbol{H}}_B \right]_{\boldsymbol{r},\mathrm{mag}}$ is defined by

$$\begin{aligned} \left[\bar{\boldsymbol{H}}_A, \bar{\boldsymbol{H}}_B \right]_{\boldsymbol{r},\mathrm{mag}} := {} & \bar{\boldsymbol{H}}_{\boldsymbol{r},A} \times \bar{\boldsymbol{H}}_{\boldsymbol{r},B} + \frac{\alpha \boldsymbol{m}_{\boldsymbol{r}}}{m_s} \times \left(\bar{\boldsymbol{H}}_{\boldsymbol{r},A} \times \bar{\boldsymbol{H}}_{\boldsymbol{r},B} \right) \\ & + \sum_{\boldsymbol{r}'} \left[\left(\bar{\boldsymbol{H}}_{\boldsymbol{r}',A} \cdot \boldsymbol{L}_{\boldsymbol{r}'} \right) \bar{\boldsymbol{H}}_{\boldsymbol{r},B} - \left(\bar{\boldsymbol{H}}_{\boldsymbol{r}',B} \cdot \boldsymbol{L}_{\boldsymbol{r}'} \right) \bar{\boldsymbol{H}}_{\boldsymbol{r},A} \right] \\ & + \frac{\alpha}{m_s} \sum_{\boldsymbol{r}'} \left[\left(\boldsymbol{m}_{\boldsymbol{r}'} \cdot \bar{\boldsymbol{H}}_{\boldsymbol{r}',A} \times \boldsymbol{L}_{\boldsymbol{r}'} \right) \bar{\boldsymbol{H}}_{\boldsymbol{r},B} - \left(\boldsymbol{m}_{\boldsymbol{r}'} \cdot \bar{\boldsymbol{H}}_{\boldsymbol{r}',B} \times \boldsymbol{L}_{\boldsymbol{r}'} \right) \bar{\boldsymbol{H}}_{\boldsymbol{r},A} \right]. \end{aligned} \tag{B.33}$$

Thus, $[\mathcal{L}_A, \mathcal{L}_B]$ defines the drift field with magnetic field $\left[\bar{\boldsymbol{H}}_A, \bar{\boldsymbol{H}}_B \right]_{\boldsymbol{r},\mathrm{mag}}$. For example, when $\boldsymbol{H}_{\boldsymbol{r},A} = \boldsymbol{B}_{-1}$ and $\boldsymbol{H}_{\boldsymbol{r},B} = \boldsymbol{B}_{+1}$, we obtain

$$\left[\bar{\boldsymbol{H}}_A, \bar{\boldsymbol{H}}_B \right]_{\boldsymbol{r},\mathrm{mag}} = \frac{\boldsymbol{B}_{-1} \times \boldsymbol{B}_{+1}}{(1+\alpha^2)\omega} + \frac{\alpha \boldsymbol{m}_{\boldsymbol{r}}}{m_s} \times \frac{\boldsymbol{B}_{-1} \times \boldsymbol{B}_{+1}}{(1+\alpha^2)\omega} = \boldsymbol{b}^{(1)} + \frac{\alpha \boldsymbol{m}_{\boldsymbol{r}}}{m_s} \times \boldsymbol{b}^{(1)}. \tag{B.34}$$

Therefore, we have

$$\mathcal{L}_F^{(1)} := \sum_{\boldsymbol{r}} \boldsymbol{L}_{\boldsymbol{r}} \cdot \left(\boldsymbol{b}^{(1)} + \frac{\alpha \boldsymbol{m}_{\boldsymbol{r}}}{m_s} \times \boldsymbol{b}^{(1)} \right), \tag{B.35}$$

which gives Eq. (6.105).

B.3 Two-dimensional ferromagnet: second order

The second-order vV HFE $\mathcal{L}_F^{(2)}$ is given by

$$\mathcal{L}_F^{(2)} = -\frac{[\mathcal{L}_{-1}[\mathcal{L}_0, \mathcal{L}_1]] + [\mathcal{L}_1[\mathcal{L}_0, \mathcal{L}_{-1}]]}{2\omega^2}. \tag{B.36}$$

We decompose $\mathcal{L}_0$ into the terms on the external field, the nearest-neighbor interaction, and the diffusion as follows:

$$\mathcal{L}_0^{\mathrm{ext}} = \frac{1}{1+\alpha^2}\sum_{\boldsymbol{r}} \boldsymbol{L}_{\boldsymbol{r}} \cdot \boldsymbol{B}_0, \quad \mathcal{L}_0^{\mathrm{int}} = \frac{J}{1+\alpha^2}\sum_{\boldsymbol{r}} \boldsymbol{L}_{\boldsymbol{r}} \cdot \sum_{\boldsymbol{r}':n.n} \boldsymbol{m}_{\boldsymbol{r}'}, \quad \mathcal{L}_0^{\mathrm{dif}} = \mathrm{div}_2\left(\mathcal{D}\ \cdot\ \right), \tag{B.37}$$

and decompose $\mathcal{L}_F^{(2)}$ accordingly; $\mathcal{L}_F^{(2)} = \mathcal{L}_F^{(2),\mathrm{ext}} + \mathcal{L}_F^{(2),\mathrm{int}} + \mathcal{L}_F^{(2),\mathrm{dif}}$. Combining Eqs. (B.33) and (B.37), we obtain

$$\mathcal{L}_F^{(2),\mathrm{ext}} = \sum_{\boldsymbol{r}} \boldsymbol{L}_{\boldsymbol{r}} \cdot \left((1-\alpha^2)\boldsymbol{b}^{(2)} + \frac{2\alpha \boldsymbol{m}_{\boldsymbol{r}}}{m_s} \times \boldsymbol{b}^{(2)}\right), \tag{B.38}$$

$$\mathcal{L}_F^{(2),\mathrm{int}} = \sum_{\boldsymbol{r}} \boldsymbol{L}_{\boldsymbol{r}} \cdot J\left(\frac{\alpha B_d}{m_s\omega(1+\alpha^2)}\right)^2 \sum_{\boldsymbol{r}':n,n} m_{\boldsymbol{r}',z} \begin{pmatrix} m_{\boldsymbol{r}',x}\delta m_{\boldsymbol{r},\boldsymbol{r}',z} \\ m_{\boldsymbol{r}',y}\delta m_{\boldsymbol{r},\boldsymbol{r}',z} \\ -m_{\boldsymbol{r}',z}\delta m_{\boldsymbol{r},\boldsymbol{r}',x} - m_{\boldsymbol{r}',y}\delta m_{\boldsymbol{r},\boldsymbol{r}',y} \end{pmatrix} \tag{B.39}$$

$$=: \sum_{\boldsymbol{r}} \boldsymbol{L}_{\boldsymbol{r}} \cdot \sum_{\boldsymbol{r}':n,n} \boldsymbol{\delta J}_{\boldsymbol{r},\boldsymbol{r}'}, \tag{B.40}$$

$$\mathcal{L}_F^{(2),\mathrm{dif}} = \mathrm{div}\left[\left(\frac{2\chi_{\boldsymbol{r}}}{1+\alpha^2}\boldsymbol{m}_{\boldsymbol{r}}\right)\ \cdot\ \right] + \mathrm{div}_2\left[\chi_{\boldsymbol{r}} DGG^{\mathrm{tr}}\ \cdot\ \right], \tag{B.41}$$

where $\delta\boldsymbol{m}_{\boldsymbol{r},\boldsymbol{r}'} = \boldsymbol{m}_{\boldsymbol{r}} - \boldsymbol{m}_{\boldsymbol{r}'}$. The overall effective master equation is given by

$$\partial_t P = \sum_{\boldsymbol{r}} \left(\boldsymbol{L}_{\boldsymbol{r}} \cdot \widetilde{\boldsymbol{H}}_{F,\boldsymbol{r}} P\right) + \mathrm{div}\left[\left(\frac{2(1+\chi)}{1+\alpha^2}\boldsymbol{m}_{\boldsymbol{r}}\right)P\right] + \mathrm{div}_2\left[(1+\chi)DGG^{\mathrm{tr}}P\right], \tag{B.42}$$

where the effective field $\widetilde{\boldsymbol{H}}_{F,\boldsymbol{r}}$is

$$\widetilde{\boldsymbol{H}}_{F,\boldsymbol{r}} = \sum_{\boldsymbol{r}':n,n} (J\boldsymbol{m}_{\boldsymbol{r}} + \boldsymbol{\delta J}_{\boldsymbol{r},\boldsymbol{r}'}) + \boldsymbol{B}_0 + \boldsymbol{b}^{(1)} + (1-\alpha^2)\boldsymbol{b}^{(2)} + \left(-\frac{\alpha}{m_s}\boldsymbol{b}^{(1)} - \frac{2\alpha}{m_s}\boldsymbol{b}^{(2)}\right) \times \boldsymbol{m}_{\boldsymbol{r}}. \tag{B.43}$$

By defining a new diffusion matrix G_F by $G_F := (1+\chi)^{1/2}G$, the second and third terms on the right-hand side of Eq. (B.42) are rewritten as

$$\mathrm{div}\left[\left(\frac{2(1+\chi)}{1+\alpha^2}\boldsymbol{m}_{\boldsymbol{r}}\right)P\right] = \sum_{\boldsymbol{r}} \boldsymbol{L}_{\boldsymbol{r}} \cdot \left(-\boldsymbol{b}^{(2),\mathrm{dif}} + \frac{\boldsymbol{b}^{(2),\mathrm{dif}}}{m_s} \times \boldsymbol{m}_{\boldsymbol{r}}\right) P + \mathrm{div}\left(-\boldsymbol{d}_F P\right), \tag{B.44}$$

$$\mathrm{div}_2\left[(1+\chi)DGG^{\mathrm{tr}}P\right] = \mathrm{div}_2\left[DG_F G_F^{\mathrm{tr}}P\right], \tag{B.45}$$

where $\boldsymbol{d}_{F,i} := g_{F,kl}\partial_k g_{F,il}$ and

$$\boldsymbol{b}^{(2),\mathrm{dif}} := \frac{Dm_s}{2(1+\alpha^2)}\frac{\delta\chi_{\boldsymbol{r}}}{\delta \boldsymbol{m}_{\boldsymbol{r}}}. \tag{B.46}$$

Equation (B.42) is then rewritten as

$$\partial_t P = \sum_{\boldsymbol{r}} \left(\boldsymbol{L}_{\boldsymbol{r}} \cdot \boldsymbol{H}_{F,\boldsymbol{r}} P\right) + \mathrm{div}\left(-\boldsymbol{d}_F P\right) + \mathrm{div}_2\left[DG_F G_F^{\mathrm{tr}} P\right], \tag{B.47}$$

where $\boldsymbol{H}_{F,\boldsymbol{r}}$ is the effective field defined in Eq. (6.111). Comparing this equation with Eq. (6.7), we finally arrive at the sLLG equation (6.109).

B.4 Multiferroic spin chain

The calculation is done in a manner similar to what we have done in App. B.2. The first-order FP operator $\mathcal{L}_F^{(1)}$ is given by

$$\mathcal{L}_F^{(1)} := \sum_{\boldsymbol{r}} \boldsymbol{L}_{\boldsymbol{r}} \cdot \frac{i}{\omega}\left[\bar{\boldsymbol{H}}_{-1}, \bar{\boldsymbol{H}}_1\right]_{\boldsymbol{r},\mathrm{mag}}, \tag{B.48}$$

where the Fourier harmonics $\bar{\boldsymbol{H}}_{\pm 1}$ of the effective field is

$$\bar{\boldsymbol{H}}_{\pm 1} := \sum_{\boldsymbol{r}':n.n.} \boldsymbol{D}_{\pm} \times \boldsymbol{m}_{\boldsymbol{r}'} + \boldsymbol{B}_{\pm}, \quad \boldsymbol{D}_{\pm} := \frac{g_{\mathrm{me}}E_d}{2}\left(\pm i, 1, 0\right)^{\mathrm{tr}}, \quad \boldsymbol{B}_{\pm} := \frac{B_d}{2}\left(1, \mp i, 0\right)^{\mathrm{tr}}. \tag{B.49}$$

By a straightforward calculation, we obtain

$$\mathcal{L}_F^{(1)} := \sum_{\boldsymbol{r}} \boldsymbol{L}_{\boldsymbol{r}} \cdot \boldsymbol{H}_{F,\boldsymbol{r}}^{(1)}, \tag{B.50}$$

$$\boldsymbol{H}_{F,\boldsymbol{r}}^{(1)} := \sum_{\boldsymbol{r}':n.n.} \left(\boldsymbol{D}_{F,\boldsymbol{r},\boldsymbol{r}'} \times \boldsymbol{m}_{\boldsymbol{r}'}\right) + \boldsymbol{B}_F - \alpha \boldsymbol{B}_F \times \boldsymbol{m}_{\boldsymbol{r}} - \sum_{\boldsymbol{r}':n.n.} \frac{\alpha\epsilon_B\epsilon_E}{2m_s(1+\alpha^2)\omega} \begin{pmatrix} m_s^2 + m_{\boldsymbol{r}',y}\delta m_{\boldsymbol{r},y} \\ -m_{\boldsymbol{r}',y}\delta m_{\boldsymbol{r},x} \\ 0 \end{pmatrix}, \tag{B.51}$$

where $\boldsymbol{D}_{F,\boldsymbol{r},\boldsymbol{r}'}$ and $\boldsymbol{B}_F$ are defined in Eq. (6.122). Equation (6.121) follows from the correspondence between the master equation and the EOM explained in Sec. 6.1.

Acknowledgement

The studies in this thesis were conducted when the author was a Ph.D. student at Prof. Masahito Ueda's group in the University of Tokyo. I would like to express my deep sense of gratitude to my collaborators and colleagues.

First of all, I would like to express my deepest gratitude to my supervisor, Prof. Masahito Ueda, who was a wonderful teacher to me throughout the years when I was in his group. I admire him for his excellent teaching skills, which greatly helped me to advance my research, his broad interest ranging from ultracold atomic gases to non-equilibrium statistical mechanics, and his indomitable spirit. He spent plenty of time for me discussing my research though he was always busy. Although I have caused a lot of trouble for him, he kindly and patiently taught me how I should behave to be successful in my career. It was great pleasure for me to be a member of his group and to receive a Ph.D. under his supervision. Finally, I thank him for his careful reading of this thesis, which certainly required lots of patience and time. His insightful comments substantially improved the quality and readability of this thesis.

I also appreciate all the members of the thesis committee, Prof. Yusuke Kato, Prof. Shinji Tsuneyuki, Prof. Masaki Oshikawa, Prof. Yoshio Torii, and Prof. Naomichi Hatano, for carefully reviewing this thesis and for numerous insightful comments. Especially, I acknowledge Prof. Naomichi Hatano for his careful reading of the entire thesis, which greatly improved its readability.

I sincerely appreciate considerable assistance from my collaborators. I am grateful to Dr. Masaya Nakagawa for many stimulating discussions on the study in Chapter 5. His deep understanding on Floquet physics and topological phenomena always helped me a lot to advance the study, without which I could not complete it. I would also like to thank him for waiting for me to complete the study for half a year when I temporally left from physics for a job hunting. Next, I am grateful to Prof. Masahiro Sato for his collaboration and incessant encouragement. He accepted me as a visiting student at Ibaraki University through the domestic dispatch program of the Program for Leading Graduate Schools, where the study in Chapter 6 was initiated. Dr. Hiroyuki Fujita always taught me the fundamentals of spin systems, non-equilibrium physics, and spintronics, which greatly helped me complete the study in Chapter 6. I would like to express my gratitude to the former and present members of Prof. Ueda's group, especially to my collaborators, Prof. Shunsuke Furukawa, Dr. Yuto Ashida, Zongping Gong, Takumi Yoshino, and Kohei Kawabata. I also thank Dr. Kazuya Fujimoto and Ryusuke Hamazaki for fruitful discussions on non-equilibrium statistical mechanics. I am really thankful to Mrs. Kimiko Kowashi, Mrs. Asako Takeuchi, Mrs. Aya Tamai, and Mrs. Yumiko Wada, who helped me a lot in dealing with administrative affairs.

I greatly acknowledge financial support from the Japan Society for the Promotion of Science (JSPS) through the Program for Leading Graduate Schools "Advanced Leading Graduate Course for Photon Science" (ALPS) and Grant-in-Aid for JSPS Research Fellow (KAKENHI

Grant No. JP16J03619). I would also like to thank ALPS for the support on my visit to Ibaraki University through its domestic dispatch program and Yukawa Institute for Theoretical Physics (YITP) for the support on my visit to YITP through its research-visit program. I am deeply grateful to Grant-in-Aid for Scientific Research on Innovative Areas "Topological Materials Science" (KAKENHI Grant No. JP15H05852) for the support on my visit to Kyoto University through its domestic exchange program for young researchers and for the financial support and recommendation for attending the summer school and conference in Canada. Through its conferences and exchange programs, I had learned a lot on topological quantum phenomena and condensed-matter physics. I appreciate, from the bottom of my heart, these fellowships and financial support for covering my research and living expense despite harsh economic conditions in Japan. It was sheer luck for me to be educated in comfort throughout the Ph.D. course and I believe that this would not have been possible without huge efforts of the faculty members and academic staffs of the universities as well as the officials of the Ministry of Education, Culture, Sports, Science and Technology (MEXT). Although the economic environment in Japan and the circumstance surrounding basic science remain severe, I hope that this support will continue for the present and future young scientists.

Finally, I wish to thank my parents, Osamu and Kiyomi, who have always encouraged me to pursue my own way, which is indispensable to complete the Ph.D. course.

Bibliography

[1] S. Higashikawa, M. Nakagawa, and M. Ueda, "Floquet chiral magnetic effect," *arXiv preprint arXiv:1806.06868*, 2018.

[2] S. Higashikawa, H. Fujita, and M. Sato, "Floquet engineering of classical systems," *arXiv preprint arXiv:1810.01103*, oct 2018.

[3] T. Yoshino, S. Furukawa, S. Higashikawa, and M. Ueda, "Collective modes of vortex lattices in two-component Bose-Einstein condensates under synthetic gauge fields," *New Journal of Physics*, vol. 21, p. 015001, jul 2018.

[4] K. Kawabata, S. Higashikawa, Z. Gong, Y. Ashida, and M. Ueda, "Topological unification of time-reversal and particle-hole symmetries in non-Hermitian physics," *Nature Communications*, vol. 10, no. 1, p. 297, 2019.

[5] Z. Gong, Y. Ashida, K. Kawabata, K. Takasan, S. Higashikawa, and M. Ueda, "Topological phases of non-Hermitian systems," *Phys. Rev. X*, vol. 8, no. 3, p. 031079, 2018.

[6] Z. Gong, S. Higashikawa, and M. Ueda, "Zeno Hall Effect," *Phys. Rev. Lett.*, vol. 118, no. 20, 2017.

[7] S. Higashikawa and M. Ueda, "Influence of topological constraints and topological excitations: Decomposition formulas for calculating homotopy groups of symmetry-broken phases," *Phys. Rev. B*, vol. 95, no. 13, p. 134520, 2017.

[8] S. Higashikawa and M. Ueda, "mu-symmetry breaking: An algebraic approach to finding mean fields of quantum many-body systems," *Phys. Rev. A*, vol. 94, no. 1, p. 013613, 2016.

[9] B. V. Chirikov, F. M. Izrailev, and D. L. Shepelyansky, "Dynamical stochasticity in classical and quantum mechanics," *Mathematical physics reviews*, vol. 2, pp. 209–267, 1981.

[10] D. H. Dunlap and V. M. Kenkre, "Dynamic localization of a charged particle moving under the influence of an electric field," *Phys. Rev. B*, vol. 34, no. 6, pp. 3625–3633, 1986.

[11] L. Gammaitoni, P. Hänggi, P. Jung, and F. Marchesoni, "Stochastic resonance," *Rev. Mod. Phys.*, vol. 70, no. 1, pp. 223–287, 1998.

[12] P. Jung, "Periodically driven stochastic systems," *Physics Reports*, vol. 234, no. 4, pp. 175–295, 1993.

[13] P. L. Kapitza, "Dynamic stability of the pendulum with vibrating suspension point," *Soviet Physics–JETP*, vol. 21, no. 5, pp. 588–597, 1951.

[14] W. Paul, "Electromagnetic traps for charged and neutral particles," *Rev. Mod. Phys.*, vol. 62, no. 3, pp. 531–540, 1990.

[15] E. D. Courant, M. S. Livingston, and H. S. Snyder, "The Strong-Focusing Synchroton—A New High Energy Accelerator," *Phys. Rev.*, vol. 88, no. 5, pp. 1190–1196, 1952.

[16] R. P. Feynman, R. B. Leighton, and M. Sands, "The Feynman Lectures on Physics, Vol. II: The New Millennium Edition: Mainly Electromagnetism and Matter," Feynman Lectures on Physics, ch. 29, Basic Books, 2011.

[17] T. Oka and H. Aoki, "Photovoltaic Hall effect in graphene," *Phys. Rev. B*, vol. 79, no. 8, p. 081406, 2009.

[18] T. Kitagawa, M. S. Rudner, E. Berg, and E. Demler, "Exploring topological phases with quantum walks," *Phys. Rev. A*, vol. 82, no. 3, p. 033429, 2010.

[19] Y. H. Wang, H. Steinberg, P. Jarillo-Herrero, and N. Gedik, "Observation of Floquet-Bloch States on the Surface of a Topological Insulator," *Science*, vol. 342, no. 6157, pp. 453–457, 2013.

[20] G. Jotzu, M. Messer, R. Desbuquois, M. Lebrat, T. Uehlinger, D. Greif, and T. Esslinger, "Experimental realization of the topological Haldane model with ultracold fermions," *Nature*, vol. 515, p. 237, nov 2014.

[21] F. Mahmood, C.-K. Chan, Z. Alpichshev, D. Gardner, Y. Lee, P. A. Lee, and N. Gedik, "Selective scattering between Floquet–Bloch and Volkov states in a topological insulator," *Nature Physics*, vol. 12, p. 306, jan 2016.

[22] J. W. Mclver, B. Schulte, F. Stein, T. Matsuyama, G. Jotzu, G. Meier, and A. Cavalleri, "Light-induced anomalous Hall effect in graphene," *arXiv preprint arXiv:1811.03522*, nov 2018.

[23] S. Choi, J. Choi, R. Landig, G. Kucsko, H. Zhou, J. Isoya, F. Jelezko, S. Onoda, H. Sumiya, V. Khemani, C. von Keyserlingk, N. Y. Yao, E. Demler, and M. D. Lukin, "Observation of discrete time-crystalline order in a disordered dipolar many-body system," *Nature*, vol. 543, p. 221, mar 2017.

[24] J. Zhang, P. W. Hess, A. Kyprianidis, P. Becker, A. Lee, J. Smith, G. Pagano, I.-D. Potirniche, A. C. Potter, A. Vishwanath, N. Y. Yao, and C. Monroe, "Observation of a discrete time crystal," mar 2017.

[25] N. Y. Yao, A. C. Potter, I.-D. Potirniche, and A. Vishwanath, "Discrete Time Crystals: Rigidity, Criticality, and Realizations," *Phys. Rev. Lett.*, vol. 118, no. 3, p. 030401, 2017.

[26] D. V. Else, B. Bauer, and C. Nayak, "Floquet Time Crystals," *Phys. Rev. Lett.*, vol. 117, no. 9, p. 090402, 2016.

[27] M. Bukov, L. D'Alessio, and A. Polkovnikov, "Universal high-frequency behavior of periodically driven systems: from dynamical stabilization to Floquet engineering," *Advances in Physics*, vol. 64, no. 2, pp. 139–226, 2015.

[28] A. Eckardt, "Colloquium: Atomic quantum gases in periodically driven optical lattices," *Rev. Mod. Phys.*, vol. 89, no. 1, p. 011004, 2017.

[29] T. Oka and S. Kitamura, "Floquet Engineering of Quantum Materials," *Annual Review of Condensed Matter Physics*, vol. 10, no. 1, 2019.

[30] G. Floquet, "Sur les equations differentielles lineaires," *Ann. Sci. Ecole Norm. Sup.A*, vol. 12, no. 1883, pp. 47–88, 1883.

[31] C. Chicone, *Ordinary differential equations with applications*, vol. 34. Springer Science & Business Media, 2006.

[32] A. Eckardt, C. Weiss, and M. Holthaus, "Superfluid-Insulator Transition in a Periodically Driven Optical Lattice," *Phys. Rev. Lett.*, vol. 95, no. 26, p. 260404, 2005.

[33] A. Eckardt, M. Holthaus, H. Lignier, A. Zenesini, D. Ciampini, O. Morsch, and E. Arimondo, "Exploring dynamic localization with a Bose-Einstein condensate," *Phys. Rev. A*, vol. 79, no. 1, p. 013611, 2009.

[34] A. Zenesini, H. Lignier, D. Ciampini, O. Morsch, and E. Arimondo, "Coherent Control of Dressed Matter Waves," *Phys. Rev. Lett.*, vol. 102, no. 10, p. 100403, 2009.

[35] D. Jaksch and P. Zoller, "Creation of effective magnetic fields in optical lattices: the Hofstadter butterfly for cold neutral atoms," *New Journal of Physics*, vol. 5, no. 1, p. 56, 2003.

[36] M. Aidelsburger, M. Atala, M. Lohse, J. T. Barreiro, B. Paredes, and I. Bloch, "Realization of the Hofstadter Hamiltonian with Ultracold Atoms in Optical Lattices," *Phys. Rev. Lett.*, vol. 111, no. 18, p. 185301, 2013.

[37] M. Aidelsburger, M. Lohse, C. Schweizer, M. Atala, J. T. Barreiro, S. Nascimbène, N. R. Cooper, I. Bloch, and N. Goldman, "Measuring the Chern number of Hofstadter bands with ultracold bosonic atoms," *Nature Physics*, vol. 11, p. 162, dec 2014.

[38] C. J. Kennedy, W. C. Burton, W. C. Chung, and W. Ketterle, "Observation of Bose–Einstein condensation in a strong synthetic magnetic field," *Nature Physics*, vol. 11, p. 859, aug 2015.

[39] F. D. M. Haldane, "Model for a Quantum Hall Effect without Landau Levels: Condensed-Matter Realization of the "Parity Anomaly"," *Phys. Rev. Lett.*, vol. 61, no. 18, pp. 2015–2018, 1988.

[40] S. Nakajima, T. Tomita, S. Taie, T. Ichinose, H. Ozawa, L. Wang, M. Troyer, and Y. Takahashi, "Topological Thouless pumping of ultracold fermions," *Nature Physics*, vol. 12, p. 296, jan 2016.

[41] M. Lohse, C. Schweizer, O. Zilberberg, M. Aidelsburger, and I. Bloch, "A Thouless quantum pump with ultracold bosonic atoms in an optical superlattice," *Nat. Phys.*, vol. 12, p. 350, 2016.

[42] Z. Ovadyahu, "Suppression of Inelastic Electron-Electron Scattering in Anderson Insulators," *Phys. Rev. Lett.*, vol. 108, p. 156602, apr 2012.

[43] S. Iwai, M. Ono, A. Maeda, H. Matsuzaki, H. Kishida, H. Okamoto, and Y. Tokura, "Ultrafast Optical Switching to a Metallic State by Photoinduced Mott Transition in a Halogen-Bridged Nickel-Chain Compound," *Phys. Rev. Lett.*, vol. 91, p. 057401, jul 2003.

[44] T. Ishikawa, Y. Sagae, Y. Naitoh, Y. Kawakami, H. Itoh, K. Yamamoto, K. Yakushi, H. Kishida, T. Sasaki, S. Ishihara, Y. Tanaka, K. Yonemitsu, and S. Iwai, "Optical freezing of charge motion in an organic conductor," *Nature Communications*, vol. 5, p. 5528, nov 2014.

[45] S. Kaiser, C. R. Hunt, D. Nicoletti, W. Hu, I. Gierz, H. Y. Liu, M. Le Tacon, T. Loew, D. Haug, B. Keimer, and A. Cavalleri, "Optically induced coherent transport far above Tc in underdoped YBa2Cu3O6," *Phys. Rev. B*, vol. 89, p. 184516, may 2014.

[46] A. Kirilyuk, A. V. Kimel, and T. Rasing, "Ultrafast optical manipulation of magnetic order," *Rev. Mod. Phys.*, vol. 82, no. 3, pp. 2731–2784, 2010.

[47] J.-Y. Bigot and M. Vomir, "Ultrafast magnetization dynamics of nanostructures," *Annalen der Physik*, vol. 525, pp. 2–30, feb 2013.

[48] D. Bossini, K. Konishi, S. Toyoda, T. Arima, J. Yumoto, and M. Kuwata-Gonokami, "Femtosecond activation of magnetoelectricity," *Nature Physics*, vol. 14, no. 4, pp. 370–374, 2018.

[49] Y. Kawakami, H. Itoh, K. Yonemitsu, and S. Iwai, "Strong light-field effects driven by nearly single-cycle 7 fs light-field in correlated organic conductors," *Journal of Physics B: Atomic, Molecular and Optical Physics*, vol. 51, no. 17, p. 174005, 2018.

[50] D. Fausti, R. I. Tobey, N. Dean, S. Kaiser, A. Dienst, M. C. Hoffmann, S. Pyon, T. Takayama, H. Takagi, and A. Cavalleri, "Light-Induced Superconductivity in a Stripe-Ordered Cuprate," *Science*, vol. 331, no. 6014, pp. 189–191, 2011.

[51] W. Hu, S. Kaiser, D. Nicoletti, C. R. Hunt, I. Gierz, M. C. Hoffmann, M. Le Tacon, T. Loew, B. Keimer, and A. Cavalleri, "Optically enhanced coherent transport in YBa2Cu3O6.5 by ultrafast redistribution of interlayer coupling," *Nature Materials*, vol. 13, p. 705, may 2014.

[52] M. Mitrano, A. Cantaluppi, D. Nicoletti, S. Kaiser, A. Perucchi, S. Lupi, P. Di Pietro, D. Pontiroli, M. Riccò, S. R. Clark, D. Jaksch, and A. Cavalleri, "Possible light-induced superconductivity in K3C60 at high temperature," *Nature*, vol. 530, p. 461, feb 2016.

[53] E. Beaurepaire, J.-C. Merle, A. Daunois, and J.-Y. Bigot, "Ultrafast Spin Dynamics in Ferromagnetic Nickel," *Phys. Rev. Lett.*, vol. 76, no. 22, pp. 4250–4253, 1996.

[54] J. Hohlfeld, E. Matthias, R. Knorren, and K. H. Bennemann, "Nonequilibrium Magnetization Dynamics of Nickel," *Phys. Rev. Lett.*, vol. 78, pp. 4861–4864, jun 1997.

[55] B. Koopmans, M. van Kampen, J. T. Kohlhepp, and W. J. M. de Jonge, "Ultrafast Magneto-Optics in Nickel: Magnetism or Optics?," *Phys. Rev. Lett.*, vol. 85, pp. 844–847, jul 2000.

[56] N. H. Lindner, G. Refael, and V. Galitski, "Floquet topological insulator in semiconductor quantum wells," *Nature Physics*, vol. 7, p. 490, mar 2011.

[57] B. Dóra, J. Cayssol, F. Simon, and R. Moessner, "Optically Engineering the Topological Properties of a Spin Hall Insulator," *Phys. Rev. Lett.*, vol. 108, p. 056602, jan 2012.

[58] M. Ezawa, "Photoinduced Topological Phase Transition and a Single Dirac-Cone State in Silicene," *Phys. Rev. Lett.*, vol. 110, p. 026603, jan 2013.

[59] H. Dehghani, T. Oka, and A. Mitra, "Dissipative Floquet topological systems," *Phys. Rev. B*, vol. 90, no. 19, p. 195429, 2014.

[60] K. I. Seetharam, C.-E. Bardyn, N. H. Lindner, M. S. Rudner, and G. Refael, "Controlled Population of Floquet-Bloch States via Coupling to Bose and Fermi Baths," *Phys. Rev. X*, vol. 5, no. 4, p. 041050, 2015.

[61] A. G. Grushin, Á. Gómez-León, and T. Neupert, "Floquet Fractional Chern Insulators," *Phys. Rev. Lett.*, vol. 112, p. 156801, apr 2014.

[62] M. Benito, A. Gómez-León, V. M. Bastidas, T. Brandes, and G. Platero, "Floquet engineering of long-range p-wave superconductivity," *Phys. Rev. B*, vol. 90, p. 205127, nov 2014.

[63] T. Mikami, S. Kitamura, K. Yasuda, N. Tsuji, T. Oka, and H. Aoki, "Brillouin-Wigner theory for high-frequency expansion in periodically driven systems: Application to Floquet topological insulators," *Phys. Rev. B*, vol. 93, no. 14, p. 144307, 2016.

[64] K. Takasan, M. Nakagawa, and N. Kawakami, "Laser-irradiated Kondo insulators: Controlling the Kondo effect and topological phases," *Phys. Rev. B*, vol. 96, no. 11, p. 115120, 2017.

[65] K. Takasan, A. Daido, N. Kawakami, and Y. Yanase, "Laser-induced topological superconductivity in cuprate thin films," *Phys. Rev. B*, vol. 95, p. 134508, apr 2017.

[66] D. M. Kennes, A. de la Torre, A. Ron, D. Hsieh, and A. J. Millis, "Floquet Engineering in Quantum Chains," *Phys. Rev. Lett.*, vol. 120, p. 127601, mar 2018.

[67] J. Liu, K. Hejazi, and L. Balents, "Floquet Engineering of Multiorbital Mott Insulators: Applications to Orthorhombic Titanates," *Phys. Rev. Lett.*, vol. 121, p. 107201, sep 2018.

[68] D. M. Kennes, M. Claassen, M. A. Sentef, and C. Karrasch, "Light-induced d-wave superconductivity through Floquet-engineered Fermi surfaces in cuprates," *arXiv preprint arXiv:1808.04655*, aug 2018.

[69] N. Walldorf, D. M. Kennes, J. Paaske, and A. J. Millis, "Antiferromagnetic Order and Non-Equilibrium Distributions in the Floquet-Engineered Hubbard Model," *arXiv preprint arXiv:1809.08607*, sep 2018.

[70] K. Hejazi, J. Liu, and L. Balents, "Floquet spin and spin-orbital Hamiltonians and doublon-holon generations in periodically driven Mott insulators," *arXiv preprint arXiv:1809.09800*, sep 2018.

[71] M. Sato, Y. Sasaki, and T. Oka, "Floquet Majorana Edge Mode and Non-Abelian Anyons in a Driven Kitaev Model," *arXiv preprint arXiv:1404.2010*, 2014.

[72] S. Takayoshi, H. Aoki, and T. Oka, "Magnetization and phase transition induced by circularly polarized laser in quantum magnets," *Phys. Rev. B*, vol. 90, no. 8, p. 085150, 2014.

[73] S. Takayoshi, M. Sato, and T. Oka, "Laser-induced magnetization curve," *Phys. Rev. B*, vol. 90, no. 21, p. 214413, 2014.

[74] J. H. Mentink, K. Balzer, and M. Eckstein, "Ultrafast and reversible control of the exchange interaction in Mott insulators," *Nature Communications*, vol. 6, p. 6708, mar 2015.

[75] R. V. Mikhaylovskiy, E. Hendry, A. Secchi, J. H. Mentink, M. Eckstein, A. Wu, R. V. Pisarev, V. V. Kruglyak, M. I. Katsnelson, T. Rasing, and A. V. Kimel, "Ultrafast optical modification of exchange interactions in iron oxides," *Nature Communications*, vol. 6, p. 8190, sep 2015.

[76] M. Sato, S. Takayoshi, and T. Oka, "Laser-Driven Multiferroics and Ultrafast Spin Current Generation," *Phys. Rev. Lett.*, vol. 117, no. 14, p. 147202, 2016.

[77] M. Claassen, H.-C. Jiang, B. Moritz, and T. P. Devereaux, "Dynamical time-reversal symmetry breaking and photo-induced chiral spin liquids in frustrated Mott insulators," *Nature Communications*, vol. 8, no. 1, p. 1192, 2017.

[78] S. Kitamura, T. Oka, and H. Aoki, "Probing and controlling spin chirality in Mott insulators by circularly polarized laser," *Phys. Rev. B*, vol. 96, no. 1, p. 014406, 2017.

[79] A. Ono and S. Ishihara, "Photocontrol of magnetic structure in an itinerant magnet," *Phys. Rev. B*, vol. 98, p. 214408, dec 2018.

[80] E. A. Stepanov, C. Dutreix, and M. I. Katsnelson, "Dynamical and Reversible Control of Topological Spin Textures," *Phys. Rev. Lett.*, vol. 118, p. 157201, apr 2017.

[81] S. A. Owerre, "Floquet topological magnons," *Journal of Physics Communications*, vol. 1, no. 2, p. 021002, 2017.

[82] D. Yudin, D. R. Gulevich, and M. Titov, "Light-Induced Anisotropic Skyrmion and Stripe Phases in a Rashba Ferromagnet," *Phys. Rev. Lett.*, vol. 119, p. 147202, oct 2017.

[83] M. Z. Hasan and C. L. Kane, "Colloquium: Topological insulators," *Reviews of Modern Physics*, vol. 82, no. 4, pp. 3045–3067, 2010.

[84] X. L. Qi and S. C. Zhang, "Topological insulators and superconductors," *Reviews of Modern Physics*, vol. 83, no. 4, 2011.

[85] T. Kitagawa, E. Berg, M. Rudner, and E. Demler, "Topological characterization of periodically driven quantum systems," *Phys. Rev. B*, vol. 82, no. 23, p. 235114, 2010.

[86] T. Kitagawa, T. Oka, A. Brataas, L. Fu, and E. Demler, "Transport properties of nonequilibrium systems under the application of light: Photoinduced quantum Hall insulators without Landau levels," *Phys. Rev. B*, vol. 84, no. 23, p. 235108, 2011.

[87] L. Jiang, T. Kitagawa, J. Alicea, A. R. Akhmerov, D. Pekker, G. Refael, J. I. Cirac, E. Demler, M. D. Lukin, and P. Zoller, "Majorana Fermions in Equilibrium and in Driven Cold-Atom Quantum Wires," *Phys. Rev. Lett.*, vol. 106, no. 22, p. 220402, 2011.

[88] D. J. Thouless, M. Kohmoto, M. P. Nightingale, and M. den Nijs, "Quantized hall conductance in a two-Dimensional periodic potential," *Phys. Rev. Lett.*, vol. 49, no. 6, pp. 405–408, 1982.

[89] J. C. Budich, Y. Hu, and P. Zoller, "Helical Floquet Channels in 1D Lattices," *Phys. Rev. Lett.*, vol. 118, no. 10, p. 105302, 2017.

[90] H. Nielsen and M. Ninomiya, "Absence of neutrinos on a lattice: (I). Proof by homotopy theory," *Nuclear Physics B*, vol. 185, pp. 20–40, jul 1981.

[91] H. Nielsen and M. Ninomiya, "Absence of neutrinos on a lattice: (II). Intuitive topological proof," *Nuclear Physics B*, vol. 193, pp. 173–194, dec 1981.

[92] A. Vilenkin, "Equilibrium parity-violating current in a magnetic field," *Phys. Rev. D*, vol. 22, pp. 3080–3084, dec 1980.

[93] K. Fukushima, D. E. Kharzeev, and H. J. Warringa, "Chiral magnetic effect," *Phys. Rev. D*, vol. 78, no. 7, p. 074033, 2008.

[94] A. Lazarides, A. Das, and R. Moessner, "Equilibrium states of generic quantum systems subject to periodic driving," *Phys. Rev. E*, vol. 90, no. 1, p. 012110, 2014.

[95] T. Mori, T. Kuwahara, and K. Saito, "Rigorous Bound on Energy Absorption and Generic Relaxation in Periodically Driven Quantum Systems," *Phys. Rev. Lett.*, vol. 116, no. 12, p. 120401, 2016.

[96] T. Kuwahara, T. Mori, and K. Saito, "Floquet–Magnus theory and generic transient dynamics in periodically driven many-body quantum systems," *Annals of Physics*, vol. 367, pp. 96–124, apr 2016.

[97] M. Bukov, M. Heyl, D. A. Huse, and A. Polkovnikov, "Heating and many-body resonances in a periodically driven two-band system," *Phys. Rev. B*, vol. 93, no. 15, p. 155132, 2016.

[98] D. A. Abanin, W. De Roeck, W. W. Ho, and F. b. ç. Huveneers, "Effective Hamiltonians, prethermalization, and slow energy absorption in periodically driven many-body systems," *Phys. Rev. B*, vol. 95, no. 1, p. 014112, 2017.

[99] T. Moriya, "Anisotropic Superexchange Interaction and Weak Ferromagnetism," *Phys. Rev.*, vol. 120, no. 1, pp. 91–98, 1960.

[100] I. Dzyaloshinsky, "A thermodynamic theory of "weak" ferromagnetism of antiferromagnetics," *Journal of Physics and Chemistry of Solids*, vol. 4, no. 4, pp. 241–255, 1958.

[101] A. P. Schnyder, S. Ryu, A. Furusaki, and A. W. W. Ludwig, "Classification of topological insulators and superconductors in three spatial dimensions," *Phys. Rev. B*, vol. 78, no. 19, p. 195125, 2008.

[102] A. Kitaev, "Periodic table for topological insulators and superconductors," *AIP Conference Proceedings*, vol. 1134, pp. 22–30, 2009.

[103] J. C. Y. Teo and C. L. Kane, "Topological defects and gapless modes in insulators and superconductors," *Phys. Rev. B*, vol. 82, no. 11, p. 115120, 2010.

[104] T. Morimoto and A. Furusaki, "Topological classification with additional symmetries from Clifford algebras," *Phys. Rev. B*, vol. 88, no. 12, pp. 1–16, 2013.

[105] C.-K. Chiu, J. C. Y. Teo, A. P. Schnyder, and S. Ryu, "Classification of topological quantum matter with symmetries," *Rev. Mod. Phys.*, vol. 88, no. 3, p. 035005, 2016.

[106] H. Weyl, "GRAVITATION AND THE ELECTRON," *Proceedings of the National Academy of Sciences*, vol. 15, no. 4, pp. 323–334, 1929.

[107] N. P. Armitage, E. J. Mele, and A. Vishwanath, "Weyl and Dirac semimetals in three-dimensional solids," *Rev. Mod. Phys.*, vol. 90, no. 1, p. 015001, 2018.

[108] M. J. Rice and E. J. Mele, "Elementary Excitations of a Linearly Conjugated Diatomic Polymer," *Phys. Rev. Lett.*, vol. 49, no. 19, pp. 1455–1459, 1982.

[109] N. Goldman and J. Dalibard, "Periodically Driven Quantum Systems: Effective Hamiltonians and Engineered Gauge Fields," *Phys. Rev. X*, vol. 4, no. 3, p. 031027, 2014.

[110] A. Eckardt and E. Anisimovas, "High-frequency approximation for periodically driven quantum systems from a Floquet-space perspective," *New Journal of Physics*, vol. 17, no. 9, p. 093039, 2015.

[111] T. P. Grozdanov and M. J. Rakovic, "Quantum system driven by rapidly varying periodic perturbation," *Phys. Rev. A*, vol. 38, no. 4, pp. 1739–1746, 1988.

[112] S. Rahav, I. Gilary, and S. Fishman, "Effective Hamiltonians for periodically driven systems," *Phys. Rev. A*, vol. 68, no. 1, p. 013820, 2003.

[113] S. Rahav, I. Gilary, and S. Fishman, "Time Independent Description of Rapidly Oscillating Potentials," *Phys. Rev. Lett.*, vol. 91, no. 11, p. 110404, 2003.

[114] F. Casas, J. A. Oteo, and J. Ros, "Floquet theory: exponential perturbative treatment," *Journal of Physics A: Mathematical and General*, vol. 34, no. 16, p. 3379, 2001.

[115] A. Rajak, R. Citro, and E. G. D. Torre, "Stability and pre-thermalization in chains of classical kicked rotors," *Journal of Physics A: Mathematical and General*, vol. 51, no. 46, p. 465001, 2018.

[116] O. Howell, P. Weinberg, D. Sels, A. Polkovnikov, and M. Bukov, "Asymptotic Prethermalization in Periodically Driven Classical Spin Chains," *Phys. Rev. Lett.*, vol. 122, p. 010602, jan 2019.

[117] T. Mori, "Floquet prethermalization in periodically driven classical spin systems," *Phys. Rev. B*, vol. 98, no. 10, p. 104303, 2018.

[118] P. Langevin, "Sur la théorie du mouvement brownien," *Compt. Rendus*, vol. 146, pp. 530–533, 1908.

[119] N. G. Van Kampen, *Stochastic processes in physics and chemistry*, vol. 1. Elsevier, 1992.

[120] L. Landau and E. Lifshitz, "On the theory of the dispersion of magnetic permeability in ferromagnetic bodies," *Phys. Z. Sowjetunion*, vol. 8, no. 153, pp. 101–114, 1935.

[121] T. L. Gilbert, "A phenomenological theory of damping in ferromagnetic materials," *IEEE Transactions on Magnetics*, vol. 40, no. 6, pp. 3443–3449, 2004.

[122] W. F. Brown, "Thermal Fluctuations of a Single-Domain Particle," *Phys. Rev.*, vol. 130, no. 5, pp. 1677–1686, 1963.

[123] X.-L. Qi, Y.-S. Wu, and S.-C. Zhang, "General theorem relating the bulk topological number to edge states in two-dimensional insulators," *Phys. Rev. B*, vol. 74, no. 4, p. 045125, 2006.

[124] C.-X. Liu, X.-L. Qi, X. Dai, Z. Fang, and S.-C. Zhang, "Quantum anomalous Hall effect in Hg 1-y Mn y Te quantum wells," *Phys. Rev. Lett.*, vol. 101, no. 14, p. 146802, 2008.

[125] M. Kohmoto, "Topological invariant and the quantization of the Hall conductance," *Annals of Physics*, vol. 160, no. 2, pp. 343–354, 1985.

[126] Y. Hatsugai and M. Kohmoto, "Energy spectrum and the quantum Hall effect on the square lattice with next-nearest-neighbor hopping," *Phys. Rev. B*, vol. 42, no. 13, pp. 8282–8294, 1990.

[127] K. v. Klitzing, G. Dorda, and M. Pepper, "New Method for High-Accuracy Determination of the Fine-Structure Constant Based on Quantized Hall Resistance," *Phys. Rev. Lett.*, vol. 45, no. 6, pp. 494–497, 1980.

[128] X. L. Qi, T. L. Hughes, and S. C. Zhang, "Topological field theory of time-reversal invariant insulators," *Phys. Rev. B*, vol. 78, no. 19, p. 195424, 2008.

[129] C. L. Kane and E. J. Mele, "Quantum Spin hall effect in graphene," *Phys. Rev. Lett.*, vol. 95, no. 22, p. 226801, 2005.

[130] C. L. Kane and E. J. Mele, "Z2 topological order and the quantum spin hall effect," *Phys. Rev. Lett.*, vol. 95, no. 14, p. 146802, 2005.

[131] L. Fu and C. L. Kane, "Topological insulators with inversion symmetry," *Phys. Rev. B*, vol. 76, no. 4, p. 045302, 2007.

[132] M. König, S. Wiedmann, C. Brüne, A. Roth, H. Buhmann, L. W. Molenkamp, X.-L. Qi, and S.-C. Zhang, "Quantum Spin Hall Insulator State in HgTe Quantum Wells," *Science*, vol. 318, pp. 766 LP – 770, nov 2007.

[133] B. A. Bernevig, T. L. Hughes, and S.-C. Zhang, "Quantum Spin Hall Effect and Topological Phase Transition in HgTe Quantum Wells," *Science*, vol. 314, no. 5806, pp. 1757–1761, 2006.

[134] W. P. Su, J. R. Schrieffer, and A. J. Heeger, "Solitons in Polyacetylene," *Phys. Rev. Lett.*, vol. 42, no. 25, pp. 1698–1701, 1979.

[135] A. Y. Kitaev, "Unpaired Majorana fermions in quantum wires," *Physics-Uspekhi*, vol. 44, no. 10S, p. 131, 2001.

[136] C. Nayak, S. H. Simon, A. Stern, M. Freedman, and S. Das Sarma, "Non-Abelian anyons and topological quantum computation," *Rev. Mod. Phys.*, vol. 80, no. 3, pp. 1083–1159, 2008.

[137] L. Fu and C. L. Kane, "Superconducting Proximity Effect and Majorana Fermions at the Surface of a Topological Insulator," *Phys. Rev. Lett.*, vol. 100, no. 9, p. 096407, 2008.

[138] L. Fu and C. L. Kane, "Josephson current and noise at a superconductor/quantum-spin-Hall-insulator/superconductor junction," *Phys. Rev. B*, vol. 79, no. 16, p. 161408, 2009.

[139] Y. Oreg, G. Refael, and F. von Oppen, "Helical Liquids and Majorana Bound States in Quantum Wires," *Phys. Rev. Lett.*, vol. 105, no. 17, p. 177002, 2010.

[140] L. P. Rokhinson, X. Liu, and J. K. Furdyna, "The fractional a.c. Josephson effect in a semiconductor–superconductor nanowire as a signature of Majorana particles," *Nature Physics*, vol. 8, p. 795, sep 2012.

[141] V. Mourik, K. Zuo, S. M. Frolov, S. R. Plissard, E. P. A. M. Bakkers, and L. P. Kouwenhoven, "Signatures of Majorana Fermions in Hybrid Superconductor-Semiconductor Nanowire Devices," *Science*, vol. 336, no. 6084, pp. 1003–1007, 2012.

[142] A. Altland and M. R. Zirnbauer, "Nonstandard symmetry classes in mesoscopic normal-superconducting hybrid structures," *Phys. Rev. B*, vol. 55, no. 2, p. 1142, 1997.

[143] S. Ryu, A. P. Schnyder, A. Furusaki, and A. W. W. Ludwig, "Topological insulators and superconductors: Tenfold way and dimensional hierarchy," *New Journal of Physics*, vol. 12, no. 6, p. 065010, 2010.

[144] R. Bott, "ON TORSION IN LIE GROUPS," *Proceedings of the National Academy of Sciences of the United States of America*, vol. 40, pp. 586–588, jul 1954.

[145] K. Shiozaki and M. Sato, "Topology of crystalline insulators and superconductors," *Phys. Rev. B*, vol. 90, no. 16, p. 165114, 2014.

[146] R. Roy and F. Harper, "Periodic table for Floquet topological insulators," *Phys. Rev. B*, vol. 96, no. 15, p. 155118, 2017.

[147] X. Wan, A. M. Turner, A. Vishwanath, and S. Y. Savrasov, "Topological semimetal and Fermi-arc surface states in the electronic structure of pyrochlore iridates," *Phys. Rev. B*, vol. 83, no. 20, p. 205101, 2011.

[148] S. Murakami, "Phase transition between the quantum spin Hall and insulator phases in 3D: emergence of a topological gapless phase," *New Journal of Physics*, vol. 9, no. 9, p. 356, 2007.

[149] B. Yan and C. Felser, "Topological Materials: Weyl Semimetals," *Annual Review of Condensed Matter Physics*, vol. 8, pp. 337–354, mar 2017.

[150] H. Weng, C. Fang, Z. Fang, B. A. Bernevig, and X. Dai, "Weyl Semimetal Phase in Noncentrosymmetric Transition-Metal Monophosphides," *Phys. Rev. X*, vol. 5, no. 1, p. 011029, 2015.

[151] S.-M. Huang, S.-Y. Xu, I. Belopolski, C.-C. Lee, G. Chang, B. Wang, N. Alidoust, G. Bian, M. Neupane, C. Zhang, S. Jia, A. Bansil, H. Lin, and M. Z. Hasan, "A Weyl Fermion semimetal with surface Fermi arcs in the transition metal monopnictide TaAs class," *Nature Communications*, vol. 6, p. 7373, jun 2015.

[152] S.-Y. Xu, I. Belopolski, N. Alidoust, M. Neupane, G. Bian, C. Zhang, R. Sankar, G. Chang, Z. Yuan, C.-C. Lee, S.-M. Huang, H. Zheng, J. Ma, D. S. Sanchez, B. Wang, A. Bansil, F. Chou, P. P. Shibayev, H. Lin, S. Jia, and M. Z. Hasan, "Discovery of a Weyl fermion semimetal and topological Fermi arcs," *Science*, vol. 349, no. 6248, pp. 613–617, 2015.

[153] B. Q. Lv, N. Xu, H. M. Weng, J. Z. Ma, P. Richard, X. C. Huang, L. X. Zhao, G. F. Chen, C. E. Matt, F. Bisti, V. N. Strocov, J. Mesot, Z. Fang, X. Dai, T. Qian, M. Shi, and H. Ding, "Observation of Weyl nodes in TaAs," *Nat. Phys.*, vol. 11, p. 724, 2015.

[154] L. X. Yang, Z. K. Liu, Y. Sun, H. Peng, H. F. Yang, T. Zhang, B. Zhou, Y. Zhang, Y. F. Guo, M. Rahn, D. Prabhakaran, Z. Hussain, S.-K. Mo, C. Felser, B. Yan, and Y. L. Chen, "Weyl semimetal phase in the non-centrosymmetric compound TaAs," *Nat. Phys.*, vol. 11, p. 728, 2015.

[155] X. Huang, L. Zhao, Y. Long, P. Wang, D. Chen, Z. Yang, H. Liang, M. Xue, H. Weng, Z. Fang, X. Dai, and G. Chen, "Observation of the Chiral-Anomaly-Induced Negative Magnetoresistance in 3D Weyl Semimetal TaAs," *Phys. Rev. X*, vol. 5, no. 3, p. 031023, 2015.

[156] F. Arnold, C. Shekhar, S.-C. Wu, Y. Sun, R. D. dos Reis, N. Kumar, M. Naumann, M. O. Ajeesh, M. Schmidt, A. G. Grushin, J. H. Bardarson, M. Baenitz, D. Sokolov, H. Borrmann, M. Nicklas, C. Felser, E. Hassinger, and B. Yan, "Negative magnetoresistance without well-defined chirality in the Weyl semimetal TaP," *Nature Communications*, vol. 7, p. 11615, may 2016.

[157] C.-L. Zhang, S.-Y. Xu, I. Belopolski, Z. Yuan, Z. Lin, B. Tong, G. Bian, N. Alidoust, C.-C. Lee, S.-M. Huang, T.-R. Chang, G. Chang, C.-H. Hsu, H.-T. Jeng, M. Neupane, D. S. Sanchez, H. Zheng, J. Wang, H. Lin, C. Zhang, H.-Z. Lu, S.-Q. Shen, T. Neupert, M. Zahid Hasan, and S. Jia, "Signatures of the Adler–Bell–Jackiw chiral anomaly in a Weyl fermion semimetal," *Nature Communications*, vol. 7, p. 10735, feb 2016.

[158] H. B. Nielsen and M. Ninomiya, "The Adler-Bell-Jackiw anomaly and Weyl fermions in a crystal," *Physics Letters B*, vol. 130, no. 6, pp. 389–396, 1983.

[159] S. L. Adler, "Axial-Vector Vertex in Spinor Electrodynamics," *Phys. Rev.*, vol. 177, no. 5, pp. 2426–2438, 1969.

[160] J. S. Bell and R. Jackiw, "A PCAC puzzle: $\pi 0 \to \gamma\gamma$ in the σ-model," *Il Nuovo Cimento A (1965-1970)*, vol. 60, no. 1, pp. 47–61, 1969.

[161] K. Fujikawa and H. Suzuki, *Path Integrals and Quantum Anomalies*. Oxford: Oxford University Press, 2014.

[162] A. A. Zyuzin and A. A. Burkov, "Topological response in Weyl semimetals and the chiral anomaly," *Phys. Rev. B*, vol. 86, no. 11, p. 115133, 2012.

[163] D. T. Son and N. Yamamoto, "Berry Curvature, Triangle Anomalies, and the Chiral Magnetic Effect in Fermi Liquids," *Phys. Rev. Lett.*, vol. 109, no. 18, p. 181602, 2012.

[164] A. A. Burkov, "Chiral Anomaly and Diffusive Magnetotransport in Weyl Metals," *Phys. Rev. Lett.*, vol. 113, no. 24, p. 247203, 2014.

[165] P. Goswami and S. Tewari, "Axionic field theory of (3+1)-dimensional Weyl semimetals," *Phys. Rev. B*, vol. 88, no. 24, p. 245107, 2013.

[166] N. Yamamoto, "Generalized Bloch theorem and chiral transport phenomena," *Phys. Rev. D*, vol. 92, no. 8, p. 085011, 2015.

[167] M. M. Vazifeh and M. Franz, "Electromagnetic Response of Weyl Semimetals," *Phys. Rev. Lett.*, vol. 111, no. 2, p. 027201, 2013.

[168] D. T. Son and B. Z. Spivak, "Chiral anomaly and classical negative magnetoresistance of Weyl metals," *Phys. Rev. B*, vol. 88, no. 10, p. 104412, 2013.

[169] P. Goswami, J. H. Pixley, and S. Das Sarma, "Axial anomaly and longitudinal magnetoresistance of a generic three-dimensional metal," *Phys. Rev. B*, vol. 92, no. 7, p. 075205, 2015.

[170] H.-J. Kim, K.-S. Kim, J.-F. Wang, M. Sasaki, N. Satoh, A. Ohnishi, M. Kitaura, M. Yang, and L. Li, "Dirac versus Weyl Fermions in Topological Insulators: Adler-Bell-Jackiw Anomaly in Transport Phenomena," *Phys. Rev. Lett.*, vol. 111, no. 24, p. 246603, 2013.

[171] K. Taguchi, T. Imaeda, M. Sato, and Y. Tanaka, "Photovoltaic chiral magnetic effect in Weyl semimetals," *Phys. Rev. B*, vol. 93, no. 20, p. 201202, 2016.

[172] H. Sumiyoshi and S. Fujimoto, "Torsional Chiral Magnetic Effect in a Weyl Semimetal with a Topological Defect," *Phys. Rev. Lett.*, vol. 116, no. 16, p. 166601, 2016.

[173] Y. Ibe and H. Sumiyoshi, "Chiral Magnetic Effect due to Inhomogeneous Magnetic Fields in Noncentrosymmetric Weyl Semimetals," *Journal of the Physical Society of Japan*, vol. 86, no. 5, p. 054707, 2017.

[174] A. Cortijo, D. Kharzeev, K. Landsteiner, and M. A. H. Vozmediano, "Strain-induced chiral magnetic effect in Weyl semimetals," *Phys. Rev. B*, vol. 94, no. 24, p. 241405, 2016.

[175] D. I. Pikulin, A. Chen, and M. Franz, "Chiral Anomaly from Strain-Induced Gauge Fields in Dirac and Weyl Semimetals," *Phys. Rev. X*, vol. 6, no. 4, p. 041021, 2016.

[176] T. Meng and J. C. Budich, "Unpaired Weyl nodes from Long-Ranged Interactions: Fate of Quantum Anomalies," *arXiv preprint arXiv:1804.05078*, 2018.

[177] M. N. Chernodub and A. Cortijo, "Non-Hermitian Chiral Magnetic Effect in Equilibrium," *arXiv preprint arXiv:1901.06167*, jan 2019.

[178] D. J. Thouless, "Quantization of particle transport," *Phys. Rev. B*, vol. 27, no. 10, pp. 6083–6087, 1983.

[179] R. D. King-Smith and D. Vanderbilt, "Theory of polarization of crystalline solids," *Phys. Rev. B*, vol. 47, no. 3, pp. 1651–1654, 1993.

[180] D. Xiao, M.-C. Chang, and Q. Niu, "Berry phase effects on electronic properties," *Rev. Mod. Phys.*, vol. 82, no. 3, pp. 1959–2007, 2010.

[181] Q. Niu and D. J. Thouless, "Quantised adiabatic charge transport in the presence of substrate disorder and many-body interaction," *Journal of Physics A: Mathematical and General*, vol. 17, no. 12, p. 2453, 1984.

[182] C. Schweizer, M. Lohse, R. Citro, and I. Bloch, "Spin Pumping and Measurement of Spin Currents in Optical Superlattices," *Phys. Rev. Lett.*, vol. 117, no. 17, p. 170405, 2016.

[183] L. Wang, M. Troyer, and X. Dai, "Topological Charge Pumping in a One-Dimensional Optical Lattice," *Phys. Rev. Lett.*, vol. 111, no. 2, p. 026802, 2013.

[184] L. Fu and C. L. Kane, "Time reversal polarization and a Z2 adiabatic spin pump," *Phys. Rev. B*, vol. 74, no. 19, p. 195312, 2006.

[185] A. M. Essin, J. E. Moore, and D. Vanderbilt, "Magnetoelectric Polarizability and Axion Electrodynamics in Crystalline Insulators," *Phys. Rev. Lett.*, vol. 102, no. 14, p. 146805, 2009.

[186] J. P. van der Ziel, P. S. Pershan, and L. D. Malmstrom, "Optically-Induced Magnetization Resulting from the Inverse Faraday Effect," *Phys. Rev. Lett.*, vol. 15, no. 5, pp. 190–193, 1965.

[187] P. S. Pershan, J. P. van der Ziel, and L. D. Malmstrom, "Theoretical Discussion of the Inverse Faraday Effect, Raman Scattering, and Related Phenomena," *Phys. Rev.*, vol. 143, no. 2, pp. 574–583, 1966.

[188] J. H. Shirley, "Solution of the Schrödinger Equation with a Hamiltonian Periodic in Time," *Phys. Rev.*, vol. 138, no. 4B, pp. B979—-B987, 1965.

[189] S. Blanes, F. Casas, J. A. Oteo, and J. Ros, "The Magnus expansion and some of its applications," *Physics Reports*, vol. 470, no. 5, pp. 151–238, 2009.

[190] N. Goldman, J. Dalibard, M. Aidelsburger, and N. R. Cooper, "Periodically driven quantum matter: The case of resonant modulations," *Phys. Rev. A*, vol. 91, p. 033632, mar 2015.

[191] A. S. Sorensen, E. Demler, and M. D. Lukin, "Fractional Quantum Hall States of Atoms in Optical Lattices," *Phys. Rev. Lett.*, vol. 94, no. 8, p. 086803, 2005.

[192] N. Goldman, G. Juzeliunas, P. Öhberg, and I. B. Spielman, "Light-induced gauge fields for ultracold atoms," *Reports on Progress in Physics*, vol. 77, no. 12, p. 126401, 2014.

[193] J. Struck, C. Ölschläger, R. Le Targat, P. Soltan-Panahi, A. Eckardt, M. Lewenstein, P. Windpassinger, and K. Sengstock, "Quantum Simulation of Frustrated Classical Magnetism in Triangular Optical Lattices," *Science*, vol. 333, no. 6045, pp. 996–999, 2011.

[194] J. Struck, M. Weinberg, C. Ölschläger, P. Windpassinger, J. Simonet, K. Sengstock, R. Höppner, P. Hauke, A. Eckardt, M. Lewenstein, and L. Mathey, "Engineering Ising-XY spin-models in a triangular lattice using tunable artificial gauge fields," *Nature Physics*, vol. 9, p. 738, sep 2013.

[195] F. Görg, M. Messer, K. Sandholzer, G. Jotzu, R. Desbuquois, and T. Esslinger, "Enhancement and sign change of magnetic correlations in a driven quantum many-body system," *Nature*, vol. 553, p. 481, jan 2018.

[196] M. C. Rechtsman, J. M. Zeuner, Y. Plotnik, Y. Lumer, D. Podolsky, F. Dreisow, S. Nolte, M. Segev, and A. Szameit, "Photonic Floquet topological insulators," *Nature*, vol. 496, p. 196, apr 2013.

[197] I. Bialynicki-Birula, B. Mielnik, and J. Plebański, "Explicit solution of the continuous Baker-Campbell-Hausdorff problem and a new expression for the phase operator," *Annals of Physics*, vol. 51, no. 1, pp. 187–200, 1969.

[198] L. D'Alessio and A. Polkovnikov, "Many-body energy localization transition in periodically driven systems," *Annals of Physics*, vol. 333, pp. 19–33, 2013.

[199] L. D'Alessio and M. Rigol, "Long-time Behavior of Isolated Periodically Driven Interacting Lattice Systems," *Phys. Rev. X*, vol. 4, no. 4, p. 041048, 2014.

[200] P. Ponte, A. Chandran, Z. Papić, and D. A. Abanin, "Periodically driven ergodic and many-body localized quantum systems," *Annals of Physics*, vol. 353, pp. 196–204, 2015.

[201] H. Kim, T. N. Ikeda, and D. A. Huse, "Testing whether all eigenstates obey the eigenstate thermalization hypothesis," *Phys. Rev. E*, vol. 90, no. 5, p. 052105, 2014.

[202] J. M. Deutsch, "Quantum statistical mechanics in a closed system," *Phys. Rev. A*, vol. 43, no. 4, pp. 2046–2049, 1991.

[203] M. Srednicki, "Chaos and quantum thermalization," *Phys. Rev. E*, vol. 50, no. 2, pp. 888–901, 1994.

[204] M. Rigol, V. Dunjko, and M. Olshanii, "Thermalization and its mechanism for generic isolated quantum systems," *Nature*, vol. 452, p. 854, apr 2008.

[205] A. Russomanno, A. Silva, and G. E. Santoro, "Periodic Steady Regime and Interference in a Periodically Driven Quantum System," *Phys. Rev. Lett.*, vol. 109, no. 25, p. 257201, 2012.

[206] A. Lazarides, A. Das, and R. Moessner, "Fate of Many-Body Localization Under Periodic Driving," *Phys. Rev. Lett.*, vol. 115, no. 3, p. 030402, 2015.

[207] V. Khemani, A. Lazarides, R. Moessner, and S. L. Sondhi, "Phase Structure of Driven Quantum Systems," *Phys. Rev. Lett.*, vol. 116, no. 25, p. 250401, 2016.

[208] T. Ishii, T. Kuwahara, T. Mori, and N. Hatano, "Heating in Integrable Time-Periodic Systems," *Phys. Rev. Lett.*, vol. 120, p. 220602, may 2018.

[209] D. A. Abanin, W. De Roeck, and F. b. ç. Huveneers, "Exponentially Slow Heating in Periodically Driven Many-Body Systems," *Phys. Rev. Lett.*, vol. 115, no. 25, p. 256803, 2015.

[210] M. Gring, M. Kuhnert, T. Langen, T. Kitagawa, B. Rauer, M. Schreitl, I. Mazets, D. A. Smith, E. Demler, and J. Schmiedmayer, "Relaxation and Prethermalization in an Isolated Quantum System," *Science*, vol. 337, no. 6100, pp. 1318–1322, 2012.

[211] M. Moeckel and S. Kehrein, "Interaction Quench in the Hubbard Model," *Phys. Rev. Lett.*, vol. 100, no. 17, p. 175702, 2008.

[212] M. Kollar, F. A. Wolf, and M. Eckstein, "Generalized Gibbs ensemble prediction of prethermalization plateaus and their relation to nonthermal steady states in integrable systems," *Phys. Rev. B*, vol. 84, no. 5, p. 054304, 2011.

[213] T. Mori, T. N. Ikeda, E. Kaminishi, and M. Ueda, "Thermalization and prethermalization in isolated quantum systems: a theoretical overview," *Journal of Physics B: Atomic, Molecular and Optical Physics*, vol. 51, no. 11, p. 112001, 2018.

[214] N. Fläschner, B. S. Rem, M. Tarnowski, D. Vogel, D.-S. Lühmann, K. Sengstock, and C. Weitenberg, "Experimental reconstruction of the Berry curvature in a Floquet Bloch band," *Science*, vol. 352, pp. 1091 LP – 1094, may 2016.

[215] M. Tarnowski, F. N. Ünal, N. Fläschner, B. S. Rem, A. Eckardt, K. Sengstock, and C. Weitenberg, "Characterizing topology by dynamics: Chern number from linking number," *arXiv preprint arXiv:1709.01046*, 2017.

[216] J. Struck, C. Ölschläger, M. Weinberg, P. Hauke, J. Simonet, A. Eckardt, M. Lewenstein, K. Sengstock, and P. Windpassinger, "Tunable Gauge Potential for Neutral and Spinless Particles in Driven Optical Lattices," *Phys. Rev. Lett.*, vol. 108, no. 22, p. 225304, 2012.

[217] H. Miyake, G. A. Siviloglou, C. J. Kennedy, W. C. Burton, and W. Ketterle, "Realizing the Harper Hamiltonian with Laser-Assisted Tunneling in Optical Lattices," *Phys. Rev. Lett.*, vol. 111, no. 18, p. 185302, 2013.

[218] J. Cayssol, B. Dóra, F. Simon, and R. Moessner, "Floquet topological insulators," *physica status solidi (RRL) – Rapid Research Letters*, vol. 7, no. 1-2, pp. 101–108, 2013.

[219] M. Mancini, G. Pagano, G. Cappellini, L. Livi, M. Rider, J. Catani, C. Sias, P. Zoller, M. Inguscio, M. Dalmonte, and L. Fallani, "Observation of chiral edge states with neutral fermions in synthetic Hall ribbons," *Science*, vol. 349, no. 6255, pp. 1510–1513, 2015.

[220] B. K. Stuhl, H.-I. Lu, L. M. Aycock, D. Genkina, and I. B. Spielman, "Visualizing edge states with an atomic Bose gas in the quantum Hall regime," *Science*, vol. 349, no. 6255, pp. 1514–1518, 2015.

[221] A. Celi, P. Massignan, J. Ruseckas, N. Goldman, I. B. Spielman, G. Juzeliūnas, and M. Lewenstein, "Synthetic Gauge Fields in Synthetic Dimensions," *Phys. Rev. Lett.*, vol. 112, no. 4, p. 043001, 2014.

[222] H. Dehghani, T. Oka, and A. Mitra, "Out-of-equilibrium electrons and the Hall conductance of a Floquet topological insulator," *Phys. Rev. B*, vol. 91, no. 15, p. 155422, 2015.

[223] T. Iadecola, T. Neupert, and C. Chamon, "Occupation of topological Floquet bands in open systems," *Phys. Rev. B*, vol. 91, no. 23, p. 235133, 2015.

[224] S. Vajna, B. Horovitz, B. Dóra, and G. Zaránd, "Floquet topological phases coupled to environments and the induced photocurrent," *Phys. Rev. B*, vol. 94, no. 11, p. 115145, 2016.

[225] M. S. Rudner, N. H. Lindner, E. Berg, and M. Levin, "Anomalous Edge States and the Bulk-Edge Correspondence for Periodically Driven Two-Dimensional Systems," *Phys. Rev. X*, vol. 3, no. 3, p. 031005, 2013.

[226] F. Gao, Z. Gao, X. Shi, Z. Yang, X. Lin, H. Xu, J. D. Joannopoulos, M. Soljačić, H. Chen, L. Lu, Y. Chong, and B. Zhang, "Probing topological protection using a designer surface plasmon structure," *Nature Communications*, vol. 7, p. 11619, may 2016.

[227] S. Mukherjee, A. Spracklen, M. Valiente, E. Andersson, P. Öhberg, N. Goldman, and R. R. Thomson, "Experimental observation of anomalous topological edge modes in a slowly driven photonic lattice," *Nature Communications*, vol. 8, p. 13918, jan 2017.

[228] L. J. Maczewsky, J. M. Zeuner, S. Nolte, and A. Szameit, "Observation of photonic anomalous Floquet topological insulators," *Nature Communications*, vol. 8, p. 13756, jan 2017.

[229] M. Fruchart, "Complex classes of periodically driven topological lattice systems," *Phys. Rev. B*, vol. 93, no. 11, p. 115429, 2016.

[230] X. Liu, F. Harper, and R. Roy, "Chiral Flow in One-dimensional Floquet Topological Insulators," *Phys. Rev. B*, vol. 98, no. 16, p. 165116, 2018.

[231] T. Kitagawa, M. A. Broome, A. Fedrizzi, M. S. Rudner, E. Berg, I. Kassal, A. Aspuru-Guzik, E. Demler, and A. G. White, "Observation of topologically protected bound states in photonic quantum walks," *Nature Communications*, vol. 3, p. 882, jun 2012.

[232] D. Carpentier, P. Delplace, M. Fruchart, and K. Gawedzki, "Topological Index for Periodically Driven Time-Reversal Invariant 2D Systems," *Phys. Rev. Lett.*, vol. 114, no. 10, p. 106806, 2015.

[233] S. Ryu and S.-C. Zhang, "Interacting topological phases and modular invariance," *Phys. Rev. B*, vol. 85, no. 24, p. 245132, 2012.

[234] O. M. Sule, X. Chen, and S. Ryu, "Symmetry-protected topological phases and orbifolds: Generalized Laughlin's argument," *Phys. Rev. B*, vol. 88, no. 7, p. 075125, 2013.

[235] C.-T. Hsieh, G. Y. Cho, and S. Ryu, "Global anomalies on the surface of fermionic symmetry-protected topological phases in (3+1) dimensions," *Phys. Rev. B*, vol. 93, no. 7, p. 075135, 2016.

[236] C. E. Creffield, F. Sols, D. Ciampini, O. Morsch, and E. Arimondo, "Expansion of matter waves in static and driven periodic potentials," *Phys. Rev. A*, vol. 82, no. 3, p. 035601, 2010.

[237] H. Lignier, C. Sias, D. Ciampini, Y. Singh, A. Zenesini, O. Morsch, and E. Arimondo, "Dynamical Control of Matter-Wave Tunneling in Periodic Potentials," *Phys. Rev. Lett.*, vol. 99, no. 22, p. 220403, 2007.

[238] F. Meinert, M. J. Mark, K. Lauber, A. J. Daley, and H.-C. Nägerl, "Floquet Engineering of Correlated Tunneling in the Bose-Hubbard Model with Ultracold Atoms," *Phys. Rev. Lett.*, vol. 116, no. 20, p. 205301, 2016.

[239] Y. Tokura, S. Seki, and N. Nagaosa, "Multiferroics of spin origin," *Reports on Progress in Physics*, vol. 77, no. 7, p. 76501, 2014.

[240] Y. Tokura and S. Seki, "Multiferroics with Spiral Spin Orders," *Advanced Materials*, vol. 22, no. 14, pp. 1554–1565.

[241] K. F. Wang, J.-M. Liu, and Z. F. Ren, "Multiferroicity: the coupling between magnetic and polarization orders," *Advances in Physics*, vol. 58, no. 4, pp. 321–448, 2009.

[242] S. Maekawa, S. O. Valenzuela, T. Kimura, and E. Saitoh, eds., *Spin current*. Oxford University Press, 2017.

[243] H. Katsura, N. Nagaosa, and A. V. Balatsky, "Spin Current and Magnetoelectric Effect in Noncollinear Magnets," *Phys. Rev. Lett.*, vol. 95, no. 5, p. 057205, 2005.

[244] M. Mostovoy, "Ferroelectricity in Spiral Magnets," *Phys. Rev. Lett.*, vol. 96, no. 6, p. 067601, 2006.

[245] I. A. Sergienko and E. Dagotto, "Role of the Dzyaloshinskii-Moriya interaction in multiferroic perovskites," *Phys. Rev. B*, vol. 73, no. 9, p. 094434, 2006.

[246] H. Katsura, A. V. Balatsky, and N. Nagaosa, "Dynamical Magnetoelectric Coupling in Helical Magnets," *Phys. Rev. Lett.*, vol. 98, no. 2, p. 027203, 2007.

[247] L. D. Landau and E. M. Lifschic, *Course of theoretical physics. vol. 1: Mechanics*. Oxford, 1978.

[248] C. M. Bender and S. A. Orszag, *Advanced mathematical methods for scientists and engineers I: Asymptotic methods and perturbation theory*. Springer Science & Business Media, 2013.

[249] S. H. Strogatz, *Nonlinear dynamics and chaos: with applications to physics, biology, chemistry, and engineering*. CRC Press, 2018.

[250] G. Casati, I. Guarneri, and G. Mantica, "Classical stabilization of periodically kicked hydrogen atoms," *Phys. Rev. A*, vol. 50, no. 6, pp. 5018–5024, 1994.

[251] H. Wiedemann, J. Mostowski, and F. Haake, "Alternating kicks approximating quasimonochromatic fields in ionization and stabilization," *Phys. Rev. A*, vol. 49, no. 2, pp. 1171–1176, 1994.

[252] C. O. Reinhold, J. Burgdörfer, M. T. Frey, and F. B. Dunning, "Dynamical Stabilization of the Periodically Kicked Rydberg Atom," *Phys. Rev. Lett.*, vol. 79, no. 26, pp. 5226–5229, 1997.

[253] H. Saito and M. Ueda, "Dynamically Stabilized Bright Solitons in a Two-Dimensional Bose-Einstein Condensate," *Phys. Rev. Lett.*, vol. 90, no. 4, p. 040403, 2003.

[254] F. K. Abdullaev, J. G. Caputo, R. A. Kraenkel, and B. A. Malomed, "Controlling collapse in Bose-Einstein condensates by temporal modulation of the scattering length," *Phys. Rev. A*, vol. 67, no. 1, p. 013605, 2003.

[255] R. Citro, E. G. Dalla Torre, L. D'Alessio, A. Polkovnikov, M. Babadi, T. Oka, and E. Demler, "Dynamical stability of a many-body Kapitza pendulum," *Annals of Physics*, vol. 360, pp. 694–710, 2015.

[256] T. M. Hoang, C. S. Gerving, B. J. Land, M. Anquez, C. D. Hamley, and M. S. Chapman, "Dynamic Stabilization of a Quantum Many-Body Spin System," *Phys. Rev. Lett.*, vol. 111, no. 9, p. 090403, 2013.

[257] X. Bian, C. Kim, and G. E. Karniadakis, "111 years of Brownian motion," *Soft Matter*, vol. 12, no. 30, pp. 6331–6346, 2016.

[258] R. KUBO, "Brownian Motion and Nonequilibrium Statistical Mechanics," *Science*, vol. 233, no. 4761, pp. 330–334, 1986.

[259] B. Øksendal, "Stochastic differential equations," in *Stochastic differential equations*, pp. 65–84, Springer, 2003.

[260] F. Black and M. Scholes, "The pricing of options and corporate liabilities," *Journal of political economy*, vol. 81, no. 3, pp. 637–654, 1973.

[261] H. Risken, "Fokker-planck equation," in *The Fokker-Planck Equation*, pp. 63–95, Springer, 1996.

[262] I. D. Mayergoyz, G. Bertotti, and C. Serpico, *Nonlinear magnetization dynamics in nanosystems*. Elsevier, 2009.

[263] W. T. Coffey and Y. P. Kalmykov, *The Langevin equation: with applications to stochastic problems in physics, chemistry and electrical engineering*. World Scientific, 2004.

[264] J. L. Garcia-Palacios and F. J. Lázaro, "Langevin-dynamics study of the dynamical properties of small magnetic particles," *Phys. Rev. B*, vol. 58, no. 22, pp. 14937–14958, 1998.

[265] A. Brataas, A. D. Kent, and H. Ohno, "Current-induced torques in magnetic materials," *Nature Materials*, vol. 11, p. 372, apr 2012.

[266] U. Atxitia, O. Chubykalo-Fesenko, R. W. Chantrell, U. Nowak, and A. Rebei, "Ultrafast Spin Dynamics: The Effect of Colored Noise," *Phys. Rev. Lett.*, vol. 102, no. 5, p. 057203, 2009.

[267] N. Kazantseva, U. Nowak, R. W. Chantrell, J. Hohlfeld, and A. Rebei, "Slow recovery of the magnetisation after a sub-picosecond heat pulse," *EPL (Europhysics Letters)*, vol. 81, no. 2, p. 27004, 2008.

[268] C. Vicario, C. Ruchert, F. Ardana-Lamas, P. M. Derlet, B. Tudu, J. Luning, and C. P. Hauri, "Off-resonant magnetization dynamics phase-locked to an intense phase-stable terahertz transient," *Nature Photonics*, vol. 7, p. 720, aug 2013.

[269] G.-M. Choi, B.-C. Min, K.-J. Lee, and D. G. Cahill, "Spin current generated by thermally driven ultrafast demagnetization," *Nature Communications*, vol. 5, p. 4334, jul 2014.

[270] A. J. Schellekens, K. C. Kuiper, R. de Wit, and B. Koopmans, "Ultrafast spin-transfer torque driven by femtosecond pulsed-laser excitation," *Nature Communications*, vol. 5, p. 4333, jul 2014.

[271] M. Taherinejad and D. Vanderbilt, "Adiabatic Pumping of Chern-Simons Axion Coupling," *Phys. Rev. Lett.*, vol. 114, no. 9, p. 096401, 2015.

[272] M. Nakahara, *Geometry, topology and physics*. CRC Press, 2003.

[273] N. Manton and P. Sutcliffe, *Topological solitons*. Cambridge: Cambridge University Press, 2004.

[274] C.-K. Chan, Y.-T. Oh, J. H. Han, and P. A. Lee, "Type-II Weyl cone transitions in driven semimetals," *Phys. Rev. B*, vol. 94, no. 12, p. 121106, 2016.

[275] H. Hübener, M. A. Sentef, U. De Giovannini, A. F. Kemper, and A. Rubio, "Creating stable Floquet–Weyl semimetals by laser-driving of 3D Dirac materials," *Nature Communications*, vol. 8, p. 13940, jan 2017.

[276] H. Wang, L. Zhou, and Y. D. Chong, "Floquet Weyl phases in a three-dimensional network model," *Phys. Rev. B*, vol. 93, no. 14, p. 144114, 2016.

[277] J.-Y. Zou and B.-G. Liu, "Floquet Weyl fermions in three-dimensional stacked graphene systems irradiated by circularly polarized light," *Phys. Rev. B*, vol. 93, no. 20, p. 205435, 2016.

[278] L. Bucciantini, S. Roy, S. Kitamura, and T. Oka, "Emergent Weyl nodes and Fermi arcs in a Floquet Weyl semimetal," *Phys. Rev. B*, vol. 96, no. 4, p. 041126, 2017.

[279] R. Wang, B. Wang, R. Shen, L. Sheng, and D. Y. Xing, "Floquet Weyl semimetal induced by off-resonant light," *EPL (Europhysics Letters)*, vol. 105, no. 1, p. 17004, 2014.

[280] S. Ebihara, K. Fukushima, and T. Oka, "Chiral pumping effect induced by rotating electric fields," *Phys. Rev. B*, vol. 93, no. 15, p. 155107, 2016.

[281] X.-X. Zhang, T. T. Ong, and N. Nagaosa, "Theory of photoinduced Floquet Weyl semimetal phases," *Phys. Rev. B*, vol. 94, no. 23, p. 235137, 2016.

[282] Z. Yan and Z. Wang, "Tunable Weyl Points in Periodically Driven Nodal Line Semimetals," *Phys. Rev. Lett.*, vol. 117, no. 8, p. 087402, 2016.

[283] X.-Q. Sun, M. Xiao, T. Bzdusek, S.-C. Zhang, and S. Fan, "Three-Dimensional Chiral Lattice Fermion in Floquet Systems," *Phys. Rev. Lett.*, vol. 121, p. 196401, nov 2018.

[284] M. Hafezi, A. S. Sorensen, E. Demler, and M. D. Lukin, "Fractional quantum Hall effect in optical lattices," *Phys. Rev. A*, vol. 76, p. 023613, aug 2007.

[285] S. Aubry and G. André, "Analyticity breaking and Anderson localization in incommensurate lattices," *Ann. Israel Phys. Soc*, vol. 3, no. 133, p. 18, 1980.

[286] P. G. Harper, "Single Band Motion of Conduction Electrons in a Uniform Magnetic Field," *Proceedings of the Physical Society. Section A*, vol. 68, no. 10, p. 874, 1955.

[287] I. Bloch, J. Dalibard, and W. Zwerger, "Many-body physics with ultracold gases," *Rev. Mod. Phys.*, vol. 80, no. 3, pp. 885–964, 2008.

[288] I. H. Deutsch and P. S. Jessen, "Quantum-state control in optical lattices," *Phys. Rev. A*, vol. 57, no. 3, pp. 1972–1986, 1998.

[289] D. Jaksch, H.-J. Briegel, J. I. Cirac, C. W. Gardiner, and P. Zoller, "Entanglement of Atoms via Cold Controlled Collisions," *Phys. Rev. Lett.*, vol. 82, no. 9, pp. 1975–1978, 1999.

[290] G. K. Brennen, C. M. Caves, P. S. Jessen, and I. H. Deutsch, "Quantum Logic Gates in Optical Lattices," *Phys. Rev. Lett.*, vol. 82, no. 5, pp. 1060–1063, 1999.

[291] O. Mandel, M. Greiner, A. Widera, T. Rom, T. W. Hänsch, and I. Bloch, "Controlled collisions for multi-particle entanglement of optically trapped atoms," *Nature*, vol. 425, p. 937, oct 2003.

[292] O. Mandel, M. Greiner, A. Widera, T. Rom, T. W. Hänsch, and I. Bloch, "Coherent Transport of Neutral Atoms in Spin-Dependent Optical Lattice Potentials," *Phys. Rev. Lett.*, vol. 91, no. 1, p. 010407, 2003.

[293] J. C. Budich, C. Laflamme, F. Tschirsich, S. Montangero, and P. Zoller, "Synthetic helical liquids with ultracold atoms in optical lattices," *Phys. Rev. B*, vol. 92, no. 24, p. 245121, 2015.

[294] B. Song, C. He, S. Zhang, E. Hajiyev, W. Huang, X.-J. Liu, and G.-B. Jo, "Spin-orbit-coupled two-electron Fermi gases of ytterbium atoms," *Phys. Rev. A*, vol. 94, no. 6, p. 061604, 2016.

[295] K. Enomoto, K. Kasa, M. Kitagawa, and Y. Takahashi, "Optical Feshbach Resonance Using the Intercombination Transition," *Phys. Rev. Lett.*, vol. 101, no. 20, p. 203201, 2008.

[296] F. Nathan and M. S. Rudner, "Topological singularities and the general classification of Floquet–Bloch systems," *New Journal of Physics*, vol. 17, no. 12, p. 125014, 2015.

[297] T. Morimoto, H. C. Po, and A. Vishwanath, "Floquet topological phases protected by time glide symmetry," *Phys. Rev. B*, vol. 95, no. 19, p. 195155, 2017.

[298] C. J. Pethick and H. Smith, *Bose-Einstein condensation in dilute gases*. Cambridge: Cambridge university press, 2002.

[299] D. M. Stamper-Kurn and M. Ueda, "Spinor Bose gases: Symmetries, magnetism, and quantum dynamics," *Reviews of Modern Physics*, vol. 85, no. 3, pp. 1191–1244, 2013.

[300] W. Kohn, "Periodic Thermodynamics," *Journal of Statistical Physics*, vol. 103, no. 3, pp. 417–423, 2001.

[301] M. Grifoni and P. Hänggi, "Driven quantum tunneling," *Physics Reports*, vol. 304, no. 5, pp. 229–354, 1998.

[302] D. W. Hone, R. Ketzmerick, and W. Kohn, "Statistical mechanics of Floquet systems: The pervasive problem of near degeneracies," *Phys. Rev. E*, vol. 79, no. 5, p. 051129, 2009.

[303] R. Ketzmerick and W. Wustmann, "Statistical mechanics of Floquet systems with regular and chaotic states," *Phys. Rev. E*, vol. 82, no. 2, p. 021114, 2010.

[304] M. Langemeyer and M. Holthaus, "Energy flow in periodic thermodynamics," *Phys. Rev. E*, vol. 89, no. 1, p. 012101, 2014.

[305] D. Vorberg, W. Wustmann, R. Ketzmerick, and A. Eckardt, "Generalized Bose-Einstein Condensation into Multiple States in Driven-Dissipative Systems," *Phys. Rev. Lett.*, vol. 111, no. 24, p. 240405, 2013.

[306] D. Vorberg, W. Wustmann, H. Schomerus, R. Ketzmerick, and A. Eckardt, "Nonequilibrium steady states of ideal bosonic and fermionic quantum gases," *Phys. Rev. E*, vol. 92, no. 6, p. 062119, 2015.

[307] S. B. Dutta and M. Barma, "Asymptotic distributions of periodically driven stochastic systems," *Phys. Rev. E*, vol. 67, no. 6, p. 061111, 2003.

[308] S. B. Dutta, "Phase transitions in periodically driven macroscopic systems," *Phys. Rev. E*, vol. 69, no. 6, p. 066115, 2004.

[309] Y. Wan and R. Moessner, "Nonequilibrium selection of magnetic order in driven triangular XY antiferromagnet," *Phys. Rev. B*, vol. 98, no. 18, p. 184432, 2018.

[310] T. M. Liggett, *Interacting particle systems*, vol. 276. Springer Science & Business Media, 2012.

[311] H. Spohn, *Large scale dynamics of interacting particles*. Springer Science & Business Media, 2012.

[312] P. Bak, C. Tang, and K. Wiesenfeld, "Self-organized criticality: An explanation of the 1/f noise," *Phys. Rev. Lett.*, vol. 59, pp. 381–384, jul 1987.

[313] P. Bak, C. Tang, and K. Wiesenfeld, "Self-organized criticality," *Phys. Rev. A*, vol. 38, pp. 364–374, jul 1988.

[314] M. V. Moreno, Z. G. Arenas, and D. G. Barci, "Langevin dynamics for vector variables driven by multiplicative white noise: A functional formalism," *Phys. Rev. E*, vol. 91, no. 4, p. 042103, 2015.

[315] P. C. Hohenberg and A. P. Krekhov, "An introduction to the Ginzburg–Landau theory of phase transitions and nonequilibrium patterns," *Physics Reports*, vol. 572, pp. 1–42, 2015.

[316] M. J. Bhaseen, J. Mayoh, B. D. Simons, and J. Keeling, "Dynamics of nonequilibrium Dicke models," *Phys. Rev. A*, vol. 85, no. 1, p. 013817, 2012.

[317] L. Bakemeier, A. Alvermann, and H. Fehske, "Dynamics of the Dicke model close to the classical limit," *Phys. Rev. A*, vol. 88, no. 4, p. 043835, 2013.

[318] K. Kanazawa, T. Sagawa, and H. Hayakawa, "Stochastic Energetics for Non-Gaussian Processes," *Phys. Rev. Lett.*, vol. 108, no. 21, p. 210601, 2012.

[319] K. Kanazawa, T. Sagawa, and H. Hayakawa, "Heat conduction induced by non-Gaussian athermal fluctuations," *Phys. Rev. E*, vol. 87, no. 5, p. 052124, 2013.

[320] R. Zwanzig, "Memory effects in irreversible thermodynamics," *Physical Review*, vol. 124, no. 4, p. 983, 1961.

[321] H. Mori and H. Fujisaka, "On nonlinear dynamics of fluctuations," *Progress of Theoretical Physics*, vol. 49, no. 3, pp. 764–775, 1973.

[322] F. Haake, "Statistical treatment of open systems by generalized master equations," in *Springer tracts in modern physics*, pp. 98–168, Springer, 1973.

[323] H. Hinrichsen, "Non-equilibrium critical phenomena and phase transitions into absorbing states," *Advances in Physics*, vol. 49, no. 7, pp. 815–958, 2000.

[324] M. Bukov, M. Kolodrubetz, and A. Polkovnikov, "Schrieffer-Wolff Transformation for Periodically Driven Systems: Strongly Correlated Systems with Artificial Gauge Fields," *Phys. Rev. Lett.*, vol. 116, no. 12, p. 125301, 2016.

[325] K. Kanazawa, T. G. Sano, T. Sagawa, and H. Hayakawa, "Asymptotic Derivation of Langevin-like Equation with Non-Gaussian Noise and Its Analytical Solution," *Journal of Statistical Physics*, vol. 160, no. 5, pp. 1294–1335, 2015.

[326] Schnell Alexander, E. André, and D. Sergey, "Is there a Floquet Lindbladian?," *arXiv preprint arXiv:1809.11121*, 2018.

[327] F. Spirig, "Algebraic aspects of perturbation theories," *Celestial mechanics*, vol. 20, no. 4, pp. 343–354, 1979.

[328] A. A. Agrachev and R. V. Gamkrelidze, "Chronological algebras and nonstationary vector fields," *Journal of Soviet Mathematics*, vol. 17, no. 1, pp. 1650–1675, 1981.

[329] A. A. A. Gamkrelidze and R. V, "THE EXPONENTIAL REPRESENTATION OF FLOWS AND THE CHRONOLOGICAL CALCULUS," *Mathematics of the USSR-Sbornik*, vol. 35, no. 6, p. 727, 1979.

[330] J. A. Oteo and J. Ros, "The Magnus expansion for classical Hamiltonian systems," *Journal of Physics A: Mathematical and General*, vol. 24, no. 24, p. 5751, 1991.

[331] S. Tani, "Canonical Transformation Governing Temporal Development in Classical Mechanics," *American Journal of Physics*, vol. 36, pp. 29–32, jan 1968.

[332] R. A. Marcus, "High-Order Time-Dependent Perturbation Theory for Classical Mechanics and for Other Systems of First-Order Ordinary Differential Equations," *The Journal of Chemical Physics*, vol. 52, pp. 4803–4807, may 1970.

[333] J. A. Blackburn, H. J. T. Smith, and N. Gro/nbech-Jensen, "Stability and Hopf bifurcations in an inverted pendulum," *American Journal of Physics*, vol. 60, pp. 903–908, oct 1992.

[334] M. V. Bartuccelli, G. Gentile, and K. V. Georgiou, "On the dynamics of a vertically driven damped planar pendulum," *Proceedings of the Royal Society of London A: Mathematical, Physical and Engineering Sciences*, vol. 457, no. 2016, pp. 3007–3022, 2001.

[335] B. P. Mann and M. A. Koplow, "Symmetry breaking bifurcations of a parametrically excited pendulum," *Nonlinear Dynamics*, vol. 46, no. 4, pp. 427–437, 2006.

[336] E. I. Butikov, "An improved criterion for Kapitza's pendulum stability," *Journal of Physics A: Mathematical and Theoretical*, vol. 44, no. 29, p. 295202, 2011.

[337] S. Wiggins, *Introduction to applied nonlinear dynamical systems and chaos*, vol. 2. Springer Science & Business Media, 2003.

[338] V. Gorini, A. Kossakowski, and E. C. G. Sudarshan, "Completely positive dynamical semigroups of N-level systems," *Journal of Mathematical Physics*, vol. 17, pp. 821–825, may 1976.

[339] G. Lindblad, "On the generators of quantum dynamical semigroups," *Comm. Math. Phys.*, vol. 48, no. 2, pp. 119–130, 1976.

[340] H. P. Breuer and F. Petruccione, *The theory of open quantum systems*. Great Clarendon Street: Oxford University Press, 2002.

[341] H.-P. Breuer, E.-M. Laine, and J. Piilo, "Measure for the Degree of Non-Markovian Behavior of Quantum Processes in Open Systems," *Phys. Rev. Lett.*, vol. 103, p. 210401, nov 2009.

[342] F. Haddadfarshi, J. Cui, and F. Mintert, "Completely Positive Approximate Solutions of Driven Open Quantum Systems," *Phys. Rev. Lett.*, vol. 114, no. 13, p. 130402, 2015.

[343] S. Restrepo, J. Cerrillo, V. M. Bastidas, D. G. Angelakis, and T. Brandes, "Driven Open Quantum Systems and Floquet Stroboscopic Dynamics," *Phys. Rev. Lett.*, vol. 117, no. 25, p. 250401, 2016.

[344] C. M. Dai, Z. C. Shi, and X. X. Yi, "Floquet theorem with open systems and its applications," *Phys. Rev. A*, vol. 93, no. 3, p. 032121, 2016.

[345] C. M. Dai, H. Li, W. Wang, and X. X. Yi, "Generalized Floquet theory for open quantum systems," *arXiv preprint arXiv:1707.05030*, 2017.

[346] M. M. Wolf, J. Eisert, T. S. Cubitt, and J. I. Cirac, "Assessing Non-Markovian Quantum Dynamics," *Phys. Rev. Lett.*, vol. 101, p. 150402, oct 2008.

[347] Á. Rivas, S. F. Huelga, and M. B. Plenio, "Entanglement and Non-Markovianity of Quantum Evolutions," *Phys. Rev. Lett.*, vol. 105, p. 50403, jul 2010.

[348] P. Weinberg, M. Bukov, L. D'Alessio, A. Polkovnikov, S. Vajna, and M. Kolodrubetz, "Adiabatic perturbation theory and geometry of periodically-driven systems," *Physics Reports*, vol. 688, pp. 1–35, 2017.

[349] P. W. Claeys, S. De Baerdemacker, O. E. Araby, and J.-S. Caux, "Spin Polarization through Floquet Resonances in a Driven Central Spin Model," *Phys. Rev. Lett.*, vol. 121, p. 080401, aug 2018.

[350] T. Shirai, J. Thingna, T. Mori, S. Denisov, P. Hänggi, and S. Miyashita, "Effective Floquet–Gibbs states for dissipative quantum systems," *New Journal of Physics*, vol. 18, no. 5, p. 053008, 2016.

[351] J. C. Slonczewski, "Current-driven excitation of magnetic multilayers," *Journal of Magnetism and Magnetic Materials*, vol. 159, no. 1, pp. L1–L7, 1996.

[352] L. Berger, "Emission of spin waves by a magnetic multilayer traversed by a current," *Phys. Rev. B*, vol. 54, no. 13, pp. 9353–9358, 1996.

[353] M. Tsoi, A. G. M. Jansen, J. Bass, W.-C. Chiang, M. Seck, V. Tsoi, and P. Wyder, "Excitation of a Magnetic Multilayer by an Electric Current," *Phys. Rev. Lett.*, vol. 80, no. 19, pp. 4281–4284, 1998.

[354] E. B. Myers, D. C. Ralph, J. A. Katine, R. N. Louie, and R. A. Buhrman, "Current-Induced Switching of Domains in Magnetic Multilayer Devices," *Science*, vol. 285, no. 5429, pp. 867–870, 1999.

[355] S. Seki and M. Mochizuki, *Skyrmions in magnetic materials*. Springer, 2016.

[356] T. Miyadai, K. Kikuchi, H. Kondo, S. Sakka, M. Arai, and Y. Ishikawa, "Magnetic Properties of Cr1/3NbS2," *Journal of the Physical Society of Japan*, vol. 52, pp. 1394–1401, apr 1983.

[357] M. Shinozaki, S. Hoshino, Y. Masaki, J.-i. Kishine, and Y. Kato, "Finite-Temperature Properties of Three-Dimensional Chiral Helimagnets," *Journal of the Physical Society of Japan*, vol. 85, p. 074710, jun 2016.

[358] H. Hirori, K. Shinokita, M. Shirai, S. Tani, Y. Kadoya, and K. Tanaka, "Extraordinary carrier multiplication gated by a picosecond electric field pulse," *Nature Communications*, vol. 2, p. 594, dec 2011.

[359] A. Pashkin, F. Junginger, B. Mayer, C. Schmidt, O. Schubert, D. Brida, R. Huber, and A. Leitenstorfer, "Quantum Physics With Ultrabroadband and Intense Terahertz Pulses," *IEEE Journal of Selected Topics in Quantum Electronics*, vol. 19, no. 1, p. 8401608, 2013.

[360] Y. Takahashi, R. Shimano, Y. Kaneko, H. Murakawa, and Y. Tokura, "Magnetoelectric resonance with electromagnons in a perovskite helimagnet," *Nature Physics*, vol. 8, p. 121, dec 2011.

[361] D. Hüvonen, U. Nagel, T. Rõõm, Y. J. Choi, C. L. Zhang, S. Park, and S.-W. Cheong, "Magnetic excitations and optical transitions in the multiferroic spin-1/2 system LiCu2O2," *Phys. Rev. B*, vol. 80, no. 10, p. 100402, 2009.

[362] S. Furukawa, M. Sato, and S. Onoda, "Chiral Order and Electromagnetic Dynamics in One-Dimensional Multiferroic Cuprates," *Phys. Rev. Lett.*, vol. 105, no. 25, p. 257205, 2010.

[363] J.-i. Kishine, K. Inoue, and Y. Yoshida, "Synthesis, Structure and Magnetic Properties of Chiral Molecule-Based Magnets," *Progress of Theoretical Physics Supplement*, vol. 159, pp. 82–95, 2005.

[364] Y. Togawa, Y. Kousaka, S. Nishihara, K. Inoue, J. Akimitsu, A. S. Ovchinnikov, and J. Kishine, "Interlayer magnetoresistance due to chiral soliton lattice formation in hexagonal chiral magnet CrNb3S6," *Phys. Rev. Lett.*, vol. 111, no. 19, p. 197204, 2013.

[365] L. Fidkowski and A. Kitaev, "Effects of interactions on the topological classification of free fermion systems," *Phys. Rev. B*, vol. 81, no. 13, p. 134509, 2010.

[366] L. Fidkowski and A. Kitaev, "Topological phases of fermions in one dimension," *Phys. Rev. B*, vol. 83, no. 7, p. 075103, 2011.

[367] H. C. Po, L. Fidkowski, T. Morimoto, A. C. Potter, and A. Vishwanath, "Chiral Floquet Phases of Many-Body Localized Bosons," *Phys. Rev. X*, vol. 6, no. 4, p. 041070, 2016.

[368] A. C. Potter, T. Morimoto, and A. Vishwanath, "Classification of Interacting Topological Floquet Phases in One Dimension," *Phys. Rev. X*, vol. 6, no. 4, p. 041001, 2016.

[369] L. Fidkowski, H. C. Po, A. C. Potter, and A. Vishwanath, "Interacting invariants for Floquet phases of fermions in two dimensions," *arXiv preprint arXiv:1703.07360*, 2017.

[370] J. Herbrych and X. Zotos, "Light-induced magnetization in a spin S=1 easy-plane antiferromagnetic chain," *Phys. Rev. B*, vol. 93, no. 13, p. 134412, 2016.

[371] A. A. Zvyagin, "Magnetization of a quantum spin system induced by a linear polarized laser," *Phys. Rev. B*, vol. 92, no. 5, p. 054405, 2015.

[372] C. den Broeck, J. M. R. Parrondo, and R. Toral, "Noise-Induced Nonequilibrium Phase Transition," *Phys. Rev. Lett.*, vol. 73, no. 25, pp. 3395–3398, 1994.

[373] B. K. Chakrabarti and M. Acharyya, "Dynamic transitions and hysteresis," *Rev. Mod. Phys.*, vol. 71, no. 3, pp. 847–859, 1999.

[374] H. Fujisaka, H. Tutu, and P. A. Rikvold, "Dynamic phase transition in a time-dependent Ginzburg-Landau model in an oscillating field," *Phys. Rev. E*, vol. 63, no. 3, p. 036109, 2001.

[375] V. Popkov, M. Salerno, and G. M. Schütz, "Asymmetric simple exclusion process with periodic boundary driving," *Phys. Rev. E*, vol. 78, no. 1, p. 011122, 2008.

[376] C. E. Rüter, K. G. Makris, R. El-Ganainy, D. N. Christodoulides, M. Segev, and D. Kip, "Observation of parity–time symmetry in optics," *Nature Physics*, vol. 6, p. 192, jan 2010.

[377] Y. C. Hu and T. L. Hughes, "Absence of topological insulator phases in non-Hermitian PT-symmetric Hamiltonians," *Phys. Rev. B*, vol. 84, no. 15, p. 153101, 2011.

[378] H. Schomerus, "Topologically protected midgap states in complex photonic lattices," *Opt. Lett.*, vol. 38, no. 11, pp. 1912–1914, 2013.

[379] G. Barontini, R. Labouvie, F. Stubenrauch, A. Vogler, V. Guarrera, and H. Ott, "Controlling the Dynamics of an Open Many-Body Quantum System with Localized Dissipation," *Phys. Rev. Lett.*, vol. 110, no. 3, p. 035302, 2013.

[380] S. Malzard, C. Poli, and H. Schomerus, "Topologically Protected Defect States in Open Photonic Systems with Non-Hermitian Charge-Conjugation and Parity-Time Symmetry," *Phys. Rev. Lett.*, vol. 115, no. 20, p. 200402, 2015.

[381] H. Cao and J. Wiersig, "Dielectric microcavities: Model systems for wave chaos and non-Hermitian physics," *Rev. Mod. Phys.*, vol. 87, no. 1, pp. 61–111, 2015.

[382] T. E. Lee, "Anomalous Edge State in a Non-Hermitian Lattice," *Phys. Rev. Lett.*, vol. 116, no. 13, p. 133903, 2016.

[383] P. Peng, W. Cao, C. Shen, W. Qu, J. Wen, L. Jiang, and Y. Xiao, "Anti-parity–time symmetry with flying atoms," *Nature Physics*, vol. 12, p. 1139, aug 2016.

[384] B. Peng, S. K. Özdemir, M. Liertzer, W. Chen, J. Kramer, H. Yilmaz, J. Wiersig, S. Rotter, and L. Yang, "Chiral modes and directional lasing at exceptional points," *Proceedings of the National Academy of Sciences*, vol. 113, no. 25, pp. 6845–6850, 2016.

[385] W. Chen, S. K. Özdemir, G. Zhao, J. Wiersig, and L. Yang, "Exceptional points enhance sensing in an optical microcavity," *Nature*, vol. 548, p. 192, aug 2017.

[386] D. Leykam, K. Y. Bliokh, C. Huang, Y. D. Chong, and F. Nori, "Edge Modes, Degeneracies, and Topological Numbers in Non-Hermitian Systems," *Phys. Rev. Lett.*, vol. 118, no. 4, p. 040401, 2017.

[387] Y. Xu, S.-T. Wang, and L.-M. Duan, "Weyl Exceptional Rings in a Three-Dimensional Dissipative Cold Atomic Gas," *Phys. Rev. Lett.*, vol. 118, no. 4, p. 045701, 2017.

[388] H. Zhou, C. Peng, Y. Yoon, C. W. Hsu, K. A. Nelson, L. Fu, J. D. Joannopoulos, M. Soljačić, and B. Zhen, "Observation of bulk Fermi arc and polarization half charge from paired exceptional points," *Science*, vol. 359, no. 6379, pp. 1009–1012, 2018.

[389] M. A. Bandres, S. Wittek, G. Harari, M. Parto, J. Ren, M. Segev, D. N. Christodoulides, and M. Khajavikhan, "Topological insulator laser: Experiments," *Science*, vol. 359, no. 6381, 2018.

[390] K. Kawabata, K. Shiozaki, M. Ueda, and M. Sato, "Symmetry and Topology in Non-Hermitian Physics," *arXiv preprint arXiv:1812.09133*, dec 2018.

[391] H. Zhou and J. Y. Lee, "Periodic Table for Topological Bands with Non-Hermitian Bernard-LeClair Symmetries," *arXiv preprint arXiv:1812.10490*, dec 2018.

[392] A. P. Schnyder, S. Ryu, A. Furusaki, and A. W. W. Ludwig, "Classification of topological insulators and superconductors," *AIP Conference Proceedings*, vol. 1134, pp. 10–21, 2009.

[393] M. S. Rudner and L. S. Levitov, "Topological Transition in a Non-Hermitian Quantum Walk," *Phys. Rev. Lett.*, vol. 102, no. 6, p. 065703, 2009.

[394] D. Kim, M. Ken, N. Kawakami, and H. Obuse, "Floquet Topological Phases Driven by PT Symmetric Nonunitary Time Evolution," *arXiv preprint arXiv:1609.09650*, 2016.

[395] L. Xiao, X. Zhan, Z. H. Bian, K. K. Wang, X. Zhang, X. P. Wang, J. Li, K. Mochizuki, D. Kim, N. Kawakami, W. Yi, H. Obuse, B. C. Sanders, and P. Xue, "Observation of topological edge states in parity–time-symmetric quantum walks," *Nature Physics*, vol. 13, p. 1117, jul 2017.

[396] D. Dhar, "An exactly solved model for interfacial growth," in *Phase transitions*, vol. 9, p. 51, GORDON BREACH SCI PUBL LTD C/O STBS LTD PO BOX 90, READING, BERKS, ENGLAND RG1 8JL, 1987.

[397] L.-H. Gwa and H. Spohn, "Bethe solution for the dynamical-scaling exponent of the noisy Burgers equation," *Phys. Rev. A*, vol. 46, no. 2, pp. 844–854, 1992.

[398] J. E. Moore and L. Balents, "Topological invariants of time-reversal-invariant band structures," *Phys. Rev. B*, vol. 75, no. 12, pp. 3–6, 2007.

[399] K. Shiozaki, *Topological insulators and superconductors: classification of topological crystalline phases and axion phenomena*. PhD thesis, Kyoto University, 2015.

[400] A. P. Schnyder and S. Ryu, "Topological phases and surface flat bands in superconductors without inversion symmetry," *Phys. Rev. B*, vol. 84, p. 060504, aug 2011.

[401] X.-L. Qi, T. L. Hughes, and S.-C. Zhang, "Topological invariants for the Fermi surface of a time-reversal-invariant superconductor," *Phys. Rev. B*, vol. 81, p. 134508, apr 2010.

[402] L. Fu, C. L. Kane, and E. J. Mele, "Topological insulators in three dimensions," *Phys. Rev. Lett.*, vol. 98, no. 10, p. 106803, 2007.

[403] Z. Wang, X.-L. Qi, and S.-C. Zhang, "Equivalent topological invariants of topological insulators," *New Journal of Physics*, vol. 12, no. 6, p. 065007, 2010.

[404] H. Spohn, "Approach to equilibrium for completely positive dynamical semigroups of N-level systems," *Reports on Mathematical Physics*, vol. 10, no. 2, pp. 189–194, 1976.

[405] H. Spohn, "An algebraic condition for the approach to equilibrium of an open N-level system," *Letters in Mathematical Physics*, vol. 2, no. 1, pp. 33–38, 1977.